

Nine-Year Wilkinson Microwave Anisotropy Probe (*WMAP*) Observations: Final Maps and Results

C. L. Bennett¹, D. Larson¹, J. L. Weiland¹, N. Jarosik², G. Hinshaw³, N. Odegard⁴, K. M. Smith^{5,6}, R. S. Hill⁴, B. Gold⁷, M. Halpern³, E. Komatsu^{8,9,10}, M. R.olta¹¹, L. Page², D. N. Spergel^{6,9}, E. Wollack¹², J. Dunkley¹³, A. Kogut¹², M. Limon¹⁴, S. S. Meyer¹⁵, G. S. Tucker¹⁶, E. L. Wright¹⁷

cbennett@jhu.edu

ABSTRACT

¹Dept. of Physics & Astronomy, The Johns Hopkins University, 3400 N. Charles St., Baltimore, MD 21218-2686

²Dept. of Physics, Jadwin Hall, Princeton University, Princeton, NJ 08544-0708

³Dept. of Physics and Astronomy, University of British Columbia, Vancouver, BC Canada V6T 1Z1

⁴ADNET Systems, Inc., 7515 Mission Dr., Suite A100 Lanham, Maryland 20706

⁵Perimeter Institute for Theoretical Physics, Waterloo, ON N2L 2Y5, Canada

⁶Dept. of Astrophysical Sciences, Peyton Hall, Princeton University, Princeton, NJ 08544-1001

⁷University of Minnesota, School of Physics & Astronomy, 116 Church Street S.E., Minneapolis, MN 55455

⁸Max-Planck-Institut für Astrophysik, Karl-Schwarzschild Str. 1, 85741 Garching, Germany

⁹Kavli Institute for the Physics and Mathematics of the Universe, Todai Institutes for Advanced Study, the University of Tokyo, Kashiwa, Japan 277-8583 (Kavli IPMU, WPI)

¹⁰Texas Cosmology Center and Dept. of Astronomy, Univ. of Texas, Austin, 2511 Speedway, RLM 15.306, Austin, TX 78712

¹¹Canadian Institute for Theoretical Astrophysics, 60 St. George St, University of Toronto, Toronto, ON Canada M5S 3H8

¹²Code 665, NASA/Goddard Space Flight Center, Greenbelt, MD 20771

¹³Oxford Astrophysics, Denys Wilkinson Building, Keble Road, Oxford, OX1 3RH, UK

¹⁴Columbia Astrophysics Laboratory, 550 W. 120th St., Mail Code 5247, New York, NY 10027-6902

¹⁵Depts. of Astrophysics and Physics, KICP and EFI, University of Chicago, Chicago, IL 60637

¹⁶Dept. of Physics, Brown University, 182 Hope St., Providence, RI 02912-1843

¹⁷UCLA Physics & Astronomy, PO Box 951547, Los Angeles, CA 90095-1547

We present the final nine-year maps and basic results from the *Wilkinson Microwave Anisotropy Probe* (*WMAP*) mission. The full nine-year analysis of the time-ordered data provides updated characterizations and calibrations of the experiment. We also provide new nine-year full sky temperature maps that were processed to reduce the asymmetry of the effective beams. Temperature and polarization sky maps are examined to separate cosmic microwave background (CMB) anisotropy from foreground emission, and both types of signals are analyzed in detail. We provide new point source catalogs as well as new diffuse and point source foreground masks. An updated template-removal process is used for cosmological analysis; new foreground fits are performed, and new foreground-reduced CMB maps are presented. We now implement an optimal C^{-1} weighting to compute the temperature angular power spectrum.

The *WMAP* mission has resulted in a highly constrained Λ CDM cosmological model with precise and accurate parameters in agreement with a host of other cosmological measurements.

When *WMAP* data are combined with finer scale CMB, baryon acoustic oscillation, and Hubble constant measurements, we find that Big Bang nucleosynthesis is well supported and there is no compelling evidence for a non-standard number of neutrino species ($N_{\text{eff}} = 3.84 \pm 0.40$). The model fit also implies that the age of the universe is $t_0 = 13.772 \pm 0.059$ Gyr, and the fit Hubble constant is $H_0 = 69.32 \pm 0.80$ km s $^{-1}$ Mpc $^{-1}$. Inflation is also supported: the fluctuations are adiabatic, with Gaussian random phases; the detection of a deviation of the scalar spectral index from unity, reported earlier by the *WMAP* team, now has high statistical significance ($n_s = 0.9608 \pm 0.0080$); and the universe is close to flat/Euclidean ($\Omega_k = -0.0027^{+0.0039}_{-0.0038}$).

Overall, the *WMAP* mission has resulted in a reduction of the cosmological parameter volume by a factor of 68,000 for the standard six-parameter Λ CDM model, based on CMB data alone. For a model including tensors, the allowed seven-parameter volume has been reduced by a factor 117,000. Other cosmological observations are in accord with the CMB predictions, and the combined data reduces the cosmological parameter volume even further. With no significant anomalies and an adequate goodness-of-fit, the inflationary flat Λ CDM model and its precise and accurate parameters rooted in *WMAP* data stands as the standard model of cosmology.

Subject headings: cosmic background radiation, cosmology: observations, early universe, dark matter, space vehicles, space vehicles: instruments, instrumentation: detectors, telescopes

1. Introduction

Since its discovery in 1965, the cosmic microwave background (CMB) has played a central role in cosmology. The discovery of the CMB (Penzias & Wilson 1965) confirmed a major prediction of the big bang theory and was difficult to reconcile with the steady state theory. The precision measurement of the CMB spectrum by NASA’s *Cosmic Background Explorer (COBE)* mission (Mather et al. 1990, 1994) confirmed the predicted CMB blackbody spectrum, which results from thermal equilibrium between matter and radiation in the hot, dense early universe. The *COBE* detection of CMB anisotropy (Smoot et al. 1992; Bennett et al. 1992; Kogut et al. 1992; Wright et al. 1992) established the amplitude of the primordial scalar fluctuations and supported the case for the gravitational evolution of structure in the universe from primordial fluctuations. While *COBE* mapped the full sky anisotropy on angular scales $> 7^\circ$, greater than the horizon size at decoupling, *WMAP* mapped the full sky CMB anisotropy on both superhorizon and subhorizon angular scales. *WMAP* provided independent replication and confirmation of the *COBE* maps on angular scales $> 7^\circ$ as well as the determination of precision cosmological parameters from fits to the well-established physics of the observed sub-horizon acoustic oscillations.

This paper together with its companion paper on cosmological parameter determination (Hinshaw et al. 2012) mark the nine-year and final official data release of the *Wilkinson Microwave Anisotropy Probe (WMAP)* mission. *WMAP* was designed to make full sky maps of the CMB in five frequency bands straddling the spectral region where the CMB-to-foreground ratio is near its maximum.

The overall *WMAP* mission design was described by Bennett et al. (2003c). The optical design was described by Page et al. (2003c) with the feeds and pre-flight beam patterns described by Barnes et al. (2002). The radiometer design and characterization was presented by Jarosik et al. (2003a).

The *WMAP* Science Team previously issued four major data releases, each with an accompanying set of publications. The first-year results included a presentation of the full sky maps and basic results (Bennett et al. 2003b), on-orbit radiometer characteristics (Jarosik et al. 2003b), beam profiles and window functions (Page et al. 2003a), Galactic emission contamination in the far-sidelobes of the beams (Barnes et al. 2003), a description of data processing and systematic measurement errors (Hinshaw et al. 2003a), an assessment of foreground emission (Bennett et al. 2003a), tests of CMB Gaussianity (Komatsu et al. 2003), the angular power spectrum (Hinshaw et al. 2003b), the temperature-polarization correlation (Kogut et al. 2003), cosmological parameters (Spergel et al. 2003), parameter estimation methodology Verde et al. (2003), implications for inflation (Peiris et al. 2003), and an interpretation of the temperature-temperature and temperature-polarization cross-power

spectrum peaks (Page et al. 2003b).

The three-year *WMAP* results included full use of the polarization data and improvements to temperature data analysis. The beam profile analysis, data processing changes, radiometer characterization, and systematic error limits were presented in Jarosik et al. (2007). An analysis of the temperature data carried through to the angular power spectrum was described by Hinshaw et al. (2007), and the corresponding polarization analysis was presented by Page et al. (2007). An analysis of the polarization of the foregrounds was presented by Kogut et al. (2007). The cosmological implications of the three-year results were summarized by Spergel et al. (2007).

The five-year *WMAP* results included updates on data processing, sky maps, and the basic results (Hinshaw et al. 2009), and updates on the beam maps and window functions (Hill et al. 2009). The five-year results also included improvements to characterizing the Galactic foreground emission (Gold et al. 2009) and the point source catalog Wright et al. (2009). The angular power spectra (Nolta et al. 2009), likelihoods and parameter estimates (Dunkley et al. 2009), a discussion of the cosmological interpretation of these data (Komatsu et al. 2009), and a Bayesian estimation of the CMB polarization maps (Dunkley et al. 2009) completed the five-year results.

The seven-year *WMAP* results comprised sky maps, systematic errors, and basic results (Jarosik et al. 2011), observations of planets and celestial calibration sources (Weiland et al. 2011), Galactic foreground emission (Gold et al. 2011), angular power spectra and cosmological parameters based only on *WMAP* data (Larson et al. 2011), cosmological interpretations based on a wider set of cosmological data (Komatsu et al. 2011), and a discussion of the goodness of fit of the Λ CDM model and potential anomalies (Bennett et al. 2011).

All of the *WMAP* data releases have been accompanied by an up-to-date Explanatory Supplement, including this final nine-year release (Greason et al. 2012). All *WMAP* data are public along with a large number of associated data products; they are made available by the Legacy Archive for Microwave Background Data Analysis (LAMBDA)¹.

Each *WMAP* release improved cosmological constraints through three types of advances: (1) the addition of *WMAP* data from extended observations; (2) improvements in the analysis of all of the *WMAP* data included in the release, including more optimal analysis approaches and the use of additional seasons of data to arrive at improved experiment models (e.g., by trending); and (3) improvements in non-*WMAP* cosmological measurements that are combined into the *WMAP* team’s combined likelihood analysis.

¹<http://lambda.gsfc.nasa.gov/>

This paper is organized as follows. The data processing changes from previous analyses are described in Section 2. Beam patterns and window functions are discussed in Section 3. Temperature and polarization sky maps are presented in Section 4. In Section 5 updated masks and an updated point source catalog are presented in addition to several different approaches to diffuse foreground evaluation, which are compared. Angular power spectra are given in Section 6. An analysis of the model goodness-of-fit and a discussion of anomalies are in Section 7. Cosmological implications are then presented in Section 8. Conclusions are given in Section 9. The accompanying paper (Hinshaw et al. 2012) presents an in-depth analysis of cosmological parameter solutions from various combinations of data and models and offers cosmological conclusions.

2. Data Processing: Overview and Updates

In this section we summarize changes in the *WMAP* data processing since the previous (seven-year) data release.

2.1. Time-Ordered Data

2.1.1. Data Archive Definition

The full nine-year *WMAP* archive of nominal survey data covers 00:00:00 UT 2001 August 10 (day number 222) to 00:00:00 UT 2010 August 10 (day number 222). Individual year demarcations begin at 00:00:00 UT on day number 222 of a year and end at 23:59:59 UT on day 221 of the following year. In addition to processing improvements, the *WMAP* nine-year release includes new data accumulated during mission years 8 and 9. Flight operations during those final two years included five scheduled station-keeping maneuvers, a lunar shadow passage, and special commanding procedures invoked within the last mission year to accommodate a compromised battery and transmitter. Overall, *WMAP* achieved a total mission observing efficiency of roughly 98.4%. The bulk of data excluded from science analysis use are dominated by time intervals that do not exhibit sufficient thermal stability.

2.1.2. Battery-Driven Thermal Effects

The *WMAP* solar arrays were exposed to constant sunlight so the battery was trickle charged for almost a decade. This activated an internal battery design imperfection and

caused battery voltage fluctuations in the final months of the mission (Greason et al. 2012). The resulting thermal variations were beyond what had been experienced earlier in the mission. A detailed analysis of time-ordered data with sky signal subtracted showed no detectable dependence on thermal variations associated with battery events, and thus preservation of data was preferred to excision. Out of an abundance of caution, time sequences that contained some of the more egregious temperature excursions were flagged as suspect and omitted from use in the nine-year data processing even though there was no specific evidence of adverse effects.

2.1.3. Pointing

For each observation, sky pointings of individual *WMAP* feed horns are computed using boresight vectors in spacecraft body coordinates coupled with the spacecraft attitude solution provided by on-board star trackers. After the first mission year, it was discovered that the apparent attitude computed by the trackers includes small errors induced by thermal flexure of the tracker mounting structure, as described by Jarosik et al. (2007). The amplitude of the flexure is time-dependent and driven by spacecraft temperature gradients. The spacecraft temperature responds both to solar heating and internal power dissipation, and is monitored by thermistors mounted at different locations on the spacecraft (Greason et al. 2012).

Telemetered spacecraft quaternions from the star trackers are corrected for this thermal effect at the very beginning of ground processing, when the raw science archive is created. Originally, we adopted a simple linear model, assuming a fixed angular rate of elevation change in units of arcsec per unit temperature change. As the mission progressed and additional data was used to improve the accumulated thermal profile history, the model has evolved to include angular corrections both in elevation (the dominant term) and azimuth. The nine-year quaternion correction model updates the rate coefficients in both azimuth and elevation, and uses readings from two separate thermistors to characterize the spacecraft temperature gradients. A more detailed description is provided by Greason et al. (2012). The residual pointing error after applying of the correction algorithm is computed using observations of Jupiter and Saturn. The upper limit of the estimated error is $10''$.

Beam boresight vectors have been updated based on the full nine-year archive. The largest difference between the seven-year and nine-year line-of-sight vectors is $3''$. Both the calibrated and uncalibrated *WMAP* archive data products include documentation of these line-of-sight vectors.

2.1.4. Calibration

Calibration of time-ordered data (TOD) from each *WMAP* radiometer channel requires the derivation of time-dependent gains (responsivity, in units of counts mK^{-1}) and baselines (in units of counts) that are used to convert raw differential data into temperature units. Algorithmic details and underlying concepts are set forth in Hinshaw et al. (2007). Jarosik et al. (2011) outline the calibration process as consisting of two general steps. The first step determines baselines and preliminary gains on an hourly or daily basis via an iterative process that combines a sky-map estimation with a calibration solution that updates with each iteration. Baselines and gains are computed by fitting sky-subtracted TOD to the dipole anisotropy induced by the motion of the *WMAP* spacecraft with respect to the CMB rest frame. The second calibration step determines absolute gain and fits a parameterized gain model to the dipole gains derived in the first step.

The form of the parameterized gain model is based on a physical understanding of radiometer performance, and uses telemetered measures of instrument temperatures and the radio frequency (RF) biases. The model provides a smooth characterization of the responsivity with time and allows higher time resolution than provided by the dipole-fit gains. For the nine-year analysis, we augment the gain model by adding a time-dependent linear trend term, $m\Delta t+c$, to the parameterized form presented in Jarosik et al. (2007). Here Δt is an elapsed mission time in days, and m , c are additional fit parameters. Physically, the linear trend can be thought of as a radiometer aging term. Without the addition of this term, model fits to the nine-year dipole gain measurements exhibited small systematic deviations from zero-mean residuals for nine of the 40 *WMAP* channels. The four Ka1 channels were most affected; the inclusion of the gain model aging term prevents an induced total gain error of about 0.1% in this band. Of the 40 *WMAP* radiometer channels, W323 alone has shown poor convergence in the iterative procedure that determines dipole-fit gains. Upon investigation we found that this problem is peculiar to the iterative algorithm and not the data itself. The W323 calibration has not been substantially affected in previous releases, but for the nine-year analysis the diverging mode was identified and we disallowed it in the gain model fit.

We continue to conservatively estimate an absolute calibration uncertainty of 0.2% (1-sigma), based on end-to-end gain recovery simulations. The overall change in calibration for the nine-year processing relative to the seven-year release is -0.031,+0.048,-0.005,+0.041 and +0.025 % for K-, Ka-, Q-, V- and W-bands respectively; a positive change indicates that features in the nine-year maps are slightly larger than those in the equivalent seven-year maps (i.e., a slight decrease in nine-year absolute gain compared to seven-year).

2.1.5. *Transmission Imbalance Factors*

The transmission efficiencies of sky signals through the A-side and B-side optical systems into each *WMAP* radiometer differ slightly from one another. This deviation from ideal behavior is characterized in map-making and data analysis through the use of time-independent transmission imbalance factors. The method by which these factors are determined from the *WMAP* data was described by Jarosik et al. (2007). The determination improves with additional data. These factors have been updated for the nine-year analysis and are presented in Table 1. The nine-year values compare well against the previously published seven-year values (Jarosik et al. 2011) within the quoted uncertainties.

2.2. Map-Making

2.2.1. *Standard Map-Making*

The standard *WMAP* map-making procedure is unchanged from the previous release and the resulting maps are used for the core cosmological analyses. Progress has been made on the algorithm for estimating the noise properties of the maps. The Stokes I noise levels (σ_0) are now more self-consistent between maps at angular resolution r9 and r10² than they had been previously. Another difference from previous analyses is that this procedure now determines the noise in the polarized maps from the Stokes Q and U year-to-year differences while including a spurious (“S”) map term, and a mean monopole is subtracted from each S map, as is done separately for Stokes I in the temperature map analysis. A detailed discussion is in Section 4.1.

Data are masked in the map-making process when one feed observes bright foregrounds (e.g., in the Galactic plane) while the corresponding differencing feed observes a far fainter sky. This masking prevents the contamination of faint pixels. Previous *WMAP* data analysis efforts used a single processing mask, based on the K-band temperature maps, to define which pixel-pairs to mask for all of the frequency bands. In the current processing we have changed to masking based on the brightness in each individual band.

²The map resolution levels refer to the HEALPix pixelization scheme (Gorski et al. 2005) where r4, r5, r9, and r10 refer to N_{side} values of 16, 32, 512, and 1024, respectively.

Table 1. Nine-year Fractional Transmission Imbalance

Radiometer	x_{im}	Uncertainty	Radiometer	x_{im}	Uncertainty
K11	-0.00067	0.00017	K12	0.00536	0.00014
Ka11	0.00353	0.00014	Ka12	0.00154	0.00008
Q11	-0.00013	0.00046	Q12	0.00414	0.00025
Q21	0.00756	0.00052	Q22	0.00986	0.00115
V11	0.00053	0.00020	V12	0.00250	0.00057
V21	0.00352	0.00033	V22	0.00245	0.00098
W11	0.01134	0.00199	W12	0.00173	0.00036
W21	0.01017	0.00216	W22	0.01142	0.00121
W31	-0.00122	0.00062	W32	0.00463	0.00041
W41	0.02311	0.00380	W42	0.02054	0.00202

Note. — The fractional transmission imbalance, x_{im} , and its uncertainty is determined from the nine-year observational data. The fractional transmission imbalance is defined as $x_{im} = (\epsilon_A - \epsilon_B)/(\epsilon_A + \epsilon_B)$, where ϵ_A and ϵ_B are the input transmission coefficients for the A- and B-side optics (Jarosik et al. 2003b). For an ideal differential radiometer, $x_{im} = 0$.

2.2.2. Beam Pattern Determination

The standard maps are used to subtract the background from Jupiter observations to create beam maps, as has been done in previous processing. We correct three seasons of Jupiter maps in the latter part of the mission for the proximity of Uranus and Neptune to Jupiter. Two-dimensional profiles from the newly updated beam map data are now also used as inputs for the new beam-symmetrized map-making procedure, described below.

2.2.3. Beam-Symmetrized Map-Making

In addition to the standard map-making, a new map-making procedure, described in Section 4.2, effectively deconvolves the beam sidelobes to produce maps with the true sky signal convolved by symmetrized beams. As a result of this new procedure, the previously reported map power asymmetry, which we speculated was due to the asymmetric beams and not cosmology (Bennett et al. 2011) has indeed been mitigated in the new beam-symmetrized maps.

In this paper we use the beam-symmetrized maps for diffuse foreground analysis (Section 5.3), but not for estimating the angular power spectrum and cosmological parameters. This is because the deconvolution process introduces correlations in the pixel noise on the beam scale and it is impractical to track these correlations at the full pixel resolution. Diffuse foreground analyses, on the other hand, used maps smoothed to a 1° scale. Appendix B of Hinshaw et al. (2007) demonstrated that the cosmological power spectrum, C_l , is insensitive to beam asymmetry at *WMAP*'s sensitivity level. (It is the 4-point bipolar power spectrum, not the 2-point angular power spectrum, that is sensitive to beam asymmetry.) Use of the beam symmetrized maps for high- l angular power spectrum estimation would invoke the need for high resolution noise covariance matrices, along with far greater computational and storage demands than are now feasible. Given that dense noise covariance matrices are computationally undesirable and the cosmological power spectrum is insensitive to beam asymmetry, we do not use beam-symmetrized maps for cosmology.

3. Beam Maps and Window Functions

The *WMAP* full beams are considered as a combination of main beams and sidelobes. These are treated separately in the data processing. The sidelobe beam patterns were determined from early mission observations of the moon together with pre-flight ground-based measurements, as described in Barnes et al. (2003). Potential contamination from side-

lobe pickup was computed and removed from the calibrated time-ordered data prior to map-making (Hinshaw et al. 2009). In this section, we address the main-beam response; treatment of the sidelobes remains unchanged from the seven-year release.

WMAP beams are measured using observations of the planet Jupiter that occur during the normal course of full-sky observing. Two Jupiter observing seasons of ~ 50 days each occur every 395 – 400 days. In the nine-year *WMAP* mission, a total of 17 seasons of Jupiter data were obtained. Time intervals for the four observing seasons occurring during the last two mission years are presented in Table 2; those for seasons 1 - 13 are presented in Table 1 of Weiland et al. (2011).

The beams enter into CMB data analysis primarily through the 10 beam transfer functions, b_l , which give the beam response in spherical harmonic space for each differencing assembly (DA). Beam response on the sphere is measured in a coordinate system fixed to the *WMAP* spacecraft (Barnes et al. 2003), and a computation of several steps is required to generate b_l . The nine-year beam analysis follows the process described previously by Hill et al. (2009) and Jarosik et al. (2011).

For a given DA, Jupiter is observed with only one feed at a time, so initially the A and B side beams are mapped separately. After correction for the static sky background, the data are coadded in a planar grid surrounding each of the 20 A- and B-side boresights. A physical optics code³ is used to compute beam models, which are optimized by χ^2 minimization using a modified conjugate gradient algorithm. Two minor refinements were added to this process for the nine-year analysis: first, a more rigorous treatment of the removal of the Galactic signal was adopted by including the common-mode loss imbalance term; in practice this is a small effect since strong Galactic signals are masked from use in the beam archive. Second, computation of the interpolated beam model utilized an increase in secondary mirror samplings from 200×200 to 235×235 ; this produced a smoother far-field tail for the W2 and W3 DAs.

Standard processing nominally rejects from analysis those Jupiter observations whose sky positions lie within a 7° radius of other planets. Table 2 shows the seasonal range of projected sky separations between Jupiter and planets that lie within the exclusion radius for the last three observing seasons. Based on projected proximity to Uranus or Neptune, application of nominal exclusion criteria would have excised these three Jupiter seasons from use. To preserve the ability to characterize the beam response during the latter part of the mission, we chose instead to correct the last three seasons of Jupiter data for excess contributions from Uranus and Neptune. Excess response from these planets is computed and

³DADRA: Y. Rahmat-Sahmi, W. Imbriale, & V. Galindo-Israel 1995, YRS Associates, rahmat@ee.ucla.edu

removed from each Jupiter observation assuming that the response to Uranus and Neptune may be modeled using a symmetrized beam template with peak response inferred from Weiland et al. (2011). An estimate of the magnitude of the correction is provided in the last column of Table 2, provided as a percentage contribution in excess of the uncontaminated integrated Jupiter beam response for each season. Observations which occur when Jupiter’s sky coordinates lie within the confines of a spatial “Galaxy mask” are also excluded from use in the analysis (Weiland et al. 2011). During observing season 14, the Galactic latitude of Jupiter is $\sim -18^\circ$, close enough to the Galactic plane that some observations are rejected based on the masking criterion. Masking is frequency dependent: roughly 30% of season 14 K-band observations are excluded, decreasing to 17% for Ka, 13% for Q and less than 0.1% for V- and W-bands.

For each DA, the Jupiter data for sides A and B are combined with the best-fit models in a “hybrid” beam map, which is used to construct the symmetrized radial beam profile, $b(\theta)$. A Legendre transform gives b_l . The beam hybridization procedure is described in detail by Hill et al. (2009). Essentially, the process edits the Jupiter TOD by replacing faint, noisy Jupiter samples with noise-free predicted values taken from the 2-dimensional beam model. This process is controlled by one parameter for each DA, the threshold gain, B_{thresh} : all observed beam samples with gain lower than B_{thresh} are replaced with their counterpart model values. This test is applied to the model samples, rather than the observed ones, in order to avoid bias from observational noise. B_{thresh} is optimized statistically for each DA using a Monte Carlo method, whereby uncertainty belonging to the beam model is traded against the noise in the observed data points. The figure of merit to be minimized is the uncertainty of the resultant solid angle in the hybridized beam. For this purpose, the error in the model is assumed to be a 100% uncertainty in the overall scaling of the low-sensitivity “tails,” which is the only portion of a beam model that is used in the hybrid. For the nine-year data, B_{thresh} is set 1 dB lower than for the seven-year data; values are 2, 3, 5, 6 and 9 dBi for K- through W-bands, respectively.

Hill et al. (2009) give the procedure for transforming the hybrid beam profiles into beam transfer functions. This computation also yields main beam solid angles and estimates of the temperature of the Jupiter disk. Beam-related quantities are summarized in Table 3. The last three columns list quantities that are valid for a point source with spectral index $\alpha = -0.1$ (flux $F_\nu \propto \nu^\alpha$), typical of sources in the *WMAP* point source catalog. They were determined as described in Jarosik et al. (2011), except a small correction for bandpass drift was included in the calculation of effective frequency for K-, Ka-, Q-, and V-bands as described in Appendix A.

The nine-year and seven-year b_l are consistent with each other, although the b_l for W4

is about 0.6% higher in the nine-year analysis than in the seven-year analysis for $l > 100$, a shift that is at the edge of the error band.

The error bands for b_l are computed using Monte Carlo simulations of the beam map hybridization; details of the simulations follow the description provided in Hill et al. (2009). As Jupiter observations have accumulated over the *WMAP* mission lifetime, the contribution of the model tails to the hybrid beam has become less important. The nine-year hybrid beams are data dominated: for each of the ten beams, less than 0.25% of the integrated hybrid beam response is attributable to the model tails.

4. Map-making

4.1. Standard Map Processing

4.1.1. Individual Band Processing Masks

The algorithm used to reconstruct sky maps from differential data masks selected observations to minimize artifacts associated with regions of high foreground intensity. (Jarosik et al. 2011). Observations for which one of the telescope beams is in a region of high foreground intensity gradients while the other is in a low gradient region are only applied to the pixel in the high foreground region as the map solutions are generated. This ‘asymmetric’ masking suppresses map reconstruction artifacts in the low foreground emission regions used for CMB analysis. These artifacts arise from small variations in the power sampled by the telescope beams for different observations that fall within the same map pixel. The variations result from a combination of the finite pixel size and beam ellipticity that both couple to spatial intensity gradients. A processing mask is used to delineate the regions of high foreground intensity gradients. Previous data releases used a common processing mask for all frequency bands based on the K-band temperature maps, even though the foreground intensities vary greatly by band. The current release uses different masks for each frequency band and therefore utilizes the data more efficiently.

Masks for each frequency band are generated using an algorithm that estimates the magnitude of processing artifacts in each r4 pixel given the *WMAP* scan pattern, a candidate processing mask and the seven-year map of the sky temperature in that band. The magnitude of artifacts, ξ , in a resolution r4 pixel, p_4 , is modeled as proportional to the mean magnitude of the temperature gradients within all the reference pixels used in the

observations contributing to the original pixel,

$$\xi(p_4, n) \simeq \frac{\alpha}{N_{tot}(p_4, n)} \left[\sum_{p_A(i)=p_4} w_n(p_B(i)) |\nabla T(p_B(i))| + \sum_{p_B(i)=p_4} w_n(p_A(i)) |\nabla T(p_A(i))| \right], \quad (1)$$

$$N_{tot}(p_4, n) = \sum_{p_A(i)=p_4} w_n(p_B(i)) + \sum_{p_B(i)=p_4} w_n(p_A(i)). \quad (2)$$

Here $p_A(i)$ and $p_B(i)$ are the r4 pixel indices for the A and B side beams for TOD observation i , w_n represents a candidate processing mask with n pixels masked, and the sums are over observations for which the A-side beam and B-side beam point to pixel p_4 . The proportionality constant α was evaluated as the amplitude of the response for each telescope beam as it was rotated about its axis while viewing a uniform temperature gradient, yielding values from 0°032 to 0°087 for the different beams. The magnitude of the temperature gradient in each r4 pixel is approximated as the standard deviation of the r9 pixels comprising each r4 pixel

$$|\nabla T(p_4)| \simeq \beta \cdot [\text{var}(p_9 \in p_4) - \sigma^2(p_4)]^{1/2}, \quad (3)$$

$$\sigma^2(p_4) = \frac{\sum_{p_9 \in p_4} \sigma_0^2 / N_{obs}(p_9)}{\sum_{p_9 \in p_4} 1}, \quad (4)$$

where the last term in Equation (3) removes the bias introduced by the radiometer noise, σ_0 is the noise for one observation and $N_{obs}(p_9)$ is the number of observations in r9 pixel p_9 . The constant $\beta \simeq 1.1 \text{ deg}^{-1}$ for r4 pixels.

Figure 1 shows a map of $\xi(p_4, 0)$ for the Ka1 DA with no pixels masked in the candidate processing mask ($n=0$). The highest value areas in this map correspond to regions that are $\approx 140^\circ$ from the Galactic center corresponding to the spacing between the *WMAP* A-side and B-side telescope beams. Processing masks for each frequency band are generated iteratively starting from an empty mask, $n = 0$. The r4 pixel added to the candidate mask w_n at each step is that which produces the greatest reduction in the mean value of $\xi(p_4, n)$ for the current value of n . The value of ξ is then recalculated with the updated candidate mask, w_{n+1} , and the process repeated. Figure 2 displays how the maximum and mean value of $\xi(p_4, n)$ vary as pixels are added to the mask. The mean and maximum values decrease rapidly as n increases and asymptotes to an approximately constant value for large n . The value maximum values in the asymptotic region is calculated as

$$\xi^{max}(n) = \max_{p_4} \xi(p_4, n), \quad (5)$$

$$\xi_{sat}^{max} = \overline{\xi^{max}(n)}, \quad 180 \geq n \geq 360. \quad (6)$$

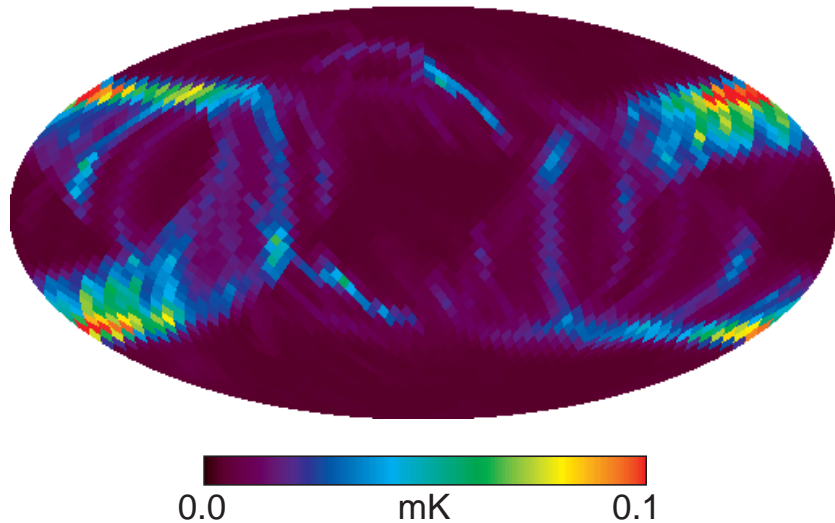


Fig. 1.— The estimated level of artifacts (ξ) that would have occurred in the Ka-band map if no processing mask had been used. Band-dependent processing masks were used and tailored to minimize these artifacts when converting from time-ordered to sky map data. This map is in Galactic coordinates and the high intensity regions arise from observations when one of the beams is near the Galactic center and the processing mask is not used. (See Figure 17 to compare with the analysis sky cuts.) Since bright artifacts originate primarily from beam crossings of bright Galactic plane regions, the nature of the unmasked artifact pattern is similar for all DAs. Although the patterns are similar for all bands, the highest amplitude artifacts occur in K- and Ka- bands because these have the brightest foregrounds. To prevent significant artifacts, processing masks are constructed for each band by growing the number of pixels in the mask until ξ is sufficiently reduced. The estimated mean residual level of artifacts ($\bar{\xi}$) is given in Table 4. We required $\bar{\xi} < 5 \mu\text{K}$ for all but K-band. Construction of the K-band mask is more complex (see text) yet still achieves $\bar{\xi} < 8 \mu\text{K}$.

(A color version of this figure is available in the online journal.)

These steps are executed for each DA and masks for the Ka1-, Q-, V-, and W-band DAs are selected by choosing the smallest value of n for which $\xi^{max}(n) < 1.15 \xi_{sat}^{max}$. This criterion was selected by requiring that $\bar{\xi} < 5\mu\text{K}$ for Ka-, Q-, V- and W-bands and that the resulting Q-band mask have approximately the same number of excluded pixels as the mask used in earlier data releases. The mask created in this manner for the Ka1 DA is the final processing mask. Masks for frequency bands with multiple DAs are formed by merging the individual DA masks such that if a pixel was masked in either of the DA masks it is masked in the combined mask. The K-band processing mask requires special treatment due to the brightness of the foregrounds. Applying the criterion above yields a very large sky mask that leaves many pixels with few or no observations causing convergence problems in the conjugate gradient map solution. The adopted K-band processing mask is the largest w_n formed with K-band inputs for which the sky map solution converges for all years except year 2. Year 2 is particularly problematic due to the location of Jupiter. Achieving convergence requires selection of the w_{270} mask and reduction of the Jupiter exclusion radius to $2^\circ.5$. Even with these special considerations the size of the processing mask is still substantially larger than used in previous data releases and should result in reduced artifacts. Table 4 summarizes the mask sizes and planet exclusion radii for the nine-year maps.

4.1.2. Summary of Standard Map-making

The time-ordered-data (TOD), \mathbf{d} , for a differential radiometer sensitive only to a Stokes I signal may be written as

$$\mathbf{d} = \mathbf{M}\mathbf{t} + \mathbf{n}. \quad (7)$$

Here \mathbf{M} is a sparse $N_t \times N_p$ matrix that contains information about the scan pattern and transforms the input sky signal array, \mathbf{t} , into a sequence of differential observations, \mathbf{d} . The number of time-ordered observations is given by N_t , the number of pixels in array \mathbf{t} is N_p , and \mathbf{n} is an N_t element array representing the radiometer noise. For the standard map processing each row of \mathbf{M} contains two non-zero elements representing the weights given to the input map pixels nearest the A and B-side telescope lines-of-sight (LOS). The first step in generating a sky map is evaluation of the “iteration zero” map,

$$\tilde{\mathbf{t}}_0 = \mathbf{M}_{am}^T \mathbf{N}^{-1} \mathbf{d}, \quad (8)$$

where \mathbf{M}_{am}^T is the transpose of a masked version of the observation matrix, and \mathbf{N}^{-1} is the inverse of the radiometer noise covariance matrix,

$$\mathbf{N}^{-1} = \langle \mathbf{nn}^T \rangle^{-1}, \quad (9)$$

Table 2. WMAP Jupiter Observing Seasons (2008-2010)

Season ^a	Begin	End	Nearby Planet ^b	Projected Separation ^c	% excess ^d
14	2008 Aug 21	2008 Oct 06
15	2009 May 17	2009 Jul 03	Neptune	0.4° - 2.4°	0.4 - 0.2
16	2009 Sep 26	2009 Nov 10	Neptune	3.8° - 6.8°	0.08 - 0.0
17	2010 Jun 24	2010 Aug 10	Uranus	0.5° - 3.1°	0.9 - 0.4

^aAn observing season is defined as a contiguous time interval during which an object is in the WMAP viewing swath. Observing seasons 1-13 are listed in Weiland et al. (2011)

^bJupiter sky coordinates are in proximity to those of the planet listed.

^cSeasonal range of projected separations between Jupiter’s position and that of the other planet.

^dEstimated excess integrated beam response, in %, that would have been contributed to the Jupiter beam by contaminating planet, if no correction had been applied. Provided as a range; the first number is for K-band, the last is for W-band; other frequencies are between these two values.

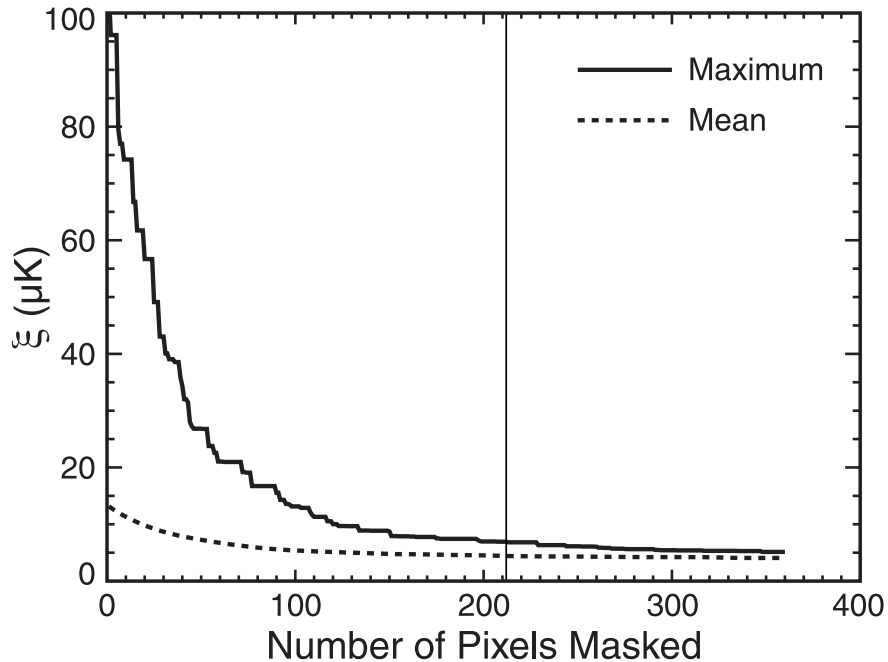


Fig. 2.— Plots of the maximum and mean magnitude of the estimated map artifacts (ξ) for Ka-band versus the number of pixels masked by the processing mask. The vertical line indicates the adopted mask which is the smallest mask for which $\max(\xi) < 1.15 \xi_{sat}^{max}$ as described in the text.

Table 3. WMAP Nine-year Main Beam Parameters

DA	$\Omega_{9\text{yr}}^S$ ^a (sr)	$\Delta(\Omega_{9\text{yr}}^S)/\Omega^S$ ^b (%)	$\frac{\Omega_{9\text{yr}}^S}{\Omega_{7\text{yr}}^S} - 1$ ^c (%)	G_m ^d (dBi)	$\nu_{\text{eff}}^{\text{ff}}$ ^e (GHz)	$\Omega_{\text{eff}}^{\text{ff}}$ ^f (sr)	$\Gamma_{\text{ff}}^{\text{g}}$ ($\mu\text{K Jy}^{-1}$)
For 10 Maps							
K1	2.469×10^{-4}	0.5	0.1	47.07	22.69	2.522×10^{-4}	250.6
Ka1	1.442×10^{-4}	0.4	0.0	49.40	32.94	1.465×10^{-4}	204.9
Q1	8.815×10^{-5}	0.5	-0.2	51.54	40.72	8.934×10^{-5}	219.7
Q2	9.113×10^{-5}	0.5	-0.1	51.40	40.51	9.234×10^{-5}	214.8
V1	4.164×10^{-5}	0.4	-0.1	54.80	60.09	4.226×10^{-5}	213.3
V2	4.236×10^{-5}	0.4	0.1	54.72	60.96	4.283×10^{-5}	204.5
W1	2.038×10^{-5}	0.4	-0.2	57.90	92.87	2.040×10^{-5}	185.0
W2	2.204×10^{-5}	0.4	0.2	57.56	93.43	2.203×10^{-5}	169.2
W3	2.135×10^{-5}	0.5	-0.2	57.70	92.44	2.135×10^{-5}	178.4
W4	1.994×10^{-5}	0.5	-0.6	57.99	93.22	1.997×10^{-5}	187.6
For 5 Maps							
K	2.469×10^{-4}	0.5	0.1	47.07	22.69	2.522×10^{-4}	250.6
Ka	1.442×10^{-4}	0.4	0.0	49.40	32.94	1.465×10^{-4}	204.9
Q	8.964×10^{-5}	0.5	-0.2	51.47	40.62	9.084×10^{-5}	217.2
V	4.200×10^{-5}	0.4	0.0	54.76	60.52	4.255×10^{-5}	208.9
W	2.093×10^{-5}	0.5	-0.2	57.78	92.99	2.094×10^{-5}	180.0

^aSolid angle in azimuthally symmetrized beam.

^bRelative error in Ω^S .

^cRelative change in Ω^S between nine-year and seven-year analyses.

^dForward gain = maximum of gain relative to isotropic, defined as $4\pi/\Omega^S$. Values of G_m in Table 2 of Hill et al. (2009) were taken from the physical optics model, rather than computed from the solid angle in the table, and therefore are slightly different.

^eThe effective center frequency for a point source with flux spectral index $\alpha = -0.1$. The estimated uncertainty, due to uncertainties in the pre-flight passband response measurements, is 0.1% for all DAs.

^fThe effective beam solid angle for a point source with flux spectral index $\alpha = -0.1$. The uncertainties are estimated as 0.5, 0.4, 0.5, 0.4, and 0.5% for K-, Ka-, Q-, V-, and W-band DAs, respectively. These include contributions from uncertainty in the beam solid angles, $\Delta(\Omega_{9\text{yr}}^S)/\Omega^S$ (column 3), and uncertainty in the correction of pre-flight forward gain measurements for scattering described in Jarosik et al. (2011).

^gConversion factor to obtain flux density from the peak WMAP antenna temperature, for a point source with flux spectral index $\alpha = -0.1$. Uncertainties in these factors are estimated as 0.6, 0.4, 0.5, 0.5 and 0.7% for K-, Ka-, Q-, V- and W-band DAs respectively. These include contributions from uncertainty in the beam solid angles, $\Delta(\Omega_{9\text{yr}}^S)/\Omega^S$ (column 3), uncertainty in the pre-flight passband response measurements, and uncertainty in the correction of pre-flight forward gain measurements for scattering described in Jarosik et al. (2011).

with the angle brackets representing an average. The masking contained in $\mathbf{M}_{\text{am}}^{\text{T}}$ prevents contamination of regions of the map with low foreground emission that can occur when one of the telescope beams is in a region of high foreground emission. (See Section 4.1.1.) The reconstructed sky map, $\tilde{\mathbf{t}}$, is then calculated by solving

$$\tilde{\mathbf{t}} = (\mathbf{M}_{\text{am}}^{\text{T}} \mathbf{N}^{-1} \mathbf{M})^{-1} \tilde{\mathbf{t}}_0. \quad (10)$$

The form of matrix \mathbf{M} described above ignores the effects of the finite *WMAP* beam sizes since each observation is modeled using only the value of the input sky signal nearest the LOS direction. The actual radiometric data is an average of the input sky signal spatially weighted by the beam response. Each row of \mathbf{M} should therefore contain additional non-zero elements describing the signal contribution from the off-axis beam response. If the beam response was the same for the A and B side beams and azimuthally symmetric about the LOS, the observation matrix including the off-axis signal contributions, \mathbf{M}_s , could be written in the form

$$\mathbf{M}_s = \mathbf{M}\mathbf{C}, \quad (11)$$

where \mathbf{C} is an $N_p \times N_p$ element matrix that performs a convolution by the symmetric beam pattern. Substituting \mathbf{M}_s for \mathbf{M} in Equation (7) shows that in this limit the sky map reconstructed using Equation (10) is the input map convolved by the symmetric beam pattern, $\tilde{\mathbf{t}}_c = \mathbf{C}\mathbf{t}$.

Following the approach discussed above, we present the nine-year temperature (Stokes I) full sky maps in Figure 3. The corresponding Stokes Q and Stokes U full sky maps are shown in Figures 4 and 5, respectively. Figure 6 shows the nine-year polarized intensity maps of $P = (Q^2 + U^2)^{0.5}$ with superposed polarization angle line segments where the signal-to-noise ratio exceeds unity.

Table 4. Map Generation Masking Parameters

Band	masked pixels (of 3072 total)	$\bar{\xi}$ (μK)	Planet Exclusion Radii (in $^\circ$)				
			Mars	Jupiter	Saturn	Uranus	Neptune
K(yr \neq 2)	312	7.12	2.0	3.0	2.0	2.0	2.0
K (yr = 2)	270	7.59	2.0	2.5	2.0	2.0	2.0
Ka	212	4.46	1.5	2.5	1.5	1.5	1.5
Q	201	4.31	1.5	2.5	1.5	1.5	1.5
V	125	3.78	1.5	2.2	1.5	1.5	1.5
W	98	3.66	1.5	2.0	1.5	1.5	1.5

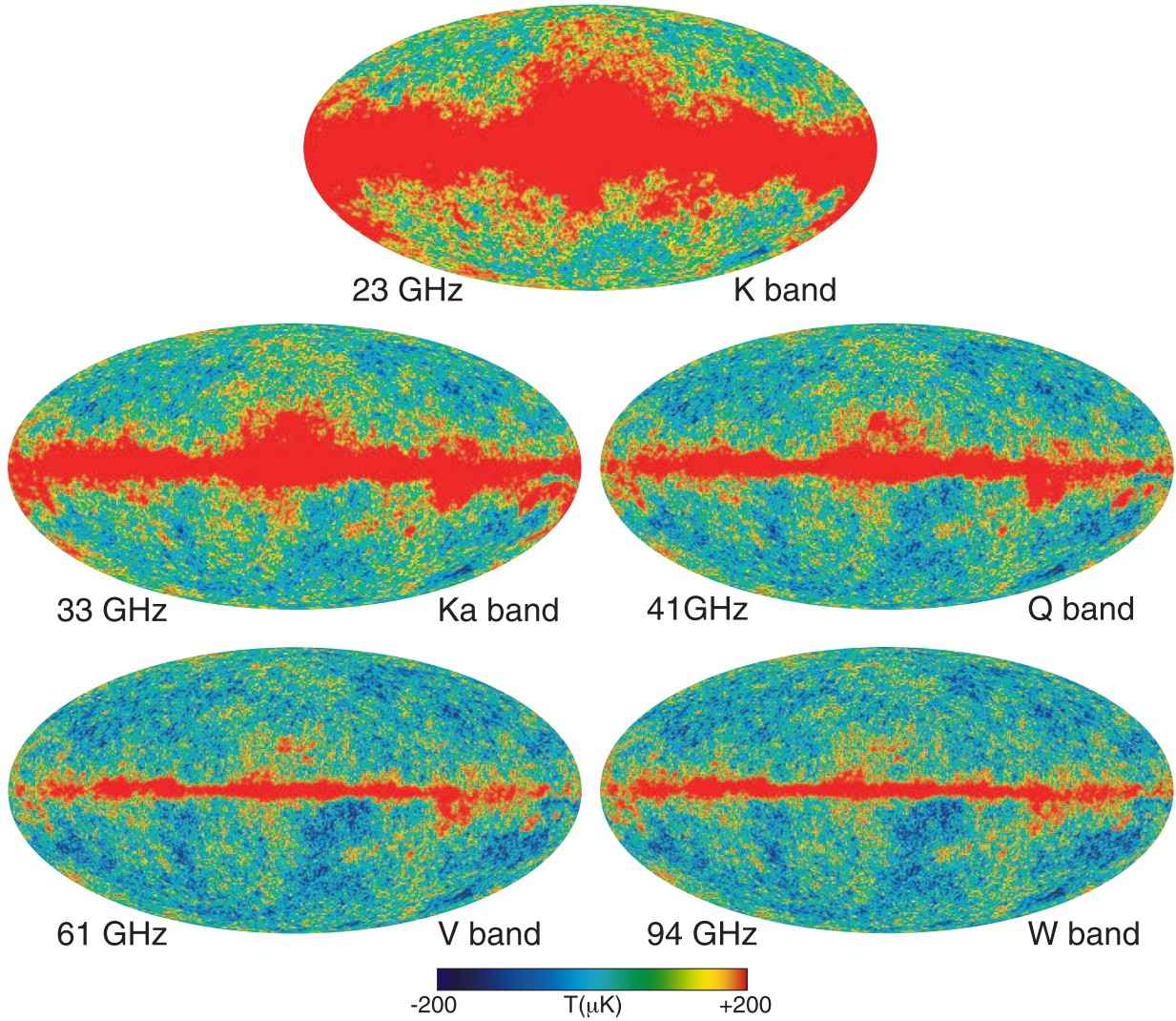


Fig. 3.— Nine-year temperature sky maps in Galactic coordinates shown in a Mollweide projection. Maps have been slightly smoothed with a $0\text{.}2$ Gaussian beam.
(A color version of this figure is available in the online journal.)

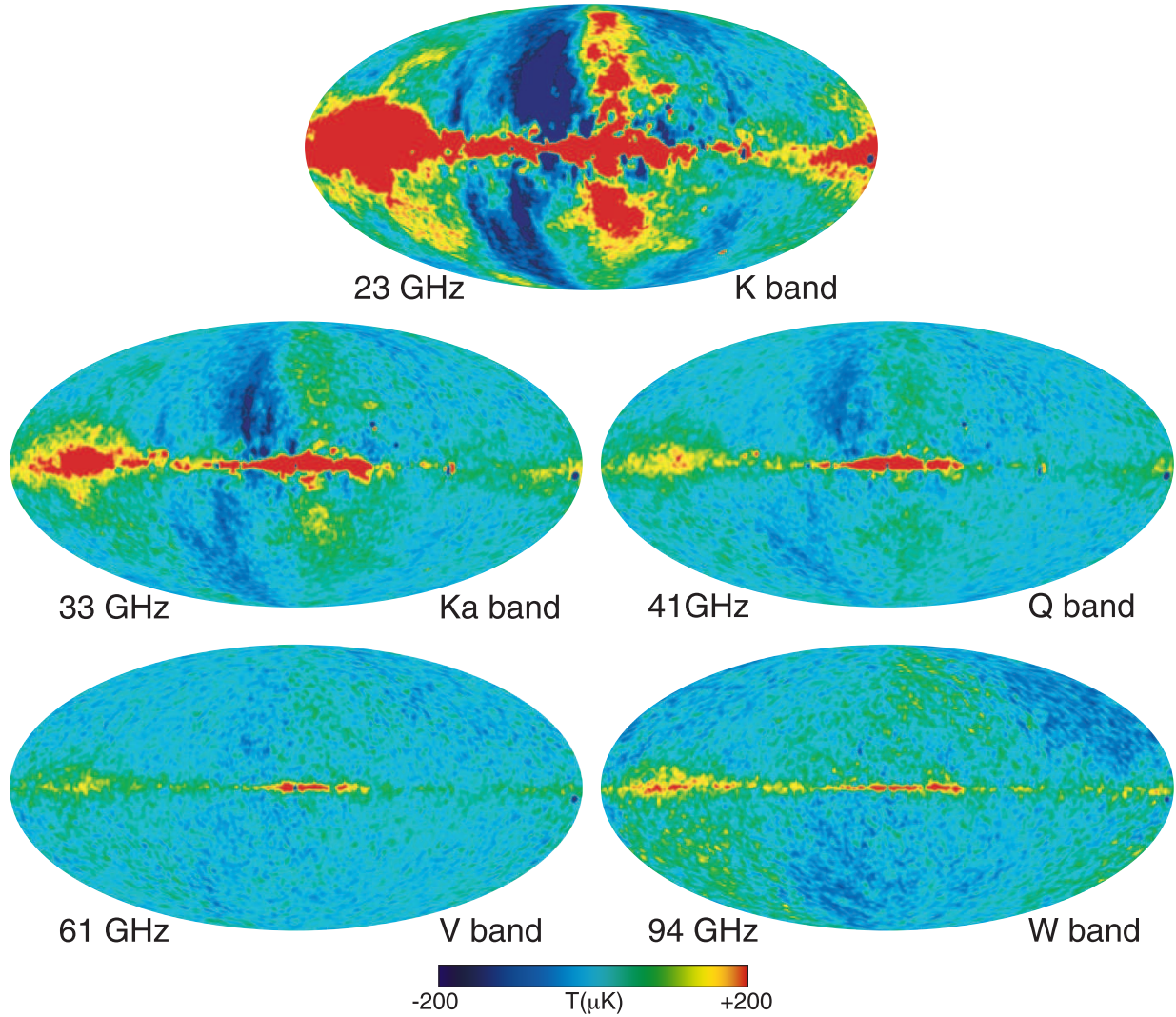


Fig. 4.— Nine-year Stokes Q polarization sky maps in Galactic coordinates shown in a Mollweide projection. Maps have been smoothed to an effective Gaussian beam of $2''.0$. The smooth large angular scale features visible in W-band, and to a lesser extent in V-band, are the result of a pair of modes that are poorly constrained in map-making, yet properly de-weighted in the analysis.

(A color version of this figure is available in the online journal.)

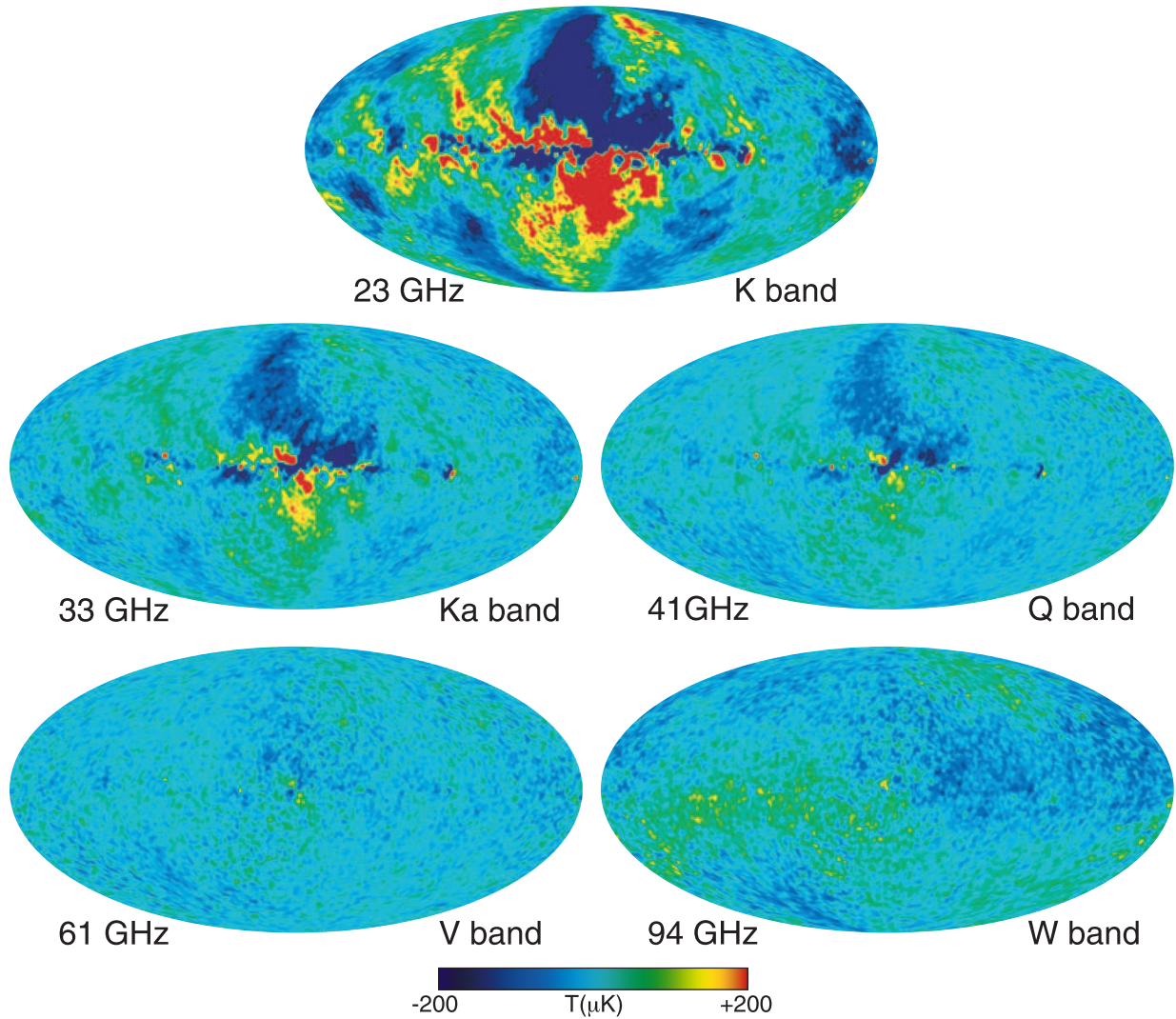


Fig. 5.— Nine-year Stokes U polarization sky maps in Galactic coordinates shown in a Mollweide projection. Maps have been smoothed to an effective Gaussian beam of $2''.0$. The smooth large angular scale features visible in W-band, and to a lesser extent in V-band, are the result of a pair of modes that are poorly constrained in map-making, yet properly de-weighted in the analysis.

(A color version of this figure is available in the online journal.)

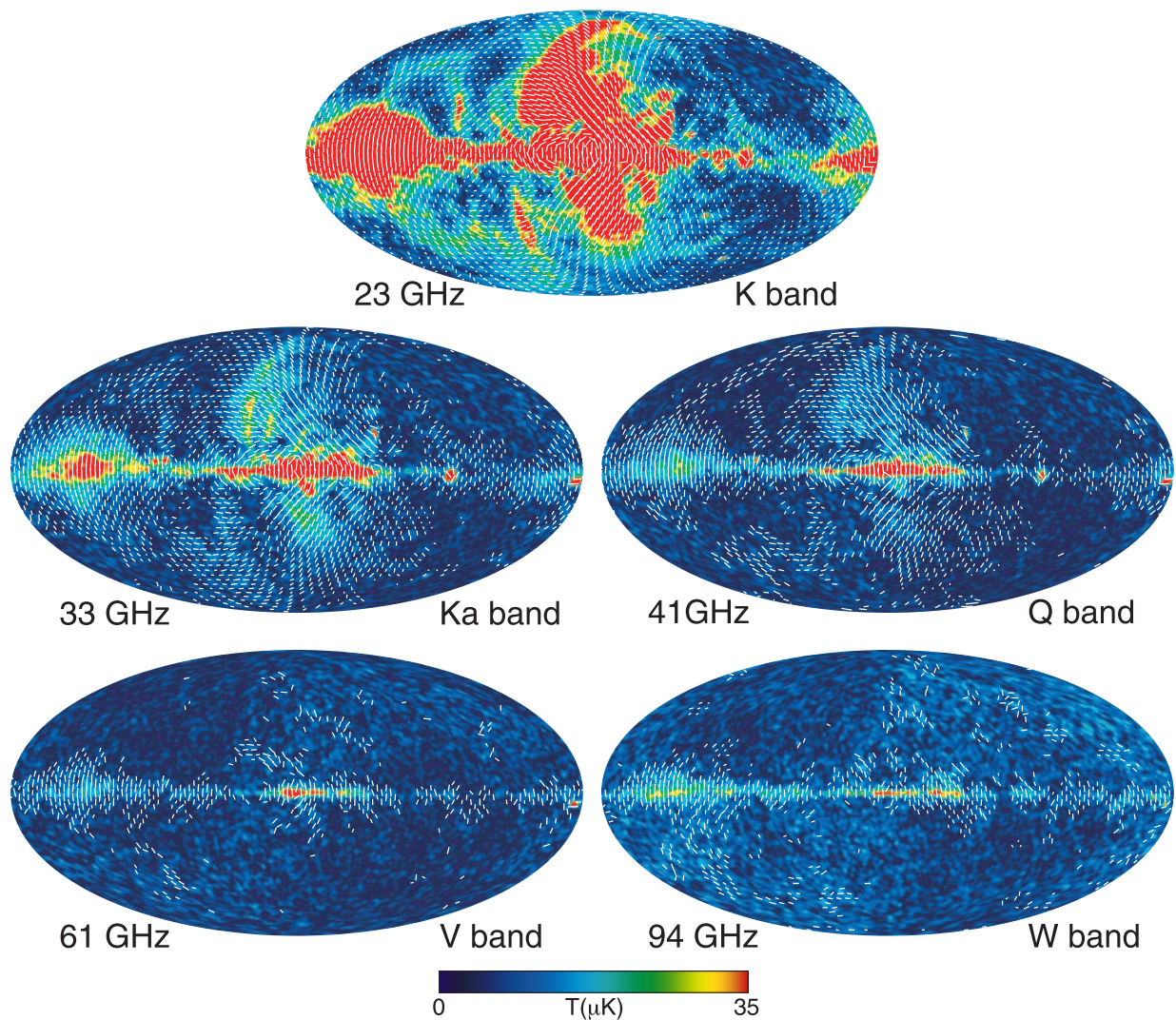


Fig. 6.— Nine-year polarized intensity (P) sky maps in Galactic coordinates shown in a Mollweide projection; $P = (Q^2 + U^2)^{0.5}$, where Q and U are Stokes parameters. Maps have been smoothed to an effective Gaussian beam of $2''.0$. Plotted line segments show polarization angles for HEALPix $n_{\text{side}} = 16$ pixels where the signal-to-noise exceeds 1.

(A color version of this figure is available in the online journal.)

4.1.3. Noise Characterization of the High Resolution Maps

The noise in the r9 and r10 maps is described assuming the radiometer noise distribution is stationary, has a white spectrum and is normally distributed. With these assumptions it can be shown that the noise component of a Stokes I sky map, \mathbf{t}_n , is given by (Jarosik et al. 2011)

$$\tilde{\mathbf{t}}_n = (\mathbf{M}^T \mathbf{M})^{-1} \cdot \mathbf{M}^T \mathbf{n}, \quad (12)$$

where \mathbf{M} is the mapping matrix as described in § 4.1.2 and \mathbf{n} is a vector of normally distributed random numbers that characterizes the radiometer noise,

$$\langle \mathbf{n} \rangle = 0, \quad \langle \mathbf{n} \mathbf{n}^T \rangle = \sigma_0^2 \mathbf{I}, \quad (13)$$

where the brackets indicate an ensemble average and σ_0 describes the noise amplitude. The pixel-pixel noise correlation matrix is then

$$\Sigma = \frac{\langle \mathbf{t}_n \mathbf{t}_n^T \rangle}{\sigma_0^2} = (\mathbf{M}^T \mathbf{M})^{-1}. \quad (14)$$

Ideally the value of σ_0 is obtained by evaluating

$$\sigma_0^2 N_{pix} = \langle \mathbf{t}_n^T \Sigma^{-1} \mathbf{t}_n \rangle, \quad (15)$$

where N_{pix} is the number of map pixels, but such a calculation is intractable with high resolution maps. In practice only the diagonal elements of Equation (15) are evaluated. Since

$$\Sigma^{-1} = \mathbf{M}^T \mathbf{M} \quad (16)$$

the diagonal elements of Σ^{-1} are simply the number of observations⁴ of each pixel, N_{obs} . Each data sample from a *WMAP* differential radiometer is a measure of the temperature difference between the sky locations at the A and B side telescope boresights. Reconstructing a map from differential data involves two different pixels for each observation, a pixel that is being updated and a reference pixel. The noise in each pixel therefore has contributions both from the noise in the radiometric data for each sample and noise in the value of the reference pixel. If σ_0 represents the radiometer noise for an individual sample, the noise contribution from the reference pixel is approximately $\sigma_0 / \sqrt{N_{obs}(p)}$, where $N_{obs}(p)$ is the number of observations used to calculate the value of the reference pixel, p . As the map resolution increases the mean value of N_{obs} decreases, making the reference pixel noise more

⁴The small correction terms arising from transmission imbalance in the radiometers, $1 \pm x_{im}$, are omitted from this equation for simplicity, but appear in the next, modified equation.

significant relative to the radiometer noise. The omission of the off-diagonal terms in the evaluation of Equation (15) ignores the contribution to the noise from the reference beam pixels in the evaluation of σ_0 . This effect is evident when the σ_0 values for r9 and r10 versions of the Stokes I sky maps are compared. The σ_0 values from the r10 maps have values from 0.3% (W-band) to 1.5% (K-band) higher than those obtained from the corresponding r9 sky maps. The low sampling rate of the K-band radiometer results in lower N_{obs} values and hence the largest effect.

A more accurate determination of σ_0 can be made by equating the diagonal elements of Equation (14) since these quantities are directly measurable from the sky maps. The diagonal elements of Σ may be calculated relatively simply given two well justified assumptions: 1) The sky map noise is uncorrelated between pixels; and 2) The reference pixels associated with each main pixel are distinct. With these assumptions diagonal elements of Σ are estimated as

$$\Sigma_{y,y} = \left[\sum_{i,p_A(i)=y} w(p_B(i)) \frac{(1+x_{im})^2}{1+1/N_{obs}(p_B(i))} + \sum_{i,p_B(i)=y} w(p_A(i)) \frac{(1-x_{im})^2}{1+1/N_{obs}(p_A(i))} \right]^{-1}, \quad (17)$$

where i is a sample index of the TOD and the sums are over observations for which the A-side and B-side beams observe pixel y . The processing mask is represented by w , which has value zero in masked pixels and unity elsewhere. The $1 \pm x_{im}$ factors are corrections arising from the transmission imbalance factors and N_{obs} represents the number of observations contained in the reference beam pixel of the sky map. The $1/N_{obs}$ terms in the denominators increase the value of $\Sigma_{y,y}$ to account for the additional noise arising from the reference beam pixels. In the limit where N_{obs} is very large for all observations the value of $\Sigma_{y,y}$ is simply $1/N_{obs}(y) = 1/\Sigma_{y,y}^{-1}$. The values of σ_0 obtained from r9 and r10 Stokes I maps, evaluated using diagonal elements of Equation (14), agree to $\approx 0.05\%$ with the worst discrepancy being $\approx 0.1\%$. This is a significant improvement relative to the former method.

The N_{obs} fields of the nine-year r9 and r10 sky maps now contain the reciprocals of the diagonal element of the Σ matrix as it is now considered a more accurate measure of the pixel noise. This change allows the map noise in each pixel to still be calculated as $N = \sigma_0/\sqrt{N_{obs}}$ providing that the values of σ_0 published with the nine-year analysis are used. Because the σ_0 values computed from r10 maps differ by less than 0.1% from those computed from r9 maps, the r9 values are adopted for all WMAP nine-year analysis.

These methods have been extended and applied to the Stokes Q and U maps and the spurious response map S. This change improved the agreement between the σ_0 values for the temperatures and polarization maps to $\approx 0.5\%$ from $\approx 1.1\%$ in earlier data releases. Table 5 gives the nine-year σ_0 values by DA for temperature (Stokes I) and polarization (Stokes

Q, Stokes U), and spurious response S.

4.2. Beam Symmetrized Map Processing

The *WMAP* telescope beams display varying degrees of asymmetry about the line-of-sight direction, with the amount of asymmetry related to the position of the feed horn relative to the center of the focal plane (Page et al. 2003a). The largest asymmetries appear in the lower frequency channels since their feed horns are furthest from the center of the focal plane. *WMAP* observes each map pixel a large number of times at various azimuthal orientations (rotations about the line-of-sight direction). The degree to which the beam asymmetry is manifest in the final sky maps depends on both the intrinsic beam asymmetry and the distribution of azimuthal beam orientations used to observe each pixel. A uniform set of finely spaced azimuth angles will result in a symmetric effective beam, while any deviations from a uniform distribution will couple some of the beam asymmetry into the sky map.

The *WMAP* scan pattern causes pixels near the ecliptic poles to be sampled relatively uniformly over a wide range of azimuthal angles, while pixels near the ecliptic plane are only sampled over a $\approx \pm 22.5^\circ$ degree range. This results in the effective beam shape varying with sky position; regions near the ecliptic poles have more symmetric effective beam shapes than those near the ecliptic plane. Each pixel is observed roughly the same number of times with the A-side and B-side beams, further symmetrizing the effective beam shape since the axis of asymmetry for the A and B side beams project to different sky directions.

The *WMAP* window functions are calculated from symmetrized beam profiles generated by azimuthally averaging beam maps obtained from observations of Jupiter. All *WMAP* data releases have window function uncertainties incorporated into the *WMAP* likelihood code. As described in Appendices A and B of Hinshaw et al. (2007), these are dominated by uncertainties in the shape of the symmetrized beam profile.

The effects of asymmetric beams (Page et al. 2003a; Hinshaw et al. 2007) were confirmed in numerical simulations by Wehus et al. (2009). More recently it was found with high statistical significance that the hot and cold spots near the ecliptic plane have a preferred ellipticity, while the angle-averaged small-scale power spectrum near the ecliptic plane is equal to the angle-averaged power spectrum near the ecliptic pole (Groeneboom & Eriksen 2009; Hanson et al. 2010). Hanson et al. (2010) and Bennett et al. (2011) suggested that this was likely due largely to the spatially varying effective beam shape and in this paper we confirm that hypothesis.

Figure 7 displays the supernova remnant Tau A as it appears in the year-1 K-band sky map. Tau A is compact relative to the K-band beam size (≈ 0.82 FWHM) and relatively isolated, so it approximates a point source for the purpose of mapping the effective beam shape. The beam asymmetry is clearly seen in both the sky map and in the residual map after removal of the best fit symmetrized beam profile. The symmetrized beam profile was fit to the map with 6 free parameters, 3 characterizing a baseline (x-slope, y-slope and offset), and three specifying the beam (x-position, y-position, and amplitude).

The *WMAP* nine-year data release includes a new set of Stokes I maps that have been processed to reduce the asymmetry of the effective beam. The processing deconvolves only the asymmetric portion of the beam from the data resulting in a sky map containing the true sky signal convolved with the symmetrized beam profile.

A more accurate representation of the signal component of *WMAP*'s TOD utilizes an observation matrix, \mathbf{M}_{ns} , parameterizing the total beam response, written as the sum of a component axisymmetric about the beam LOS, \mathbf{M}_{s} , and a non-axisymmetric component, \mathbf{M}_{n} ,

$$\mathbf{d} = \mathbf{M}_{\text{ns}}\mathbf{t}, \tag{18}$$

$$\mathbf{M}_{\text{ns}} = \mathbf{M}_{\text{s}} + \mathbf{M}_{\text{n}}. \tag{19}$$

Using Equation 11 the observation matrix may be expressed as

$$\mathbf{M}_{\text{ns}} = (\mathbf{M} + \mathbf{M}_{\text{n}}\mathbf{C}^{-1})\mathbf{C}. \tag{20}$$

Given this form of the TOD it is possible to solve for the input sky map convolved by the axisymmetric beam response, $\tilde{\mathbf{t}}_{\text{c}}$, by evaluating

$$\tilde{\mathbf{t}}_{\text{c}} = \mathbf{C}\mathbf{t} = [\mathbf{M}_{\text{am}}^{\text{T}}\mathbf{N}^{-1}(\mathbf{M} + \mathbf{M}_{\text{n}}\mathbf{C}^{-1})]^{-1} \tilde{\mathbf{t}}_{\mathbf{0}}. \tag{21}$$

The beam symmetrized maps contain the input sky signal convolved with the symmetrized beam profile independent of sky position. Figure 7 displays a map of the Taurus A region from a map processed in this manner. The improvement in the beam symmetry is evident in both the raw image and the residuals after removing the best fit symmetrized beam profile. These maps significantly improve the symmetry of the effective beam, but also have a larger window function uncertainty caused by the limited resolution and signal-to-noise ratio of the beam maps and numerical approximations needed to make their computation practical. Therefore, beam symmetrized maps are generated only for Stokes I and are not intended for the precise fitting of cosmological parameters, but should prove useful in foreground fitting, studying regions of compact emissions, and certain tests of non-Gaussianity. It should also be noted that deconvolving the asymmetric beam shape from the maps necessarily introduces

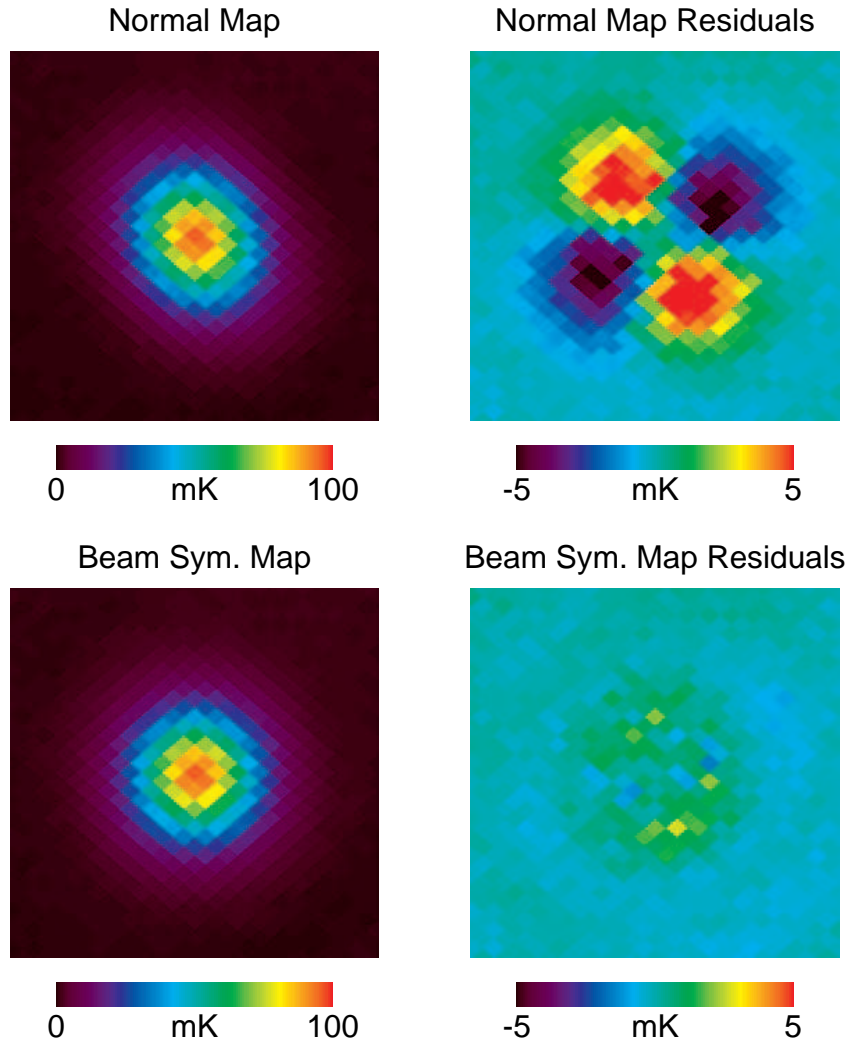


Fig. 7.— K-band images of supernova remnant Tau A (3C 144), at [J2000.0] position ($05^{\text{h}}34^{\text{m}}31^{\text{s}}$, $22^{\circ}01'$) from the first year of *WMAP* observations. The left panels display the total intensity and right the residuals after removal of a best fit circularly symmetric beam profile. The maps generated with the new partial deconvolution processing (bottom) display significantly reduced beam asymmetry compared with those generated with the standard processing (top). In other words, the apparent asymmetry in Tau A seen in the top left is a result of the asymmetric K-band beam and is not intrinsic to Tau A. The degree of a source’s apparent asymmetry is dependent on its sky position and the *WMAP* frequency at which it is observed: the effect is most pronounced for bright K-band sources at low ecliptic latitudes (Section 4.2). As such, we display the K-band observations of Tau A to demonstrate the effectiveness of the deconvolution in a worst case of beam asymmetry in the normally processed maps.

(A color version of this figure is available in the online journal.)

additional pixel-pixel noise correlations above those contained in the standard maps. No year-to-year correlations are introduced, so power spectra calculated from year-to-year cross spectra remain unbiased, but the uncertainty of the spectra cannot be accurately calculated based on the number of observations (N_{obs}) of each map pixel alone.

4.2.1. Processing Details

The beam symmetrized maps are generated by solving Equation (21) iteratively using a stabilized bi-conjugate gradient method (Barrett et al. 1994). In this procedure the product

$$\mathbf{M}_{\text{am}}^T \mathbf{N}^{-1} (\mathbf{M} + \mathbf{M}_n \mathbf{C}^{-1}) \cdot \tilde{\mathbf{t}}_{c,i} \quad (22)$$

is evaluated repeatedly and the solution $\tilde{\mathbf{t}}_{c,i}$ updated after each iteration, i , driving the value of this expression to $\tilde{\mathbf{t}}_0$. The product (22) is evaluated by looping through the TOD; each observation corresponds to multiplying one row of $\mathbf{M} + \mathbf{M}_n \mathbf{C}^{-1}$ by the current iteration of the solution, $\tilde{\mathbf{t}}_{c,i}$. The first term in each multiplication, $\mathbf{M}\tilde{\mathbf{t}}_{c,i}$, is the weighted sum of the map pixels values nearest the LOS directions of the two beams, corresponding to the differential sky signal smoothed by the axisymmetric beam response. Each row of the matrix \mathbf{M} contains two non-zero elements with values $(1 + x_{\text{im}})$ and $(-1 + x_{\text{im}})$, the weight factors for the A and B side beams. (The x_{im} term ($|x_{\text{im}}| \ll 1$) accounts for a small imbalance in radiometer response to beam filling signals from the A and B sides.)

The second term in the product of Equation (22), $\mathbf{M}_n \mathbf{C}^{-1} \tilde{\mathbf{t}}_{c,i}$, corresponds to the differential signal from the non-axisymmetric beam response for the current LOS and azimuthal beam orientations. The nonzero elements in each row of \mathbf{M}_n are the pixel weights of the non-axisymmetric beam response of the two beams, also weighted by the $(\pm 1 + x_{\text{im}})$ factors. To keep the computation time tractable only contributions within a radius r_{sl} (30 mrad for K-, Ka-band, 26 mrad for Q-, V-, and W-band) of the LOS of each beam are used. The circular regions contributing to the signal for the A and B beams do not overlap, so their contributions may be calculated separately then summed.

The matrix \mathbf{C}^{-1} performs a deconvolution by the symmetrized beam pattern. It is therefore rotationally symmetric and the product $\mathbf{M}_n \mathbf{C}^{-1}$ may be evaluated once for each beam, forming convolution kernels \mathbf{K}_A and \mathbf{K}_B . The contribution of $\mathbf{M}_n \mathbf{C}^{-1} \tilde{\mathbf{t}}_{c,i}$ for each beam is then evaluated by mapping these kernels to the corresponding pixels of $\tilde{\mathbf{t}}_{c,i}$ for the LOS and azimuthal orientation for each observation and summing their products.

Figure 8 illustrates the steps used in forming the kernel for the Q1 A-side beam. First (in panel *a*) a map of the non-axisymmetric beam response, \mathbf{M}_n , is formed on a Cartesian grid by subtracting the best fit symmetrized beam profile from the total beam profile in

Equation (19). Next the product $\mathbf{M}_n \mathbf{C}^{-1}$, is evaluated by performing a Wiener deconvolution of \mathbf{M}_n . A Wiener deconvolution is used to minimize the impact of noise on the deconvolved map. (In performing the Wiener weighting the signal component of the result was assumed to be proportional to the input, \mathbf{M}_n , while the noise was assumed to be white and its magnitude obtained from portions of the beam map far from the LOS direction.) Even using the Wiener weighting, some noise remains in the deconvolved maps at relatively large radii from the LOS direction. A cosine apodization function is therefore introduced to smoothly taper the value of the kernel to zero at radial distance r_{sl} from the beam LOS. This procedure eliminates artifacts in the maps that would be caused by a sharp cutoff of the kernel noise at the radius r_{sl} . The fidelity of the kernel is demonstrated in Figures 8e and 8f that show the kernel re-convolved with the symmetrized beam. After re-convolution the majority of the non-axisymmetric beam response is recovered without the introduction of excessive noise.

Ideally the kernel weights representing the non-axisymmetric beam response sum to zero for each observation. This is only approximately true in practice since the HEALPix pixelization used for the solution $\tilde{\mathbf{t}}_{c,1}$ and the Cartesian grid of the kernel are incommensurate, resulting in slightly different combinations of weights being used for different LOS directions and azimuthal beam orientations. This results in small variations of the total weight for observation of different points on the sky.

The mean value of a map generated by ideal differential data is unconstrained. The non-idealities in the radiometers parameterized by the transmission imbalance factors, x_{im} , weakly constrain the mean value of the maps, but occasionally maps solutions with relative large mean values are generated. The spatially varying total weights described above can couple to these mean values resulting in small spurious map features. This problem is remedied by subtracting the sum of the kernel weights used for each observation from the value in \mathbf{M} corresponding to the weight of the LOS pixel, resulting in a uniform weight for each observation. This choice insures that the total weight of the A and B side observations are $(1+x_{im})$ and $(-1+x_{im})$ respectively, guaranteeing that the beam symmetrized maps agree with the normal maps at angular scales larger than the characteristic size of the convolution kernels.

Figure 9 displays the ratio of the TT power spectra of the beam symmetrized maps to those of the normally processed maps and ratios as predicted in Hinshaw et al. (2007). The spectra from the different map processings agree exactly at low l as expected and agree with the predictions within 2% in regions of adequate signal-to-noise ratios.

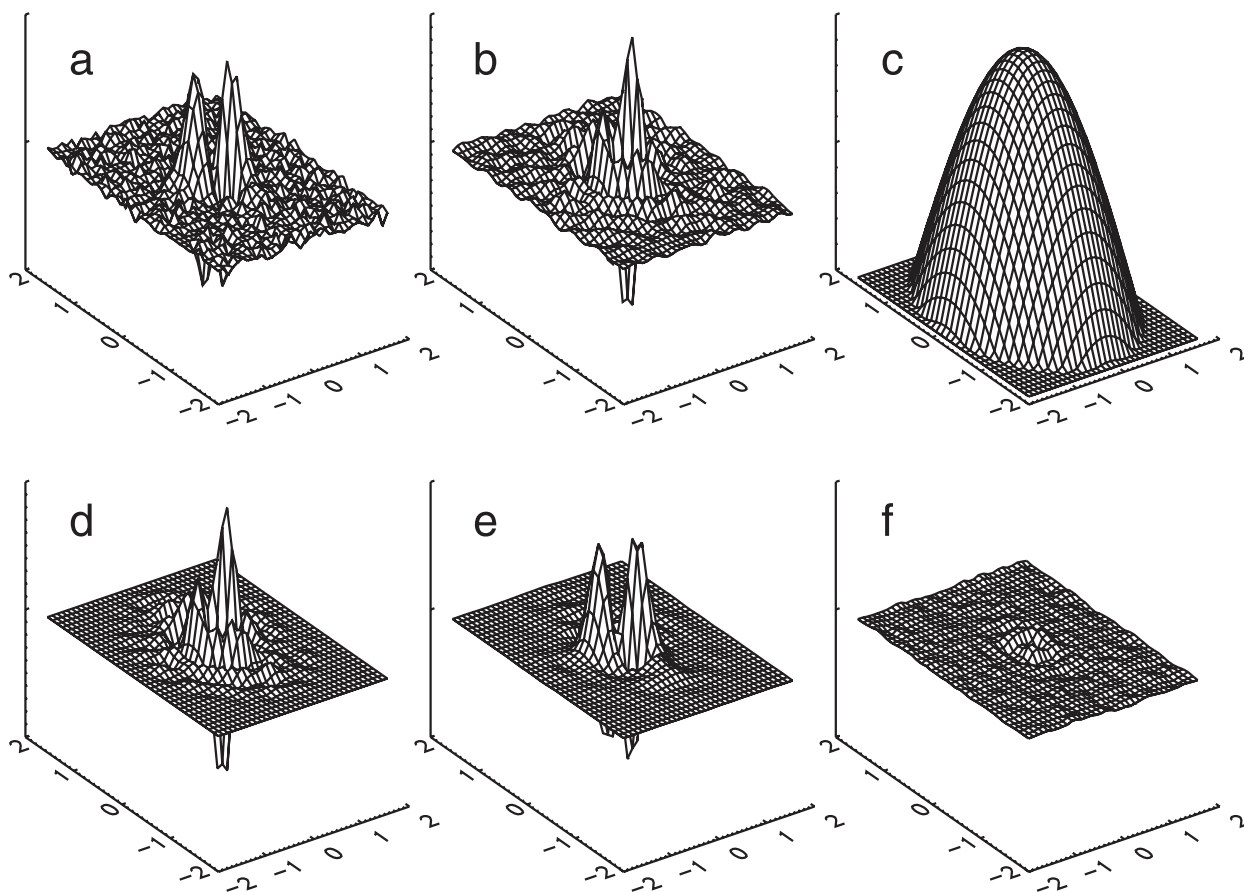


Fig. 8.— Plots illustrating the formation of the kernel used to generate the symmetrized beam maps for the Q1 DA. The x and y axes are in units of degrees centered on the beam LOS. The z-axis represents weight and panels (a), (e) and (f) use the same scale. (a) The residual (non-axisymmetric) component of the beam obtained by subtracting the best fit axisymmetric beam from the total beam map. (b) The residual beam after Wiener deconvolution. (c) The cosine apodization function. (d) The convolution kernel used to generate the symmetrized beam maps consisting of the cosine weighted Wiener deconvolved residual map. (e) The convolution kernel reconvolved with the axisymmetric beam. (f) The difference between the residual beam map (a) and the map making kernel convolved with the axisymmetric beam (e).

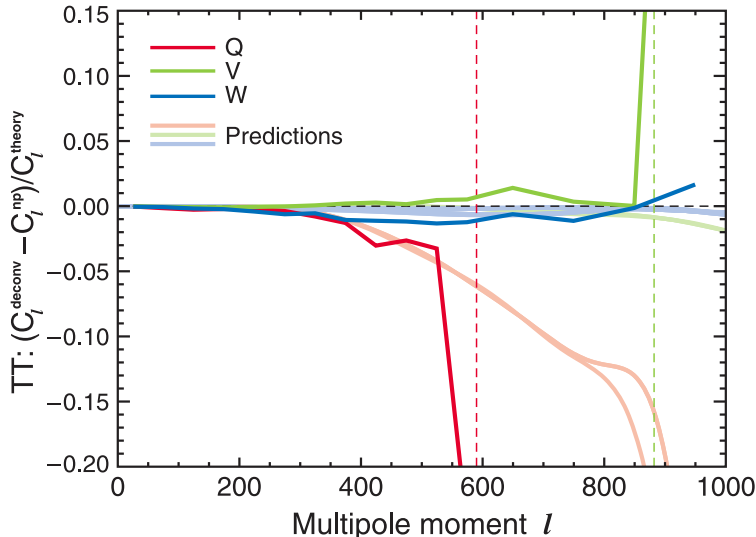


Fig. 9.— Verification of effects of asymmetric beams on the power spectrum. Given beam measurements, the formalism in Appendix B of Hinshaw et al. (2007) analytically quantifies the beam asymmetry effect on the power spectrum. This is plotted as a fractional deviation between an ideally deconvolved power spectrum (C_l^{deconv}) and the power spectrum of a normally processed map (C_l^{np}) with no correction for beam asymmetries. These “predictions” of fractional deviations are plotted per DA in the light colored solid lines. The Q-band effects become significant at $l \sim 400$, but Q-band is not used in the *WMAP* cosmological power spectrum. V-band effects become significant at $l \sim 1000$, however, V-band is deweighted compared to W-band at high l because of its larger beam size. W-band effects from the asymmetric beams can be seen to be $\lesssim 1\%$. While Hinshaw et al. (2007) provides an analytic prediction, we have explicitly deconvolved the maps in pixel space, allowing for a direct inter-comparison of the analytic with the numerical approach. The dark red, green and blue solid lines are the fractional deviations in power spectra for Q-, V- and W-bands from the directly deconvolved maps. A comparison between the light and dark colored lines per frequency band shows close agreement up to a multipole moment where we expect the spectra derived from the beam-symmetrized maps to break down because the prediction does not account for correlations introduced by the deconvolution. The Q-band deviations occur after the window function has dropped below 2.5% and the V-band deviations below 1.5%. The vertical dashed lines indicate where window functions are at 1% of their maximum value. The close agreement between the predictions and explicit deconvolution verifies our understanding of asymmetric beam effects and allows us to conclude that the spectrum from the normally processed (i.e. not deconvolved) maps differs from the ideally-deconvolved spectrum by $< 1\%$. Thus the final *WMAP* power spectrum is based on the normally-processed V- and W- band maps.

(A color version of this figure is available in the online journal.)

Table 5. Noise per Observation in Nine-Year Maps

DA	$\sigma_0(I)$ Uncleaned (mK)	$\sigma_0(Q, U)$ (mK)	$\sigma_0(Q, U)$ Template Cleaned (mK)
K1	1.429	1.435	NA
Ka1	1.466	1.472	2.166
Q1	2.245	2.254	2.710
Q2	2.131	2.140	2.572
V1	3.314	3.324	3.534
V2	2.949	2.958	3.144
W1	5.899	5.912	6.157
W2	6.562	6.577	6.850
W3	6.941	6.958	7.246
W4	6.773	6.795	7.076

5. Foreground Fits

5.1. Overview

In this section we examine the nature of the Galactic and extragalactic foreground emission. These foregrounds are important to understand so as to achieve an appropriate separation of CMB anisotropy from foreground emission, to elucidate the underlying astrophysical emission processes, and to transfer the precise *WMAP* calibration to astronomical emission sources that can be used by other observers for calibration purposes.

The separation of CMB anisotropy from foregrounds depends critically upon their different spectra. This is illustrated in Figure 10 where a model-free three-color display of *WMAP* data clearly differentiates the (pink) diffuse and point source foreground emission from the (gray) CMB anisotropy. Likewise, *WMAP* maps in different frequency bands can be convolved to a common angular resolution and subtracted to form a CMB-free, foreground emission-only map. Three such difference maps, in turn, can be combined into a three-color display that highlights the spectral differences of the foregrounds across the sky. An example of this is shown in Figure 11. Figure 12 provides an orientation of the microwave emission sources on the sky.

This section is divided into two major subsections: point source analyses are presented first in 5.2, followed by diffuse foregrounds in 5.3. The point source subsection begins with a discussion of *WMAP* observations of the planets Jupiter and Saturn (Section 5.2.1). For Saturn we separate the emission into a disk and ring component. In Section 5.2.2 we describe two techniques to identify other point sources and we provide point source catalogs in Appendices B and C. We then go on to discuss our analysis of the diffuse foregrounds. In Section 5.3.2 we describe the approach taken to mask and clean diffuse foregrounds for the purpose of carrying out the cosmological analysis of the CMB, such as the angular power spectra. In Section 5.3.3 we present the new nine-year internal linear combination (ILC) map. Since ILC error characterization is dependent on a knowledge of the foregrounds, a deeper ILC discussion is deferred until after a foreground characterization analysis. To identify the nature of the foregrounds we describe three different fitting techniques: the maximum entropy method (MEM) in Section 5.3.4; Monte Carlo Markov Chains (MCMC) in Section 5.3.5; and χ^2 fitting in Section 5.3.6. We conclude this section with a synthesis based on these analysis efforts. Section 5.3.7.1 includes an intercomparison of results from the three fitting techniques and a comparison of foreground component maps averaged over the three fits with the corresponding template maps used in foreground cleaning. Finally, Sections 5.3.7.2 and 5.3.7.3 discuss ILC errors. Estimates are presented of residual foreground bias in the ILC map and ILC error due to CMB-foreground covariance. Appendix A

describes small variations in *WMAP* bandpasses that occurred over the nine-year mission, which are taken into account in our foreground analyses. They have no significant effect on the CMB or cosmology analysis.

5.2. Point Sources

5.2.1. Planets and Celestial Analysis

A detailed analysis of *WMAP* seven-year observations of planets and selected celestial calibrators is given by Weiland et al. (2011), including intercomparisons with relevant results in the literature. Here we concentrate on updated nine-year *WMAP* results for some of these sources.

5.2.1.1. Jupiter Mean nine-year Jupiter temperatures are derived from the $l = 0$ component of the unnormalized beam transfer functions B_l . The symmetrized beam response to Jupiter, $T_{pk}\Omega_{beam}$, may be directly derived from B_0 . As described in Weiland et al. (2011), all Jupiter observations have been corrected to a fiducial solid angle $\Omega_{Jup}^{ref} = 2.481 \times 10^{-8} sr$. Mean Jupiter temperatures T_{Jup} are thus computed using the relation $T_{Jup} = T_{pk}\Omega_{beam}/\Omega_{Jup}^{ref}$. These temperatures are presented in Table 6. Quoted uncertainties are a quadrature sum of estimated beam solid angle errors from Table 3 and the uncertainty in the absolute calibration. The mean Jupiter temperatures derived from the five-year, seven-year and nine-year data releases are consistent with each other within the quoted uncertainties.

The stability of Jupiter emission over the nine-year baseline is evaluated by computing seasonal temperatures per DA and comparing them to their nine-year means. We compute $\Delta T/T$ as the mean deviation of all DAs from their nine-year mean values, and include a 1σ standard deviation as a measure of coherency. These results are listed in Table 7. From the seven-year analysis, Weiland et al. (2011) placed an upper limit on variability of $0.2 \pm 0.4\%$. Although consistent with this value, the Jupiter observations from the last two seasons introduce the statistically weak (PTE = 14%) possibility of a decreasing trend in temperature with time. Given our measurement uncertainties, a constant temperature is a very good fit to the data and that is what we use in our analysis.

Out of caution, we examined the hypothesis that there might be instrumental or calibration issues contributing to slightly lower Jupiter temperatures computed for the last few seasons of data. To determine if there might be a systematic calibration error within the last two years of the mission, yearly flux values for celestial sources Cas A, Cyg A, and Tau A were computed and compared against seven-year trends; no evidence for any calibration

inconsistency was found. Since Jupiter is not a steep-spectrum source, bandpass center frequency variations are also not an important factor; we expect an effect of less than $\pm 0.05\%$ over the 9 years in the K- through V-bands. In terms of Jupiter itself, there is no clear temperature trend with Sun-Jupiter distance or sub-*WMAP* latitude.

5.2.1.2. Saturn As seen by the *WMAP* satellite, the spatially unresolved microwave brightness of Saturn varies with orbital phase as the projected area of the ring system and oblate planetary spheroid changes aspect. Weiland et al. (2011) developed an empirical, geometrically motivated model to predict Saturn’s apparent brightness at *WMAP* frequencies, based on the first seven years (14 seasons) of observations. The available range of observable ring opening angles during this seven year interval falls in the range $-28^\circ < B < -6^\circ$. Weiland et al. (2011) found that parameter covariance and potential systematics in their model fit permitted a determination of Saturn’s disk temperature to within roughly 3-4 K, but noted that the inclusion of lower inclination observations in the fit should decrease the uncertainty in the derived model parameters. *WMAP* observations from the last two mission years include four new Saturn observing seasons, numbered 15 through 18. Since the Saturn ring system presented an “edge-on” configuration in early 2009, these four new seasons span the cross-over from viewing the rings from below (negative B) to viewing them from above (positive B) as seen in Table 8. These new observations at low B provide the opportunity to better constrain the predictive model for *WMAP* frequencies.

We apply the analysis methods of Weiland et al. (2011) to the nine-year compendium of Saturn observations to derive mean apparent temperatures of the Saturn system per DA per observing season, presented in Table 8. The analysis can be summarized as a three-step process. First, a time-ordered archive of Saturn observations is created, and sky signals arising from the Galaxy and CMB are removed, either through use of sky subtraction or masking. Second, the individual observations from this background subtracted archive are binned to form mean radial Saturn response profiles for each season and DA. Finally, the *WMAP* beam radial profile per DA (as determined from Jupiter observations) is fit to the Saturn radial response for that DA and an apparent temperature is derived. Temperature entries for the first 14 seasons listed in Table 8 may be directly compared against those in Table 9 of Weiland et al. (2011). There are small differences of order 0.5 to 1 σ between some of entries in common between the seven-year analysis and the nine-year analysis presented here. Differences of this nature are expected and can be traced to small variations in calibration, beam characterization and data masking between the seven-year and nine-year processing.

The temperatures in Table 8 may be fit with an empirical model that predicts Saturn’s

Table 6. Nine-Year Mean Jupiter Temperatures

	ν_e^{RJ} ^a (GHz)	λ ^b (mm)	T^{c} (K)	$\sigma(T)^{\text{d}}$ (K)
per DA				
K1	22.82	13.1	136.1	0.75
Ka1	33.07	9.1	147.1	0.68
Q1	40.88	7.3	153.9	0.78
Q2	40.67	7.4	154.7	0.76
V1	60.37	5.0	164.9	0.71
V2	61.24	4.9	165.9	0.68
W1	93.25	3.2	172.5	0.84
W2	93.73	3.2	173.4	0.85
W3	92.72	3.2	173.1	0.87
W4	93.57	3.2	172.3	0.86
per band				
K	22.82	13.1	136.1	0.75
Ka	33.07	9.1	147.1	0.68
Q	40.78	7.3	154.3	0.59
V	60.81	4.9	165.4	0.54
W	93.32	3.2	172.8	0.52

^anine-year values; see Appendix A

^b $\lambda = c/\nu_e^{\text{RJ}}$

^cBrightness temperature calculated for a solid angle $\Omega_{\text{ref}} = 2.481 \times 10^{-8}$ sr at a fiducial distance of 5.2 AU. Temperature is with respect to blank sky: absolute brightness temperature is obtained by adding 2.2, 2.0, 1.9, 1.5 and 1.1 K in bands K, Ka, Q, V and W respectively (Page et al. 2003a). Jupiter temperatures are uncorrected for a small synchrotron emission component (see Weiland et al. (2011)).

^dComputed from errors in Ω_B (Table 3) summed in quadrature with absolute calibration error of 0.2%.

Table 7. Jupiter Temperature Changes by Season

Season ^a	Start	End	$\Delta T/T$ (%)	
			Mean ^b	Scatter ^c
1	2001 Oct 08	2001 Nov 22	0.33	0.26
3	2002 Nov 10	2002 Dec 24	-0.01	0.33
4	2003 Mar 15	2003 Apr 29	-0.14	0.51
5	2003 Dec 11	2004 Jan 23	0.17	0.22
6	2004 Apr 15	2004 May 30	0.12	0.23
7	2005 Jan 09	2005 Feb 21	0.13	0.35
8	2005 May 16	2005 Jul 01	0.07	0.37
9	2006 Feb 07	2006 Mar 24	0.32	0.33
10	2006 Jun 16	2006 Aug 02	0.18	0.47
11	2007 Mar 10	2007 Apr 24	0.53	0.34
12	2007 Jul 19	2007 Sep 03	-0.04	0.44
13	2008 Apr 11	2008 May 27	-0.05	0.34
14	2008 Aug 21	2008 Oct 06	-0.11	0.30
15	2009 May 17	2009 Jul 03	-0.46	0.61
16	2009 Sep 26	2009 Nov 10	-0.39	0.34
17	2010 Jun 24	2010 Aug 10	-0.47	0.27

^aSeason 2 omitted from analysis because Jupiter is aligned with the Galactic plane.

^bMean of the percentage temperature change among the DAs for each season, relative to the nine-year mean.

^c 1σ scatter in the percentage temperature change among the DAs for each season.

unresolved microwave brightness T as a function of ring opening angle and frequency. We adopt the same model formulation as in the seven-year analysis of Weiland et al. (2011), which employs a simple geometrical summation of emission from the unobscured planetary disk, emission from the ring system and emission from those portions of the disk obscured by the rings:

$$T(\nu, B) = T_{\text{disk}}(\nu)[A_{\text{ud}} + \sum_{i=1}^7 e^{-\tau_{0,i}|\csc B|} A_{\text{od},i}] + T_{\text{ring}}(\nu) \sum_{i=1}^7 A_{r,i}. \quad (23)$$

At a given frequency ν , a single temperature is assumed for the planetary disk, $T_{\text{disk}}(\nu)$. The model allows for seven radially concentric ring divisions. All rings are characterized by the same temperature $T_{\text{ring}}(\nu)$, but each of the seven ring sectors has its own ring-normal optical depth $\tau_{0,i}$, with $1 \leq i \leq 7$. Each $\tau_{0,i}$ is assumed to be both constant within its ring and frequency independent. A_{ud} , $A_{\text{od},i}$ and $A_{r,i}$ are the projected areas of the unobscured disk, the portion of the disk that is obscured by ring i , and i^{th} ring, respectively. These areas are normalized to the total (obscured+unobscured) disk area. Model fit parameters are the five Saturn uniform disk temperatures and five mean ring temperatures (one for each *WMAP* frequency). The geometrical ring boundaries and relative ratios $\tau_{0,i}/\tau_{0,\text{max}}$ are constrained as per Table 10 of Weiland et al. (2011), where $\tau_{0,\text{max}}$ is the ring-normal optical depth for the most optically thick ring (ring 3, i.e. the outer B ring). For the nine-year fit, the value of $\tau_{0,\text{max}}$ was also allowed to be a fit parameter, although in practice its inclusion makes very little difference in the fit results.

The nine-year model fit returns a reduced χ^2 of ~ 1.04 for ~ 150 degrees of freedom; the model fit and residuals per *WMAP* frequency are shown in Figure 13. On average, the rms of the residuals is $\sim 1\%$ per frequency; the value for Q-band is somewhat higher (1.3%) and that for V-band is lowest (0.7%). Model parameters and their formal errors σ_{fit} are presented in Table 9. By construction, the T_{disk} and T_{ring} model parameters are anti-correlated. The covariance between these parameters allows the possibility of systematic errors not accounted for in the fitting formalism. Although the mean disk temperature is reasonably well constrained by the new *WMAP* observations from seasons 15-18, hemispheric temperature gradients or local hot spots would negate the assumed symmetry of the empirical model, and would affect the derived mean ring temperatures. The nine-year baseline unfortunately does not extend far enough toward positive B to assess the limits of the symmetry assumption. Additionally, the model's assumed ring optical depth profile may not be accurate. As with the seven-year analysis, we use a model variant to estimate systematic differences between models which return similar values of χ^2 . Our worst case estimate allows for differences of 0.9 K in T_{disk} and 0.7 K in T_{ring} ; we add these to the formal fitting errors in Table 9 to produce the tabulated adopted error, σ_{adopted} . The T_{disk} and T_{ring} parameters are plotted along

with their adopted errors in Figure 14. Within the conservative adopted errors, the nine-year derived disk and ring temperatures are in agreement with those from the seven-year fit; the nine-year adopted errors for T_{disk} are roughly half those quoted for the seven-year fit.

5.2.2. Point Source Catalogs

As for the seven-year analysis, two separate methods have been used for the identification of point sources from *WMAP* maps and two separate point source tables have been produced. Both methods are largely unchanged from the seven-year analysis (Gold et al. 2011). Since the use of beam-symmetrized maps would result in only minor changes to the recovered source fluxes and since there is benefit to continuity with previous *WMAP* point source analyses, we have generated the source catalogs from maps that are not deconvolved. The first method searches for point sources in each of the five *WMAP* wavelength bands. The nine-year signal-to-noise ratio map in each band is filtered in harmonic space by $b_l/(b_l^2 C_l^{\text{cmb}} + C_l^{\text{noise}})$, where b_l is the transfer function of the *WMAP* beam response, C_l^{cmb} is the CMB angular power spectrum, and C_l^{noise} is the noise power (Tegmark & de Oliveira-Costa 1998; Refregier et al. 2000). The filtering suppresses CMB and Galactic foreground fluctuations relative to point sources. For each peak in the filtered maps that is $> 5\sigma$ in any band, the unfiltered temperature map in each band is fit with the sum of a planar base level and a beam template formed by convolving an azimuthally symmetrized beam profile with a skymap pixel. (This method was previously used by Weiland et al. (2011) for selected celestial calibration sources and is more accurate than the Gaussian fitting that was used for the seven-year and earlier point source analyses.) The peak temperature from each beam template fit is converted to a source flux density using the conversion factor Γ given in Table 3. The flux density uncertainty is calculated from the 1σ uncertainty in the peak temperature, and does not include any additional uncertainty due to Eddington bias. Uncertainty due to beam asymmetry effects has been found to be negligible, about 0.1% or less, by comparing results from beam template fits to the normally processed K-band map with those to the beam-symmetrized K-band map for Tau A, Cas A, and Cyg A. Flux density values are entered into the catalog for bands where they exceed 2σ and where the source width from an initial Gaussian fit is within a factor of two of the beam width. A point source catalog mask is used to exclude sources in the Galactic plane and Magellanic cloud regions. This mask has changed from the seven-year analysis in accordance with changes in the KQ85 temperature analysis mask. A map pixel is outside of the nine-year point source catalog mask if it is either outside of the diffuse component of the nine-year KQ85 temperature analysis mask or outside of the seven-year point source catalog mask. The new catalog mask admits 83% of the sky.

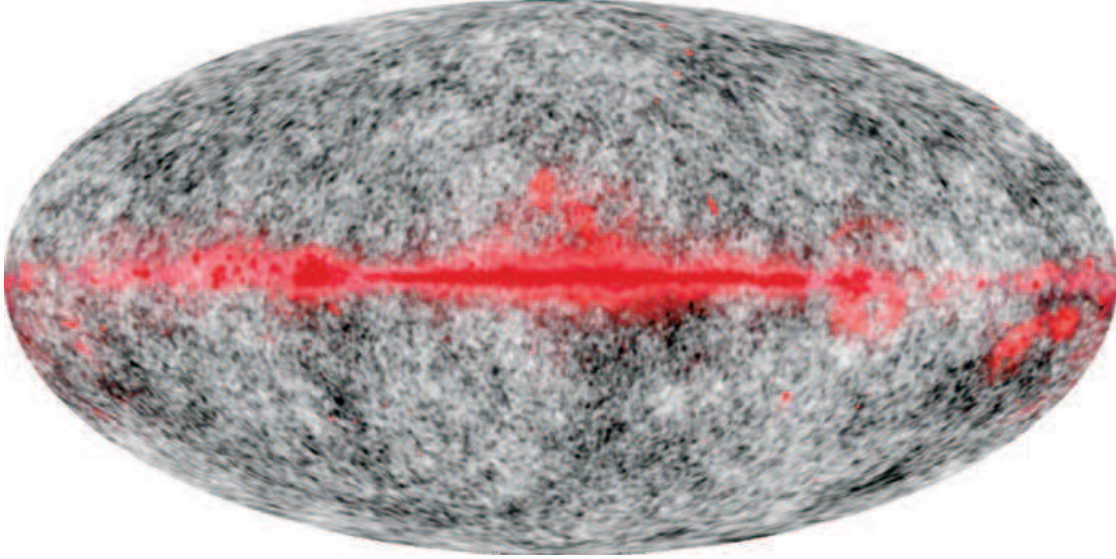


Fig. 10.— False color image representing the spectral information from multiple *WMAP* bands. Q-band is red, V-band is green, and W-band is blue. In this representation, a CMB thermodynamic spectrum appears as grey.

(A color version of this figure is available in the online journal.)

Table 8. Derived Saturn Temperatures Per Observing Season Per DA

Season ^a	wRJD ^b	B^c	T_b (K) ^d									
			K	Ka	Q1	Q2	V1	V2	W1	W2	W3	W4
1	2172.50	-26	133.5 ± 1.5	141.0 ± 1.2	145.6 ± 1.4	149.2 ± 1.4	156.9 ± 1.2	156.7 ± 1.1	164.2 ± 1.1	164.4 ± 1.4	166.2 ± 1.4	165.9 ± 1.3
2	2302.56	-26	133.6 ± 1.6	142.6 ± 1.3	145.7 ± 1.4	147.9 ± 1.3	154.9 ± 1.2	156.4 ± 1.1	161.4 ± 1.2	165.5 ± 1.4	164.3 ± 1.4	163.8 ± 1.3
3	2551.27	-26	130.9 ± 1.6	141.6 ± 1.2	149.2 ± 1.3	149.9 ± 1.3	158.1 ± 1.2	157.4 ± 1.1	165.9 ± 1.2	166.9 ± 1.4	164.0 ± 1.4	164.3 ± 1.3
5	2928.95	-25	131.2 ± 1.5	138.4 ± 1.2	144.1 ± 1.3	146.1 ± 1.3	153.4 ± 1.2	153.4 ± 1.1	161.2 ± 1.2	162.0 ± 1.4	160.5 ± 1.4	159.8 ± 1.3
7	3305.67	-22	125.8 ± 1.5	135.3 ± 1.2	140.2 ± 1.3	140.1 ± 1.3	147.2 ± 1.1	147.9 ± 1.1	154.0 ± 1.1	154.2 ± 1.4	154.2 ± 1.4	153.2 ± 1.2
8	3437.14	-24	129.9 ± 1.6	137.8 ± 1.3	141.0 ± 1.5	141.7 ± 1.4	147.9 ± 1.3	150.2 ± 1.1	155.0 ± 1.2	159.3 ± 1.5	159.8 ± 1.5	156.9 ± 1.3
9	3685.29	-17	121.4 ± 1.5	130.6 ± 1.2	134.8 ± 1.3	134.1 ± 1.3	140.9 ± 1.2	141.3 ± 1.1	146.2 ± 1.1	146.9 ± 1.4	147.1 ± 1.4	146.3 ± 1.3
10	3794.29	-20	125.1 ± 2.0	131.3 ± 1.6	134.5 ± 3.5	132.8 ± 4.1	143.4 ± 1.6	142.2 ± 1.4	150.0 ± 1.5	150.0 ± 2.1	148.7 ± 2.2	150.7 ± 1.7
11	4061.48	-12	122.9 ± 1.5	129.9 ± 1.2	131.5 ± 1.3	137.3 ± 1.3	139.8 ± 1.2	140.4 ± 1.1	141.9 ± 1.1	144.6 ± 1.4	143.1 ± 1.4	143.2 ± 1.2
12	4189.02	-15	121.5 ± 2.0	132.1 ± 1.7	131.4 ± 1.4	135.5 ± 1.4	140.4 ± 1.5	140.8 ± 1.4	143.1 ± 1.5	143.7 ± 1.3	143.1 ± 1.3	142.4 ± 1.7
13	4436.82	-7	128.1 ± 1.6	131.5 ± 1.2	135.3 ± 1.4	137.8 ± 1.3	140.3 ± 1.2	139.9 ± 1.1	143.0 ± 1.2	146.2 ± 1.4	141.3 ± 1.4	144.8 ± 1.3
14	4570.98	-10	122.8 ± 1.6	129.7 ± 1.3	132.3 ± 1.3	133.0 ± 1.3	139.9 ± 1.2	141.1 ± 1.1	140.0 ± 1.2	141.4 ± 1.4	141.4 ± 1.4	140.1 ± 1.4
15	4814.77	-1	130.6 ± 1.6	137.2 ± 1.3	139.1 ± 1.4	139.4 ± 1.4	144.5 ± 1.2	147.2 ± 1.1	146.6 ± 1.2	149.4 ± 1.5	146.8 ± 1.5	146.5 ± 1.3
16	4949.58	-4	127.4 ± 1.6	131.5 ± 1.2	138.0 ± 1.3	139.9 ± 1.3	142.6 ± 1.2	142.4 ± 1.1	144.8 ± 1.2	143.7 ± 1.5	144.9 ± 1.5	146.1 ± 1.3
17	5191.93	5	125.9 ± 1.7	132.6 ± 1.3	136.9 ± 1.4	136.9 ± 1.4	141.4 ± 1.2	141.6 ± 1.1	143.5 ± 1.2	145.0 ± 1.5	146.0 ± 1.5	144.2 ± 1.3
18	5326.82	2	128.8 ± 1.7	134.7 ± 1.3	138.5 ± 1.4	137.6 ± 1.4	143.9 ± 1.2	145.7 ± 1.1	145.2 ± 1.2	146.5 ± 1.5	144.6 ± 1.5	148.0 ± 1.4

^aSeasons 4 and 6 omitted from analysis because Saturn is aligned with the Galactic plane.

^bApproximate mean time of observations in each season: wRJD = Julian Day –2450000.

^cApproximate mean ring opening angle for each season, degrees.

^dBrightness temperature calculated for a solid angle $\Omega_{\text{ref}} = 5.096 \times 10^{-9}$ sr at a fiducial distance of 9.5 AU. A correction for planetary disk oblateness has not been applied, as that is accounted for in modeling. Temperature is with respect to blank sky: absolute brightness temperature is obtained by adding 2.2, 2.0, 1.9, 1.5 and 1.1 K in bands K, Ka, Q, V and W respectively (Page et al. 2003a).

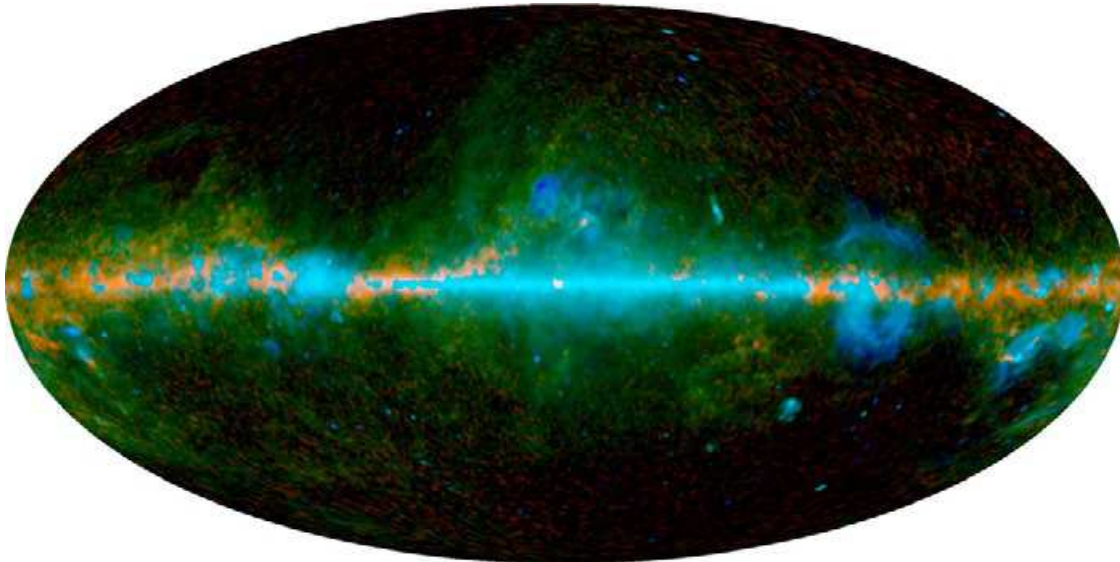


Fig. 11.— False color image derived from a combination of *WMAP* band differences chosen to highlight differing spectral components. Red (W-V) highlights regions where thermal emission from dust is highest. Blue (Q-W) is dominated by free-free emission. Green ((K-Ka)-1.7(Q-W)) illustrates contributions from synchrotron and spinning dust.

(A color version of this figure is available in the online journal.)

Table 9. Nine-Year Saturn Model Fit Parameters^a

Freq Band	Disk			Rings		
	T_{disk} [K]	σ_{fit} [K]	σ_{adopted} [K]	T_{ring} [K]	σ_{fit} [K]	σ_{adopted} [K]
K	132.2	0.8	1.7	8.0	0.8	1.5
Ka	137.8	0.6	1.5	10.6	0.7	1.4
Q	141.6	0.5	1.4	11.9	0.6	1.3
V	146.6	0.4	1.3	14.5	0.5	1.2
W	147.3	0.3	1.2	18.9	0.3	1.0

^aA frequency independent maximum ring-normal optical depth, $\tau_{0,\text{max}}$ is also a fit parameter. Its fit value is 2.1, with a statistical error $\sigma_{\text{fit}} = 0.3$; the seven-year model used a fixed value of 2.0.

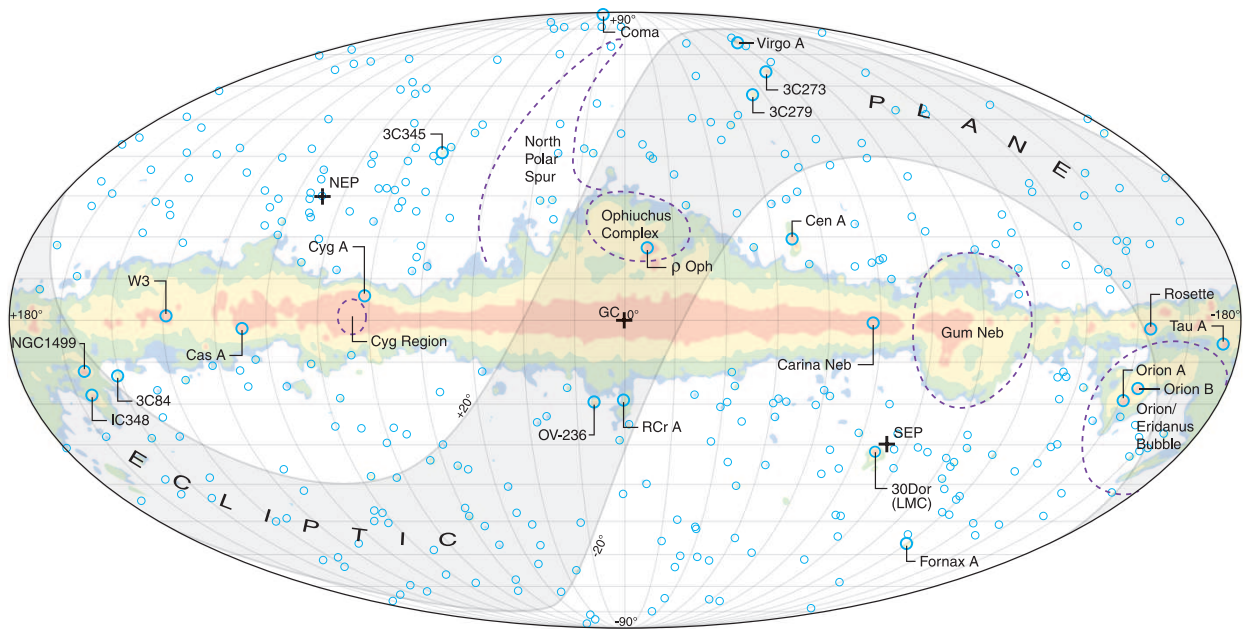


Fig. 12.— Microwave emission near the Galactic plane is traced by a K-band minus W-band difference map, which eliminates CMB anisotropy. A log scale is used for the color region and blue circles represent the positions of the brightest point sources, as seen by *WMAP*. (A color version of this figure is available in the online journal.)

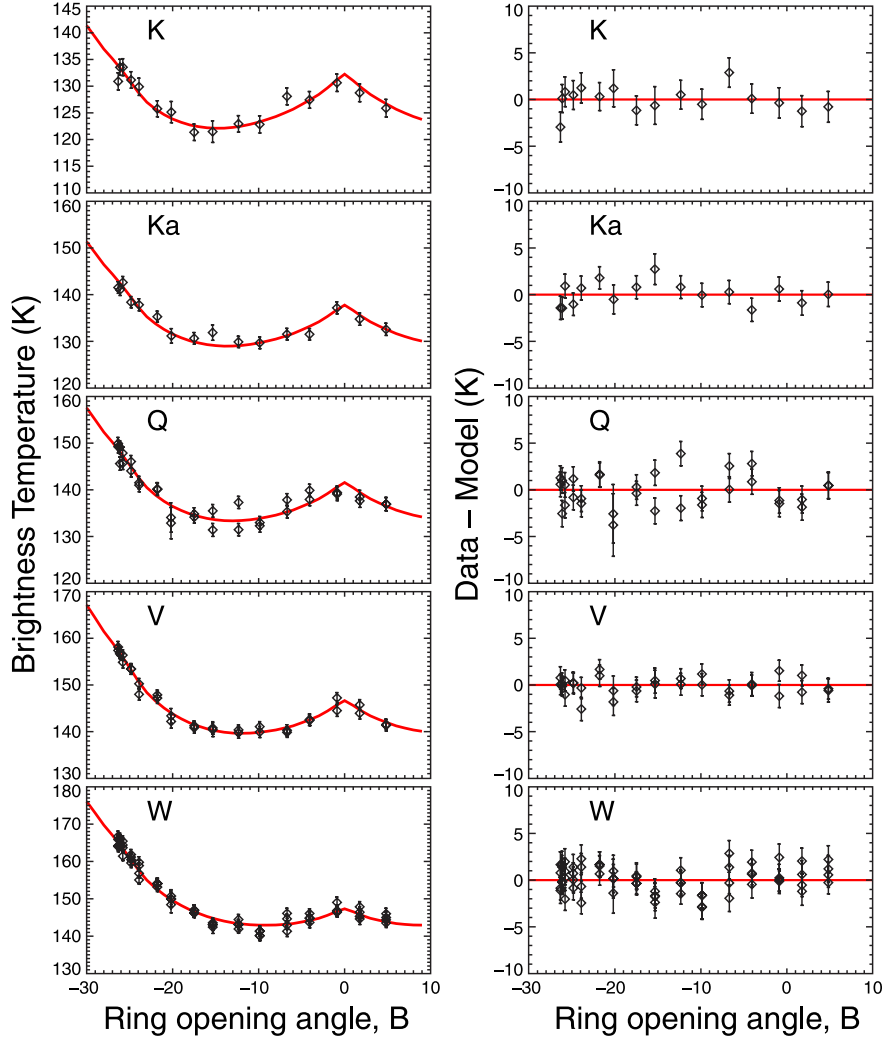


Fig. 13.— Modeling results for Saturn. (Left) Brightness temperatures based on unresolved Saturn observations as a function of ring inclination B are shown in black for each *WMAP* frequency band. Where there are multiple differencing assemblies per frequency, multiple points are plotted at each inclination. An empirical model including both ring and disk components (see text) is plotted in red. The temperature of the planetary disk predicted by the model occurs at $B=0^\circ$, when the rings are viewed edge-on. The model is symmetric about $B=0^\circ$. (Right) Residuals (data-model) of the model fit to the data are plotted as a function of the ring opening angle.

(A color version of this figure is available in the online journal.)

The second method of point source identification is the CMB-free method originally applied to one-year and three-year V- and W-band maps by Chen & Wright (2008) and to five-year V- and W-band maps by Wright et al. (2009). The method used here is that applied to five-year Q-, V-, and W-band maps by Chen & Wright (2009) and to seven-year Q-, V-, and W-band maps by Gold et al. (2011). The V- and W-band maps are smoothed to Q-band resolution. An internal linear combination (ILC) map (see Section 5.3.3) is then formed from the three maps using weights such that CMB fluctuations are removed, flat-spectrum point sources are retained with fluxes normalized to Q-band, and the variance of the ILC map is minimized. The ILC map is filtered to reduce noise and suppress large angular scale structure. Peaks in the filtered map that are $> 5\sigma$ and outside of the nine-year point source catalog mask are identified as point sources, and source positions are obtained by fitting the beam profile plus a baseline to the filtered map for each source. For the nine-year analysis, the position of the brightest pixel is adopted instead of the fit position in rare instances where they differ by $> 0.1^\circ$. Source fluxes are estimated by integrating the Q, V, and W temperature maps within 1.25° of each source position, with a weighting function to enhance the contrast of the point source relative to background fluctuations, and applying a correction for Eddington bias due to noise (sometimes called “deboosting”).

We identify possible 5 GHz counterparts to the *WMAP* sources found by both methods by cross-correlating with the GB6 (Gregory et al. 1996), PMN (Griffith et al. 1994, 1995; Wright et al. 1994, 1996), Kühr et al. (1981), and Healey et al. (2009) catalogs. A 5 GHz source is identified as a counterpart if it lies within $11'$ of the *WMAP* source position (the mean *WMAP* source position uncertainty is $4'$). When two or more 5 GHz sources are within $11'$, the brightest is assumed to be the counterpart and a multiple identification flag is entered in the catalog.

The nine-year five-band point source catalog is presented in Appendix B and the nine-year QVW point source catalog is presented in Appendix C. The five-band catalog contains 501 sources, the QVW catalog contains 502 sources, and the two catalogs have 387 sources in common. As noted by Gold et al. (2011), differences in the source populations detected by the two search methods are largely caused by Eddington bias in the five-band source detections due to CMB fluctuations and noise. At low flux levels, the five-band method tends to detect point sources located on positive CMB fluctuations and to overestimate their fluxes, and it tends to miss sources located in negative CMB fluctuations. Other point source detection methods have been applied to *WMAP* data and have identified sources not found by our methods (e.g., Scodeller et al. (2012); Lanz (2012); Ramos et al. (2011), and references therein).

5.3. Diffuse Foregrounds

5.3.1. Introduction to diffuse foreground analysis

In this section we evaluate the diffuse foreground emission both for the purpose of separation from the CMB anisotropy and for characterizing the nature of the foreground components. As a prelude to our cosmological analyses we fit and remove external foreground template map data from the *WMAP* maps and we mask remaining regions estimated to be significantly contaminated. We discuss this temperature and polarization cleaning, and the masks, below. To elucidate the characteristics and nature of the diffuse foregrounds we implement four techniques: internal linear combination (ILC) technique; Maximum Entropy Method (MEM); Markov Chain Monte Carlo (MCMC) fits; and χ^2 fits.

Our analysis of the diffuse foregrounds generally uses the five bands of *WMAP* data in conjunction with other data sets. *WMAP* was designed to observe in the spectral region where the ratio of the CMB to the foregrounds is at its maximum. This minimizes the amplitude of contamination and needed corrections or masking, which is good for cosmology. To achieve an improved signal-to-noise ratio of the foregrounds themselves, it is sometimes useful to use external data where the foreground emission is weak.

Foreground analyses are done using 1° smoothed beam-symmetrized nine-year temperature maps in the five *WMAP* bands. As in our previous foreground studies, the zero level of each map is set such that a fit to the ILC-subtracted map of the form $T(|b|) = T_p \csc |b| + c$, over the range $-90^\circ < b < -15^\circ$, yields $c = 0$. This assumes a plane-parallel slab model for the Galactic emission. Formal 1σ uncertainties in the map zero levels (calculated as the quadrature sum of (1) the uncertainty in the fit intercept c and (2) the difference in intercepts from southern and northern Galactic hemisphere fits) are 7.2, 5.9, 3.6, 1.8, and $0.76 \mu\text{K}$ in thermodynamic units for K-, Ka-, Q-, V-, and W-bands respectively. The South Galactic pole brightness T_p from the fitting is 77.9 ± 1.5 , 30.1 ± 0.6 , 17.7 ± 0.4 , 8.6 ± 0.2 , and $9.4 \pm 0.3 \mu\text{K}$ in thermodynamic units for K-, Ka-, Q-, V-, and W-bands respectively. The Stokes Q and U maps have well-defined zero levels and no monopole corrections are applied to them.

Previous *WMAP* team analyses have used the Finkbeiner (2003) $\text{H}\alpha$ map corrected for extinction as a template for free-free emission (Bennett et al. 2003a). The Finkbeiner map is a composite of the Virginia Tech Spectral line Survey (Dennison et al. 1998), the Southern H-alpha Sky Survey Atlas (Gaustad et al. 2001), and the Wisconsin H alpha Mapper survey (Haffner et al. 2003). The extinction correction assumes that $\text{H}\alpha$ emission and extinction

are uniformly mixed along each line of sight,

$$I(\text{H}\alpha)_{\text{extinction-corrected}} = I(\text{H}\alpha) \tau / (1 - e^{-\tau}). \quad (24)$$

Here τ is the dust optical depth at the wavelength of $\text{H}\alpha$ and was calculated from the $E(B - V)$ map of Schlegel et al. (1998) as

$$\tau = 2.2 E(B - V), \quad (25)$$

which assumes an extinction law for $R_V = 3.1$, characteristic of the diffuse interstellar medium.

Recent studies of selected dust clouds at $20^\circ < |b| < 40^\circ$ have shown that scattered $\text{H}\alpha$ can make a significant contribution to the observed $\text{H}\alpha$ brightness for some lines of sight (Mattila et al. 2007; Lehtinen et al. 2010; Witt et al. 2010). Here we apply an approximate correction to our previous $\text{H}\alpha$ template for the contribution of scattered $\text{H}\alpha$, based on correlations between $\text{H}\alpha$ and $100 \mu\text{m}$ emission found by Witt et al. (2010) for four selected clouds and by Brandt & Draine (2012) for Sloan Digital Sky Survey blank sky regions at intermediate to high Galactic latitudes. Brandt and Draine noted that $I(100\mu\text{m})$ varies in proportion to the product of the dust column density and the radiation field that heats the dust. If the spatial variation of the illuminating $\text{H}\alpha$ radiation field in the Galaxy is similar to that of the radiation responsible for dust heating, $I(100\mu\text{m})$ may be a good tracer of scattered $\text{H}\alpha$. The scattering correction we adopt is

$$I(\text{H}\alpha)_{\text{scattering-corrected}} = I(\text{H}\alpha)_{\text{extinction-corrected}} - 0.11 I(100\mu\text{m}), \quad (26)$$

where $I(\text{H}\alpha)$ is in Rayleighs, $I(100\mu\text{m})$ is the Schlegel et al. (1998) $100 \mu\text{m}$ map in MJy sr^{-1} , and the $I(100\mu\text{m})$ coefficient is a mean of the values of $0.129 \pm 0.015 \text{ R}/(\text{MJy sr}^{-1})$ found by Witt et al. (2010) and $0.090 \pm 0.017 \text{ R}/(\text{MJy sr}^{-1})$ found by Brandt & Draine (2012). These correlation slopes were measured for regions with $\tau < 1$, but we apply Equation (26) over the entire sky. This assumes that the Equation (24) extinction correction is valid for the scattered component (*i.e.*, the scattered $\text{H}\alpha$ emissivity and the dust extinction are uniformly mixed along each line of sight) and it neglects effects of multiple scattering that may be important for lines of sight with high optical depth. The $\text{H}\alpha$ template is made by applying the corrections for extinction and scattering to version 1.1 of the Finkbeiner $\text{H}\alpha$ map, smoothing from $6'$ FWHM to 1° FWHM, and setting a small number of negative pixels to zero. The resulting $\text{H}\alpha$ -based microwave template is shown in Figure 15 as the “Free-Free Template”.

Uncertainties in both the extinction correction and the scattering correction are large for high τ , but we find that results of our analyses using the template are not sensitive

to these uncertainties. For the foreground cleaning of the temperature maps, the mask used in template fitting is chosen to minimize the combined effects of template error and foreground-CMB covariance (Section 5.3.2). For the MEM foreground fitting, the free-free prior is formed from the $H\alpha$ template, but for high τ lines of sight the observed brightness in the *WMAP* bands is great enough that the MEM results are not strongly affected by the free-free prior.

Prior to the nine-year analysis, the Haslam map used in the MCMC fitting and as a prior in the MEM fitting was the Fourier-filtered version available from LAMBDA. This version mitigates scan striping in the Haslam map, but also removes many strong point sources. Removal of the point sources affected the quality of some foreground fits for pixels in the Galactic plane. For this reason, the unfiltered Haslam map (also available on LAMBDA) is now used for these applications and its projection to K-band is shown in Figure 15.

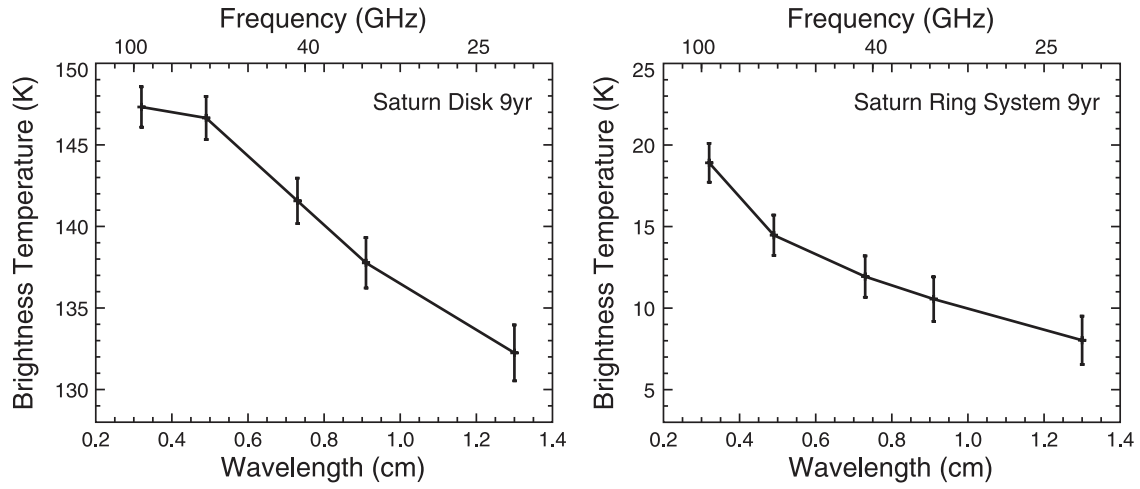


Fig. 14.— Saturn model parameters derived from the nine-year analysis. Left: Disk temperatures for 5 *WMAP* frequencies. Right: Ring system temperatures. Adopted errors for the nine-year analysis have been reduced compared to those in Weiland et al. (2011); errors for T_{disk} are smaller by a factor of 2.

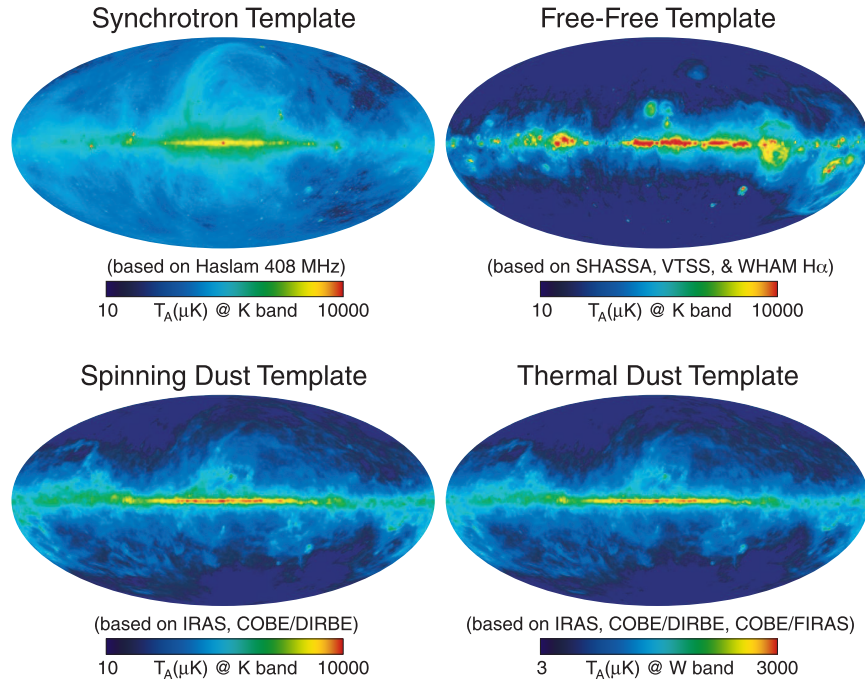


Fig. 15.— Foreground evaluation is generally based on a combination of the data from the five *WMAP* bands and external observations where the CMB contamination is negligible. The external observations used for foreground fitting and template removal are shown. These provide approximate probes of the synchrotron, free-free, spinning dust, and thermal dust emission.

(A color version of this figure is available in the online journal.)

5.3.2. Template Cleaning and Masks

All-sky templates of Galactic foregrounds or combinations of foregrounds which are “CMB-free” are fit in a least-squares sense to the *WMAP* sky maps to construct a foreground model at each frequency. The foreground model is subtracted from the *WMAP* sky maps to produce reduced foreground, or “cleaned” maps, which are used in turn for power spectrum analysis. The cleaning is applied to sky maps from the standard map-making procedure, not to beam-symmetrized sky maps. Cleaning of temperature and polarization maps is treated independently.

5.3.2.1. Temperature cleaning A limited set of all-sky foreground templates is available for use in modeling potential contributions from synchrotron, free-free and dust emission. After testing a number of different template combinations, we continue to adopt a foreground model map, $M(\nu, p)$, of the form

$$M(\nu, p) = c_1(\nu)[T_K(p) - T_{Ka}(p)] + c_2(\nu)I_{H\alpha}(p) + c_3M_{dust}(p), \quad (27)$$

where p indicates the pixel, the frequency dependence is entirely contained in the coefficients c_i , and the spatial templates are the *WMAP* K-Ka temperature difference map in thermodynamic mK ($T_K - T_{Ka}$), an $H\alpha$ map ($I_{H\alpha}$) in units of Rayleighs, and dust model 8 from Finkbeiner et al. (1999) evaluated at 94 GHz in units of mK antenna temperature (M_{dust}). The K-Ka template is formed using standard (not beam symmetrized) maps. The values of the coefficients c are such that the model map $M(\nu, p)$ is in thermodynamic mK.

However, although the form of the model is the same as that used in previous *WMAP* analyses, there are modifications in the details of its application. As described in Section 5.3.1, the nine-year extinction corrected $H\alpha$ template incorporates a scattering correction, a refinement not present in the seven-year analysis. Also, in recognition of the possible contribution of spinning dust to the Galactic emission and the uncertain synchrotron behavior with frequency, spectral and coefficient positivity constraints are no longer imposed in the template fitting. This allows maximum freedom in the fit, but makes physical interpretation of model coefficients more difficult.

There has also been a change in the portion of sky used in computing the foreground model fit. Derived model coefficients are dependent on the fraction of the sky which is fit: a full sky fit minimizes the covariance of the templates with the CMB signature in the *WMAP* data, but maximizes potential template cleaning residuals (bias) by including sky regions where the templates are more uncertain (generally close to the Galactic plane). For example, the extinction correction applied to the $H\alpha$ map is only approximate and this template is an imperfect tracer of free-free emission in optically thick regions. In general, as more sky

is excluded from the fit, CMB-template covariance increases, while template cleaning bias decreases. The “optimal” sky cut for template fitting may be determined by examining these two competing errors as a function of sky cut, and choosing the mask for which the sum of the two errors is a minimum. For this purpose, several simulated five-band Galaxy models of differing complexity were constructed. Each model is added to a CMB realization, and then cleaned using the algorithm in Equation (27) and a chosen sky cut. This is performed for 100 CMB realizations per sky cut; the mean bias is the template cleaning error and the variance is the CMB covariance. We have used the “KpX” series of Galactic masks, described by Bennett et al. (2003c) as a graduated set of sky cuts. The masking in the “KpX” series is based on K-band intensity: higher values of X indicate a smaller portion of bright sky is cut. For each simulation, the sum of both errors were plotted as a function of sky cut and a rough minimum chosen. Prior to the nine-year analysis, we had used the Kp2 mask for template fitting. However, the simulations indicated a more conservative choice would employ a smaller sky cut. The Kp8 mask was adopted for the nine-year cleaning.

Template cleaning coefficients derived using the updated procedure are shown in Table 10 for the Q,V and W DAs. As noted previously, the ability of the fit to trade freely among the three templates makes physical interpretation difficult. Monte Carlo simulations have shown that the negative coefficients c_1 derived for W-band result from template covariance with the CMB. The change of template cleaning method from the seven-year to the nine-year analysis has little effect on power spectrum analysis. There is a slight change in the evaluated low- l power spectrum. For $2 \leq l \leq 16$, using the MASTER method with the KQ85y9 mask, the absolute value of the change in $l(l+1)/(2\pi)C_l$ due to the change in template cleaning is typically 4% of cosmic variance per l .

5.3.2.2. Polarization cleaning The polarization cleaning method is unchanged from the seven-year analysis. The nine-year Stokes Q and U maps are degraded to low resolution ($N_{\text{side}}=16$) and the data for pixels outside of the Q-band processing mask are fit to a linear combination of low resolution templates. The fit has the form

$$[Q(\nu), U(\nu)] = a_1(\nu) [Q, U]_{\text{K}} + a_2(\nu) [Q, U]_{\text{dust}}. \quad (28)$$

The template used for synchrotron is the nine-year *WMAP* K-band polarization, $[Q, U]_{\text{K}}$. The template for dust, $[Q, U]_{\text{dust}}$, is constructed from the Finkbeiner et al. (1999) dust model 8 evaluated at 94 GHz together with a polarization direction map derived from starlight measurements and a geometric suppression map to account for the magnetic field geometry, as described in Page et al. (2007). The coefficients of the fit to the nine-year data are listed in Table 11 and plotted against frequency in Figure 16.

Table 10. Template Cleaning Temperature Coefficients

DA ^a	c_1^b	c_2 ($\mu\text{K}/\text{R}^{-1}$) ^b	c_3^b
Q1	0.284	0.890	0.231
Q2	0.284	0.898	0.226
V1	0.0630	0.554	0.686
V2	0.0567	0.541	0.716
W1	-0.0179	0.351	1.609
W2	-0.0182	0.349	1.617
W3	-0.0146	0.342	1.587
W4	-0.0153	0.345	1.594

^aWMAP has two differencing assemblies (DAs) for the Q- and V-bands, and four for the W-band; the high signal-to-noise total intensity allows each DA to be fit independently.

^bThe c_i coefficients produce model maps in thermodynamic mK.

Table 11. Template cleaning polarization coefficients

Band	a_1^a	$\beta_s(\nu_K, \nu)^b$	a_2^a	$\beta_d(\nu, \nu_W)^b$
Ka	0.3204	-3.13	0.0145	1.41
Q	0.1682	-3.13	0.0182	1.50
V	0.0594	-2.97	0.0364	1.41
W	0.0398	-2.43	0.0758	...

^aThe a_i coefficients are dimensionless and produce model maps in thermodynamic mK.

^bThe spectral indices refer to antenna temperature.

Full-resolution ($N_{\text{side}} = 512$) foreground-reduced Stokes Q and U maps were produced using the coefficients in Table 11 with full-resolution versions of the K-band and dust polarization templates smoothed to 1° FWHM. In making the full resolution dust template, the starlight polarization map used to determine polarization direction was upgraded to full resolution using nearest neighbor sampling. Smoothing of the templates to 1° FWHM potentially leaves artifacts in the foreground-reduced maps due to small-scale power or beam asymmetries, but previous analyses have found no sign of these effects (Gold et al. 2011). Data sets for all templates are available on the LAMBDA website.

The spectrum of K-band polarization template coefficients flattens significantly with increasing frequency, which is unexpected for synchrotron emission. This flattening can be understood if, due to shortcomings of the dust polarization template, some fraction of the dust polarization is traced by the K-band template. We illustrate this using a simple model. The polarization maps are modeled as a sum of synchrotron and thermal dust components,

$$[Q(\nu), U(\nu)] = [Q(\nu), U(\nu)]_{\text{synch}} + [Q(\nu), U(\nu)]_{\text{dust}}. \quad (29)$$

Assuming the synchrotron polarization has a power law spectrum and is traced exactly in all bands by the K-band polarization template, the synchrotron component is

$$[Q(\nu), U(\nu)]_{\text{synch}} = \frac{g(\nu)}{g(\nu_K)} \left(\frac{\nu}{\nu_K} \right)^{\beta_{\text{synch}}} [Q, U]_{\text{K}}, \quad (30)$$

where the antenna temperature to thermodynamic temperature conversion factors g are needed because the polarization maps and K-band template are in thermodynamic units. Assuming the dust polarization has a power law spectrum and is traced by a combination of the dust polarization template and the K-band polarization template, with the relative contributions of the two templates independent of frequency, the dust component is

$$[Q(\nu), U(\nu)]_{\text{dust}} = \frac{g(\nu)}{g(\nu_W)} \left(\frac{\nu}{\nu_W} \right)^{\beta_{\text{dust}}} (f_1 [Q, U]_{\text{dust}} + f_2 [Q, U]_{\text{K}}), \quad (31)$$

where f_1 and f_2 are constants. Inserting Equations (30) and (31) in Equation (29) and comparing with Equation (28) gives expressions for the template fit coefficients,

$$a_1(\nu) = \frac{g(\nu)}{g(\nu_K)} \left(\frac{\nu}{\nu_K} \right)^{\beta_{\text{synch}}} + f_2 \frac{g(\nu)}{g(\nu_W)} \left(\frac{\nu}{\nu_W} \right)^{\beta_{\text{dust}}} \quad (32)$$

and

$$a_2(\nu) = f_1 \frac{g(\nu)}{g(\nu_W)} \left(\frac{\nu}{\nu_W} \right)^{\beta_{\text{dust}}}. \quad (33)$$

Fitting these expressions to the $a_1(\nu)$ and $a_2(\nu)$ values in Table 11 gives $\beta_{\text{synch}} = -3.13$, $\beta_{\text{dust}} = 1.44$, $f_1 = 0.076$, and $f_2 = 0.024$. The fits are shown by the curves in Figure

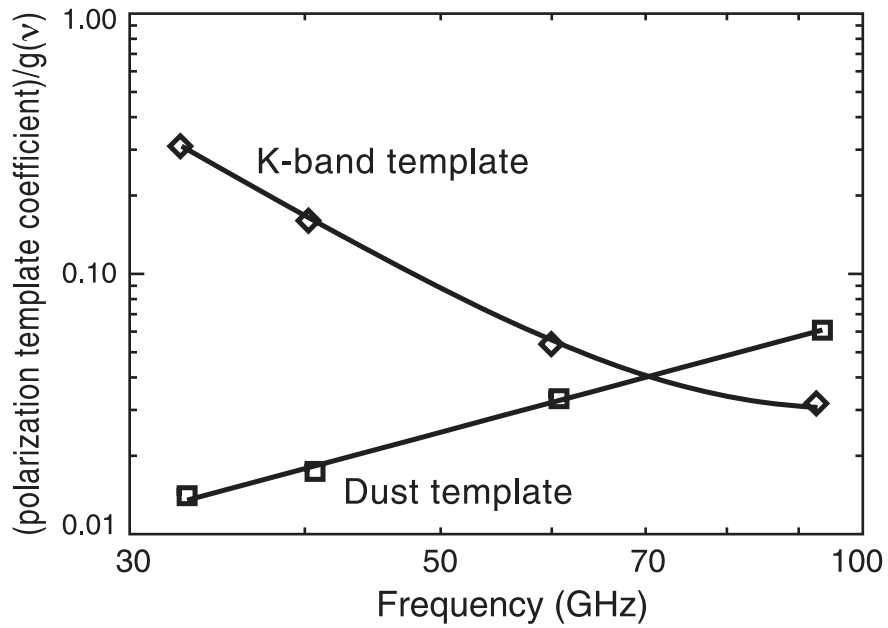


Fig. 16.— Polarization template coefficients, scaled to produce model maps in antenna temperature, as a function of frequency. The curves show the predictions of a simple model with synchrotron and thermal dust polarization in which about $2/3$ of the dust polarization is traced by the dust template and about $1/3$ is traced by the K-band template.

16. They match the template coefficients very well with no need for an additional emission mechanism such as spinning dust or magnetic dust polarization. In this simple model, the K-band template component contributes about 1/3 of the rms dust polarization and the dust template component contributes about 2/3.

This suggests that there is room for improvement in the dust polarization template. Some alternate dust templates were tested in fitting the polarization maps, but none of them gave significant improvement in χ^2 . These include a template based on K-band polarization directions instead of directions from starlight measurements, a template based on a geometric suppression map calculated from the ratio of observed K-band polarized intensity to K-band synchrotron total intensity from the seven-year MCMC shifted spinning dust model (Gold et al. 2011), and two templates from O’Dea et al. (2012) based on different Galactic magnetic field models.

5.3.2.3. Masks Sky masks for CMB temperature analysis are generated as described by Gold et al. (2011). The process begins with K- and Q-band maps smoothed to 1 deg resolution, from which an estimate of the CMB is subtracted to leave maps that effectively consist of foreground emission alone. The CMB is estimated using the internal linear combination (ILC) method (Hinshaw et al. 2007). Both the K and the Q maps are masked at a flux contour that leaves either 75% or 85% of the sky unmasked. The K and Q-band sky masks for each cut level are combined so that any pixel excluded by either cut is excluded by the combination. The resulting combinations, dominated by diffuse Galactic emission, are called KQ75 and KQ85, labeled by the admitted sky fraction (f_{sky}) of the input masks.

These masks are intended primarily to be applied to the foreground-cleaned versions of the sky maps for power spectrum and non-Gaussian analysis. They are made more effective for this purpose by extending them to include regions where the cleaning algorithm is subject to possible systematic error. A χ^2 analysis is done using differences Q–V and V–W between cleaned band maps at a reduced HEALPix resolution of $N_{\text{side}} = 32$ (Gorski et al. 2005), or “res 5” in *WMAP* terminology. Regions of four or more contiguous pixels with χ^2 higher than 4 times that of the polar caps are used to define the mask extensions, after 3 deg smoothing and cleanup steps to remove small “islands” caused by noise.

A point source mask is added to each of the diffuse sky masks. The point source mask from the seven-year analysis is updated to include newly detected *WMAP* point sources and the 100 GHz sources in the Planck early release compact source catalog. An exclusion radius of 1.2° is used for sources stronger than 5 Jy in any band and an exclusion radius of 0.6° is used for weaker sources.

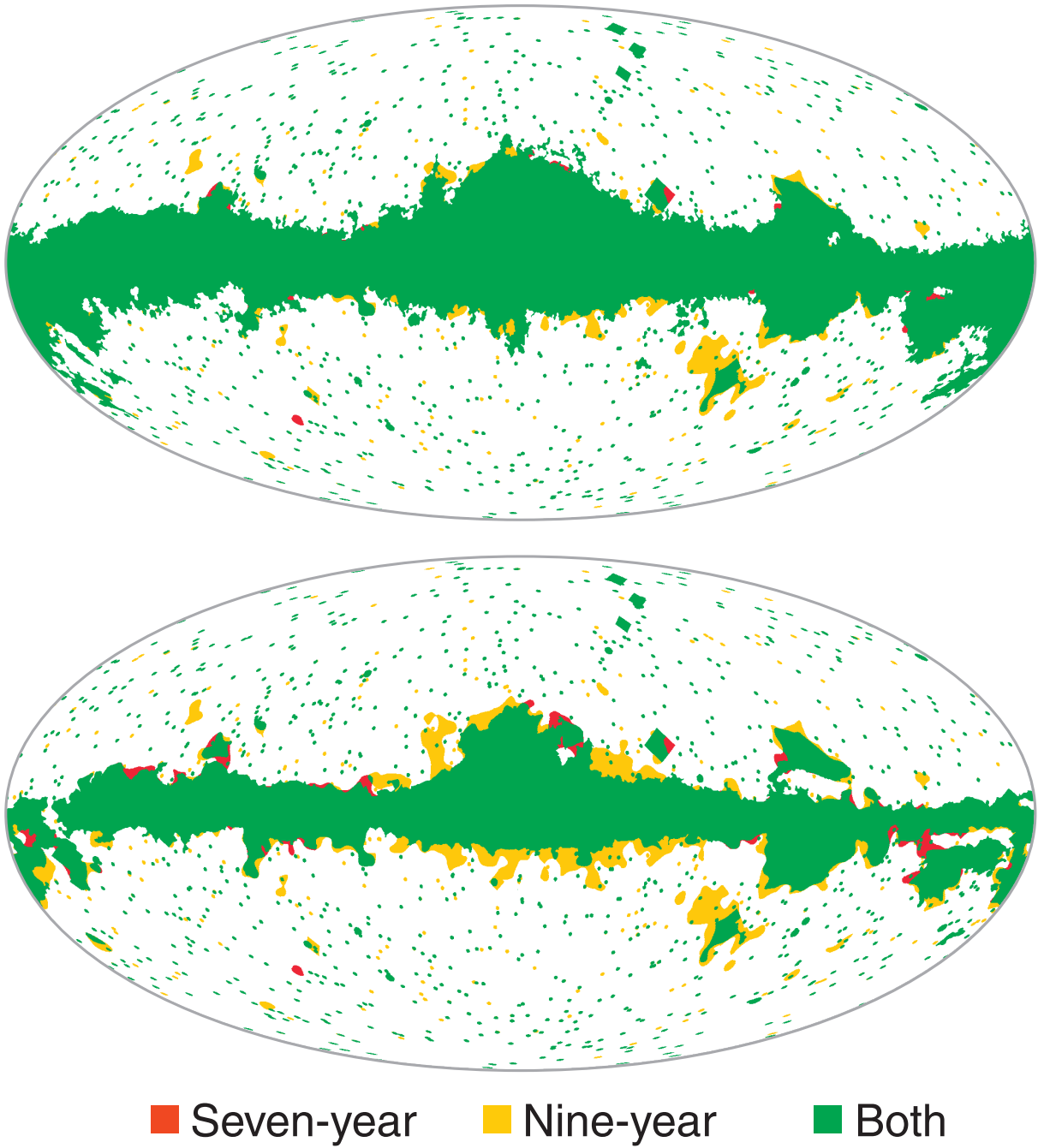


Fig. 17.— Comparison of nine-year masks to seven-year masks. At the top KQ75y7 and KQ75y9 are compared, and at the bottom KQ85y7 and KQ85y9. Green regions are masked in both the nine-year and seven-year masks, yellow regions are newly masked in the nine-year masks, and red regions are masked in the seven-year masks but no longer in the nine-year masks.

(A color version of this figure is available in the online journal.)

The nine-year versions of the final KQ85 and KQ75 sky masks, called KQ85y9 and KQ75y9, respectively, are compared to the seven-year versions in Figure 17. Changes in the foreground cleaning residuals have altered the morphology of the mask in the vicinity of the Gum Nebula, the Large Magellanic Cloud, and the Galactic center, with the largest relative changes occurring in the KQ85 mask. For KQ75, f_{sky} is decreased from 70.6% to 68.8%, a difference of 1.8% of the sky, and for KQ85, f_{sky} is decreased from 78.2% to 74.8%, a difference of 3.7% of the sky.

The sky mask for CMB polarization analysis is generated using cuts in K-band polarized intensity and a model of polarized dust emission, together with masking of point sources, as described by Page et al. (2007) and Gold et al. (2009). The nine-year polarization mask is the same as the seven-year version except that three additional point sources were added using a 1 degree exclusion radius - Hydra A, HB89 1055+018, and BL Lac.

5.3.3. *Internal Linear Combination (ILC)*

The internal linear combination (ILC) method seeks to produce a map of the CMB anisotropy from a linear combination of the five *WMAP* frequency bands. A first application of the method is described by Bennett et al. (2003a). The algorithm was revised slightly by Hinshaw et al. (2007); we refer to this version of the algorithm as the “classic ILC”, it has remained unchanged throughout subsequent *WMAP* data releases. As described in Hinshaw et al. (2007), the algorithm divides the sky into 12 regions – a larger high latitude region and 11 smaller regions spread across the galactic plane. Use of the smaller regions along the plane allows for spatially varying foreground complexity. For each of these smaller regions, five band-weights are computed by minimizing the temperature variance in the region, under the constraint that common-mode CMB signal is unaffected. Weights for the larger high latitude region are computed in a similar manner, but using pixels from locations near the outer-Galactic plane. Exact definitions of these regions are provided on LAMBDA.

We compute the nine-year classic ILC using the coadded deconvolved band maps which have been smoothed to a FWHM of 1° . The weights applied to the 5 frequency maps for each of the 12 sky regions are shown in Table 12. Values for the weights change slightly compared to previous *WMAP* releases as pixel noise, calibration and beam profiles have been refined.

To the eye, the ILC presents a reasonably foreground-free image of the CMB anisotropy. The beauty of the algorithm is that it is relatively independent of assumptions about foregrounds. However, assessing the underlying uncertainty in the resultant anisotropy map is a difficult problem which heavily relies on knowledge of the Galactic foregrounds. In subsequent sections, we will discuss efforts to improve the classic ILC, as well as characterize the level to which foreground residuals remain.

5.3.4. *Maximum Entropy Method (MEM)*

A MEM-based approach originally developed by Bennett et al. (2003a) and Hinshaw et al. (2007) is used to model the Galactic foreground emission spectrum in the *WMAP* bands on a pixel-by-pixel basis. Spatial templates of different emission components from external data are used as priors, and the model is designed to revert to the priors in regions of low signal-to-noise ratio. Thus the analysis is of most interest for separating and characterizing the different emission components in high signal-to-noise regions. The model foreground maps that are produced have complicated noise properties so they are not useful for foreground removal in cosmological analyses.

The nine-year MEM analysis differs from previous analyses (Bennett et al. 2003a; Hinshaw et al.

Table 12. ILC Coefficients per Region^a

Region	K-band	Ka-band	Q-band	V-band	W-band
0	0.1555	-0.7572	-0.2689	2.2845	-0.4138
1	0.0375	-0.5137	0.0223	2.0378	-0.5839
2	0.0325	-0.3585	-0.3103	1.8521	-0.2157
3	-0.0910	0.1741	-0.6267	1.5870	-0.0433
4	-0.0762	0.0907	-0.4273	0.9707	0.4421
5	0.1998	-0.7758	-0.4295	2.4684	-0.4629
6	-0.0880	0.1712	-0.5306	1.0097	0.4378
7	0.1578	-0.8074	-0.0923	2.1966	-0.4547
8	0.1992	-0.1736	-1.8081	3.7271	-0.9446
9	-0.0813	-0.1579	-0.0551	1.2108	0.0836
10	0.1717	-0.8713	-0.1700	2.8314	-0.9618
11	0.2353	-0.8325	-0.6333	2.8603	-0.6298

^aThe ILC temperature (in thermodynamic units) at pixel p of region n is $T_n(p) = \sum_{i=1}^5 \zeta_{n,i} T^i(p)$, where ζ are the coefficients above and the sum is over *WMAP*'s frequency bands. In addition (and as has been done before), the region smoothing from Hinshaw et al. (2007) has been applied and an ILC bias has been subtracted.

2007; Gold et al. 2009, 2011) in that spinning dust emission is treated as a separate emission component. Previously, synchrotron emission and spinning dust emission were treated together as a single component and an iterative method was used to solve for the spectrum of this component for each pixel.

The analysis is done using 1° smoothed beam-symmetrized nine-year sky maps in the five *WMAP* bands, with the ILC map subtracted from each map and conversion to antenna temperature applied. The zero level of each map is set such that a $\csc |b|$ fit, for HEALPix $N_{\text{side}} = 512$ pixels at $b < -15^\circ$ and outside of the KQ85 mask, yields a value of zero for the intercept. The maps are degraded to HEALPix $N_{\text{side}} = 128$ pixelization, and a model is fit for each pixel p by minimizing the function

$$H = \chi^2 + \lambda(p) \sum_c T_c(p) \ln \left[\frac{T_c(p)}{eP_c(p)} \right]. \quad (34)$$

Here T_c and P_c are the model brightness and template prior brightness for foreground component c (e is the base of natural logarithms). The form of the second term ensures positivity of the solution T_c for each component, which alleviates degeneracy between the components. The parameter λ controls the relative weight of the data and the priors in the fit. As in previous analyses, we base $\lambda(p)$ on the foreground signal strength: $\lambda(p) = 0.6 [T_K(p)]^{-1.5}$, where $T_K(p)$ is the K-band ILC-subtracted map in mK antenna temperature.

The MEM foreground model is a sum of synchrotron, free-free, spinning dust, and thermal dust components. The adopted spectra for synchrotron, free-free, and thermal dust emission are fixed power laws with $\beta = -3.0, -2.15,$ and $+1.8,$ respectively. The adopted synchrotron spectral index is consistent with measurements of K- to Ka-band spectral index from *WMAP* polarization data, for which free-free and spinning dust contributions are expected to be negligible. For spinning dust emission, we adopt a spectral shape predicted by the model of Ali-Haïmoud et al. (2009) and Silsbee et al. (2011). The top panel of Figure 18 compares predictions of this model for different interstellar environments. We adopt the spectral shape for their nominal cold neutral medium conditions. The bottom panel shows that the predicted shape does not vary much for different conditions if a multiplicative frequency shift is allowed for. The MEM model includes a frequency scale factor for the spinning dust spectrum for pixels where the spinning dust prior is brighter than 0.1 mK. This is constrained such that the peak frequency is in the range from 10 to 30 GHz. For other pixels, the peak frequency is fixed at 14.4 GHz, a typical value found for the Galactic plane region.

The adopted priors are shown in Figure 15. The synchrotron prior is based on the 408 MHz map of Haslam et al. (1982). We use the original version of this map; our previous MEM analyses used a filtered version in which striping and point sources are suppressed. We

add a zero level offset of 3.9 K, as suggested by Tartari et al. (2008) based on absolute measurements of sky brightness at 600 and 820 MHz. We subtract the 2.725 K CMB monopole and an extragalactic contribution of 12.96 K, from the analysis of ARCADE 2 and other data by Fixsen et al. (2011). The 408 MHz map is then scaled to form the prior in K-band using a spectral index of -2.9. (The ARCADE 2 extragalactic background is used instead of a source count based value such as 2.6 K from Gervasi et al. (2008) because it gives a prior that is more consistent with the *csc b* normalized K-band map at high latitudes.) The free-free prior is the scattering-corrected, extinction-corrected $H\alpha$ template described in 5.3.1, scaled to free-free brightness temperature in K-band using $11.4 \mu\text{K R}^{-1}$ (Bennett et al. 2003a). The spinning dust prior is the temperature-corrected dust map of Schlegel et al. (1998), scaled to spinning dust brightness temperature in K-band using $9.5 \mu\text{K MJy}^{-1} \text{ sr}$. This is the slope of the correlation between the dust map and a map of spinning dust brightness from fits to Haslam et al. (1982) 408 MHz, Duncan et al. (1995) 2.4 GHz, and ILC-subtracted *WMAP* data in the Galactic plane. The thermal dust prior is the prediction of model 8 of Finkbeiner et al. (1999) at 94 GHz. All of the prior maps have been smoothed to 1° FWHM.

The adopted model provides good fits to the data without iterative adjustment of the synchrotron component spectrum as used in previous analyses. For pixels at $|b| < 5^\circ$, absolute residuals are typically less than 0.01, 0.34, 1.2, 2.1, and 0.7 % in K-, Ka-, Q-, V-, and W-bands, respectively. Maps of the foreground components and peak frequency of spinning dust from the MEM analysis are shown in Figure 19.

5.3.5. *Markov Chain Monte Carlo Fitting*

We again perform a pixel-based Markov chain Monte Carlo (MCMC) fitting technique to the five bands of *WMAP* data. Our method is similar to that of Eriksen et al. (2007), but we focus more on Galactic foregrounds rather than CMB. The fit results of the prior releases have been reproduced, with the “base” model, which uses three power-law foregrounds, producing virtually the same reduced χ^2 per pixel. We have again also included the 408 MHz map of Haslam et al. (1981) with a zero-point determined using the same *csc |b|* method as for the *WMAP* data.

There are two main changes from the previous release. The first is that the MCMC fit now uses the spinning dust spectrum for grains in a “cold neutral medium” as computed by Silsbee et al. (2011), with an optional frequency shift parameter described below. This change was made so that the MCMC fit uses the same spinning dust spectrum as the rest of the nine-year analysis. The second significant change is that the spinning-dust model is now run with the synchrotron spectral index as a free parameter. This was done to improve

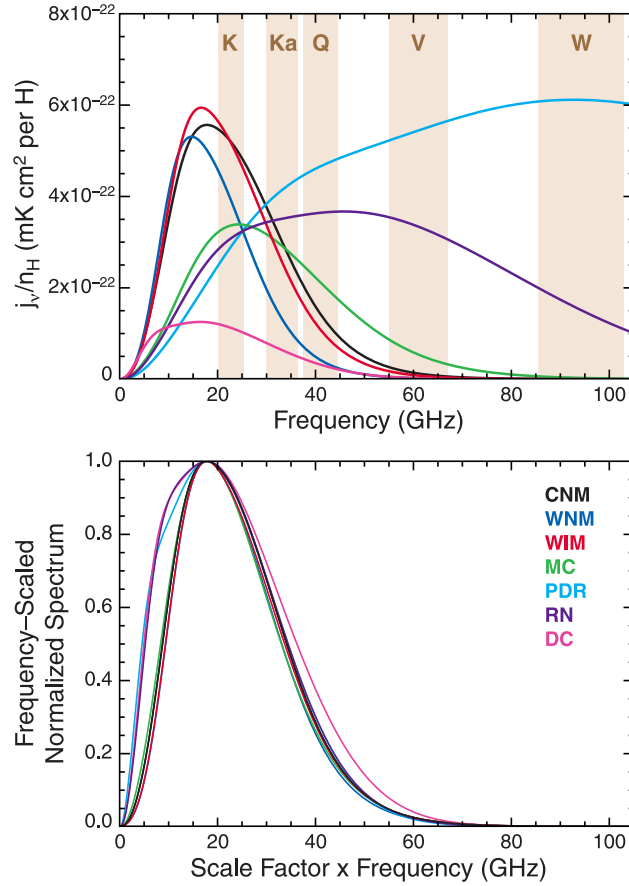


Fig. 18.— The top panel shows spinning dust emissivity spectra predicted by the model of Ali-Haïmoud et al. (2009) and Silsbee et al. (2011) for the nominal physical conditions that they adopted for different ISM environments - cold neutral medium (CNM), warm neutral medium (WNM), warm ionized medium (WIM), molecular cloud (MC), photodissociation region (PDR), reflection nebula (RN), and dark cloud (DC). The spectra were calculated using version 2.01 of the code SpDust provided by the authors, for the case where dust grains are allowed to rotate around non-principal axes. The spectra are in units of brightness temperature per H column density. The bottom panel shows the same spectra normalized to a peak of unity and scaled to a common peak frequency (that of the CNM spectrum, 17.8 GHz). The predicted spectral shapes for the different environments are similar. We adopted the CNM case for the shape of the spinning dust spectrum in our foreground fitting. We used this as an externally provided spectral template in our fits, usually with our own arbitrary amplitude and frequency scaling. The fit results in no way imply that the underlying physical mechanisms or the line-of-sight conditions have been established.

(A color version of this figure is available in the online journal.)

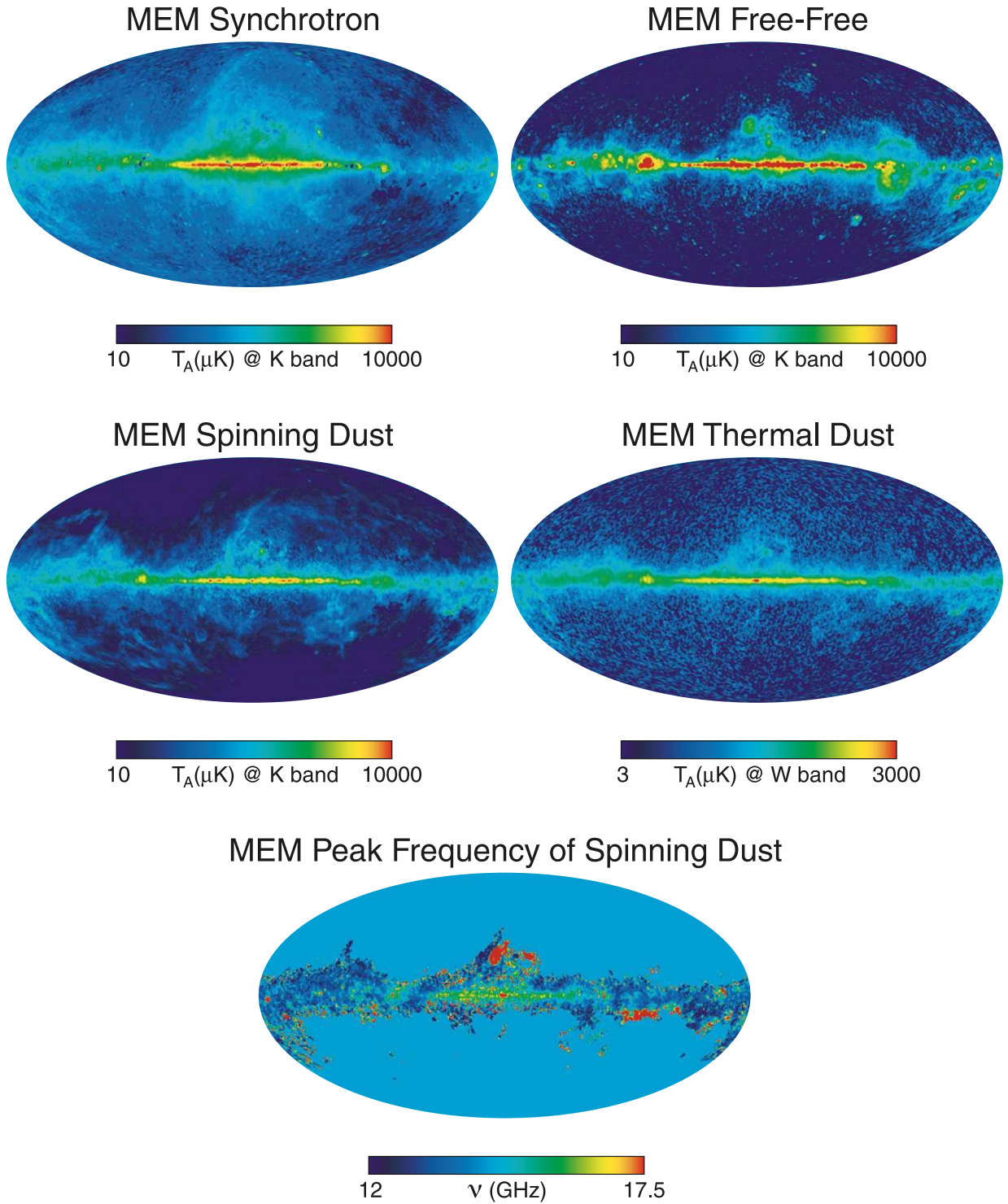


Fig. 19.— Parameter maps from the MEM model fit. The top four maps are shown on logarithmic scales and the others are on linear scales.

(A color version of this figure is available in the online journal.)

the quality of the fit, also discussed below.

The MCMC fit is performed on one-degree smoothed maps downgraded to HEALPix $N_{\text{side}} = 64$. A MCMC chain is run for each pixel, where the basic model is

$$T(\nu) = T_s \left(\frac{\nu}{\nu_K} \right)^{\beta_s(\nu)} + T_f \left(\frac{\nu}{\nu_K} \right)^{\beta_f} + a(\nu)T_{\text{cmb}} + T_d \left(\frac{\nu}{\nu_W} \right)^{\beta_d} \quad (35)$$

for the antenna temperature. The subscripts s, f, d stand for synchrotron, free-free, and dust emission, ν_K and ν_W are the effective frequencies for K- and W-bands (22.5 and 93.5 GHz), and $a(\nu)$ accounts for the slight frequency dependence of a 2.725 K blackbody using the thermodynamic to antenna temperature conversion factors found in Bennett et al. (2003a). The fit always includes polarization data as well, where the model is

$$Q(\nu) = Q_s \left(\frac{\nu}{\nu_K} \right)^{\beta_s(\nu)} + Q_d \left(\frac{\nu}{\nu_W} \right)^{\beta_d} + a(\nu)Q_{\text{cmb}} \quad (36)$$

$$U(\nu) = U_s \left(\frac{\nu}{\nu_K} \right)^{\beta_s(\nu)} + U_d \left(\frac{\nu}{\nu_W} \right)^{\beta_d} + a(\nu)U_{\text{cmb}} \quad (37)$$

for Stokes Q and U parameters. Thus there are a total of 15 pieces of data for each pixel ($T, Q,$ and U for five bands).

As for the previous two releases, the noise for each pixel at $N_{\text{side}} = 64$ is computed from maps of N_{obs} at $N_{\text{side}} = 512$. To account for the smoothing process, the noise is then rescaled by a factor calculated from simulated noise maps for each frequency band. The MCMC fit treats pixels as independent, and does not use pixel-pixel covariance, which leads to small correlations in χ^2 between neighboring pixels. This has negligible effect on results as long as goodness-of-fit is averaged over large enough regions.

K-band is used as a template for the polarization angle of synchrotron and dust emission, so U_s and U_d are not independent parameters, identical to the previous analyses. All models also fix the free-free spectral index to $\beta_f = -2.16$, the same as in the seven-year release.

Results from the models discussed below are listed in Table 13. The “base” model uses three power-law foregrounds, where the synchrotron spectral index $\beta_s(\nu)$ is taken to be independent of frequency but may vary spatially, and the dust spectral index β_d is allowed to vary spatially. We assume the same spectral indices for polarized synchrotron and dust emission as for total intensity emission. This model has a total of 10 free parameters per pixel: $T_s, T_f, T_d, T_{\text{cmb}}, \beta_s, \beta_d, Q_s, Q_d, Q_{\text{cmb}},$ and U_{cmb} .

For models with a spinning dust component, another term is added to Equation 35

$$T_{sd}(\nu) = T_{sd}(\nu_K)S_{sd}(\nu), \quad (38)$$

Where $S_{sd}(\nu)$ parameterizes the shape of the spinning dust spectrum, and is interpolated from values for the “cold neutral medium” spectrum given by Silsbee et al. (2011). An optional shift parameter can be used to rescale the frequency dependence before interpolation. This shift parameter applies to the full sky and does not vary per pixel. After shifting and interpolation, the spectrum $S_{sd}(\nu)$ is normalized to unity at K-band, leaving $T_{sd}(\nu_K)$ as the only spinning dust parameter for each pixel. Independent fits were performed to determine the best-fit shift parameter, which for the averaged sky was found to be 0.84. Inside the Kp12 mask (within a few degrees of the galactic plane) the preferred shift parameter may be somewhat lower (0.77), but the evidence is not strong.

The spinning dust component is assumed to have negligible polarization, as theoretical expectations for the polarization fraction are low compared to synchrotron radiation (Lazarian & Draine 2000), and polarization data thus far show no evidence that such a component is necessary (Section 5.3.2, López-Caraballo et al. (2011), Dickinson et al. (2011), Rubiño-Martín et al. (2012)). This model then has 11 free parameters per pixel: the 10 parameters of the base model, plus the spinning dust amplitude.

MCMC fits for the nine-year release were performed with the addition of the 408 MHz data compiled by Haslam et al. (1981). The error on the zero point for this data was estimated in that work to be ± 3 K, with an overall calibration error of 10%. As the MCMC method treats all input maps equally, for consistency we estimate and subtract a nominal zero point offset of 7.4 K, as determined by the same $\text{csc } |b|$ method we use for the *WMAP* sky maps. For comparison, Lawson et al. (1987) used a comparison with 404 MHz data to find a uniform (presumably extragalactic) component with a brightness of 5.9 K.

We find that to best fit the 408 MHz data, the spinning dust spectrum needs to have its peak frequency adjusted downward by approximately 15%, similar to the case in the

Table 13. Reduced χ^2 per pixel of MCMC fits

Dataset	Model	Galactic plane	outside Galactic plane	full-sky average
<i>WMAP</i> five-band	(a) base	2.38	1.17	1.29
	(b) sd096	1.00	1.06	1.05
<i>WMAP</i> & 408 MHz	(c) base	2.46	1.13	1.25
	(d) sd096	6.27	1.42	1.88
	(e) sd070	1.76	1.33	1.37
	(f) bsfree sd084	1.24	1.03	1.05
	(g) bsfree Strong sd084	1.05	1.01	1.01

previous release. We also find that a much better fit is achieved in the plane by varying the synchrotron spectral index, which for that region allows a $\chi^2_\nu = 1.24$ versus $\chi^2_\nu = 1.76$ with fixed index, for 8.5 effective degrees of freedom. The mean spinning dust fraction inside the KQ85 mask is somewhat lower than in the seven-year fit, at 10% of 22 GHz flux compared to 18% in the seven-year fit.

We also find that the fit is improved by taking into account some mild steepening of the synchrotron spectrum from 408 MHz to *WMAP*'s frequency range. Strong et al. (2011) have compared mid-latitude synchrotron measurements and estimates from 22 MHz to 94 GHz with predictions of cosmic ray propagation models based on cosmic ray and gamma ray data. We adopted their best fit pure diffusion model (“galdef_ID_54_z04LMPD_g0_1.3_withsecS”) to compute an effective synchrotron spectral index between 408 MHz and 23 GHz (*WMAP* K-band), as well as the index from 23 GHz to 94 GHz over which range it remains nearly constant. We calculate the difference in these two indices to be -0.12 . Our model g (hereafter MCMCg, and listed on the last line of Table 13) then uses this difference, so that while the model parameter β_s is used as the synchrotron index for the *WMAP* bands, the value $\beta_s + 0.12$ is used to extrapolate the synchrotron component down to 408 MHz for comparison to the map of Haslam et al. The parameters from this fit are shown in Figure 20.

5.3.6. Six Band Minimal Prior Chi-Squared Fitting

In this section we attempt to find a best fit foreground model that is consistent with both the *WMAP* data and Haslam. This is intended to be a faster fit than was done with the MCMC method in Section 5.3.5, and so it allows us to experiment with models more rapidly. Because this method simply finds the maximum likelihood point of the foreground model, it does not provide errors bars as the MCMC method does. Also, we avoid priors in the form of foreground component sky maps, which were used in the MEM fitting in Section 5.3.4. The priors we use in this section are mostly in the form of the foreground spectral shapes (relative antenna temperature as a function of frequency) instead of in the form of sky maps. This is a complementary form of analysis to the MEM fitting.

5.3.6.1. Data and noise Our data consists of maps smoothed to a common resolution of 1° FWHM, which we pixelize at r6. We use 6 maps: 408 MHz and the five *WMAP* bands. We use the original Haslam map (408 MHz) as in Section 5.3.4 with the same offsets, except in this case we do not use the ARCADE extragalactic background. Instead of subtracting 12.96 K, we subtract 2.6 K (Tartari et al. 2008), so the Haslam map used in this section is 10.36 K brighter in antenna temperature in all pixels. The rms noise in each pixel of the

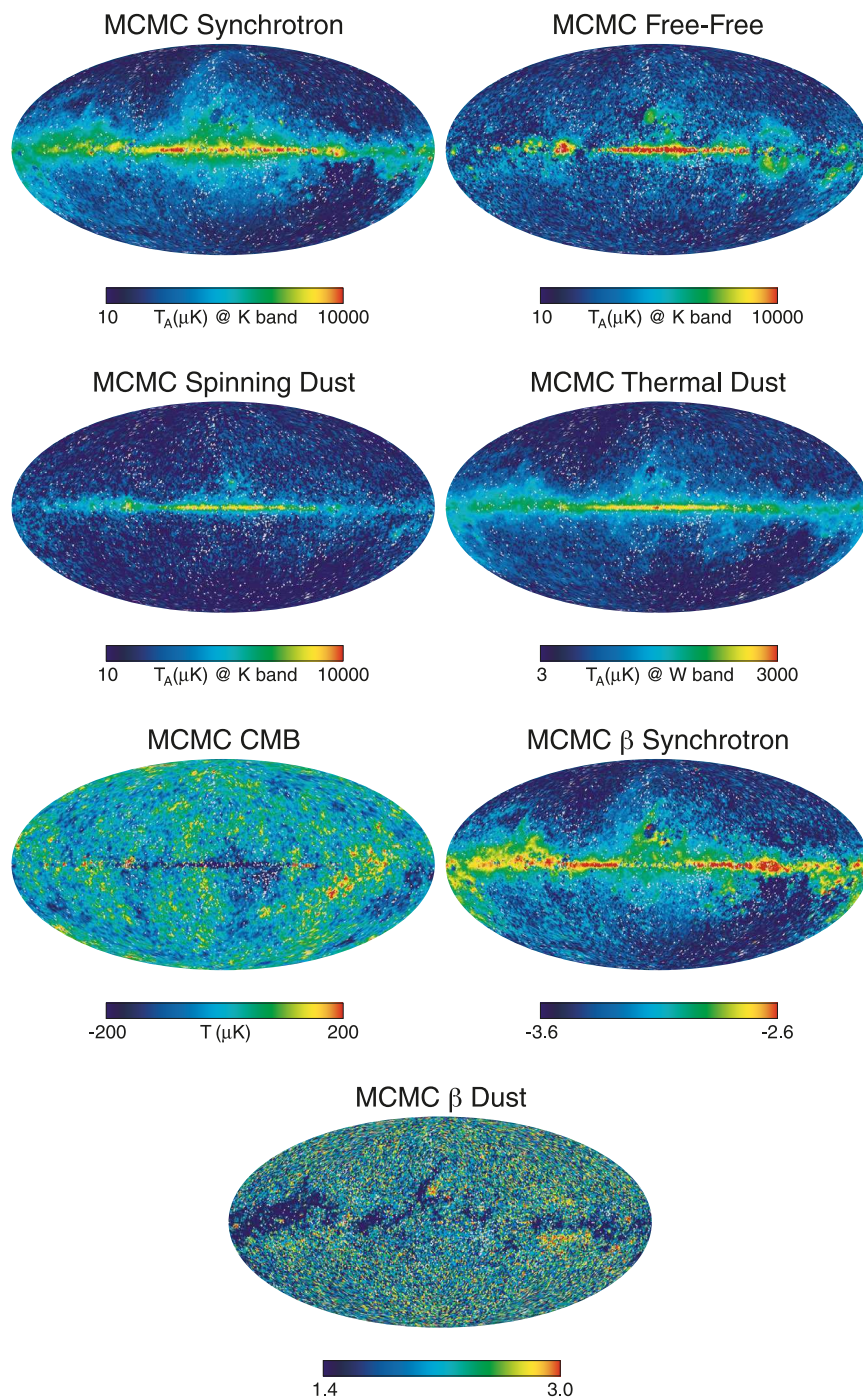


Fig. 20.— Parameter maps from the MCMCg model fit. The top four maps are shown on logarithmic scales and the others are on linear scales. Accurate determination of the CMB close to the Galactic plane is inhibited by CMB-foreground covariance. The map for β synchrotron is evaluated at 40 GHz.

(A color version of this figure is available in the online journal.)

408 MHz map is taken to be 10% of the antenna temperature, added in quadrature with a 0.6 K uncertainty in zero point (Haslam et al. 1982; Tartari et al. 2008).

We consider three noise components for the *WMAP* bands in this foreground fitting: the 0.2% overall gain uncertainty, the $\sigma_0/\sqrt{N_{\text{obs}}}$ instrument noise, and the uncertainty in the diffuse foreground monopole corrected with the $\csc |b|$ offsets, discussed previously. Because our fitting is done on a per-pixel basis, we approximate these errors as uncorrelated between pixels, and we add them in quadrature.

The instrument noise can be treated carefully to account for the smoothing to 1° FWHM. Typically it is inaccuracies in the foreground model that cause χ^2 to be large and not the details of the noise. However, a detailed treatment of the noise smoothed to 1° in r6 pixels is given in Appendix D. Again, because we fit on a per-pixel basis, we ignore the correlations in noise between nearby pixels.

5.3.6.2. Foreground Models We start with a simple foreground model consisting of several simple power laws, and progressively add complexity to the model to improve the fit. The foreground model we use involves temperature only; we did not try to fit polarization. The sequence of foreground models we use is listed in Table 14, and details are discussed below.

The synchrotron spectrum is either taken to be a pure power law in antenna temperature, $T_A \propto \nu^{\beta_{\text{sync}}}$, or derived from assuming the spectral index curve from Strong et al. (2011), Figure 6, upper right corner. This is the curve for a low-energy electron injection index of 1.3 and is the same spectrum as used in the MCMC fitting. To this spectral index curve we optionally add an offset in β_{sync} , $-0.5 \leq \Delta\beta_{\text{sync}} \leq 0.5$ independent of frequency. We numerically integrate this spectral index curve to obtain synchrotron antenna temperature.

The free-free spectrum is the slightly curved model given by Oster (1961) and rearranged for antenna temperature by Bennett et al. (2003a). This is

$$T_A^{WMAP}(\nu) \propto \frac{1 + 0.2218 \ln(T_e/8000\text{K}) - 0.1479 \ln(\nu/41\text{GHz})}{(\nu/41\text{GHz})^2 (T_e/8000\text{K})^{1/2}}. \quad (39)$$

For simplicity we use an electron temperature of 8000 K. We expect variations in electron temperature, but these do not strongly affect the shape of the spectrum.

The dust spectrum is given by a pure power law, typically with a fixed spectral index of $\beta_{\text{dust}} = 1.8$.

Finally, we add a spinning dust component. This is an antenna temperature spectrum from the Silsbee et al. (2011) model prediction for cold neutral medium (CNM) conditions,

Table 14. χ^2 Minimal Prior Fits of Foreground Models

Model	synchrotron ^a	$\Delta\beta_{\text{sync}}$ ^b	ff ^c	β_{dust}	SD ^d	SD peak ^e	ν ^f	χ^2/pixel ^g	f_{bad} ^h
1	power	0	yes	1.8	no	-	4	6.1	37%
2	power	vary	yes	1.8	no	-	5	2.5	11%
3	power	vary	yes	1.6–2.0	no	-	6	2.3	9.5%
4	power	vary	yes	1.8	yes	15.1	6	1.5	4.4%
5	power	vary	yes	1.8	yes	12.5–17.8	7	0.64	0.59%
6	Strong	0	yes	1.8	yes	15.1	5	5.4	30%
7	Strong	0	yes	1.8	yes	12.5–17.8	6	4.1	20%
8	Strong	vary	yes	1.8	yes	15.1	6	1.2	2.1%
9	Strong	vary	yes	1.8	yes	12.5–17.8	7	0.60	0.48%

^aWhether the synchrotron is treated as a pure power law or modeled according to a model from Strong et al. (2011).

^bFor both power law and Strong et al. synchrotron models, we either set the spatial variation in spectral index $\Delta\beta_{\text{sync}}$ to zero or allow it to vary: $-0.5 \leq \Delta\beta_{\text{sync}} \leq 0.5$. In the case of a power law, $\Delta\beta_{\text{sync}}$ is a perturbation added to $\beta_{\text{sync}} = -3.0$.

^cThe free-free spectrum is given by Oster (1961); we use an electron temperature of 8000 Kelvin.

^dWhether a spinning dust spectrum in the shape of the cold neutral medium is used.

^eRange of available peak frequencies for the spinning dust spectrum, in GHz. This is either fixed at 85% of the peak frequency 17.8 GHz for the cold neutral medium (which is 15.1 GHz), or allowed to be a range from 70% to 100% of the CNM peak frequency (which is 12.5 GHz to 17.8 GHz).

^fDegrees of freedom in the model. Most degrees of freedom are constrained: foreground amplitudes must all be positive, for example. The highly constrained CMB amplitude is included as a degree of freedom.

^gThe mean χ^2 per pixel, averaged over the whole sky (for temperature only, not polarization), where χ^2 values greater than 10 are set to exactly 10 so that a few extremely bad pixels don't throw off the whole fit. This χ^2 value includes deviations of the model from Haslam and WMAP bands, but not deviations from the ILC prior. Since there are 6 measurements in each pixel (and an ILC prior) and $4 \leq \nu \leq 7$ degrees of freedom in the model, we would expect $\chi^2/\text{pixel} \approx 6 - \nu$ for a good fit if we had unconstrained variables.

^hThe fraction of the pixels where $\chi^2 > 10$. This is an estimate of the sky fraction where the fit is bad. Again, the χ^2 used here includes the difference of the model from the six bands, but does not include deviations from the ILC prior.

with an optional frequency scale factor. If the spectrum is plotted as antenna temperature as a function of log frequency, the frequency scale factor simply shifts the spectrum left or right. However, instead of quoting the frequency scale factor, we instead quote the peak frequency, when the spectrum is measured in antenna temperature as a function of frequency. The peak frequency of the CNM spectrum is 17.8 GHz.

All of these foregrounds are assumed to have a positive scale factor associated with them. Synchrotron, free-free, and spinning dust are normalized to K-band antenna temperature, and dust is normalized to W-band antenna temperature.

The CMB is modeled as a blackbody with constant thermodynamic temperature. To make the CMB fit look statistically isotropic, we add a prior that the CMB must be within $5 \mu\text{K}$ rms of the nine-year ILC. Without this prior, the data do not constrain the CMB very tightly in the galactic plane, and we find the CMB preferring values lower than $-250 \mu\text{K}$.

To approximate the finite width of the *WMAP* bandpasses, we calculate these spectra at three frequencies per band and determine the *WMAP* response from a weighted average, as described in Appendix E.

5.3.6.3. Fitting Code Fitting the foregrounds is a least squares problem. However, we modify the simple linear least squares problem in two ways: we constrain the coefficients, and we allow nonlinear foreground spectra. Constraining the coefficients is essential, because we know the foregrounds are always positive. Unconstrained least squares fitting will frequently give a very negative and therefore unphysical foreground. Secondly, we allow nonlinear foregrounds, in the sense that the total foreground is not simply a linear combination of fixed foreground spectra. We allow the spectra to vary, for example by allowing the synchrotron spectral index to be a fit parameter, or by allowing the peak frequency of spinning dust to be a fit parameter.

There are several codes which can be used to solve this problem. We have not made a thorough search of all available software, and we only considered code in IDL since that is the language in which much of our other software is written. We have found two codes to be useful: a bound variable least squares routine and a Levenberg-Marquardt solver.

We found a Bound Variable Least Squares (BVLS) routine⁵ to be very fast, but it is restricted to linear foreground models and so it cannot solve for varying spectral indices or spinning dust frequency scale parameters. Because of this constraint we do not use it to report results in this paper. However, this code does have the advantage that parameters

⁵bvls.pro, available from <http://www-astro.physics.ox.ac.uk/~mxc/idl/>

can be constrained to be positive, so it can provide physically reasonable fits.

For the results reported in this section (in Table 14) we use the `mpfitfun.pro` routine⁶, which uses the Levenberg-Marquardt algorithm and was written by Craig Marquardt, for the constrained nonlinear least squares fitting. This is somewhat slower than the BVLS code because it cannot use the assumption that the χ^2 function is precisely quadratic in all of the fit coefficients. The ability to calculate foreground spectra quickly is an important factor in the speed of these calculations. We discuss a useful rapid method of calculating the integral over the *WMAP* bandpasses in Appendix E.

5.3.6.4. Results The results of this simple foreground fitting are shown in the last columns of Table 14. Additionally, maps from the Model 9 fit are shown in Figure 21. A set of three fixed power laws in Model 1 does not fit the data well. Allowing spatial variation of the synchrotron power-law spectral index in Model 2 substantially improves this, but 11% of the sky is still fit very poorly. Allowing spatial variation of the dust spectral index in Model 3 does not substantially improve the number of well fit pixels, so we fix the dust spectral index to $\beta = 1.8$. Adding a spinning dust component with peak frequency of 15.1 GHz (which is 0.85 times the CNM peak frequency of 17.8 GHz) does improve the fit, and allowing that peak frequency to vary between 12.5 GHz and 17.8 GHz helps even more. See Models 4 and 5.

Because it is probable that the synchrotron is not a pure power law and because we use the Haslam data at 408 MHz, which is much lower in frequency than the *WMAP* data, we test a curved synchrotron model from Strong et al. (2011). If we do not allow the spectral index to vary, we again get bad fits in Models 6 and 7. However, a varying spectral index combined with a spinning dust component produces results that are fractionally better than a pure power law with the same spinning dust components, as can be seen by comparing models 5 and 9, and comparing models 4 and 8.

None of these fits is perfect. Even in Model 9, there remain a few pixels that are not fit well. These are primarily in Ophiuchus, the galactic plane, and the Gum nebula.

5.3.7. Diffuse Foreground Results

5.3.7.1. Cross-Comparison of Foreground Fits Maps of parameters from the MEM, MCMCg, and six-band χ^2 Model 9 fits are shown in Figures 19, 20, and 21. A summary of

⁶available from <http://cow.physics.wisc.edu/~craigm/idl/idl.html>

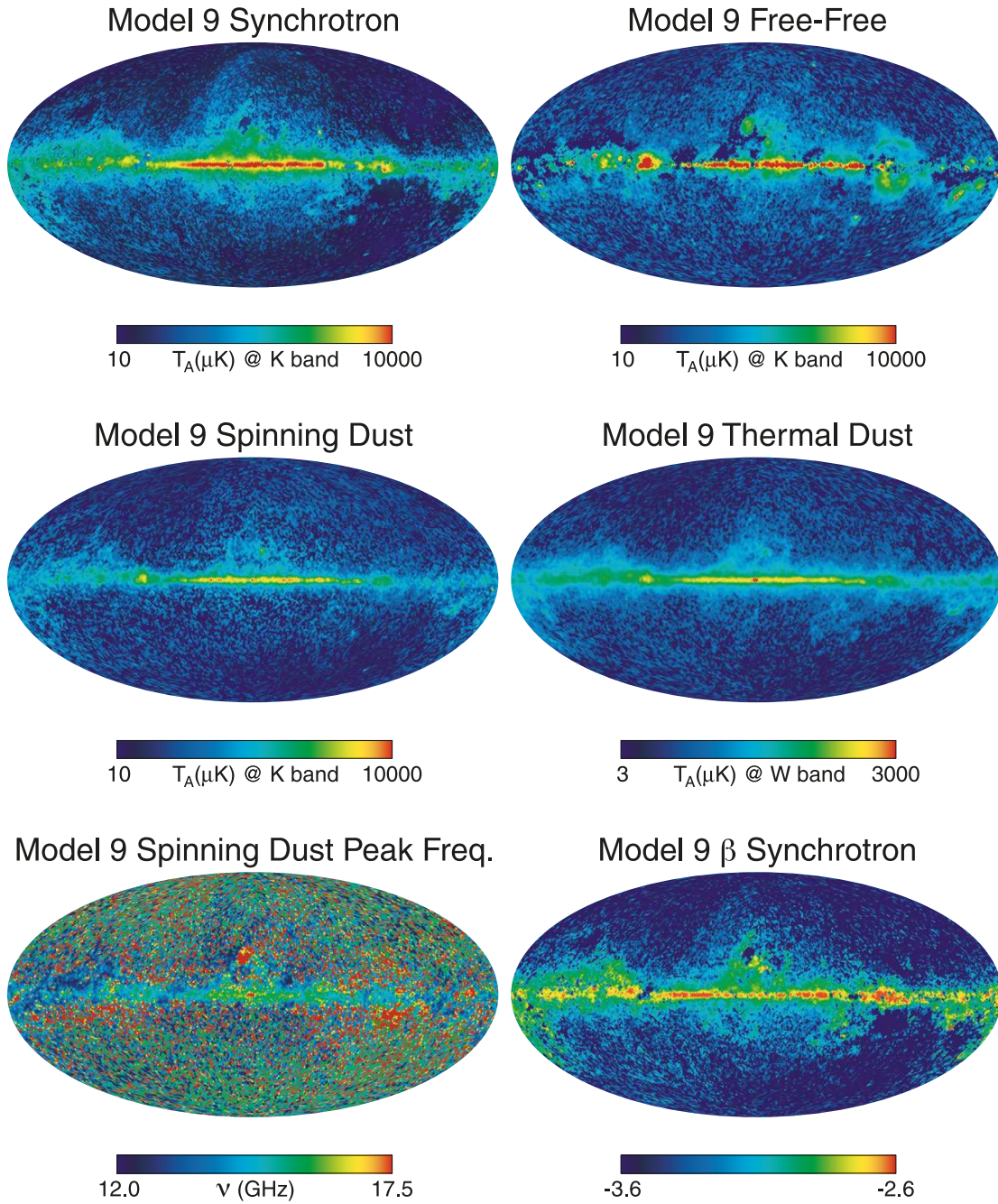


Fig. 21.— Parameter maps from the Model 9 fit. The top four maps are shown on logarithmic scales and the others are on linear scales. The map for β synchrotron is evaluated at 40 GHz. (A color version of this figure is available in the online journal.)

the parameter treatment for each of these three models is provided in Table 15.

Results from these three models are a sampling of the possible parameter space which can be used to produce a total foreground model in each *WMAP* band. Each of these models possesses strengths and weaknesses, which can be used to offset one another. Included in these considerations are the treatment of the CMB component, the use of spatial priors, and the use of spectral constraints.

Treatment of the CMB. Both the MEM and Model 9 make use of the ILC as the CMB estimator: the MEM subtracts the ILC from the *WMAP* data before fitting, and Model 9 uses the ILC as a strong prior. As discussed in Section 5.3.7.2, the ILC is an imperfect estimate of the true CMB, containing a residual foreground bias signal. MCMCg, on the other hand, treats the CMB as a free parameter in its fit solution. While this is a strength for MCMCg at high latitudes, CMB-foreground covariance is strongest in the Galactic plane, and MCMCg does not separate the CMB and foregrounds well there. Use of the ILC provides a better constraint in that case.

Use of spatial priors. The MEM uses spatial templates to constrain its fitting solution at high latitudes where signal-to-noise is lower than in the Galactic plane. This produces a less noisy parameter solution at high latitudes when compared to the MCMCg and Model 9 χ^2 fit. This is valuable to the extent that one trusts those priors, both in terms of zero levels and spatial structure.

Use of spectral constraints. The synchrotron spectral index β_s is a pivotal parameter in model fitting, since its behavior influences the model allocation between synchrotron, free-free and spinning dust. The MEM assumes a constant value of $\beta_s = -3$ at *WMAP* frequencies. Model 9 and MCMCg allow each pixel to fit for this parameter independently, within the constraints of a Strong et al. (2011) spectral dependence. Positional gradients, including a latitudinal gradient, are probably closer to physical reality than a constant value (Kogut et al. 2007). However, with this degree of freedom comes the possibility for degeneracies with the free-free and spinning dust parameters. In Figure 23 we show results from a foreground degeneracy analysis for a representative pixel in the six-band Model 9 fit. There are significant degeneracies between parameter pairs that include either synchrotron amplitude or β_s . (A similar result was presented by Gold et al. (2009) for the five-year MCMC analysis, although that lacked a spinning dust component). We believe degeneracies are a factor in the appearance of the MCMCg and Model 9 β_s maps, which show a strong latitudinal gradient and a dust-like morphology in some regions, e.g., extending south of the plane over $150^\circ < l < 190^\circ$ and in the North Celestial Pole HI loop that extends north of the plane over $120^\circ < l < 150^\circ$ (Meyerdierks et al. 1991). All three models share a common spectral shape for the spinning dust spectrum. This shape is allowed to shift peak

Table 15. Summary of Foreground Decomposition Model Assumptions

Parameter	MEM	MCMCg	χ^2 Model 9
$\beta_{\text{sync}}^{\text{a}}$	–3.0, fixed	Strong, $ \Delta\beta < 0.5$	Strong, $ \Delta\beta < 0.5$
β_{dust}	+1.8, fixed	free	+1.8, fixed
β_{ff}	–2.15, fixed	–2.16, fixed	–2.09 – –2.17, fixed ^b
$\nu_{\text{peak}}^{\text{sd c}}$	10–30, constrained	14.95, fixed	12.5–17.8, constrained
CMB	ILC subtracted	free	ILC prior
polarization data fit	no	yes	no
external foreground spatial priors	Haslam, SFD, FDS, $\text{H}\alpha^{\text{d}}$	no	no

^aSynchrotron is assumed to be a power law with a fixed spectral index, β_{sync} , or a variable power law based on a Strong et al. (2011) model, with a best fit value of $\Delta\beta$ added to the spectral index.

^bThe free-free spectrum for the χ^2 Model 9 fit is given by Oster (1961) with a fixed electron temperature $T_e = 8000$ K. The spectral index, $\beta_{\text{ff}} = -2.14$ at K-band and -2.17 at W-band. It increases to -2.09 at 408 MHz.

^cA spinning dust cold neutral medium spectral shape is used with an allowed range of a peak frequency shift, specified in GHz.

^d“Haslam”: the 408 MHz survey of Haslam et al. (1982); “SFD”: the temperature-corrected dust map of Schlegel et al. (1998); “FDS”: thermal dust model 8 from Finkbeiner et al. (1999); “ $\text{H}\alpha$ ”: $\text{H}\alpha$ all-sky mosaic from Finkbeiner (2003).

frequencies for MEM and Model 9, while MCMCg adopts a fixed peak frequency. Although the use of a common shape seems well motivated (see Figure 18), there is no guarantee that it is correct for all pixels. This is an additional source of uncertainty in the fits, as observational deviations from this shape will be distributed primarily among free-free and synchrotron components. We note an apparent power deficit in the Model 9 free-free map, present to a lesser extent in the MCMCg result, which is dust-like in signature. Finally, we note that all models assume a fixed β_{ff} , and only MCMCg allows for a free β_{dust} . These are less uncertain values, but errors in fixed values can ripple into other components.

It is nevertheless possible to find relative agreement among these models, especially at higher latitudes. The high latitude foreground spectral components in the *WMAP* bands are shown in Figure 22 and all of the fitting techniques support this spectral decomposition of the foregrounds.

The actual foregrounds, especially at low Galactic latitudes, are clearly more complex than our parameterizations allow, since variations in physical conditions exist along any line of sight. There are some sky locations that were not well fit even with all of the degrees of freedom allowed by the χ^2 fitting, such as in Ophiuchus. Given the complexity of the foreground emission mechanisms sampled by the *WMAP* bands, separating the CMB from the total observed foreground is a more straightforward and reliable process than the decomposition of that total foreground into physical components. Although we have found imperfections in the dust and free-free templates we use for foreground cleaning, those imperfections are primarily confined to regions which are masked from use in the cosmological analysis, and the use of foreground cleaned maps in the power spectrum analysis is robust.

A remaining item of interest is the microwave “haze”. The first claim of a haze (Finkbeiner 2004) suggested an excess of free-free emission compared to the expectation from $H\alpha$, and was dubbed a “free-free haze”. No longer believed to be free-free emission, its exact shape and attribution has evolved in the literature. In general the haze is described as an excess extended diffuse emission near the Galactic center. This excess appeared as a residual from the decomposition of *WMAP* K, Ka and Q maps using external templates (Finkbeiner 2004; Dobler & Finkbeiner 2008). The templates most often used for this purpose are the Haslam 408 MHz map, a de-extincted form of the Finkbeiner (2003) $H\alpha$ all-sky mosaic and the Finkbeiner et al. (1999) thermal dust models.

While the excess compared to external templates is clear, the attribution to a physical mechanism associated with Galactic emission is not. One interesting possibility characterizes the haze as a separate hard spectrum synchrotron component associated with the Gamma-ray bubbles (Planck Collaboration IX 2012; Dobler et al. 2010). Planck Collaboration IX (2012) uses a Gibbs sampler to fit a foreground model outside a Galactic mask that assumes

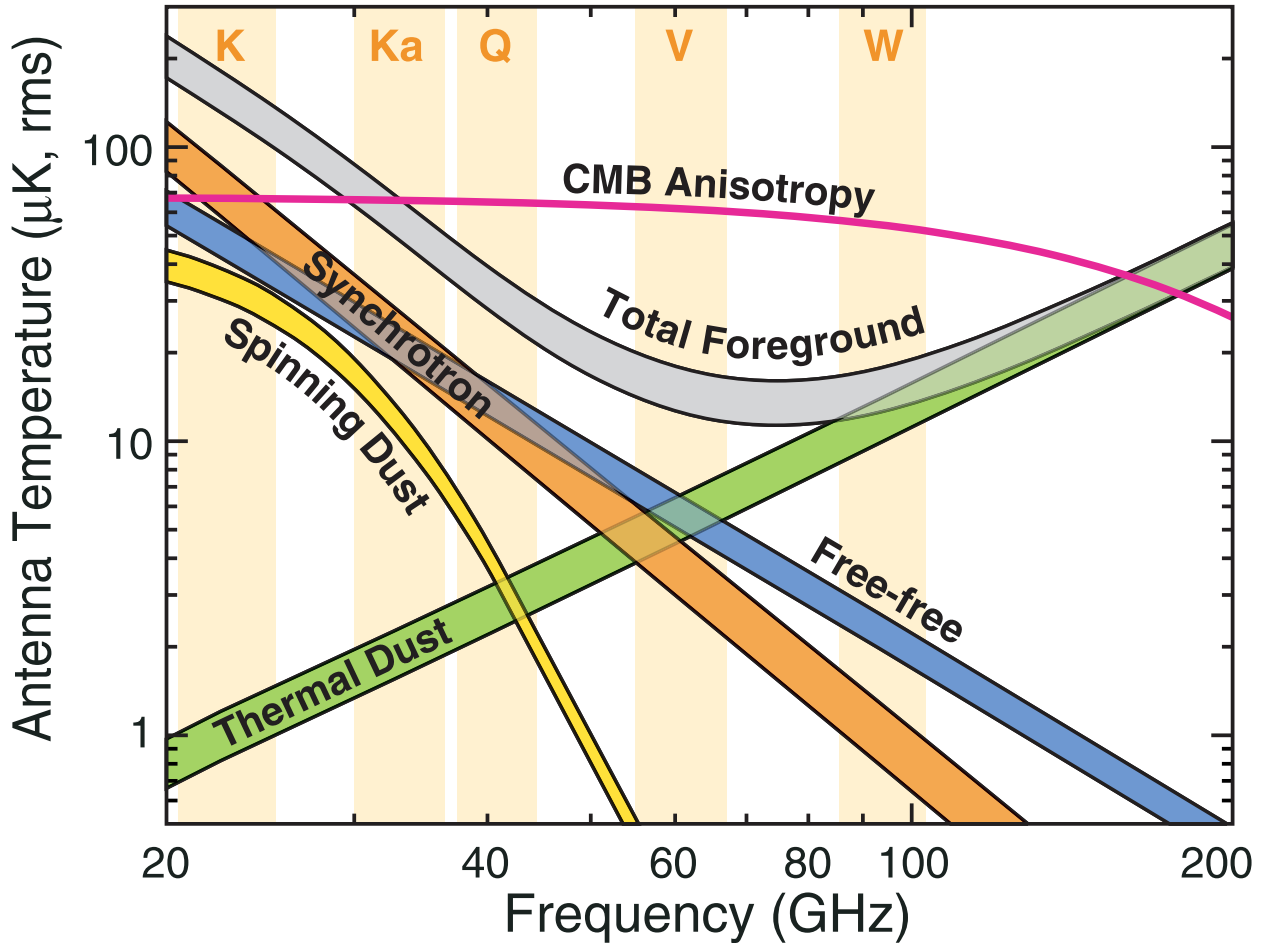


Fig. 22.— Spectra of CMB and foreground anisotropy. The foreground anisotropy results are averages over the three foreground models (MCMCg, MEM, and Model 9). The upper curve for each foreground component shows results for pixels outside of the KQ85 mask, and the lower curve shows results outside of the KQ75 mask. The different foreground models are in good agreement for the total foreground anisotropy. Results for the individual foreground components depend on model assumptions discussed in the text, and typically differ among the three models by 5% to 25%.

(A color version of this figure is available in the online journal.)

separate hard and soft power-law spectra. The cut-sky maps with these spectra are further decomposed, using external templates, into emission components with a distinct residual identified as a $\beta_s \sim -2.55$ synchrotron haze. It is also possible to find reasonable models which adequately describe the data without the invocation of a haze component, as in e.g. Dickinson et al. (2009). In these cases, the haze excess is absorbed and distributed amongst other low frequency Galactic components. For example, a typical K-band haze intensity at roughly $\pm 20^\circ$ latitude near the Galactic center is $\sim 100 \mu\text{K}$ (Planck Collaboration IX 2012), whereas K-band residuals in those locations for the MEM, MCMCg, and Model 9 models are roughly zero with a 1σ deviation of a few μK . Existence of the haze as a separate spatial component is model dependent. It depends on foreground spectral assumptions, which affect the emission allocation between the CMB and the decomposition of the Galactic foregrounds into physical components. Because the haze is easily absorbed into other model components if not explicitly accounted for, and a number of remaining uncertainties exist in the morphology and behavior of low-frequency emissions in general (e.g. spinning dust), we feel this is a topic which remains open. Additional observations would be beneficial, especially at frequencies below K-band.

Although the thermal dust and free-free parameter amplitudes differ between the models presented here in details, there are clear common-mode similarities when they are compared against their externally derived equivalents (which we have used in Section 5.3.2 for template cleaning). Figure 24 illustrates these common-mode features by taking the mean parameter amplitudes from three models presented in this paper (MCMCg, MEM and chi-square fitting Model 9), and differencing them against their template counterparts. On the left in Figure 24 is the mean thermal dust amplitude at W-band minus the 94 GHz estimate derived from IRAS and COBE data by Finkbeiner et al. (1999). We have chosen to difference against their model 8, but a similar result is obtained for their other two-component dust model, model 7. In the Galactic plane, all of the three *WMAP* models show more emission in the outer plane and less in the inner plane than that predicted from the FDS models. A more quantitative representation of the planar differences is shown in Figure 25. Correlations between MEM, MCMCg and Model 9 have roughly unity slopes, whereas correlations against FDS model 8 indicate FDS is brighter by up to $\sim 20\%$ in high intensity regions in the inner Galaxy.

The right-hand image in Figure 24 shows the difference between a mean K-band free-free emission estimate from the same three models in this paper and that from scattering-corrected de-extincted $\text{H}\alpha$ using a conversion factor of $11.4 \mu\text{K R}^{-1}$. Scatter between models in the plane generally disallows a definitive free-free mapping there. However, differences between the free-free emission predicted from $\text{H}\alpha$ and the free-free model estimates in this paper consistently indicate that the $\text{H}\alpha$ prediction is higher by roughly 20-30% in the Gum and Orion regions. Free-free differences for the Gum away from the plane, where the optical

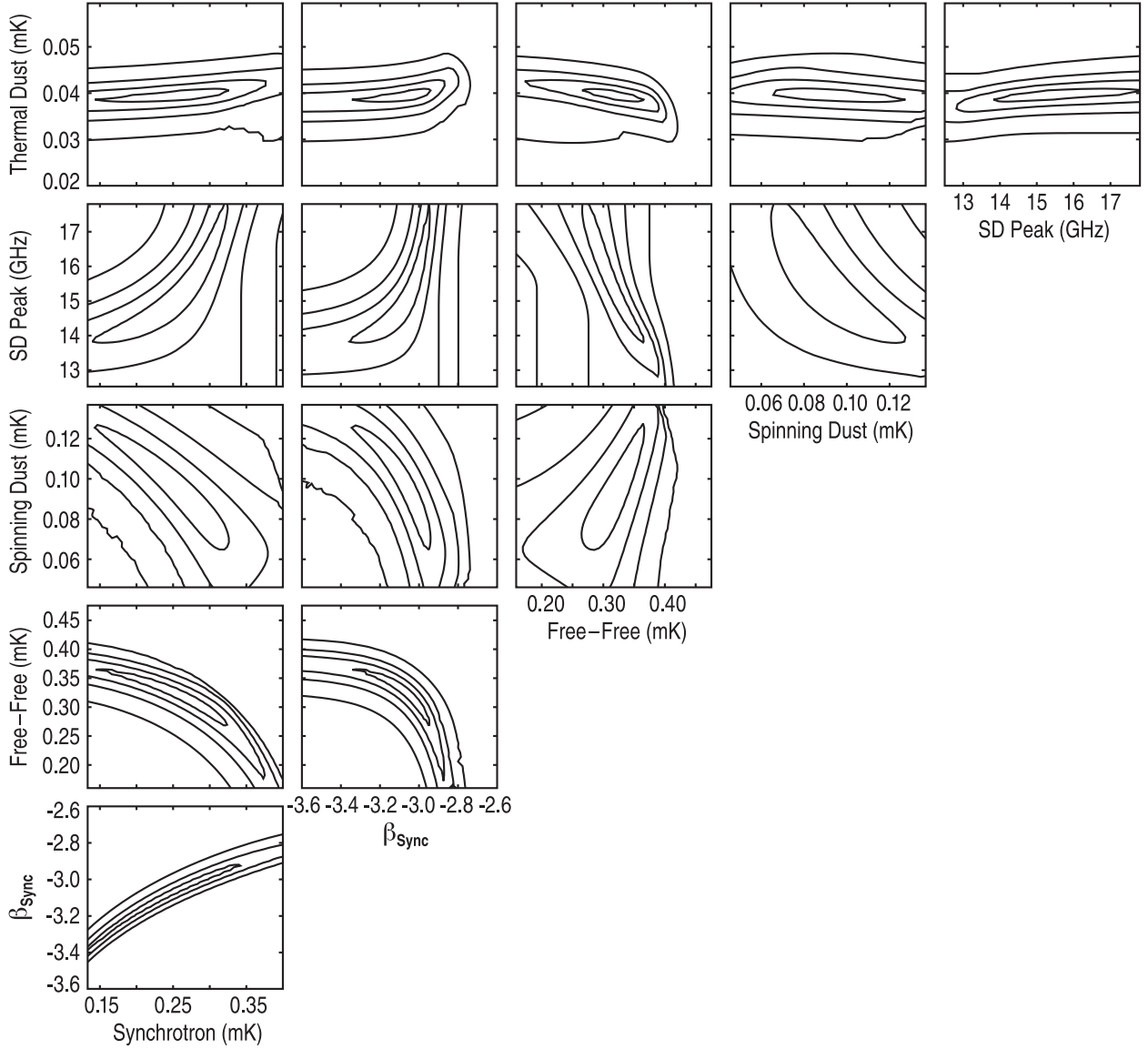


Fig. 23.— Results from foreground degeneracy analysis for six-band Model 9 fitting. The contour plots illustrate the degeneracy between model parameters for a representative single pixel foreground spectrum. Each panel shows the change in χ^2 as the selected pair of parameters are varied from their best-fit values while marginalizing over the other parameters. Contours are shown for $\Delta\chi^2$ values of 0.2, 1, 3, and 10, except values of 0.5, 3, and 10 are used for β_{sync} vs. synchrotron amplitude. There are significant degeneracies between parameter pairs that include either synchrotron amplitude or synchrotron spectral index, except for those that include thermal dust amplitude.

depth is < 1 , can be explained by a low electron temperature for this region (Dickinson et al. 2003; Woermann et al. 2000). Differences for other regions are most likely due to errors in the extinction correction, since the assumption of uniformly mixed dust and gas may not be valid. Although W-band Galactic emission is primarily either from thermal dust or free-free, linear combinations of the FDS dust model and $H\alpha$ predicted free-free have consistently been unable to describe the *WMAP* data in the plane; these apparent errors in both templates are consistent with those fitting errors.

5.3.7.2. ILC Errors Here we consider two types of error in the ILC: error due to CMB-foreground covariance, and error due to an incorrect estimate of the bias. See for example Hinshaw et al. (2007). These are errors which leave residual foreground signatures in the ILC estimate of the CMB.⁷

The bias correction is directly related to the foreground model. To determine the ILC bias, we take maps of our foreground-only estimate (without CMB) in each of the five *WMAP* bands and construct an ILC directly. The specific attribution of the foregrounds to individual components (synchrotron, free-free, etc.) is not needed in this step; we only require maps of the total foreground in each band. If the foregrounds are sufficiently complex (if they are not a linear combination of 4 or fewer spectra in each region), then there will be residuals in this foreground-only ILC, and this is the ILC bias. The ILC bias consists of foregrounds that cannot be removed by any set of ILC weights. With enough diversity in foreground spectral components, we can find a linear combination of foreground spectra that mimics the CMB, and we cannot remove the CMB signature from the ILC by construction, because the ILC weights must sum to 1. To deal with the ILC bias, we construct a foreground model, compute the ILC bias, and subtract it directly from the ILC. Inaccuracies in the foreground model will translate to an incorrect subtraction of the ILC bias.

An estimate of the ILC bias was computed by Hinshaw et al. (2007) from simulations and three-year data. We revisit the bias computation using the Galactic emission estimates in the five *WMAP* bands from Model 9, MEM and MCMCg. If these models perfectly describe the total Galactic emission at *WMAP* frequencies, then a bias map can easily be constructed by applying the flight ILC weights (given in Table 12) to these foreground maps. Such an application is shown in Figure 26. For comparison, Figure 26 also shows the bias correction from the three-year analysis, which is non-zero within the Kp2 mask and zero

⁷The ILC also has the three types of errors in the band maps mentioned in Section 5.3.6.1: gain calibration error, instrument noise, and $\csc|b|$ foreground monopole errors. These can be propagated through to the ILC using the ILC regions and the weights given in Table 12.

everywhere outside the mask.

Close to the Galactic plane, the bias computed from the MCMCg model is larger than that for the other two models. Removal of this bias from the uncorrected *WMAP* data ILC shows a clear negative residual in the plane for $|l| < 120^\circ$, indicating over-correction. In addition, ILC regional weights computed for the MCMCg model are sufficiently different from flight data values to render the model “goodness” suspect near the plane within the Kp2 cut. This is in part due to poorly constrained apportionment between CMB and Galactic signals in the plane. In particular there is an inverse correlation between CMB and dust spectral index, resulting in higher fractional residuals in portions of the plane for the MCMCg fit to V-band. V-band typically has the highest ILC weight, so these residuals lead to a higher bias for this model. Within the Kp2 cut, both Model 9 and the MEM bias maps show similar behavior to the three-year bias map, although details vary. Both models also return foreground ILC regional weights similar to data values, with the MEM showing the closest correspondence. Bias levels within the Kp2 cut are estimated from these two models as near $20 \mu\text{K}$ or less. These levels are either of similar magnitude or smaller compared to those computed for the CMB-foreground covariance in the same location (see below).

Estimating the foreground bias at higher latitudes is more difficult than for the Galactic plane regions. Since classic ILC weights are primarily determined using sky pixels within the Kp2 cut (even for the high latitude region 0), correspondence between derived model and data weights is only a useful diagnostic for pixels within the Kp2 mask. In addition, both the MEM and Model 9 results are ILC dependent: MEM subtracts the ILC from the data as a prelude to foreground fitting, and the six-band χ^2 Model 9 fit relies on the ILC as a strong prior. Since the classic ILC algorithm applies no bias correction outside the Kp2 cut, it is possible for any existing high-latitude ILC foreground bias to either remove or add power to the high latitude sky which is being fit to a Galaxy model. Since Galactic signals are generally weaker here than in the plane, the fractional error is potentially higher. Here the MCMC method provides the most objective model for estimating high latitude bias, since the CMB contribution is determined independently as part of the fitting process. We have used an amalgam of the three model bias maps to construct a very crude estimate of ILC bias outside of the Kp2 cut, giving the most weight to the MCMCg result. All three bias maps show a common characteristic dust-like excess in the outer Galaxy near the edges of the Kp2 cut. Two of the three bias maps show a low-level inner Galaxy deficit with a synchrotron-like signature. Noise in the bias maps makes a clear determination of the morphology difficult; we have used templates to represent the spatial structure, but the fine structural detail of the templates should not be taken as truth. Our rough estimate of the high latitude ILC bias is shown at the bottom right of Figure 26. High-latitude ILC bias is estimated at $10 \mu\text{K}$ or less.

The CMB-foreground covariance was discussed in Hinshaw et al. (2007). Because the ILC weights are constructed by minimizing the variance in a region, the weights adjust to allow foreground fluctuations to cancel CMB fluctuations as much as possible. This is more of a problem for small regions. Because the total foreground level is well measured in the plane (even if we allow complete uncertainty in the CMB for an error term of $\sigma \approx 70 \mu\text{K}$, the foregrounds are bright enough to make this term small), we can estimate how much the foregrounds could correlate with a random CMB sky with a given power spectrum. This estimate will not change substantially with different foreground models (different estimates of how much of the *WMAP* data is CMB and how much is foreground) because it only requires knowledge of the total foreground level, which is well constrained by the data. We can experimentally determine the CMB-foreground covariance by generating many CMB simulations, adding a foreground model to each CMB simulation, making a bias-subtracted ILC, and forming an error map by subtracting the true CMB from the ILC in each simulation. This gives us an ensemble of error maps, which span a 48 dimensional space. Since the CMB simulation is perfectly subtracted by any set of weights that add to 1, our error maps contain no CMB from the simulation. They only contain errors from residual foregrounds. Since there are 60 weights (going into the 12 regions of the ILC) and 12 constraints where sets of weights must add to 1, there are 48 degrees of freedom in the ILC error. As with the ILC bias, the results do depend on foreground model, but not nearly as strongly, as mentioned above.

We construct the 48 maps showing the ILC foreground-CMB covariance modes at res 6 as follows. We take the foreground Model 9 from Section 5.3.6 and prograde it directly to r9 (with no extra smoothing), where the ILC regions are defined. Then we form ILCs by the usual method, except that we do not smooth between regions as described in Equation (18) of Hinshaw et al. (2007) because we next degrade back to r6, which has a similar effect. We do this for 1000 CMB realizations, and form a 49152×1000 matrix of the maps, of which we take a singular value decomposition to determine the most common modes, taking care to normalize properly. There are only 48 singular values that are not effectively zero; we use the 1000 simulations to better sample these 48 modes and better determine their eigenvalues.

These modes provide the eigenvalues with nonzero eigenvectors of the foreground-CMB covariance error matrix. We compute the square root of the diagonal elements of this matrix to provide a visual estimate (that ignores correlations) of this error. The nine-year ILC map and this error map are shown in Figure 27.

We demonstrate the use of this error description by propagating the foreground-CMB error to the quadrupole-octupole alignment, which we describe in Section 7.4.

5.3.7.3. ILC Considerations The primary difficulty with any method of extracting the CMB from the data is determining how much of the temperature in each pixel is foreground and how much is CMB. The data only constrain the sum of these two, and we must make other assumptions in order to separate them.

The ILC specifically assumes that the CMB has a blackbody spectrum while the foregrounds do not. In addition, the ILC assumes that while the foregrounds may change amplitude across a region, an individual foreground does not change its spectral shape (proportional to antenna temperature as a function of frequency), so that a set of ILC weights can null a given foreground everywhere in a region. Along with this, the ILC assumes that there are four or fewer foreground spectral shapes, since if there were more, we would not be able to remove them all with only the five bands of *WMAP* data. If there were five foreground spectra, some linear combination of them would be able to mimic a blackbody spectrum, which the ILC has been designed to keep.

Figure 28 is one way to visualize the foreground complexity of the *WMAP* data. It shows in color the regions that are approximate power laws, and it shows in grayscale regions that are not well fit by a single power law. The ILC methodology can handle more than a single power law foreground (it can remove up to four of them), so this is not directly a map of where the ILC will work well. However, this figure does show the varying nature of foreground spectra across the sky.

Choosing the ILC region size is a trade-off between foreground complexity and foreground-CMB covariance. By choosing small regions, we give the foregrounds less chance to vary their shape over a region (such as by changing a synchrotron spectral index). But small regions are more susceptible to foreground-CMB covariance, as discussed in Hinshaw et al. (2007), which suppresses the variance of the ILC to the extent that the foregrounds and CMB correlate.

We could, for example, take minimum variance to be our figure of merit for an ILC map and allow arbitrary gerrymandering of the regions on a pixel-by-pixel basis. This could be done with a simulated annealing algorithm adjusting some small number of regions (e.g., 4) within a galactic mask. However, this would result in an ILC with variance inside the mask well below the expected CMB variance, because the regions optimize the foreground-CMB covariance to artificially suppress the ILC fluctuations. More knowledge than just the ILC variance is needed for intelligent region selection.

The foreground-CMB covariance can be estimated moderately well, since it only depends on an approximate foreground model and knowledge of the CMB power spectrum. We estimate this error in Section 5.3.7.2 and propagate it to the quadrupole-octupole alignment

in Section 7.4. Other errors, such as those due to foregrounds changing spectral shape over a region or more than 4 foreground spectra in a region (these cause the ILC bias), are harder to estimate because they require an accurate separation of CMB from foregrounds in the first place. The demands on this foreground model accuracy depend on the amplitude of the foregrounds. For a pixel dominated by CMB, a slight foreground correction need not be extraordinarily accurate in a fractional sense. Yet for an extremely bright foreground location on the plane (say, a bright H II region), the foreground model must have supreme fractional accuracy to distinguish meaningfully a tiny CMB contribution from the dominating foregrounds.

A more accurate ILC would require either a better bias subtraction or better region selection designed to minimize the needed bias correction; both of these require a highly accurate foreground model. A foreground model that separates out different components (such as synchrotron, free-free, etc.) is not needed, only a model that gives the total foreground in each band. The ILC bias can be directly calculated by making an ILC of this foreground-only data set, and regions could be selected to minimize the bias correction needed in each region. However, if we already have an accurate separation of the CMB from foregrounds, then the ILC method is no longer necessary, since we already have a map of the CMB.

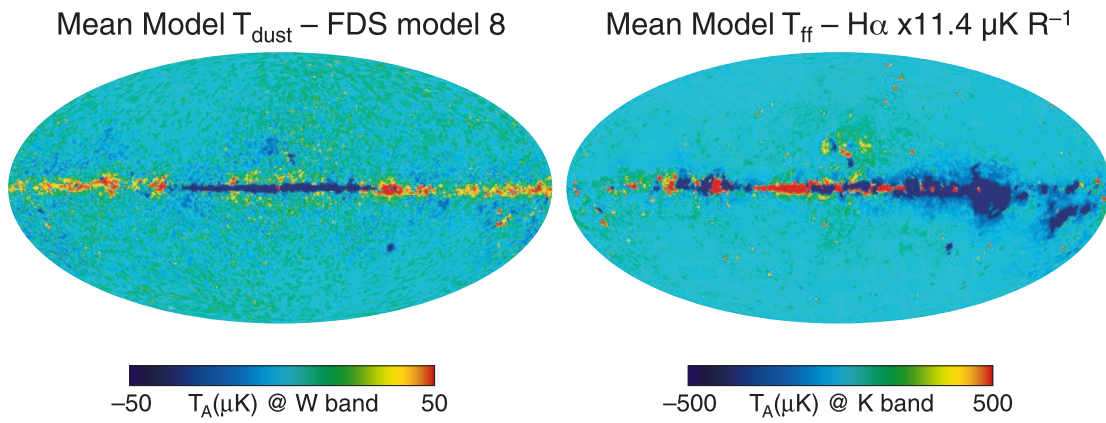


Fig. 24.— (*Left*): Thermal dust amplitude at W-band averaged over the MCMCg, MEM and Model 9 fits minus the thermal dust model 8 from Finkbeiner et al. (1999). (*Right*): Free-free amplitude at K-band averaged over the same three models, minus the free-free template estimated from $\text{H}\alpha$ observations.

(A color version of this figure is available in the online journal.)

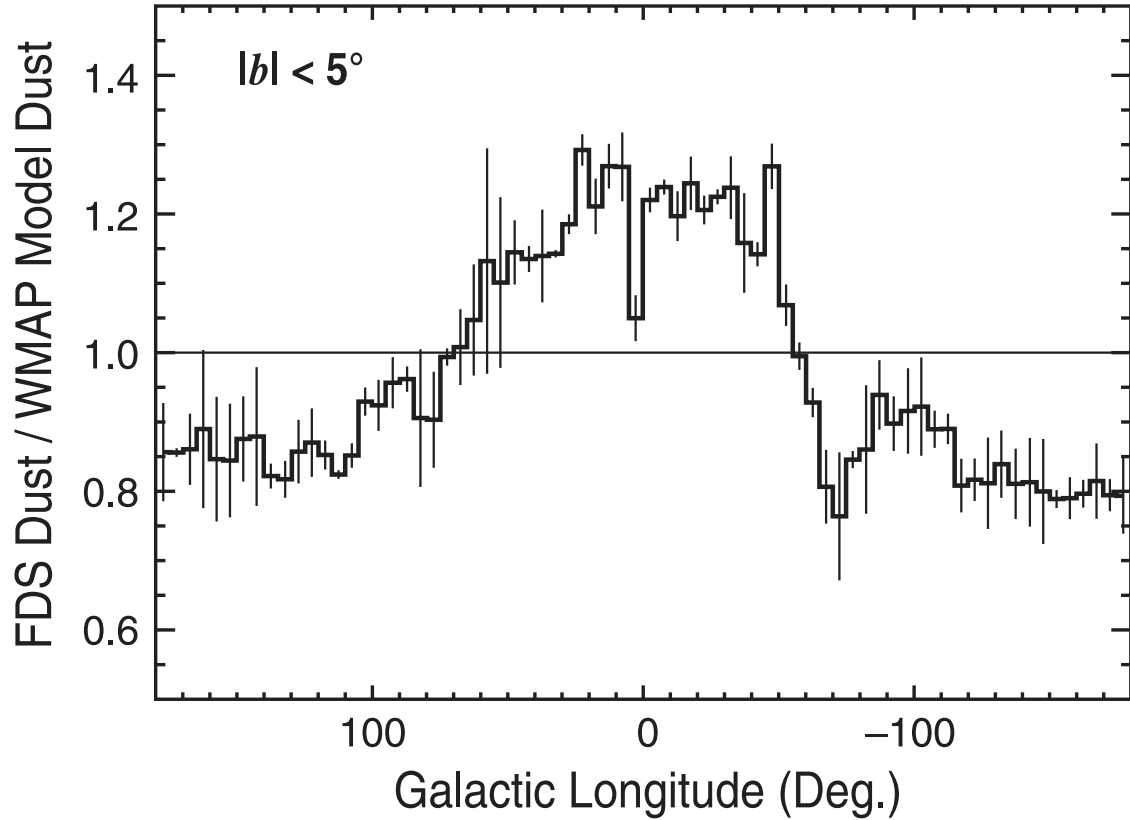


Fig. 25.— The ratio of W-band predicted thermal dust emission (Finkbeiner et al. (1999) model 8) to the mean over three models (MCMCg, MEM, Model 9) as a function of longitude for $|b| < 5^\circ$. Error bars are derived from the rms scatter of the three models about the mean. A line is plotted at 1.0 to guide the eye. Modeled emission shows systematic variations from the FDS prediction by up to 20%.

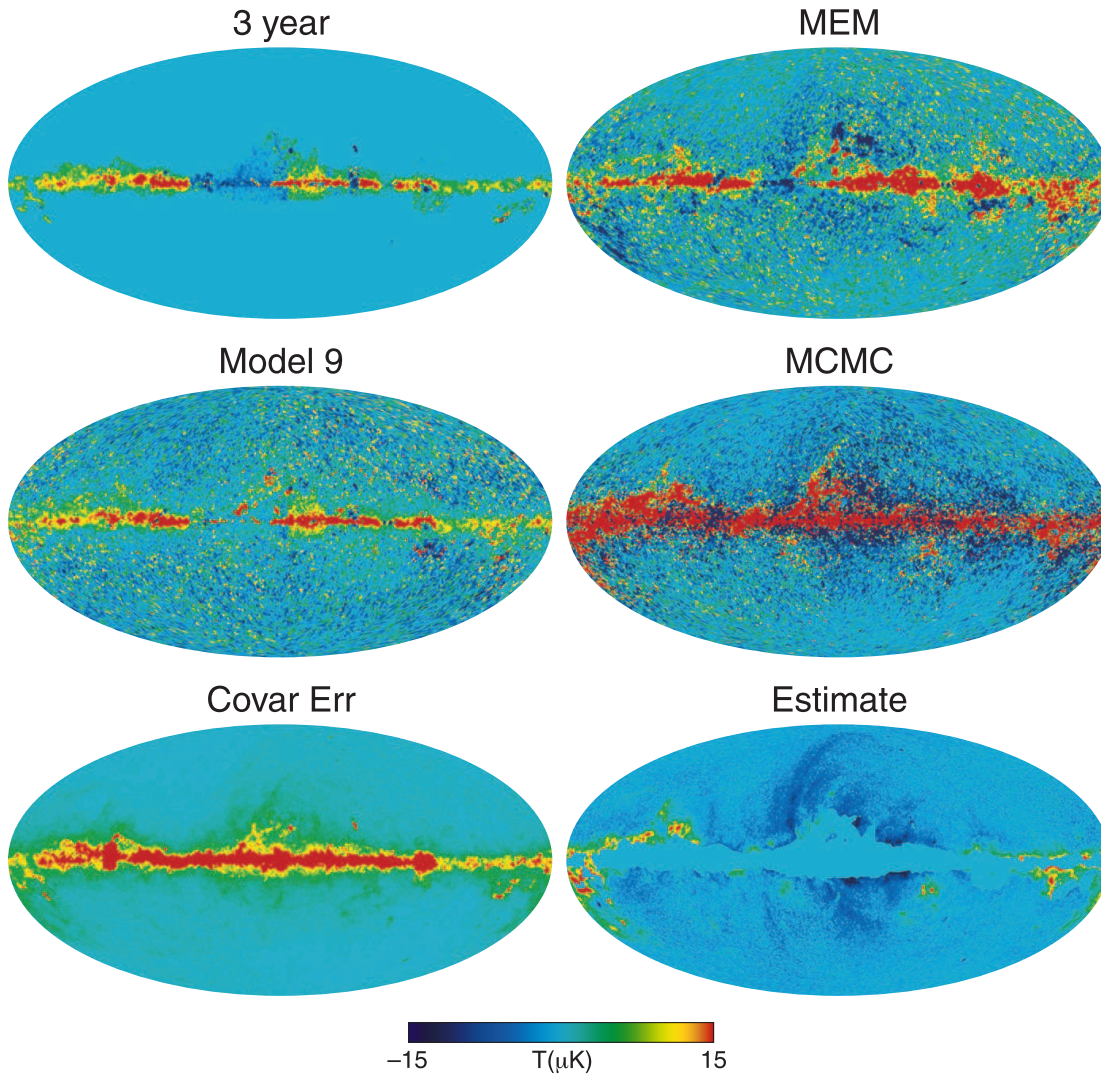


Fig. 26.— Estimates of foreground bias error remaining in the ILC map, on a scale of $\pm 15 \mu\text{K}$. *Top left*: Bias map from the three-year analysis of Hinshaw et al. (2007). The map is zeroed outside the Kp2 cut. *Top right and middle*: Bias estimates resulting from the application of the nine-year ILC coefficients to the Galaxy models from MEM, Model 9 and MCMCg analysis. The bias map from the MCMCg analysis is overestimated in the plane (see text). *Bottom left*: ILC error from foreground-CMB covariance. Within the Kp2 cut, this error and the foreground bias are of comparable magnitude. *Bottom right*: An estimate of the potential magnitude of ILC foreground bias outside the Kp2 cut, based on the various model results, with heavy weight given to the MCMCg model. Bias errors of $10 \mu\text{K}$ or less are indicated.

(A color version of this figure is available in the online journal.)

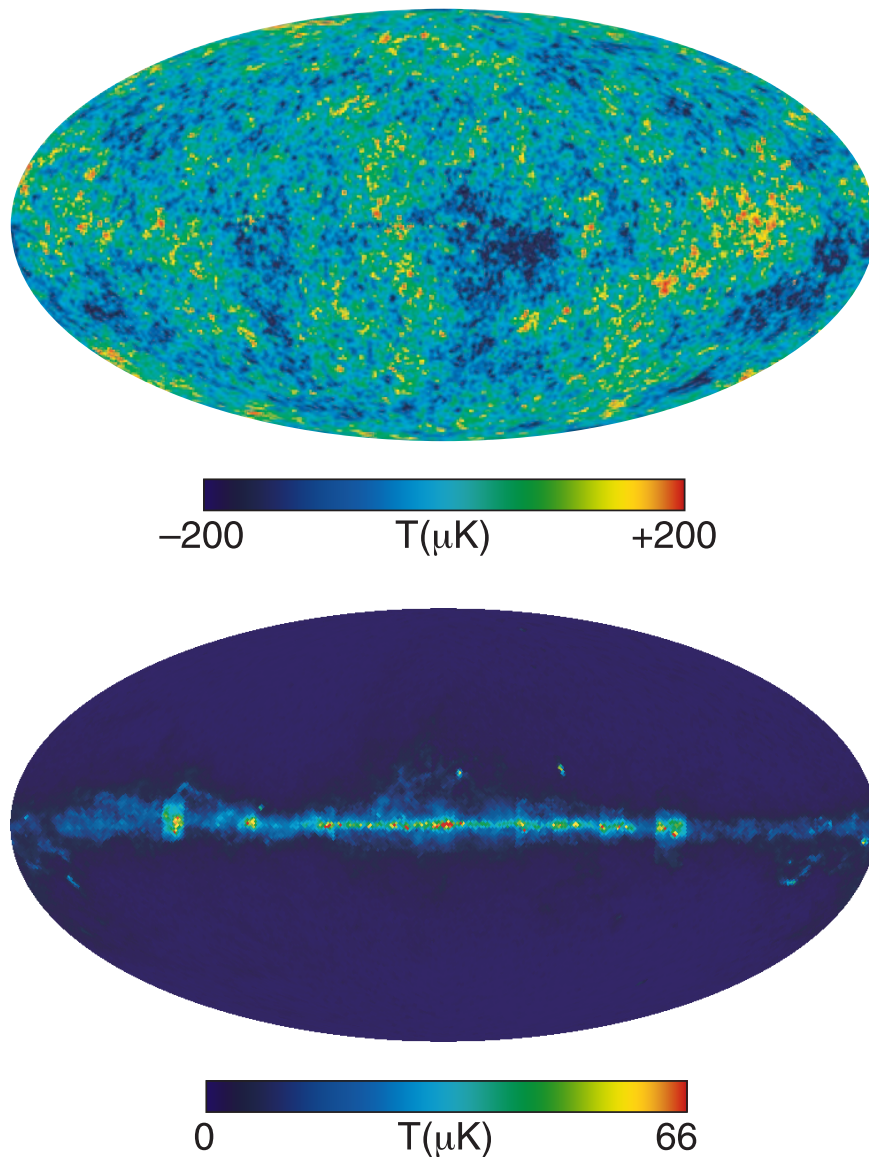


Fig. 27.— The top map is the nine-year ILC. The bottom sky map displays the part of the ILC error in each pixel due to foreground-CMB covariance, using the Model 9 foreground estimate from Section 5.3.6. This shows the square root of the diagonal of the covariance matrix, on a linear color scale. Therefore it shows the standard deviation of expected error fluctuations, marginalizing over correlations between pixels. The color scale range was chosen because the r6 ILC map has a CMB standard deviation of $66 \mu\text{K}$. Thus, full scale on this map has equal variance with the CMB, and at the halfway point on this color scale the foreground-CMB error variance is down to a quarter of the CMB variance.

(A color version of this figure is available in the online journal.)

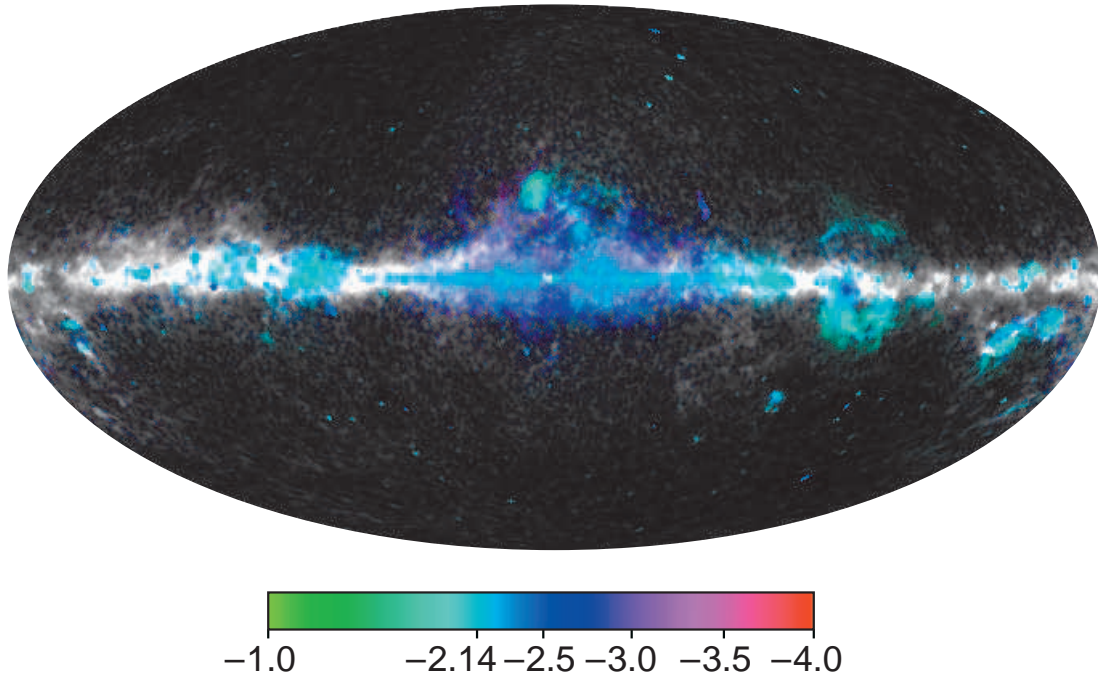


Fig. 28.— The dominant power law in a pixel, combined with information about whether the data in that pixel look like a pure power law, over the *WMAP* bands. This image was generated by individually specifying the hue, saturation, and value (HSV) for each pixel. The hue, shown in the color scale, describes which power law best fits the data. It is labeled with values of β , where the power law in antenna temperature is $T_A(\nu) \propto \nu^\beta$. The saturation describes how well the data fit a power law, so that desaturated (white, gray, black) pixels are not well fit by any power law. Specifically, let n_A be a 5-vector of the *WMAP* thermodynamic temperatures, rescaled to be a unit vector, and let n_p be a 5-vector of the best fit power law in antenna temperature, converted to thermodynamic and then also rescaled to be a unit vector. Then the saturation is $n_A \cdot n_p$, which is just the cosine of the angle between these two vectors. The scale is from 0.995 (unsaturated) to 1.0 (completely saturated), so if the two 5-vectors are more than 5.73 degrees apart, the pixel is unsaturated. The value in the HSV color space is the magnitude of the data 5-vector, so it is the square root of the sum of the squares of the *WMAP* thermodynamic temperatures, on a scale of 0 to 2 mK. Therefore blacker pixels have less emission in all bands; lighter pixels have more emission. The nine-year ILC was subtracted from the *WMAP* data, before computing the above image.

(A color version of this figure is available in the online journal.)

6. Nine-Year Angular Power Spectra

In this section we present the nine-year *WMAP* intensity and polarization angular power spectra. We describe changes in methodology from earlier analyses, and discuss the new results.

The nine-year temperature-temperature (TT) power spectrum computation uses the full set of V-band and W-band cross-power-spectra. For $2 \leq l \leq 32$ the TT power spectrum relies on the Gibbs sampled pixel likelihood, as was the case with the five-year and seven-year data releases. New for this nine-year analysis, the $32 < l \leq 1200$ TT power spectrum is calculated using unbiased and optimal C^{-1} estimation. Earlier releases provided power spectra computed using the Monte Carlo Apodised Spherical Transform Estimator (MASTER) method, an unbiased but non-optimal quadratic estimator (Hivon et al. 2002). As was the case for the seven-year *WMAP* analysis, the polarization power spectra continue to be computed using MASTER.

For the $2 \leq l \leq 32$ Gibbs sampling, we use a slightly different ILC map than we have in the past. We use a bias-corrected one-region ILC map. The same weights are used for the whole sky; these weights are chosen to minimize the variance of the ILC outside of the combination of the first-year Kp8 mask and the seven-year point source mask. The data used for this low-resolution analysis are the deconvolved one-degree-smoothed nine-year maps for K- through W-bands. The coaddition over nine years was done using a slightly older version of N_{obs} that was available at the time we did the calculation; this has a small effect on the final nine-year temperature maps.

The bias correction for this ILC requires a foreground model. We determine the foreground model by fitting four one-degree smoothed templates and a monopole term to the one-degree smoothed W-band data. We do the fit outside the combination of a Kp22 mask and seven-year source mask, to avoid requiring that the templates be highly accurate in the brightest portion of the galactic plane. The four templates are as follows. We use the FDS model 8, evaluated at 94 GHz, as described in Section 5.3.2.1; a de-extincted $\text{H}\alpha$ map with scattering correction applied, described in detail in Section 5.3.1; a dust model emission “delta correction” map, computed as FDS model 8 multiplied by $(T_{\text{dust}} - \langle T_{\text{dust}} \rangle) / \langle T_{\text{dust}} \rangle$, where T_{dust} is the dust temperature map from SFD and the average dust value $\langle T_{\text{dust}} \rangle$ was calculated outside the Kp2 mask; and a map of discrete HII region emission (primarily along the plane), evaluated at 2.7 GHz and 1 degree beam width using data from the Paladini et al. (2003) catalog of 1442 Galactic HII regions. This last map was scaled to 93 GHz assuming an optically thin free-free spectrum for each source. After removal of these foregrounds from the W-band map, we consider the remainder to be a pure CMB map. To obtain our foreground model of the galaxy, we subtract this CMB estimate from each band of the flight data. Our

foreground model therefore has information about how much temperature comes from the CMB and how much from foregrounds, but it does not break the foreground temperature into physical components, since this is not necessary to estimate ILC bias.

The ILC bias can then be calculated as the error in an ILC map, averaged over many CMB realizations but using the same foreground model. It can be directly computed by making an ILC of the foreground-only data, without adding in a CMB simulation. We subtract this ILC bias from the one-region ILC described above.

We do use CMB simulations to determine the foreground-CMB covariance error modes. Using a power spectrum from a set of seven-year simulations, we generate 100 CMB realizations, add our foreground model, and generate a one-region ILC as above. There are four error modes, since we generate the ILC from five weights with the single constraint that they must sum to 1. We determine these modes from the covariance matrix of errors. We find that one mode is negligible outside of the KQ85y9 mask that is used for Gibbs sampling, so we only marginalize over the three most important CMB-foreground covariance modes in the Gibbs sampler.

We smooth the ILC map to 5° FWHM (Full Width at Half Maximum) before any masking; this is the map over which we Gibbs sample. Since the ILC is already smoothed to 1° FWHM, this requires an additional smoothing by $\sqrt{24} \approx 4.9$. We then degrade the map to r5, and add $2 \mu\text{K}$ rms noise per pixel to the r5 ILC, as was done in the five-year and seven-year data releases. The Gibbs sampler uses a mask based on degrading the KQ85y9 mask to r5, and leaving unmasked only those r5 pixels for which $> 50\%$ of the r9 pixels are unmasked. The KQ85y9 mask allows through 2353196 out of 3145728 pixels, or 74.8% of the sky. After degrading to r5 by the above method, the mask lets through 9496 out of 12288 pixels, or 77.3% of the sky. According to our newly estimated ILC errors, the pixels near the edge of this mask may fluctuate randomly up to about $\sim 11 \mu\text{K}$, so residual foregrounds are a small fraction of the CMB variance when the masked ILC is used.

6.1. High l TT summary

The optimal (i.e. minimum variance) power spectrum estimator has been known for many years (Tegmark 1997; Bond et al. 1998) but has appeared to be computationally intractable for a large ($\gtrsim 10^6$ pixel) experiment such as *WMAP*. As a result, standard practice is to use estimators that do not achieve optimal statistical errors, in exchange for reduced computational cost. For the nine-year *WMAP* data, we replace the MASTER power spectrum estimator by the optimal unbiased quadratic estimator. This optimal estimator has

now been implemented in a computationally affordable way. We report the first *WMAP* power spectrum with optimal error bars on the TT spectrum across the entire observed range of scales $2 \lesssim l \lesssim 1200$.

The basic building block is a fast algorithm (Smith et al. 2007) for multiplying a temperature map (thought of as a length- N_{pix} vector x) by the N_{pix} -by- N_{pix} inverse covariance matrix C^{-1} . Here, the covariance matrix $C = S + N$ consists of signal and instrumental noise contributions, and incorporates the Galactic mask, the instrument beam size, and marginalization over the monopole and dipole. The multigrid algorithm from Smith et al. (2007) allows a single multiplication operation of the form $x \rightarrow C^{-1}x$ to be performed for *WMAP* in ≈ 10 core-minutes, although it is impossible to compute (or even store) the matrix C^{-1} in dense form. This means that all computations involving C^{-1} must be formulated so that they are based on a (reasonably small) number of multiplications of the form $x \rightarrow C^{-1}x$.

In practice, we need to modify the optimal estimator \widehat{C}_l by removing auto-correlations, which are highly sensitive to the instrumental noise model. For an all-sky experiment such as *WMAP* the noise must be known to $\lesssim 0.1\%$ to avoid a statistically significant additive bias to \widehat{C}_l . This level is impractical to achieve, but sensitivity to the noise model can be mitigated by constructing a modified estimator, \widehat{C}_l^\times , that only includes terms calculated from cross-spectra.

The unnormalized estimator written out for a single map d is

$$\widehat{\mathcal{E}}_l[d] = \frac{1}{2}d^T C^{-1} A \Pi_l A^T C^{-1} d \quad (40)$$

where A is the a_{lm} -to-map operator that includes beam convolution, and Π_l projects out all modes not at a given multipole l . The optimal power spectrum estimator \widehat{C}_l is constructed from

$$\widehat{C}_l[d] = F_{ll'}^{-1} \left(\widehat{\mathcal{E}}_l[d] - \mathcal{N}_l \right), \quad (41)$$

where \mathcal{N}_l is the noise bias and the Fisher matrix $F_{ll'}$ is given by

$$F_{ll'} = \frac{1}{2} \text{Tr} \left(A^T C^{-1} A \Pi_l A^T C^{-1} A \Pi_{l'} \right). \quad (42)$$

We also construct a cross-correlation-only power spectrum estimator \widehat{C}_l^\times with zero noise bias, by only keeping cross-correlations between maps with independent noise. More specifically, we divide the data into maps d_α , where $\alpha = (c, y)$ indexes a combination of a differencing assembly $c = \text{V1, V2, W1, W2, W3, W4}$ and a specific single year of *WMAP* data, y . The unnormalized estimator $\widehat{\mathcal{E}}_l$ defined in (40) can then be written as a double sum over pairs (α, β) ; we simply keep the terms with $\alpha \neq \beta$ to define an unnormalized cross-correlation estimator $\widehat{\mathcal{E}}_l^\times$. (In implementation, it is more computationally efficient to subtract the terms

with $\alpha = \beta$.) We then define the cross-correlation estimator \widehat{C}_l^\times by $\widehat{C}_l^\times = (F_{ll'}^\times)^{-1} \widehat{\mathcal{E}}_{l'}^\times$, where $F_{ll'}^\times$ is an appropriately modified Fisher matrix.

The *WMAP* C^{-1} TT pipeline provides a power spectrum estimate and an estimate for the covariance matrix $\text{Cov}(C_l, C_{l'})$. To account for the slight non-Gaussianity of the likelihood at $l > 32$, our likelihood remains the combination of a Gaussian and offset log-normal distribution in $\mathcal{C}_l^{\text{th}}$, as discussed in Verde et al. (2003). Discussion of the log-normal distribution for cosmological likelihoods is also in Bond et al. (2000) and Sievers et al. (2003). We use a noise estimate to provide the offset in our offset log-normal distribution, \mathcal{N}_l . This is the error in the power spectrum due to instrument noise, in the form of $l(l+1)C_l/(2\pi)$. Additional variables to describe the likelihood include

$$\widehat{\mathcal{C}}_l \equiv \frac{l(l+1)\widehat{C}_l}{2\pi} \quad \mathcal{C}_l^{\text{th}} \equiv \frac{l(l+1)C_l^{\text{th}}}{2\pi} \quad (43)$$

$$\widehat{z}_l \equiv \ln(\widehat{\mathcal{C}}_l + \mathcal{N}_l) \quad z_l^{\text{th}} \equiv \ln(\mathcal{C}_l^{\text{th}} + \mathcal{N}_l) \quad (44)$$

$$\mathcal{Q}_{ll'} \equiv (\mathcal{C}_l^{\text{th}} + \mathcal{N}_l) \mathcal{Q}_{ll'} (\mathcal{C}_{l'}^{\text{th}} + \mathcal{N}_{l'}), \quad (45)$$

where $\mathcal{Q}_{ll'}$ is the inverse covariance matrix of the power spectrum estimate $\widehat{\mathcal{C}}_l$ provided by the optimal estimator. Finally, we write the *WMAP* likelihood as a combination of a Gaussian and offset log-normal distribution.

$$\ln \mathcal{L}_{\text{Gauss}} = -\frac{1}{2} \sum_{ll'} (\mathcal{C}_l^{\text{th}} - \widehat{\mathcal{C}}_l) \mathcal{Q}_{ll'} (\mathcal{C}_{l'}^{\text{th}} - \widehat{\mathcal{C}}_{l'}) + \text{const.} \quad (46)$$

$$\ln \mathcal{L}_{\text{LN}} = -\frac{1}{2} \sum_{ll'} (z_l^{\text{th}} - \widehat{z}_l) \mathcal{Q}_{ll'} (z_{l'}^{\text{th}} - \widehat{z}_{l'}) \quad (47)$$

$$\ln \mathcal{L}_{\text{WMAP}} = \frac{1}{3} \ln \mathcal{L}_{\text{Gauss}} + \frac{2}{3} \ln \mathcal{L}_{\text{LN}} \quad (48)$$

6.2. The C^{-1} Pipeline

We first applied the new C^{-1} pipeline to the seven-year *WMAP* data after its publication. We performed end-to-end tests to arrive at the first *WMAP* power spectrum that is optimal for all values of l . We then compared the new power spectrum with the pseudo- C_l MASTER spectrum from the *WMAP* seven-year release. We did not propagate the optimal power spectrum to cosmological parameter constraints for the seven-year data. Based on the seven-year power spectrum comparisons, we decided to implement the C^{-1} power spectrum for what are now the nine-year *WMAP* results.

The *WMAP* seven-year data C^{-1} evaluation used foreground-cleaned maps from the six V- and W-band differencing assemblies, further subdivided by individual year data $y =$

1, 2, . . . 7, for a total of 42 cross-correlations. We masked regions of high Galactic foreground emission and bright point sources by using the KQ85 mask (Gold et al. 2011). We report a power spectrum to $l_{\max} = 1200$, but we ran the pipeline to $l_{\max} = 1500$ to avoid edge artifacts near the maximum multipole of the reported power spectrum.

Unless otherwise specified, all results are based on the power spectrum estimator \widehat{C}_l^\times , which only contains cross-correlations. After estimating the power spectrum, we subtract an estimate of the bias due to unresolved point sources, assuming a single population of radio sources with frequency dependence $g_{\text{ant}}(\nu) \propto \nu^{-2.09}$ in antenna temperature, or equivalently

$$g(\nu) \propto \left(\frac{h\nu}{kT_{\text{CMB}}} \right)^{-2} \frac{(\exp(h\nu/kT_{\text{CMB}}) - 1)^2}{\exp(h\nu/kT_{\text{CMB}})} \nu^{-2.09} \quad (49)$$

in thermodynamic temperature units, where h is Planck’s constant, k is the Boltzmann constant, and T_{CMB} is the CMB monopole temperature.

6.2.1. C^{-1} Pipeline Tests

In our power spectrum pipeline, we precompute three quantities: a transfer matrix $F_{ll'}$ that represents the mean response of the unnormalized estimator at multipole l to CMB power at multipole l' ; the bias of the power spectrum estimator due to unresolved point sources; and the noise bias, for the auto-correlation estimator \widehat{C}_l (but not for the cross-correlation estimator \widehat{C}_l^\times). In Figure 29, we present end-to-end Monte Carlo tests of these precomputations using three simulated ensembles: CMB-only simulations, point source simulations, and noise-only simulations. In all cases the ratio of the recovered power spectrum (averaged over many Monte Carlo realizations) to the expected power spectrum is consistent with unity.

Our pipeline uses interpolation in l to estimate transfer matrices, noise bias, and point source bias. We did an end-to-end test of the interpolation accuracy as follows. We reran the pipeline with half the interpolation step size, treated the difference between the two estimates as a power spectrum bias, and then we did a Fisher matrix forecast to determine whether the resulting bias was statistically significant. In all three cases, we found that the resulting bias is $\lesssim 0.02\sigma$, i.e. much too small to be important.

We estimate the power spectrum covariance matrix $\text{Cov}(\widehat{C}_l^\times, \widehat{C}_{l'}^\times)$ using Monte Carlo simulations. A direct Monte Carlo estimation of a 1200-by-1200 covariance matrix would require a prohibitive number of simulations, but this can be sped up using computational tricks: (1) the covariance $\text{Cov}(\widehat{C}_l, \widehat{C}_{l'})$ of the auto-estimator is equal to the inverse Fisher matrix $F_{ll'}^{-1}$, so we only need Monte Carlos for the estimator difference $(\widehat{C}_l^\times - \widehat{C}_l)$; (2) we

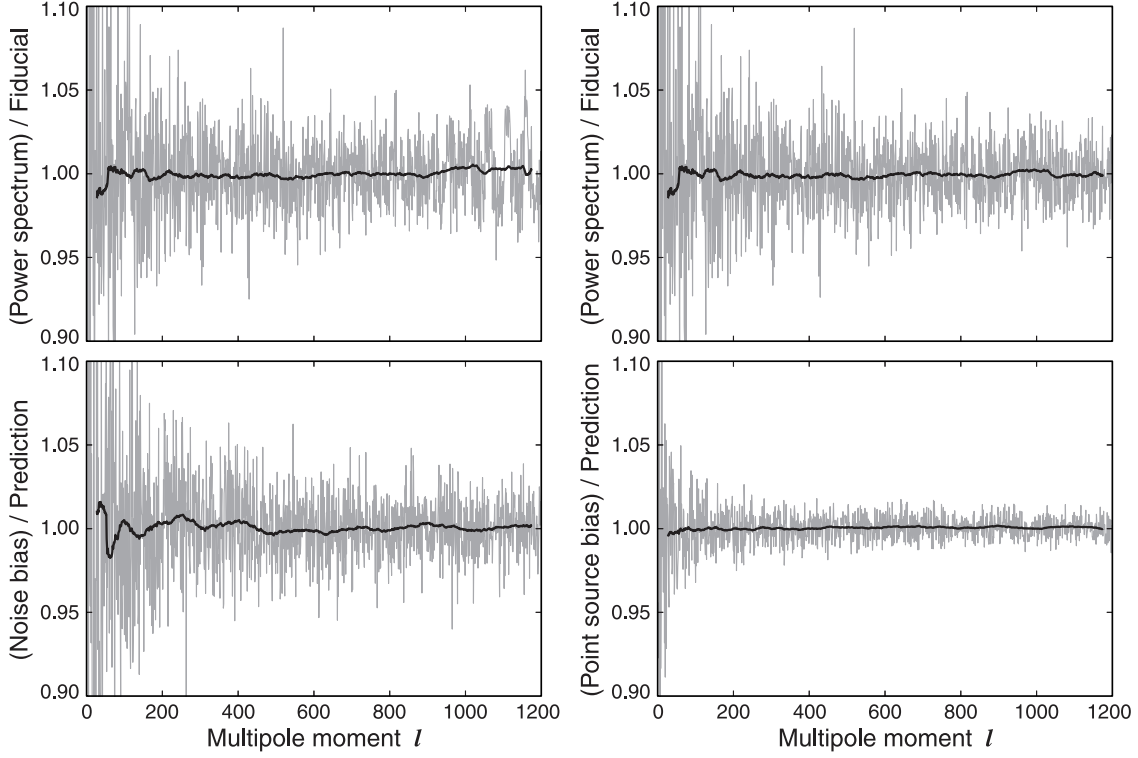


Fig. 29.— End-to-end Monte Carlo pipeline tests. The gray lines are individual l 's and the black lines are boxcar smoothed with $\Delta l = 50$. In all four cases, the ratio of the Monte Carlo estimated power spectrum and the predicted value is consistent with unity. *Top left.* Ratio $\langle \widehat{C}_l^\times \rangle_{\text{sig}} / C_l^{\text{fid}}$ between mean estimated power spectrum of CMB-only simulations and the fiducial input spectrum. *Top right.* Same as top left panel, but using the auto-correlation estimator \widehat{C}_l instead of the no-auto estimator \widehat{C}_l^\times . *Bottom left.* Ratio between mean estimated power spectrum of noise-only simulations and the predicted noise bias, using the auto-estimator \widehat{C}_l . *Bottom right.* Ratio between mean estimated power spectrum of point source simulations and predicted bias.

only estimate variances and assume that off-diagonal covariances are given by appropriately rescaling Fisher matrix elements; and (3) we smooth the variance estimates in l . These tricks allow the covariance matrix to be accurately estimated from a small number of simulations. As an end-to-end convergence test, we compared covariance matrices C_{256} , C_{512} constructed using 256 and 512 Monte Carlo simulations respectively. We found that all matrix entries were nearly identical in that all Karhunen-Loève eigenvalues of the matrix pair (C_{256}, C_{512}) are between 0.999 and 1.001.

6.2.2. C^{-1} Versus MASTER Comparison

In Figure 6.2.2, we show the binned power spectrum estimates for the seven-year *WMAP* data obtained using the optimal pipeline, described above, with the sub-optimal MASTER results used in the seven-year *WMAP* release (Larson et al. 2011) shown for comparison. The agreement is excellent; the two estimators agree to better than 1σ in every l -bin, as expected when comparing an optimal and near-optimal analysis of the same data.

To compare the two estimators more closely, in the left panel of Figure 31 we show the difference between the optimal and sub-optimal estimators, before and after smoothing in l . No systematic trends are seen, as expected if the difference is pure statistical scatter. There is a small region near $l = 50$ where the optimal estimator fluctuates to a lower value of C_l than the sub-optimal estimator. This fluctuation slightly shifts the best-fit value of the spectral index n_s , as discussed by Hinshaw et al. (2012). This appears to be the most important difference between the two estimators for purposes of cosmological parameter estimation, aside from the effective sensitivity improvement discussed below.

The right panel of Figure 31 shows the ratio between the power spectrum variance $\text{Var}(C_l)$ obtained using the optimal and sub-optimal estimators. The optimal estimator improves the variance by 7–17% depending on the value of l . This level of improvement is roughly comparable to the improvement in going from seven-year to nine-year data (which varies from no improvement at low l to a factor of $9/7 = 1.28$ in C_l at high l).

6.3. WMAP Power Spectra

The nine-year TT angular power spectrum is shown in Figure 32. The cosmic variance curve on the power spectrum has been adjusted to more accurately reflect cosmic variance. In the past, the value of f_{sky} that we used to expand the error bars was generated by the MASTER code, and it was roughly the geometric area of the observed sky, which was not

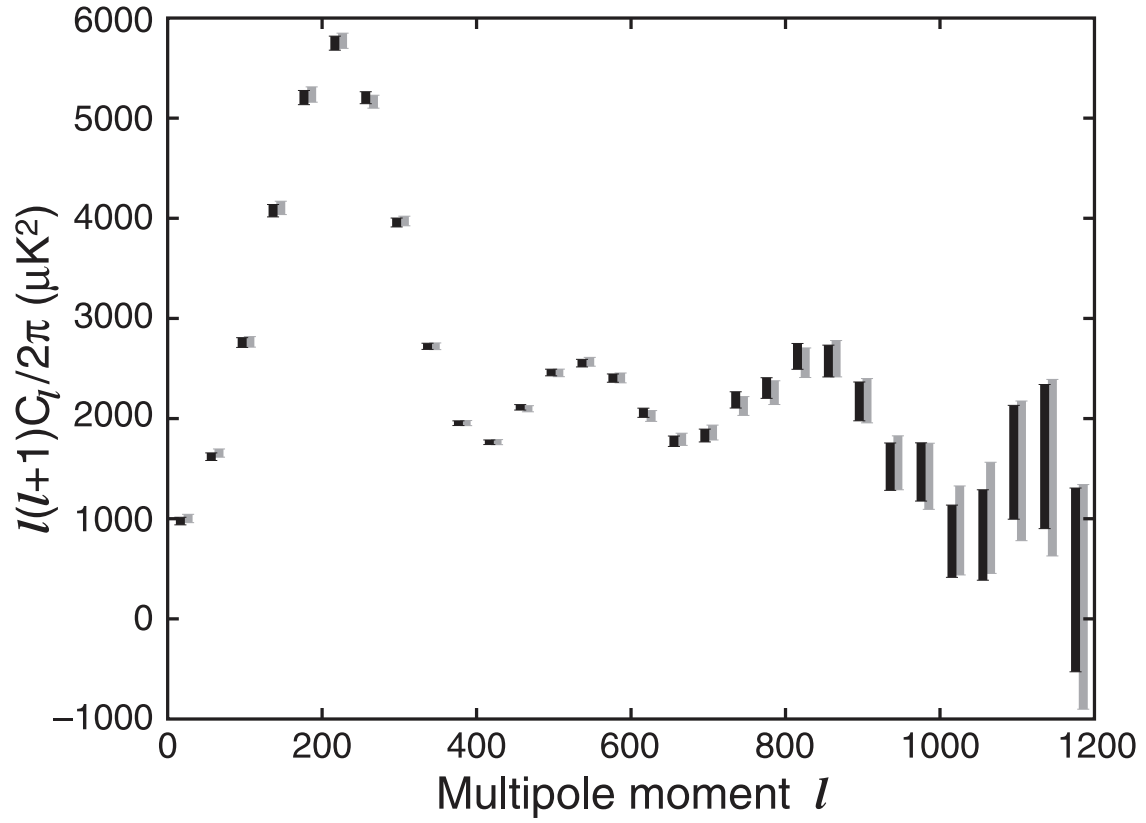


Fig. 30.— Binned *WMAP7* power spectrum estimates using the optimal pipeline from this paper (left/black error bars), with the estimates from the *WMAP7* release (Larson et al. 2011) shown for comparison (right/grey error bars).

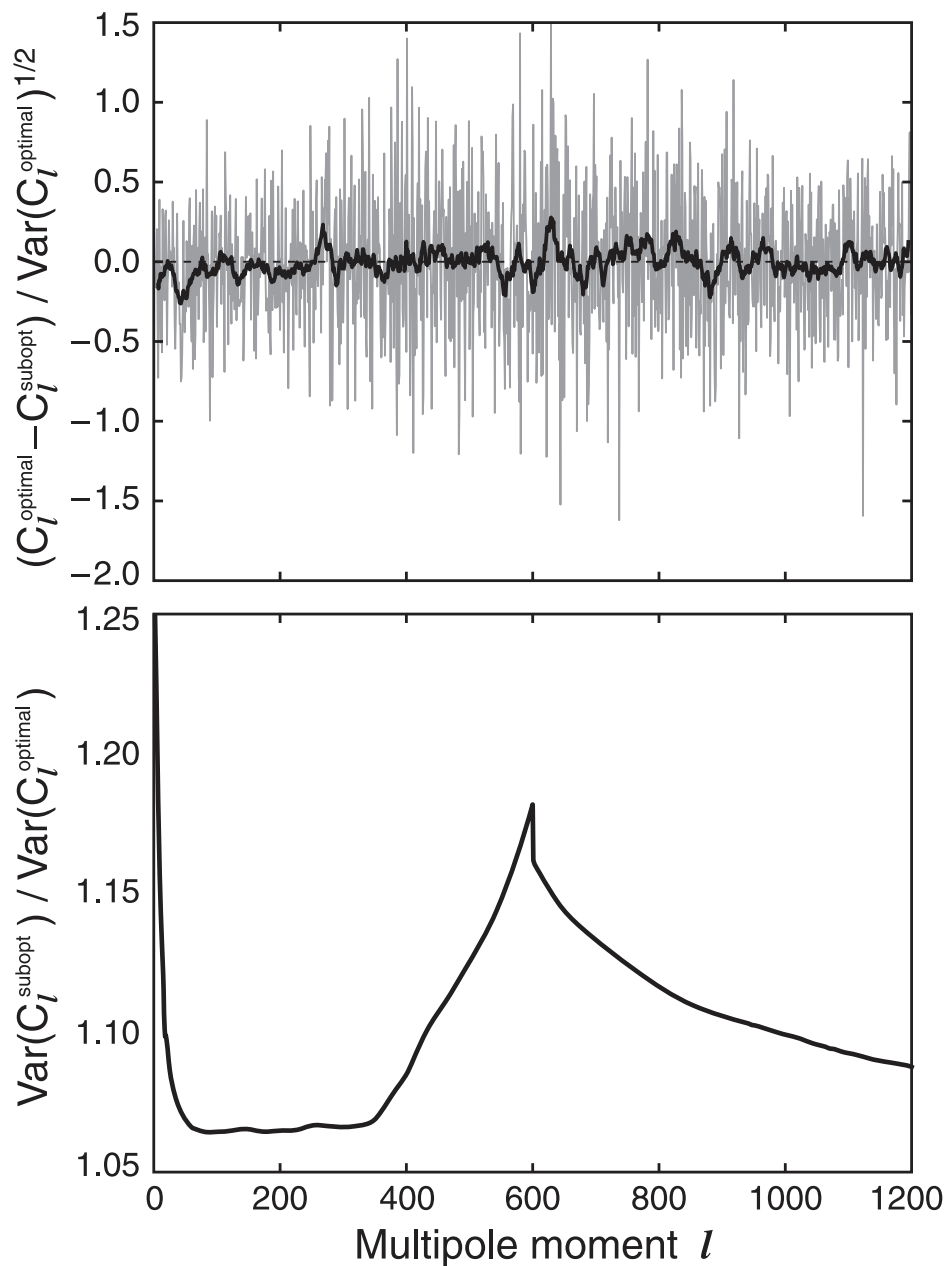


Fig. 31.— Detailed comparison between *WMAP7* optimal power spectrum estimator and suboptimal estimator from Larson et al. (2011). *Top*: Difference $(\hat{C}_l^{\text{optimal}} - \hat{C}_l^{\text{subopt}}) / \text{Var}(\hat{C}_l^{\text{optimal}})^{1/2}$ between the two estimators in “sigmas”, for every l , and boxcar-smoothed with $\Delta l = 10$. *Bottom*: Variance ratio between suboptimal and optimal estimators.

optimal. With the C^{-1} method of estimating the power spectrum, such as was used in the Gibbs sampler, one can reconstruct the low l multipoles on the full sky more accurately than one might naively expect. Doing so makes $f_{\text{sky},l}$ close to unity at very low l . In Figure 32, we use the value of $f_{\text{sky},l}$ generated by the high- l C^{-1} code, which is applicable at all lower l .

The shaded region represents the 1σ error bar from cosmic variance, which is the region where 68% of binned power spectra that are randomly sampled from the theory curve would appear. We form the error bars around the 68% with highest probability density per unit C_l . These are determined by sampling 10^6 power spectra from the theory spectrum and binning them. At each multipole l , the value of the power spectrum is sampled from a χ^2_ν distribution (which has a mean of ν) with $\nu = (2l + 1)f_{\text{sky},l}^2$ degrees of freedom. The spectrum is then scaled by $l(l + 1)C_l/(2\pi\nu)$ to give it the correct mean. Sampling from the χ^2_ν distribution rapidly is done by choosing random numbers in the interval $[0, 1]$ and then using an interpolated cumulative density function to determine the value of χ^2_ν . After binning the power spectra, we determine the location of the error bars for each bin by finding the pair of samples that enclose 68% of the other samples in the bin and are closest together.

After determining the bin error bars, we consider how to plot the cosmic variance error bar for a binned angular power spectrum. Due to the abrupt change in binning, from a bin size of 1 at $l = 2, 3$ to a bin size of 2 for the bin containing $l = 3$ and $l = 4$, the cosmic variance error bar drops significantly.

Despite using a binning scheme, we opt to plot the theory power spectrum as a curve at each l , instead of a binned quantity. Recall that for the random distribution of $l(l + 1)C_l/(2\pi)$ values, the mean of the theory spectrum values in a bin is the mean of the binned cosmic variance samples. Binning the mean of the distribution at each l gives the mean of bin. (This is not true for the median or the mode.) Likewise, we want to put an unbinned error bar on the curve with the height of the upper error bar as the height of the upper error bar on the binned value. In this way, the average height of the cosmic variance curve over the bin is the correct upper error bar for that bin. We then use a spline interpolation of the upper and lower error bars between each bin center. This makes the above statement fractionally less true, but prevents abrupt changes in the height of the cosmic variance curve at the bin edges. The measurements are cosmic variance limited for $l < 457$ and have a signal-to-noise ratio above unity for $l < 946$.

The change of the template cleaning method from the seven-year to the nine-year analysis results in a slight change in the low- l power spectrum. For $2 \leq l \leq 16$, using the MASTER method with the KQ85y9 mask, the absolute value of the change in $l(l + 1)/(2\pi)C_l$ due to the template cleaning is typically 4% of cosmic variance per l .

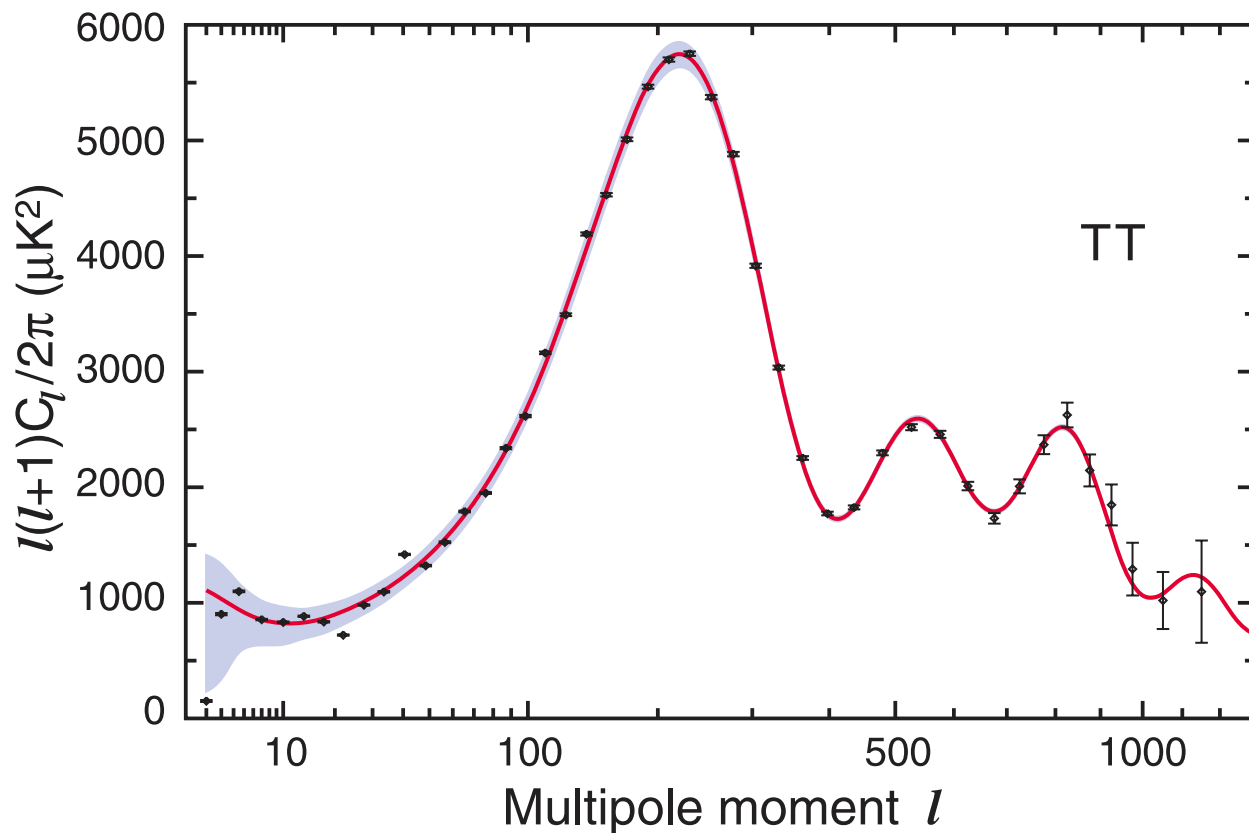


Fig. 32.— The nine-year *WMAP* TT angular power spectrum. The *WMAP* data are in black, with error bars, the best fit model is the red curve, and the smoothed binned cosmic variance curve is the shaded region. The first three acoustic peaks are well-determined. (A color version of this figure is available in the online journal.)

Figure 33 shows the temperature cross-power spectrum with the E-mode polarization (TE) spectrum. This angular cross-power spectrum is computed using the MASTER likelihood code, with the lowest $2 \leq l \leq 7$ bin determined using the more accurate pixel likelihood code. This was conditioned on the maximum likelihood power spectrum, and varied the value $(l+1)C_l^{TE}/(2\pi) = B_{2-7}$. The value B_{2-7} is independent of l . To maintain the requirement that $C_l^{TE} \leq \sqrt{C_l^{EE}C_l^{TT}}$ for a given bin value B_{2-7} , we adjust the C_l^{EE} spectrum upward from the best fit theory only as much as needed, on an l by l basis. As we vary B_{2-7} , the error bar is based on the minimum χ^2 value, and where $\Delta\chi^2 = 1$ in either direction. This gives an asymmetric error bar. Note that this would be a 1σ error bar for a Gaussian distribution, but it does not necessarily contain 68% of the likelihood due both to conditioning on the higher l TT, TE and EE power spectra, as well as to the non-Gaussian shape of the power spectrum meaning that $\Delta\chi^2 = 1$ does not correspond exactly to a 68% confidence interval.

Figure 34 shows the temperature cross-power spectrum with the B-mode polarization (TB) spectrum. This angular cross-power spectrum is computed using the MASTER likelihood code. The TB angular power spectrum is expected to be zero and the data are consistent with this expectation. The $2 \leq l \leq 7$ EE power spectrum is shown in Figure 35. The $2 \leq l \leq 7$ BB power spectrum is shown in Figure 36.

For running chains, we update the Sunyaev Zel’dovich spectrum template to the spectrum given by Battaglia et al. (2012). Their thermal SZ spectrum is multiplied by 3.61 to scale from 150 GHz to V-band (61 GHz). To convert from 150 to 148 GHz for ACT, we multiply by 1.05. The kinetic SZ spectrum does not need to be rescaled. The sum of kinetic and thermal spectra is used as the SZ template, for the frequency corresponding to each experiment; it is this sum that is multiplied by the SZ amplitude which is varied in the Markov chains.

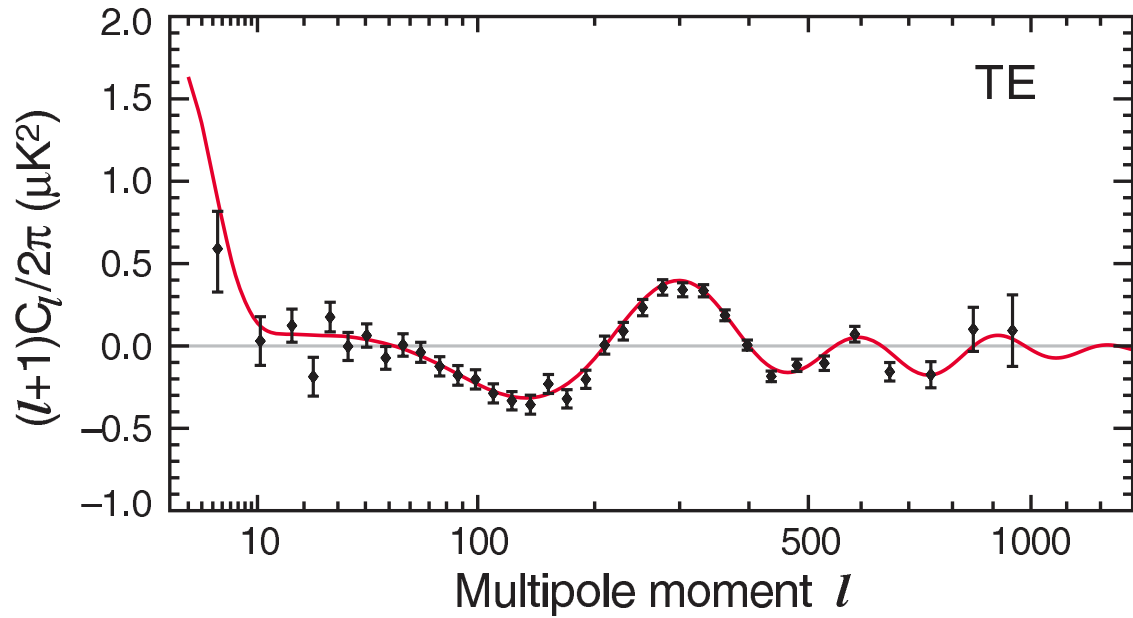


Fig. 33.— The TE spectrum. The *WMAP* data points and error bars are in black. The red theory curve is fit to the full *WMAP* data, including the TT angular power spectrum data. Note that the vertical axis on these spectra is $(l + 1)C_l/(2\pi)$ instead of $l(l + 1)C_l/(2\pi)$; this vertical scale differs from that of the TT spectrum plot by a factor of l . The lowest l TE bin where $2 \leq l \leq 7$ has been adjusted using a pixel likelihood code. (A color version of this figure is available in the online journal.)

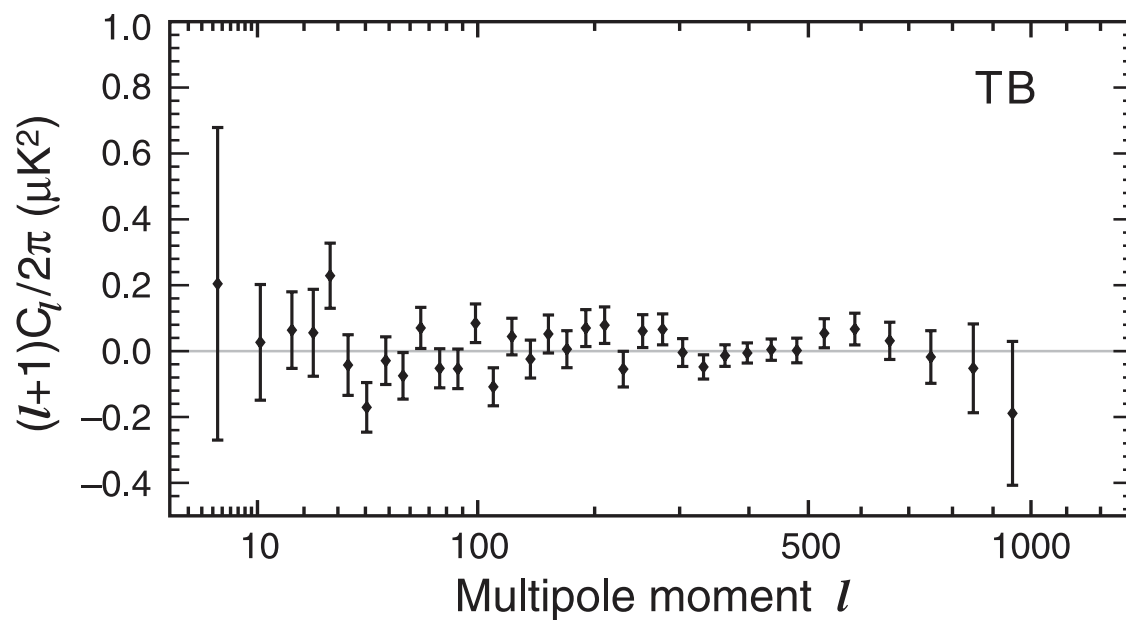


Fig. 34.— The TB spectrum. The TB spectrum uses the MASTER likelihood code. Note that the vertical axis on these spectra is $(l+1)C_l/(2\pi)$ instead of $l(l+1)C_l/(2\pi)$; this vertical scale differs from that of the TT spectrum plot by a factor of l .

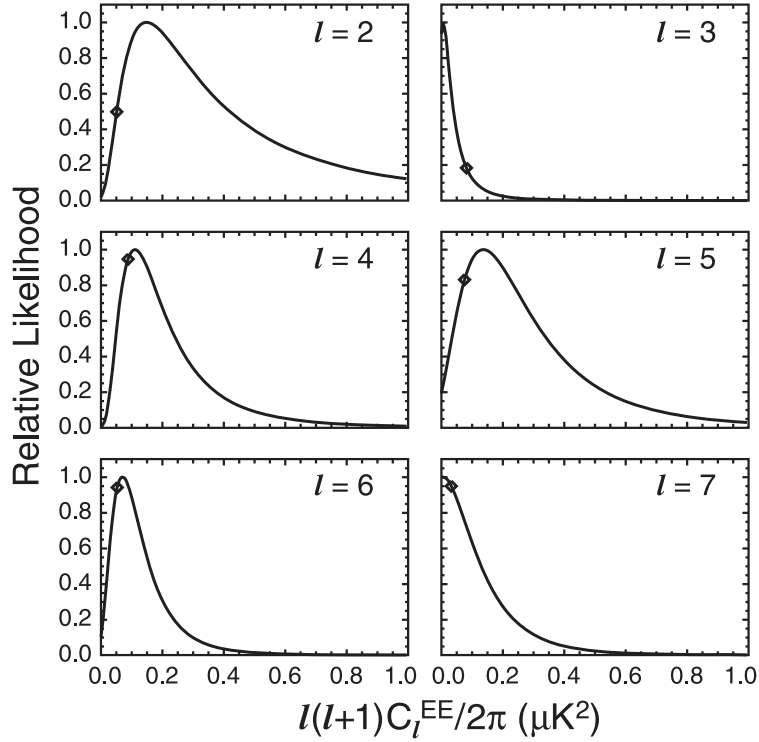


Fig. 35.— Individual likelihood functions of the low l EE polarized power are shown for $l = 2$ through 7. When fitting at a particular l , we set C_l at all other values of l to the value in the best fit WMAP power spectrum. In addition, at the l in question we set $C_l^{TE} = 0$ to maintain that $C_l^{TE} \leq \sqrt{C_l^{TT}C_l^{EE}}$. The black diamonds denote the best fit WMAP EE power spectrum. These likelihood functions include sample variance.

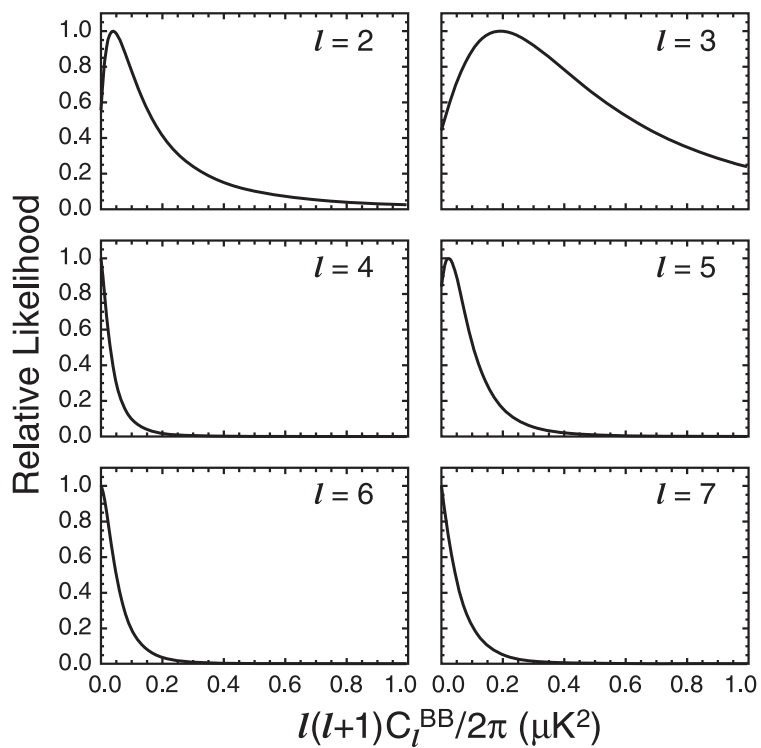


Fig. 36.— Low l BB spectra. Other C_l values are fixed to the best fit *WMAP* power spectrum.

7. Power Spectrum Goodness of Fit and Map Anomalies

7.1. Goodness of Fit

The likelihood code we release comes with a test code that runs on the *WMAP* nine-year best fit Λ CDM power spectrum (with no extra priors). This splits up the likelihood into several parts. We first look at each part and then combine the results for an overall estimate of goodness of fit. The high- l TT spectrum in the l range 33–1200 has 1168 degrees of freedom, and a χ^2 value of 1200. This gives a reduced χ^2 value of 1.027, and the probability to exceed this is 25.1%, which indicates a good fit to the data. The high- l TE spectrum in the l range 24–800 has 777 degrees of freedom and a χ^2 value of 815.4 for the same model. The probability to exceed this χ^2 value is 16.5%, which again indicates a good fit. The low- l polarized pixel-based likelihood contains 585 unmasked res 3 pixels each with a Q and U Stokes parameter, for 1170 degrees of freedom. The χ^2 value for this part of the likelihood is 1321. The probability to exceed this χ^2 value is 0.13%, which is unusually low.

We have not yet mentioned the low l TT and TE spectra. Recall that the low l polarized pixel likelihood decorrelates the temperature and polarization maps of the sky using the ILC and TT and TE spectra, as described in Appendix D of Page et al. (2007). After doing this, one obtains a χ^2 for the pixelized QU likelihood that incorporates information about TE, which is why we do not have a separate TE χ^2 value for $l \leq 23$. The $l \leq 32$ TT likelihood is computed by a Blackwell-Rao estimator, based on Gibbs samples. This code does not naturally generate a value comparable to a χ^2 quantity. However, it does provide a likelihood function which can be applied to any low l TT spectrum, and in the process of doing the sampling one obtains many spectra (not smooth, typically) which have been sampled from this likelihood function. One can look at the distribution of likelihoods resulting from these spectra and determine whether our best fit spectrum creates an unusually low likelihood. We do this and find that our best fit power spectrum generates an acceptable likelihood value.

Adding the three χ^2 values mentioned above gives 3115 degrees of freedom with a total χ^2 value of 3336.4. The probability to exceed this χ^2 value is 0.3%, which is still unusually low. This is driven completely by the low l polarized likelihood.

We investigated the origin of the excess χ^2 in the low- l polarization data. To see if there is any evidence for systematic effects in difference maps, we computed χ^2 from six combinations of difference maps involving Ka-, Q-, and V-bands: Ka–Q, Ka–V, Ka–QV, Q–V, Q–KaV, and V–KaQ, where QV, KaV and KaQ are the corresponding weighted-averages of maps in two different frequency bands. We find that none of these combinations show an anomalous χ^2 . The average and standard deviation of χ^2 is 1180 ± 47 for 1170 degrees of freedom. The largest value of χ^2 is 1236 from Ka–QV, and the probability to

exceed (PTE) is 8.8%. We then computed the optical depth, τ , from Ka–QV, finding that it is consistent with zero (the maximum likelihood value lies in $\tau < 0.002$, well below the 68% CL statistical uncertainty of $\delta\tau = 0.014$). Therefore, we conclude that the low- l polarization data pass the null test, and any residual systematic error we do not detect in difference maps has a negligible impact on our estimation of τ . This null test also shows that the residual polarized synchrotron emission in Ka, if any, has a negligible impact on τ .

To get an idea of how much additional noise we would need to include in the noise covariance matrix of the co-added KaQV map to explain the χ^2 , we add an uncorrelated noise variance to each r3 pixel ($N_{side} = 8$), $N_{ij} \rightarrow N_{ij} + \sigma_{r3}^2 \delta_{ij}$. We find $\sigma_{r3} = 0.27 \mu\text{K}$ brings the reduced χ^2 to unity. The instrumental noise per r3 pixel of the co-added KaQV map ranges from 0.43 to 1.57 μK , with the average and standard deviation of $0.86 \pm 0.17 \mu\text{K}$. Therefore, an additional noise variance, σ_{r3}^2 , required to explain the excess χ^2 is an order of magnitude smaller than a typical instrumental noise variance per r3 pixel of the co-added KaQV map.

Next, we computed the tensor-to-scalar ratio, r , from the low- l B-mode polarization data only. We found that r was consistent with zero, with the 95% CL upper bound of $r < 2.0$. The maximum likelihood value occurs at $r = 0.40$, which is already ruled out by the limit from the CMB temperature power spectrum, $r < 0.17$ (95% CL); thus, it cannot be due to inflationary B-modes. For $r = 0.4$, the low- l B-mode power spectrum amplitude is less than the scalar E-mode amplitude by a factor of six, and thus it is a small signal (and is consistent with zero).

We next examined residual foregrounds. By enlarging the edges of the polarization P06 mask by 1, 2, and 3 pixels, we found that the PTE increased from 0.1% to 0.9%, 5%, and 12%, respectively. While this may suggest the presence of residual foregrounds in the polarization data, this may also be partly due to the reduction of degrees of freedom (the degrees of freedom decrease from 1170 to 850, 582, and 344, respectively), as fewer degrees of freedom are more forgiving for larger values of the reduced χ^2 . Indeed, changes in the values of the reduced χ^2 are modest: it drops from 1.13 to 1.12, 1.10, and 1.09, respectively.

Therefore, we conclude that the excess χ^2 likely to be at least partially due to residual foregrounds, which we do not include in the noise covariance matrix. These foregrounds may not mostly be from the regions near the mask edges. However, the effect on our estimation of τ is negligible compared with the statistical uncertainty.

7.2. Power Spectra Goodness of Fit with Even-Odd multipoles

The analysis of the even excess effect seen in the seven-year TT power spectrum (Bennett et al. 2011) has been repeated using the nine-year data. The even excess statistic compares the mean C_l at even values of l with the mean C_l at odd values of l within a defined l domain. More formally, we define

$$\mathcal{E}_l = \frac{\langle \mathcal{C}_l^{\text{obs}} - \mathcal{C}_l^{\text{th}} \rangle_{\text{even}} - \langle \mathcal{C}_l^{\text{obs}} - \mathcal{C}_l^{\text{th}} \rangle_{\text{odd}}}{\langle \mathcal{C}_l^{\text{th}} \rangle},$$

where $\mathcal{C}_l = l(l+1)C_l/2\pi$, the superscript “obs” refers to the observed power spectrum, and the superscript “th” refers to a fiducial theoretical power spectrum used for normalization. In this paper, as before, we bin \mathcal{E}_l by $\Delta l = 50$.

The seven-year analysis used a set of more than 11000 Monte Carlo CMB simulations to probe the significance of the even excess. This large set was computationally inexpensive because the TT power spectra were estimated using the Monte Carlo Apodised Spherical Transform EstimatoR (MASTER; Hivon et al. 2002). However, in the nine-year analysis, the TT power spectra are computed using a new estimator weighted using the C^{-1} matrix, and the Monte Carlo realizations are much slower. Consequently, we now use a smaller set of 512 simulations of the full nine-year C^{-1} -weighted power spectrum

Figure 37 shows \mathcal{E}_l as a function of l within bins of $\Delta l = 50$. Results from the nine-year analysis are shown in black, and those from the seven-year analysis are shown in blue (see Bennett et al. 2011, Figure 9). The overall trend of the results with l is similar in the nine-year analysis to what it was in the seven-year analysis, except that the rise in \mathcal{E}_l over the domain $50 \leq l < 350$ is no longer monotonic. Also, in the nine-year analysis, two of the three negative values of \mathcal{E}_l , which denote excess power at *odd* values of l , have higher absolute value than in the seven-year analysis.

Bennett et al. (2011) examined a combined l bin for $250 \leq l < 350$ as an example of a posteriori analysis. The value of \mathcal{E}_l in this bin was 0.0446, as compared to a Monte Carlo scatter of $\sigma = 0.0155$, for a 2.9σ level of significance. The equivalent values for the nine-year analysis using the C^{-1} power spectrum estimator are $\mathcal{E}_l = 0.0381$, with a Monte Carlo scatter of $\sigma = 0.0144$, for a reduction in the level of significance to 2.6σ .

The de-biased \mathcal{E}_l test described by Bennett et al. (2011) has also been repeated for the nine-year analysis. This test chooses the maximum value of the bin-by-bin statistical significance $\mathcal{E}_l/\sigma(\mathcal{E}_l)$ from the l bins being considered, rather than focusing on only one bin, so that the a posteriori character of the test is weakened (see Bennett et al. 2011, Figure 11). We use bins of width $\Delta l = 50$ for $50 \leq l < 600$. The nine-year test gives similar results to the seven-year test, but at a reduced significance. In the seven-year test, the de-biased \mathcal{E}_l

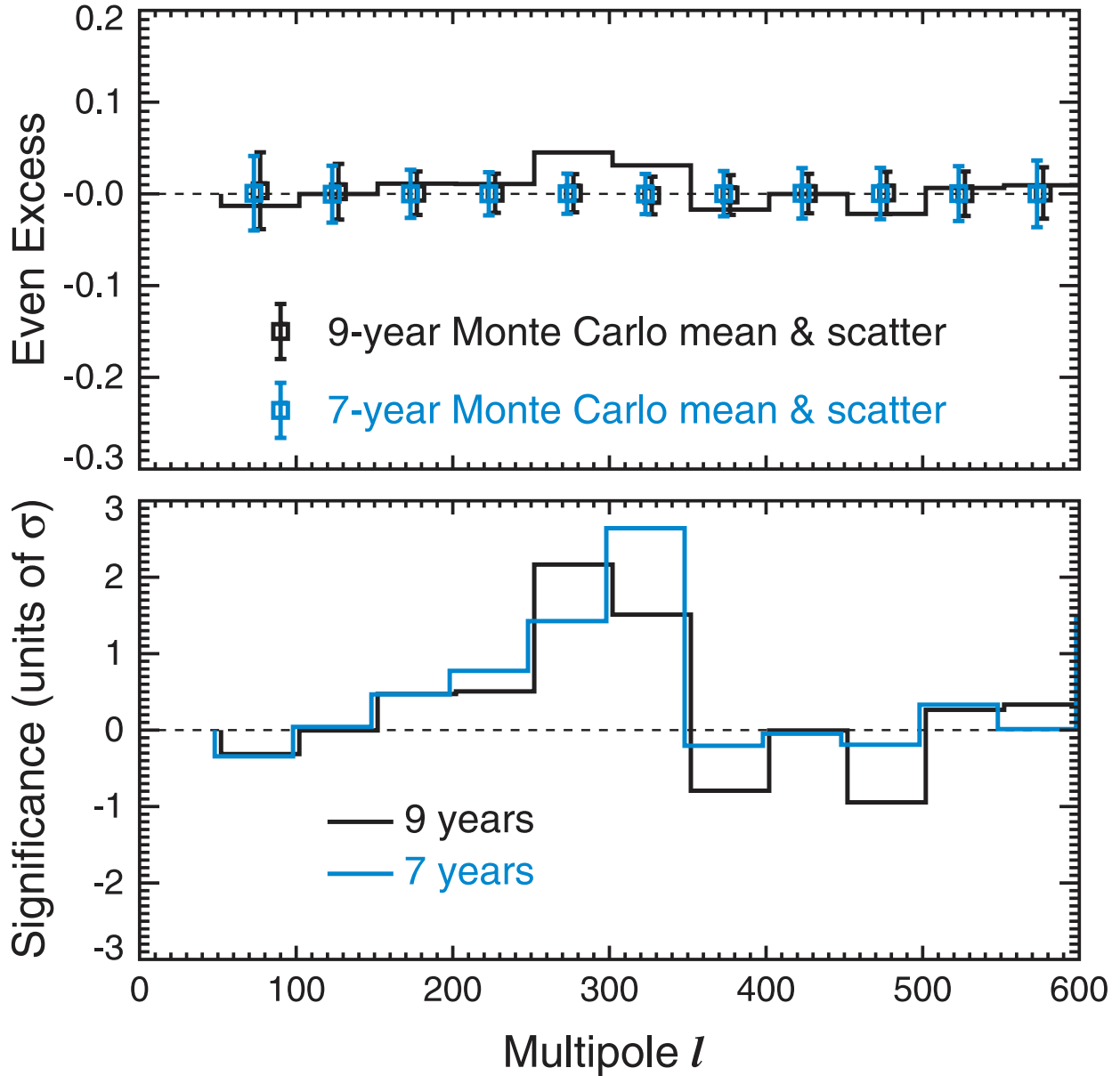


Fig. 37.— Top: Even excess \mathcal{E}_l in the observed power spectrum, in bins of $\Delta l = 50$, compared to the mean and scatter from 512 Monte Carlo realizations. Bottom: \mathcal{E}_l as in the top plot, converted to significance units by normalizing to the Monte Carlo scatter in each bin. Only the $l = 250 - 299$ and $l = 300 - 349$ bins show a significance greater than 1σ . Black: nine-year results; blue: seven-year results from Bennett et al. (2011).

(A color version of this figure is available in the online journal.)

test gave a probability to exceed (PTE) of 5.11% for the observed spectrum as compared to the Monte Carlo distribution, whereas in the nine-year test, the PTE is 14.3%, equivalent to a 1.1σ result. Similarly, bins with a high value of the odd excess ($-\mathcal{E}_l$) were less frequent than expected in the seven-year power spectrum, with a PTE of 98.9% in the de-biased test. This effect is also weaker in the nine-year power spectrum, which gives a PTE of 90.2%, equivalent to a 1.3σ result.

The even-odd effect in the observed power spectrum does not appear to be an artifact of the power spectrum estimator, since it is seen both with the MASTER method (seven years) and with the C^{-1} method (nine years). However, in the nine-year analysis, the superficial test for $250 \leq l < 350$ yields a result with reduced significance as compared to nine years, and the de-biasing strategy further reduces the significance of both the even power excess and the odd power deficit to $\sim 1\sigma$. The conclusion of Bennett et al. (2011) that the even-odd effect is probably a statistical fluke stands, and indeed is strengthened, after the nine-year tests.

7.3. Quadrupole Amplitude

Since the first-year *WMAP* data release there has been speculation about the low value of the $l = 2$ quadrupole moment. As concluded in the Bennett et al. (2011) seven-year results paper, while the quadrupole amplitude is below the mean expected amplitude for the model, it is not surprisingly or disturbingly low. Figure 38 illustrates the likelihood of the true value of $l(l+1)C_l^{TT}/(2\pi) = 6C_2^{TT}/(2\pi)$ for $l = 2$, based on our measured sky. A Blackwell-Rao estimator run on Gibbs samples and marginalized over all other values of C_l^{TT} results in the maximum likelihood quadrupole amplitude shown by the pink line. The 1σ and 2σ regions are shown as blue and green horizontal bands. The best fit Λ CDM theory spectrum computed on *WMAP* nine-year data only is shown in red. We conclude from this that the theoretically expected quadrupole amplitude (based on a Λ CDM fit to the full angular power spectrum) is well between 1σ and 2σ , hardly an unlikely event.

Looked at the other way, we can ask the relative probability of observing the particular quadrupole value given the mean expected value based again on a Λ CDM fit to the full angular power spectrum. This is shown in Figure 39. Again, one can see that the distribution is far from Gaussian and that the peak of the likelihood function is well displaced from its mean, such that the single most likely value for the expected quadrupole is close to half of the mean value. The observed quadrupole value is a relative probability of 40%, more than 1σ but less than 2σ away from expectations. The quadrupole value thus cannot be said to be anomalously low; it is well within the expected statistical variance.

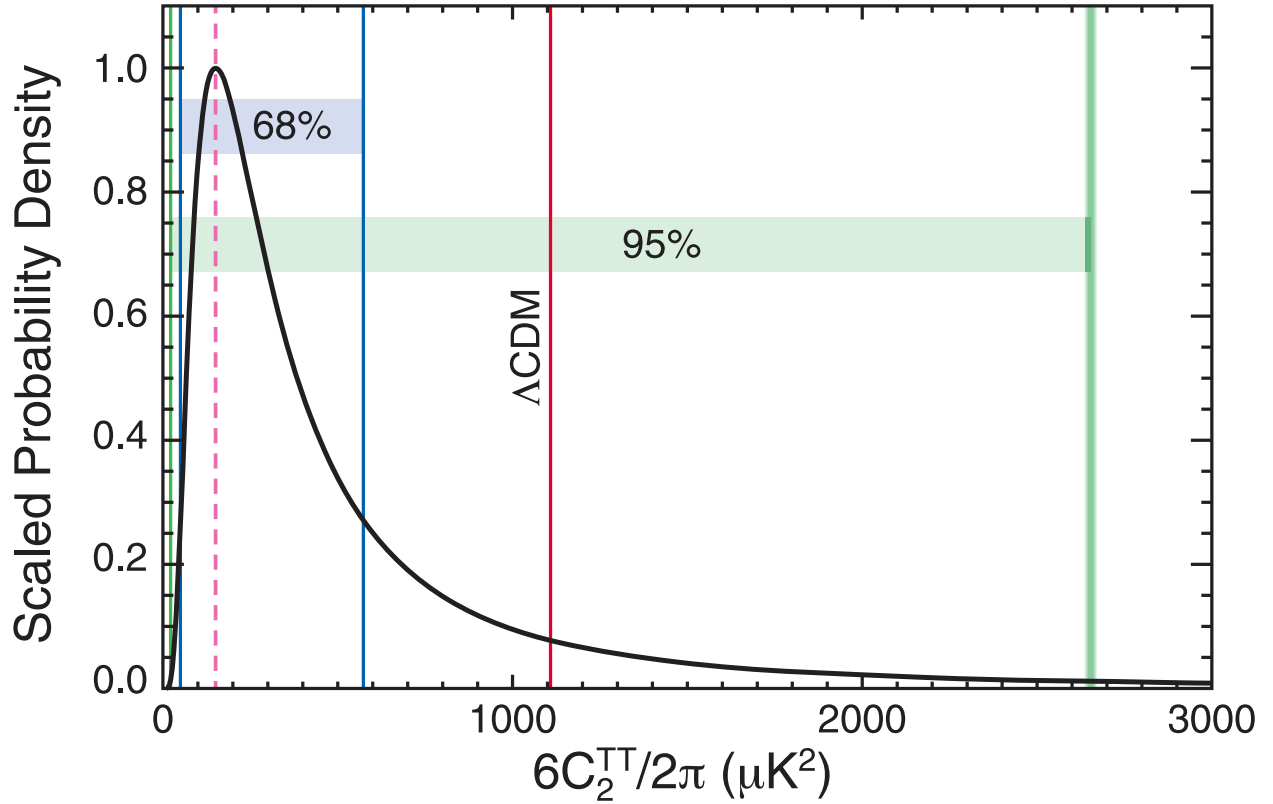


Fig. 38.— The likelihood of the true value of $l(l+1)C_l^{TT}/(2\pi) = 6C_2^{TT}/(2\pi)$ for $l = 2$, based on our measured sky. This is computed using the Blackwell-Rao estimator run on Gibbs samples, and it marginalizes over all other values of C_l^{TT} . The maximum likelihood point is shown as the pink line; one and two sigma regions are shown as blue and green lines. The best fit Λ CDM theory spectrum computed on *WMAP* nine-year data only is shown in red.

(A color version of this figure is available in the online journal.)

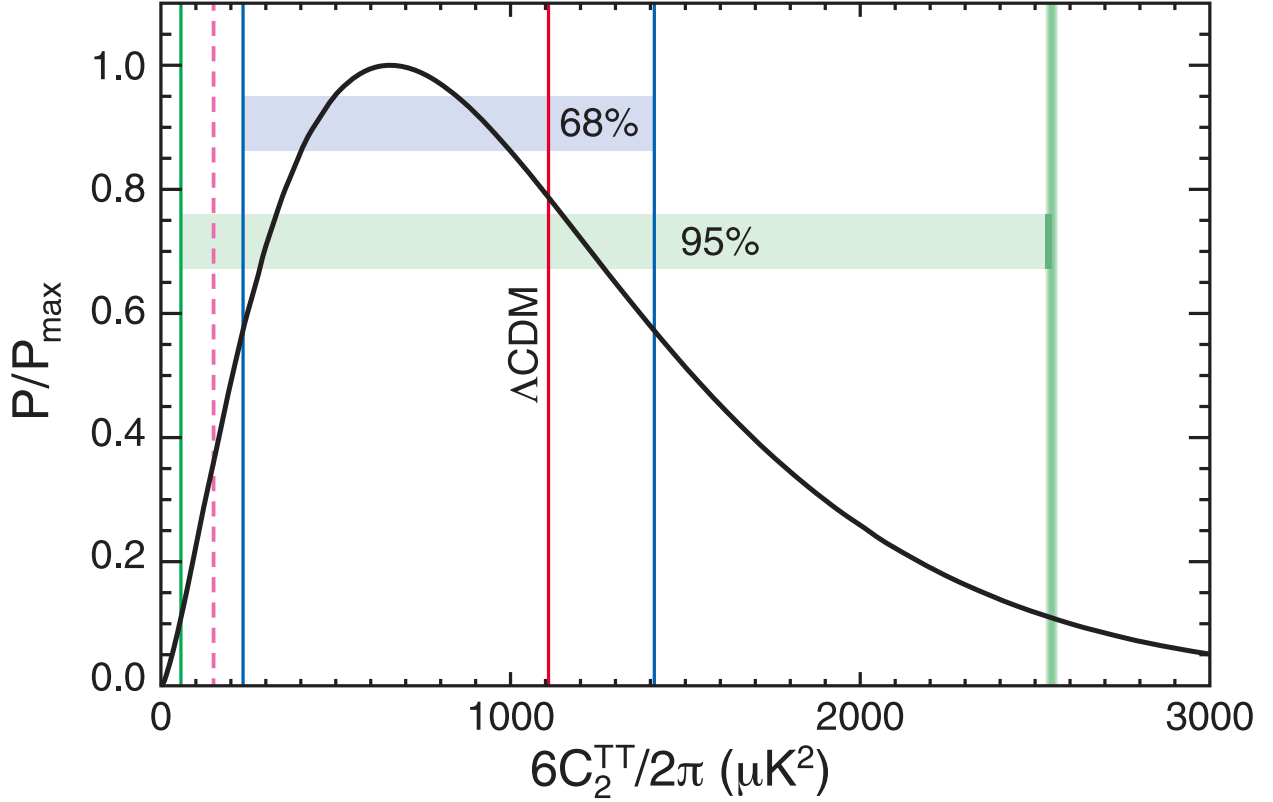


Fig. 39.— The cosmic variance probability distribution for the quadrupole, given the theory power spectrum. This assumes we know $l(l+1)C_l^{TT}/(2\pi) = 6C_2^{TT}/(2\pi) = 1109 \mu\text{K}^2$ (red line) and plots the distribution of quadrupole power values we could measure for random Hubble volumes. Note that $6C_2^{TT}/(2\pi)$ is the mean of the distribution; due to the skewness of the χ^2 distribution, the peak of the distribution is substantially lower. One and two-sigma regions are shown. The quadrupole cosmic variance distribution has $\nu = 2l + 1 = 5$ degrees of freedom. Assuming $f_{\text{sky}} \approx 0.99$, we plot a χ^2 distribution based on $\nu = (2l + 1)f_{\text{sky}}^2 \approx 4.9$ degrees of freedom. The peak of the distribution is then lower than the mean by a factor of $(\nu - 2)/\nu$, putting it at $656 \mu\text{K}^2$.

(A color version of this figure is available in the online journal.)

7.4. Alignment of the Quadrupole and Octupole

The quadrupole and octupole, expected to have independent and random orientations, were aligned to $< 0.5^\circ$ in the seven-year ILC map (Bennett et al. 2011). In the nine-year ILC map, we find that the orientations of the quadrupole and octupole differ by $\sim 3^\circ$. Most of this change is due to the fact that the nine-year ILC map has been improved by the use of the asymmetric beam deconvolution described in Section 4.2. Other minor changes are due to small improvements of the gain model and window functions from two years of additional data, as well as the updated foreground mask (which slightly changes the $\text{csc } \beta$ fits and hence the monopole offset in each ILC region). A nine-year ILC made without the beam deconvolution has a quadrupole-octupole misalignment of $\sim 1^\circ$, confirming that the improvement of the use of deconvolution is the dominant source of the change from seven to nine years of data.

We now address the significance of $\sim 3^\circ$ octupole-quadrupole alignment in the nine-year map by examining its sensitivity to the separation of the CMB from the foregrounds. To do this, we use the error description of the CMB-foreground covariance, discussed in Section 5.3.7.2. The CMB-foreground covariance in the ILC is described in terms of 48 error modes (computed at r6), which provide the eigenvectors with nonzero eigenvalues of the 49152×49152 pixel space covariance matrix. We first change bases from pixel space into the 12-dimensional space spanned by the quadrupole and octupole modes (5 for the quadrupole, 7 for the octupole). This results in a 12×12 covariance matrix for the error in the quadrupole and octupole a_{lm} coefficients. For convenience, we use real-valued harmonics and so we have a real-valued covariance matrix. Then, we generate many Gaussian random realizations of perturbations to the quadrupole and octupole (i.e. realizations of CMB quadrupole and octupole errors) based on this covariance matrix. We add these to the quadrupole and octupole from the nine-year ILC, and check the alignment for each, using the same method as described in Bennett et al. (2011).

Among these realizations, we find the median quadrupole-octupole misalignment to be 6° . The probability of a $\leq 6^\circ$ alignment is 0.55%. This means that the significance of the octupole-quadrupole alignment is $< 3\sigma$, i.e. it is not significant. Occasional perturbations to the ILC realign the quadrupole and octupole perfectly, and about 5% of the perturbations misalign them by more than 20° . Note also that this encompasses only one of the types of error in the ILC. Including an estimate of the ILC bias error will further degrade the significance of any observed alignment.

We conclude that our ability to remove foregrounds is the limiting factor in the measurement of the cosmological quadrupole-octupole alignment. The already low statistical significance ($< 3\sigma$) of the estimated alignment must be further degraded by the posterior

selection made to examine this particular quantity. Given that there is no evidence of experimental systematic effects, and that the foreground-CMB separation contributes substantially to the alignment uncertainty, the estimated alignment appears to be a low-significance chance occurrence.

8. Cosmological Results and Implications

We have seen that the *WMAP* power spectrum is well fit by only six parameters. The quadrupole amplitude is not anomalously low, and the quadrupole-octupole alignment cannot be considered anomalous as it is within the range allowed by cosmic variance and foreground subtraction uncertainties.

The bipolar power spectrum of the final nine-year maps shows a large signal similar to the one we reported in the seven-year results. This signal exhibits a strong ecliptic latitude dependence, in both the seven and nine-year data. The bipolar power spectrum of the new beam-symmetrized (deconvolved) maps shows that this signal has largely gone away, but there now appears a high- l signal with the opposite sign. This is expected since the deconvolution process correlates pixel noise in a way that we do not correct for in the estimation process. Our primary motivation was to check that the latitude-dependent signal at low- l was due to beam asymmetry, and we believe that is now well established. There is little motivation to correct the side-effects at high- l , since doing so would be non-trivial, and there was no hint of an anomaly there to begin with. In summary, our new analysis demonstrates that the latitude dependent signal in the bipolar power spectrum seen in both the seven and nine-year non-deconvolved maps was real and caused by *WMAP*'s beam asymmetry. Further, since beam asymmetry has negligible effect on the angular power spectrum, C_l , we adopt the simpler non-deconvolved maps for power spectrum estimation and cosmological parameter studies.

The power spectrum contains all of the cosmological information in the map if, and only if, the fluctuations are Gaussian with random phases across the non-masked portion of the map. In this section we show that this is indeed the case within the estimated measurement and analysis uncertainties. We then summarize the cosmological parameter discussion of Hinshaw et al. (2012) with cosmological parameters derived using only *WMAP* data and derived when combined using external data as well.

8.1. Non-Gaussianity

The simplest model of inflation, namely single-field slow-roll inflation with canonical kinetic term and a nearly flat potential $V(\phi)$, predicts that the initial adiabatic curvature $\zeta(\mathbf{k})$ has only tiny deviations from Gaussianity (Acquaviva et al. 2003; Maldacena 2003). However, alternate models of the early universe predict several possible types of deviations from Gaussian statistics, making the search for non-Gaussianity in the CMB a powerful, multifaceted probe of the early universe.

8.1.1. f_{NL}^{loc} , f_{NL}^{eq} , and f_{NL}^{orth}

We will limit our search for non-Gaussianity to the 3-point function or bispectrum, and parameterize it by:

$$\langle \zeta_{\mathbf{k}_1} \zeta_{\mathbf{k}_2} \zeta_{\mathbf{k}_3} \rangle = (f_{NL}^{\text{loc}} B_{\text{loc}}(k_1, k_2, k_3) + f_{NL}^{\text{eq}} B_{\text{eq}}(k_1, k_2, k_3) + f_{NL}^{\text{orth}} B_{\text{orth}}(k_1, k_2, k_3)) (2\pi)^3 \delta^3 \left(\sum \mathbf{k}_i \right) \quad (50)$$

where f_{NL}^{loc} , f_{NL}^{eq} , f_{NL}^{orth} are free parameters to be estimated, and the local, equilateral, and orthogonal template bispectra are defined by:

$$B_{\text{loc}}(k_1, k_2, k_3) = \frac{6}{5} (P_\zeta(k_1)P_\zeta(k_2) + 2 \text{ perm.}) \quad (51)$$

$$B_{\text{eq}}(k_1, k_2, k_3) = \frac{3}{5} \left(6P_\zeta(k_1)P_\zeta(k_2)^{2/3}P_\zeta(k_3)^{1/3} - 3P_\zeta(k_1)P_\zeta(k_2) - 2P_\zeta(k_1)^{2/3}P_\zeta(k_2)^{2/3}P_\zeta(k_3)^{2/3} + 5 \text{ perm.} \right) \quad (52)$$

$$B_{\text{orth}}(k_1, k_2, k_3) = \frac{3}{5} \left(18P_\zeta(k_1)P_\zeta(k_2)^{2/3}P_\zeta(k_3)^{1/3} - 9P_\zeta(k_1)P_\zeta(k_2) - 8P_\zeta(k_1)^{2/3}P_\zeta(k_2)^{2/3}P_\zeta(k_3)^{2/3} + 5 \text{ perm.} \right) \quad (53)$$

The $\{f_{NL}^{\text{loc}}, f_{NL}^{\text{eq}}, f_{NL}^{\text{orth}}\}$ basis for the three-point function is large enough to encompass a range of interesting models. Local-type non-Gaussianity is generic to some multi-field inflation models, for example curvaton models (Linde & Mukhanov 1997; Lyth et al. 2003) and variable reheating models (Dvali et al. 2004; Zaldarriaga 2004), and also to some alternatives to inflation, such as “new” ekpyrosis (Creminelli & Senatore 2007; Buchbinder et al. 2007) and cyclic (Lehners & Steinhardt 2008a,b) models. Also, there is a theorem (Creminelli & Zaldarriaga 2004) that implies that no single-field model of inflation can generate detectable f_{NL}^{loc} . Equilateral-type and orthogonal-type non-Gaussianity can be generated in single-field models, and generically appear when there are non-negligible interaction terms in the inflationary Lagrangian.

We constrain the f_{NL} parameters using the optimal (i.e. minimum variance unbiased) bispectrum estimator implemented in Smith et al. (2009), which builds on previous work (Komatsu et al. 2005; Creminelli et al. 2006; Smith & Zaldarriaga 2011). The estimator optimally combines channels with different noise maps and beams by filtering the data with the inverse signal+noise covariance $C^{-1} = (S + N)^{-1}$, and includes a one-point term (in addition to a three-point term) which reduces the variance. Unless otherwise specified, we use the V-band and W-band differencing assemblies from *WMAP* (six maps total), remove regions of high Galactic foreground and point source emission using the nine-year KQ75 mask, and marginalize three foreground templates corresponding to synchrotron, free-free, and dust emission. With foreground marginalization enabled, the same f_{NL} estimates are obtained on raw and template-cleaned maps.

Our “bottom line” constraints on non-Gaussianity are as follows:

$$\begin{aligned}
 f_{NL}^{\text{loc}} &= 37.2 \pm 19.9 & (-3 < f_{NL}^{\text{loc}} < 77 \text{ at } 95\% \text{ CL}) \\
 f_{NL}^{\text{eq}} &= 51 \pm 136 & (-221 < f_{NL}^{\text{eq}} < 323 \text{ at } 95\% \text{ CL}) \\
 f_{NL}^{\text{orth}} &= -245 \pm 100 & (-445 < f_{NL}^{\text{orth}} < -45 \text{ at } 95\% \text{ CL})
 \end{aligned}
 \tag{54}$$

The f_{NL}^{loc} constraint includes a correction for the ISW-lensing contribution to the bispectrum, which arises from the large-scale correlation between the CMB temperature and the CMB lensing potential. We find that the ISW-lensing bispectrum biases the f_{NL}^{loc} estimator by $\Delta f_{NL}^{\text{loc}} = 2.6$; this bias has been subtracted from the estimate in Equation (54). The ISW-lensing bias was computed using the Fisher matrix approximation, but this has been shown to be an excellent approximation to the exact result (Hanson et al. 2009; Lewis et al. 2011).

The constraint on each f_{NL} parameter in Equation (54) assumes that the other two f_{NL} parameters are zero. For a joint analysis of all three parameters, we need the bispectrum Fisher matrix:

$$F = \begin{pmatrix} 25.25 & 1.06 & -2.39 \\ 1.06 & 0.54 & 0.20 \\ -2.39 & 0.20 & 1.00 \end{pmatrix} \times 10^{-4}
 \tag{55}$$

where the ordering of the rows and columns is $f_{NL}^{\text{loc}}, f_{NL}^{\text{eq}}, f_{NL}^{\text{orth}}$. The statistical error on each f_{NL} parameter in Equation (54), with the other two f_{NL} parameters fixed to zero, is $(F_{ii})^{-1/2}$, and the correlation between two estimators in Equation (54) is equal to the rescaled off-diagonal matrix element $F_{ij}/(F_{ii}F_{jj})^{1/2}$.⁸ An example of a two-parameter joint analysis is shown in Figure 42 below.

8.1.2. f_{NL}^{orth} Diagnostic Tests and Interpretation

The most striking result in Equation (54) is the estimate for f_{NL}^{orth} , which is non-zero at 2.45σ . The (two-sided) probability of obtaining a value with this statistical significance in a Gaussian fiducial cosmology is 1.4%. This is not significant enough by itself to consider it a detection, but even further caution is required. When interpreting this probability, it must

⁸This estimator covariance is appropriate for our convention that each f_{NL} estimator is defined to be the optimal estimator assuming that the other two f_{NL} parameters are zero. There is an alternate definition in which each f_{NL} estimator is defined with the other two f_{NL} parameters marginalized; in this case the estimator covariance matrix would be the inverse Fisher matrix $(F^{-1})_{ij}$. The two definitions are linear combinations of each other, and therefore give identical results in a joint analysis, provided that the off-diagonal correlations are properly incorporated.

be kept in mind that we look for multiple deviations from the vanilla Λ CDM model⁹, so it is statistically unsurprising that *one* such deviation is at this significance level. The rest of this section will be devoted to consistency checks and interpretation of the f_{NL}^{orth} result.

One possible source of systematic error is contamination by residual foregrounds. Since we marginalize over synchrotron, free-free and dust templates in our bispectrum estimator, any foreground contribution that is a linear combination of these spatial templates does not contribute to f_{NL}^{orth} . However, since the templates are not perfect, there will be residual contributions at some level. A simple procedure that gives the rough order of magnitude is to disable template marginalization in the estimator, and compute the foreground contribution to f_{NL}^{orth} in an ensemble of simulated *raw* maps without any foreground cleaning. We simulate raw maps using random CMB and noise realizations, and a fixed dust realization given by model 8 of Finkbeiner et al. (1999). We do not include synchrotron and free-free foregrounds since dust dominates in W-band and is a significant fraction of the V-band foreground. In each simulation, we compute the difference ($\Delta f_{NL}^{\text{orth}}$) between the f_{NL}^{orth} estimate obtained from the raw map, and the f_{NL}^{orth} estimate that would be obtained from the CMB+noise contribution alone. We find that the mean value of ($\Delta f_{NL}^{\text{orth}}$) is 1.1 and the RMS scatter is 5.2. This presumably overestimates the dust contribution since we are not attempting to remove foregrounds at all. Since the shift ($\Delta f_{NL}^{\text{orth}}$) seen in these simple simulations is much smaller than the statistical error $\sigma(f_{NL}^{\text{orth}})$, we conclude that residual foregrounds are unlikely to be a significant contaminant.

As a first test for instrumental systematic effects, we check for consistency between different angular scales by splitting the f_{NL}^{orth} estimator in l -bands. Our procedure is as follows: we write the f_{NL}^{orth} estimator as a sum over triangles, restrict the sum to triangles whose maximum multipole $\max(l_1, l_2, l_3)$ is in a given bin (l_{\min}, l_{\max}) , and then appropriately normalize so that the band-restricted sum is an unbiased estimator of f_{NL}^{orth} . This prescription for binning the f_{NL}^{orth} estimator has the property that if we combine f_{NL}^{orth} estimates in all bins up to some multipole l_{\max} , the result agrees with simply rerunning the f_{NL}^{orth} estimator with maximum multipole l_{\max} . It also has the property that f_{NL}^{orth} estimates in different l -bands are nearly uncorrelated.

In Figure 40, we show the f_{NL}^{orth} estimate in l -bands, with the cumulative best-fit value $f_{NL}^{\text{orth}} = -245$ shown for comparison. Each bin is consistent with the cumulative best-fit value at 2σ , and the overall χ^2 of the fit to a constant f_{NL}^{orth} value is good ($\chi^2 = 8.8$ with seven

⁹A partial list includes the three f_{NL} parameters, the spatial curvature Ω_K , tensor-to-scalar ratio r , running of the spectral index ($dn_s/d\log k$), dark energy equation of state w , isocurvature amplitudes α_0, α_{-1} , and neutrino mass m_ν .

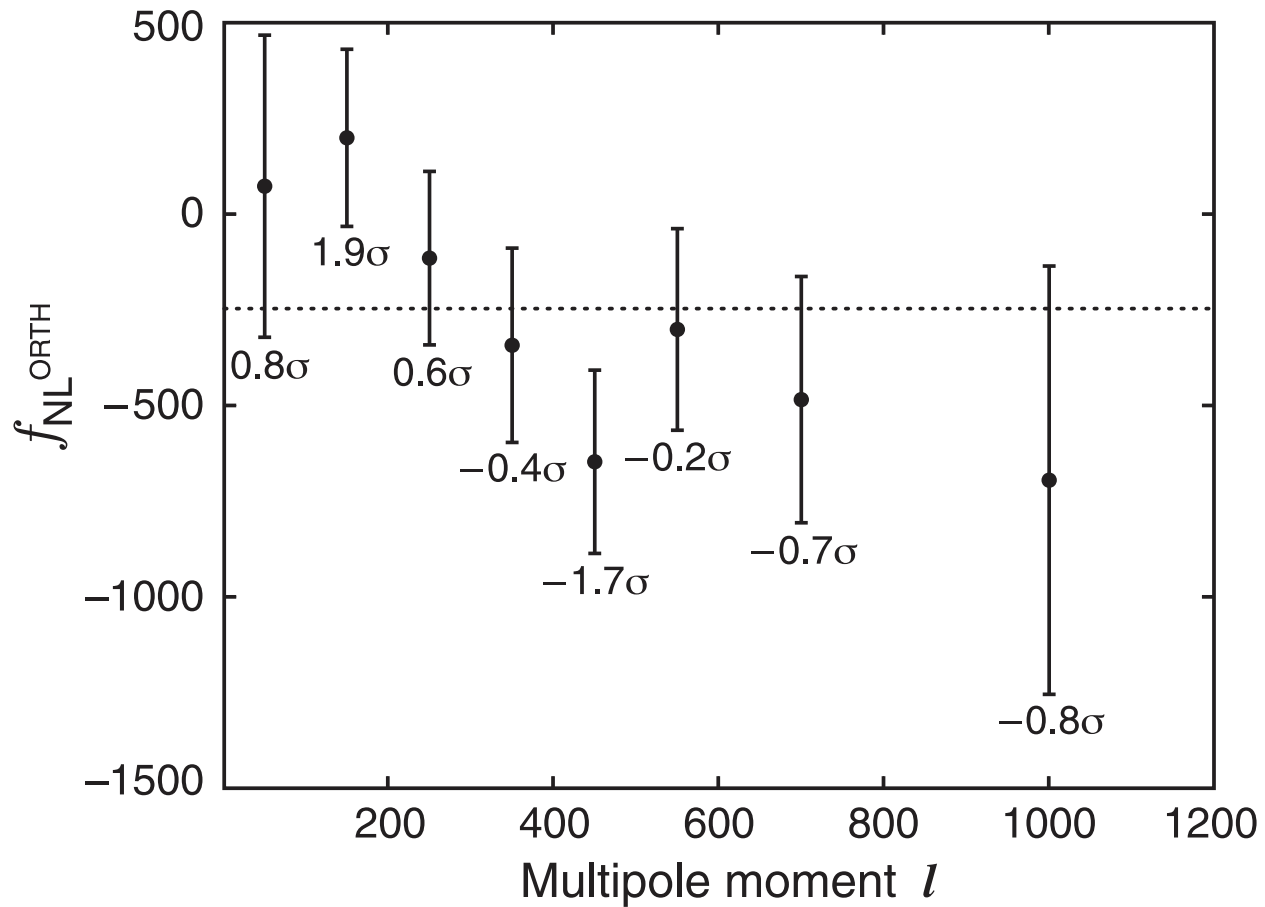


Fig. 40.— A test for scale-dependent systematics: f_{NL}^{orth} estimates in l -bands, with cumulative best-fit value $f_{NL}^{\text{orth}} = -245$ shown by the dotted horizontal line. Each error bar is labeled with the statistical significance of the deviation from the cumulative best-fit value (not the deviation from zero). No evidence for scale-dependent systematics is seen.

degrees of freedom). We therefore conclude that there is no evidence for scale-dependent systematic contamination.

As a second test for systematics, we can ask whether estimates of f_{NL}^{orth} in different parts of the sky are consistent. The bispectrum estimator is naturally written as an integral over position on the sky, so a convenient way to visualize the position dependence is to simply plot the integrand as a skymap (Figure 41). This skymap is in units of “ f_{NL}^{orth} per steradian” and has the property that its integral over the whole sky is precisely equal to the estimated $f_{NL}^{\text{orth}} = -245$. If we restrict the integral to a subregion Ω of the sky, the value of the integral will roughly equal the value that would be obtained if we re-ran the estimator using masking to isolate the subregion Ω (appropriately rescaled by the area of Ω). Visual inspection of the skymap is a convenient way to look for an unexpected feature (e.g., a large contribution near the Galactic plane would suggest foreground contamination), although it might be difficult to assess the statistical significance of an *a posteriori* feature if found. Our interpretation of Figure 41 is that no visually striking features are seen; the skymap looks qualitatively similar to skymaps obtained from Gaussian simulations.

As a more quantitative test for consistency between different parts of the sky, we estimated f_{NL}^{orth} in the portions of the following regions that lie outside the KQ75 mask: the northern Galactic hemisphere, the southern Galactic hemisphere, within 30° of the ecliptic plane, and the ecliptic poles ($> 30^\circ$ from the ecliptic plane). We find that for any pair of these regions, the estimated f_{NL}^{orth} values are consistent at 2σ , relative to an ensemble of Monte Carlo simulations. The f_{NL}^{orth} estimates in these four subregions are -139 ± 139 , -361 ± 142 , -132 ± 144 , and -336 ± 138 , respectively.

As a final test for systematics, we can compare f_{NL}^{orth} estimates from different channels, or combinations of channels. In the first two columns of Table 16, we show the result of applying the f_{NL}^{orth} estimator for several combinations of channels. To assess whether the f_{NL}^{orth} estimates from a given pair of rows are statistically consistent, we subtract the two estimates, and compare the result to the same quantity (the difference of two f_{NL}^{orth} estimates) evaluated in an ensemble of Monte Carlo simulations. This way of assessing consistency fairly incorporates the correlation between f_{NL}^{orth} estimates that arises because the CMB realization (and the noise realizations, if the two rows have channels in common) is shared. The matrix in the rightmost columns of Table 16 shows the result of doing this consistency test for all pairs of rows in the table.

This “two-way” null test can be generalized to an N -way null test that tests mutual consistency between f_{NL}^{orth} estimates obtained in all N rows of the table. We represent the f_{NL}^{orth} estimates as a length- N vector f_i , and compute the N -by- N covariance matrix C_{ij} using Monte Carlo simulations with shared CMB and noise realizations. We then compute

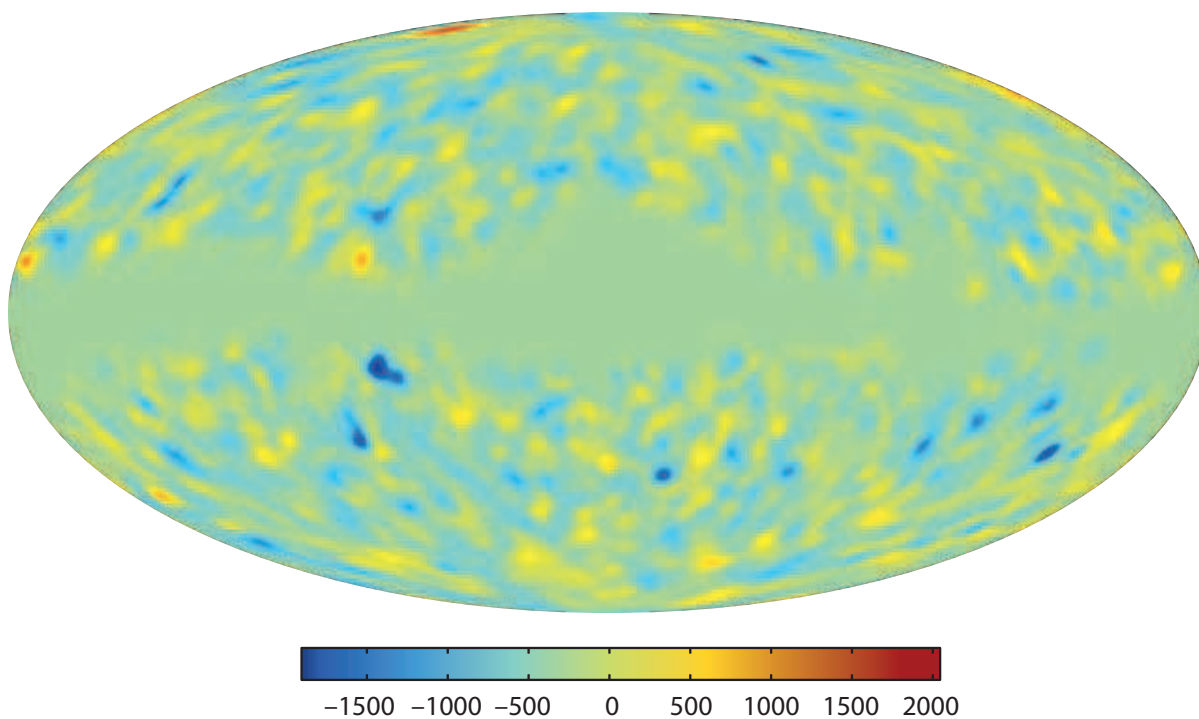


Fig. 41.— A visual test for sky location dependent systematics: skymap showing the contribution of different parts of the sky to the f_{NL}^{orth} estimator, in units of “ f_{NL}^{orth} per steradian”. We do not detect any significant localized features in this map. (A color version of this figure is available in the online journal.)

an overall best-fit f_{NL}^{orth} value F which minimizes $\chi^2 = (f_i - F)C_{ij}^{-1}(f_j - F)$. If the N estimates are mutually consistent, then the value of χ^2 at the minimum will be distributed as a χ^2 random variable with $(N - 1)$ degrees of freedom.

We find that the channel-channel null tests are marginal. The N -way null test gives $\chi^2 = 16.3$ with 8 degrees of freedom, corresponding to one-sided probability $p = 0.038$. The most discrepant pair of rows in Table 16 is (W,W4), which differ by 3.2σ relative to Monte Carlo simulations. This statistical significance should not be taken at face value since there are 36 matrix entries in Table 16, and we have chosen the most anomalous one. However, if we construct the same matrix for each member of an ensemble of simulations, we find that the probability that at least one pair of rows is discrepant by $> 3.2\sigma$ is 2.6%. Finally, we observe that the discrepancy between V-band and W-band channels, which is in some sense the most natural split, is 2.3σ , corresponding to probability $p = 0.021$.

We conclude that there is some tension in the channel-channel null tests, with p -value around a few percent depending on which test is chosen. Since we have also considered null tests that pass cleanly (i.e. the tests based on scale dependence and sky location), our interpretation is that one failure at the few-percent level does not indicate systematic contamination, although the discrepancy between V-band and W-band is of some concern. We therefore cautiously proceed to discuss the physical implications of the non-Gaussianity constraints.

We opt to work in the context of single-field inflation, and use the effective field theory developed in Cheung et al. (2008a,b). The EFT provides a master Lagrangian which is general enough to describe almost all single-field models of inflation. See also Grunzinov (2005); Chen et al. (2007). The action consists of a standard kinetic term, plus small interaction terms whose coefficients parameterize allowed non-Gaussianity:

$$S = \int d^4x \sqrt{-g} \left[-\frac{M_{\text{Pl}}^2 \dot{H}}{c_s^2} \left(\dot{\pi}^2 - c_s^2 \frac{(\partial_i \pi)^2}{a^2} \right) + (M_{\text{Pl}}^2 \dot{H}) \frac{1 - c_s^2}{c_s^2} \left(\frac{\dot{\pi}(\partial_i \pi)^2}{a^2} + \frac{A}{c_s^2} \dot{\pi}^3 \right) + \dots \right] \quad (56)$$

Non-Gaussianity is parameterized by a dimensionless sound speed c_s , and a dimensionless parameter A that represents the ratio between the coefficients the operators of $\dot{\pi}^3$ and $\dot{\pi}(\partial_i \pi)^2$. We treat c_s and A as free parameters, but specific models will make predictions. For example, in DBI inflation (Alishahiha et al. 2004), c_s is a free parameter (but related to the tensor-to-scalar ratio) and $A = -1$.

The coefficients in the action (56) can be related to the parameters f_{NL}^{eq} , f_{NL}^{orth} by calculating the bispectra generated by the cubic operators $\dot{\pi}^3$ and $\dot{\pi}(\partial_i \pi)^2$, and projecting them

onto the basis of template bispectra (Senatore et al. 2010). The result is:

$$\begin{aligned} f_{NL}^{\text{eq}} &= \frac{1 - c_s^2}{c_s^2}(-0.276 + 0.0785A) \\ f_{NL}^{\text{orth}} &= \frac{1 - c_s^2}{c_s^2}(0.0157 - 0.0163A) \end{aligned} \quad (57)$$

where the numerical coefficients are specific to the nine-year *WMAP* results and have been computed using the exact Fisher matrix, including CMB transfer functions and *WMAP* noise properties. For generic values of A , f_{NL}^{eq} is larger than f_{NL}^{orth} (by an order of magnitude) and equilateral non-Gaussianity is generated. However, there is an order-unity window of values (roughly $3.1 \lesssim A \lesssim 4.2$) where f_{NL}^{orth} is larger than f_{NL}^{eq} , and orthogonal non-Gaussianity is generated.

Since single-field models that produce f_{NL}^{orth} are also expected to produce f_{NL}^{eq} at some level, it is natural to analyze joint constraints in the two-parameter space $\{f_{NL}^{\text{eq}}, f_{NL}^{\text{orth}}\}$. To set up a joint analysis, we define notation as follows. Let $f_i = (f_{NL}^{\text{eq}}, f_{NL}^{\text{orth}})$ be a two-component vector containing model parameters, let $\hat{f}_i = (51, -245)$ be the values of the associated estimators (i.e. the last two rows of Equation (54)), and let F_{ij} be the associated 2×2 Fisher matrix (i.e. the lower right corner of Equation (55)). Then for given model parameters f_i , we define a χ^2 statistic,

$$\chi^2 = \sum_{ij} f_i F_{ij} f_j - 2 \sum_i F_{ii} f_i \hat{f}_i + \sum_{ij} \hat{f}_i F_{ii} F_{ij}^{-1} F_{jj} \hat{f}_j. \quad (58)$$

We threshold this χ^2 to obtain confidence regions in the $(f_{NL}^{\text{eq}}, f_{NL}^{\text{orth}})$ plane. These confidence regions are shown in the left panel of Figure 42. We note that the point $(f_{NL}^{\text{eq}}, f_{NL}^{\text{orth}}) = 0$ is just outside the 2σ contour, which means that it is just barely a $> 2\sigma$ event when f_{NL}^{eq} is included in the parameter space. More precisely, the relevant $\Delta\chi^2$ is 7.16 with two degrees of freedom; the probability of getting a $\Delta\chi^2$ this large in a Gaussian cosmology is 2.8%.

In the right panel of Figure 42, we change variables to show confidence regions in the parameter space (c_s, A) . These confidence regions were obtained under the assumption that the single-field bispectra are well-approximated by the equilateral and orthogonal template shapes. However, we have checked that nearly identical confidence regions are obtained if the exact tree-level bispectra for the operators $\dot{\pi}^3$ and $\dot{\pi}(\partial_i\pi)^2$ are used throughout the analysis.

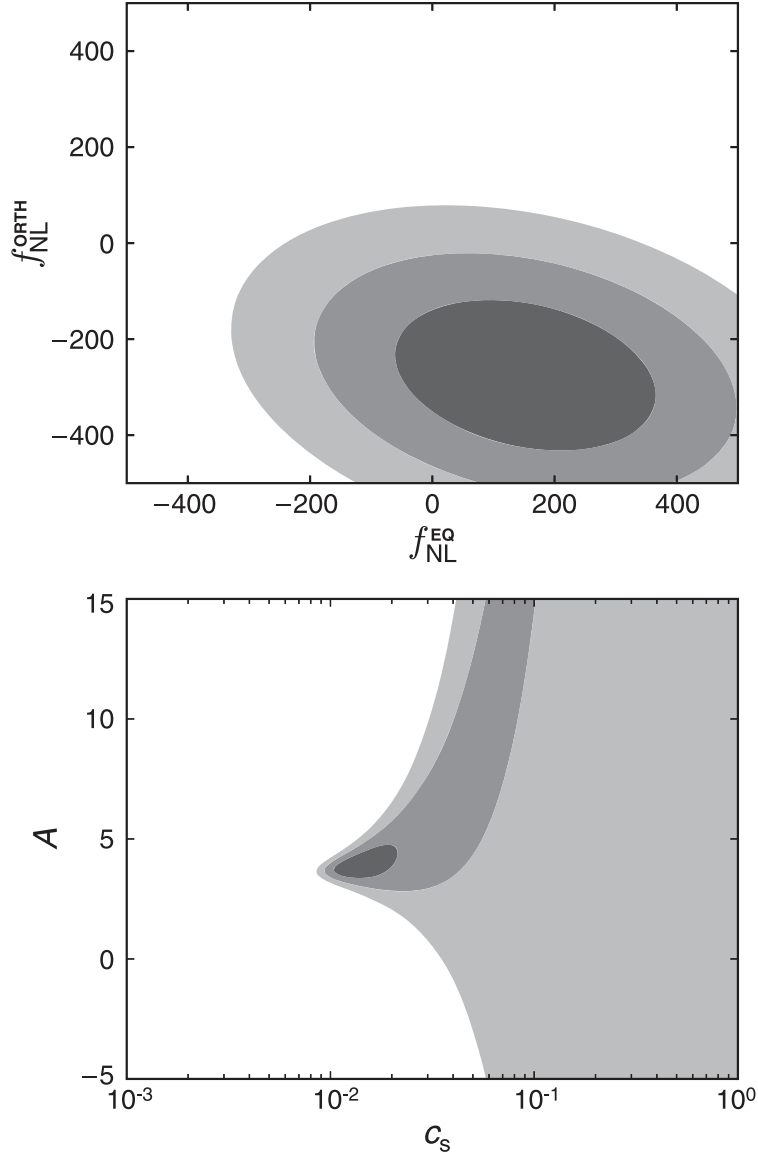


Fig. 42.— WMAP nine-year constraints on non-Gaussianity in single-field inflation. *Upper panel.* 68%, 95%, and 99.7% confidence regions in the $f_{NL}^{eq}, f_{NL}^{orth}$ plane, defined by threshold χ^2 values 2.28, 5.99, 11.62, as appropriate for a χ^2 random variable with two degrees of freedom. $(f_{NL}^{eq}, f_{NL}^{orth}) = (0, 0)$ is consistent with the data to within 99% CL. *Lower panel.* Confidence regions on the dimensionless sound speed c_s and interaction coefficient A (defined in Equation (56)), obtained from the top panel via the change of variables in Equation (57). The upper bound on f_{NL}^{eq} gives a lower bound on c_s , which is consistent with $c_s = 1$.

channels	f_{NL}^{orth}	Discrepancy in “sigmas”								
		VW	V	W	V1	V2	W1	W2	W3	W4
All VW channels	-245.5 ± 99.6	–	2.2σ	1.5σ	1.5σ	2.1σ	0.7σ	1.4σ	1.1σ	2.2σ
All V-band channels	-125.9 ± 112.7	2.2σ	–	2.3σ	0.1σ	0.7σ	0.4σ	0.3σ	0.1σ	1.1σ
All W-band channels	-320.2 ± 112.1	1.5σ	2.3σ	–	2.1σ	2.5σ	1.7σ	2.2σ	2.0σ	3.2σ
V1 only	-119.3 ± 129.1	1.5σ	0.1σ	2.1σ	–	0.3σ	0.5σ	0.3σ	0.1σ	1.0σ
V2 only	-91.3 ± 124.2	2.1σ	0.7σ	2.5σ	0.3σ	–	0.8σ	0.0σ	0.2σ	0.8σ
W1 only	-172.1 ± 140.1	0.7σ	0.4σ	1.7σ	0.5σ	0.8σ	–	0.7σ	0.5σ	1.4σ
W2 only	-88.1 ± 152.2	1.4σ	0.3σ	2.2σ	0.3σ	0.0σ	0.7σ	–	0.2σ	0.7σ
W3 only	-111.0 ± 154.2	1.1σ	0.1σ	2.0σ	0.1σ	0.2σ	0.5σ	0.2σ	–	0.9σ
W4 only	-5.7 ± 147.7	2.2σ	1.1σ	3.2σ	1.0σ	0.8σ	1.4σ	0.7σ	0.9σ	–

Table 16: A test for consistency between channels. The first two columns show f_{NL}^{orth} estimates obtained from different subsets of *WMAP* channels. The matrix on the right shows the level of discrepancy between each pair of channel subsets, in “sigmas” after comparing to an ensemble of Monte Carlo simulations.

8.2. Cosmological parameters

Hinshaw et al. (2012) examine various versions of cosmological models fit to select combinations of cosmological data. These combinations are all rooted in *WMAP* data, which strongly limits possible cosmological models. There is, however, a narrow ridge of geometric degeneracy that applies to CMB measurements. This is seen in Figure 8.2. Assuming a flat geometry breaks the degeneracy and forces a precise value for the Hubble constant. Alternatively, non-CMB cosmological measurements generally also break the CMB degeneracy and also result in a precise value for the Hubble constant. The fact that these Hubble constant values are consistent within their uncertainties is equivalent to concluding that the universe is flat within the measurement errors.

Table 8.2 gives the cosmological values for a six parameter flat Λ CDM model and a list of derived parameters that follow from it. Also tabulated are results from an additional seventh parameter added to the model. For example, if the number of relativistic degrees of freedom is allowed to vary beyond the standard three neutrinos, if tensor modes are allowed, or if the universe is allowed to deviate from a flat geometry. In addition, we summarize select constraints on non- Λ CDM models, such as deviating from a cosmological constant by allowing for a dark energy equation of state parameter $w \neq 1$.

In the last column of Table 8.2 we provide values for the same parameters described above but now arrived at by combining *WMAP* data with data from finer scale CMB measurements from ACT and SPT (extended CMB, or “eCMB”), baryon acoustic oscillation (BAO) data, and data from the direct measurements of the Hubble constant (H_0). If we assume that all of these data sets are well-described by their published uncertainties, then these parameters provide a precise and accurate description of our universe.

In an effort to provide a quantitative estimate of the overall impact of nine years of *WMAP* data on cosmological parameters, we compare the final *WMAP* nine-year likelihood with pre-*WMAP* CMB data. A paper entitled “Last Stand Before *WMAP*” (Wang et al. 2003) provides a likelihood using only CMB data, just prior to *WMAP*’s initial 2003 results. We find that the six parameter cosmological volume determined by *WMAP* data alone is a factor of 68,000 times smaller than the allowed volume before *WMAP*. To compute this factor, we take the cosmological volume to be proportional to the square root of the determinant of the covariance matrix of the parameters. Since the optical depth to last scattering was ill-constrained before *WMAP*, we assign to it a constraint of $\tau < 0.3$. We ensure that the parameter distributions are well-sampled by the *WMAP* nine-year and pre-*WMAP* parameter chains by running over a half million points in all of the relevant chains and verifying convergence, so the chains sample the likelihoods well. We use six parameters in our volume-determining covariance matrix and those same six parameters are sampled in

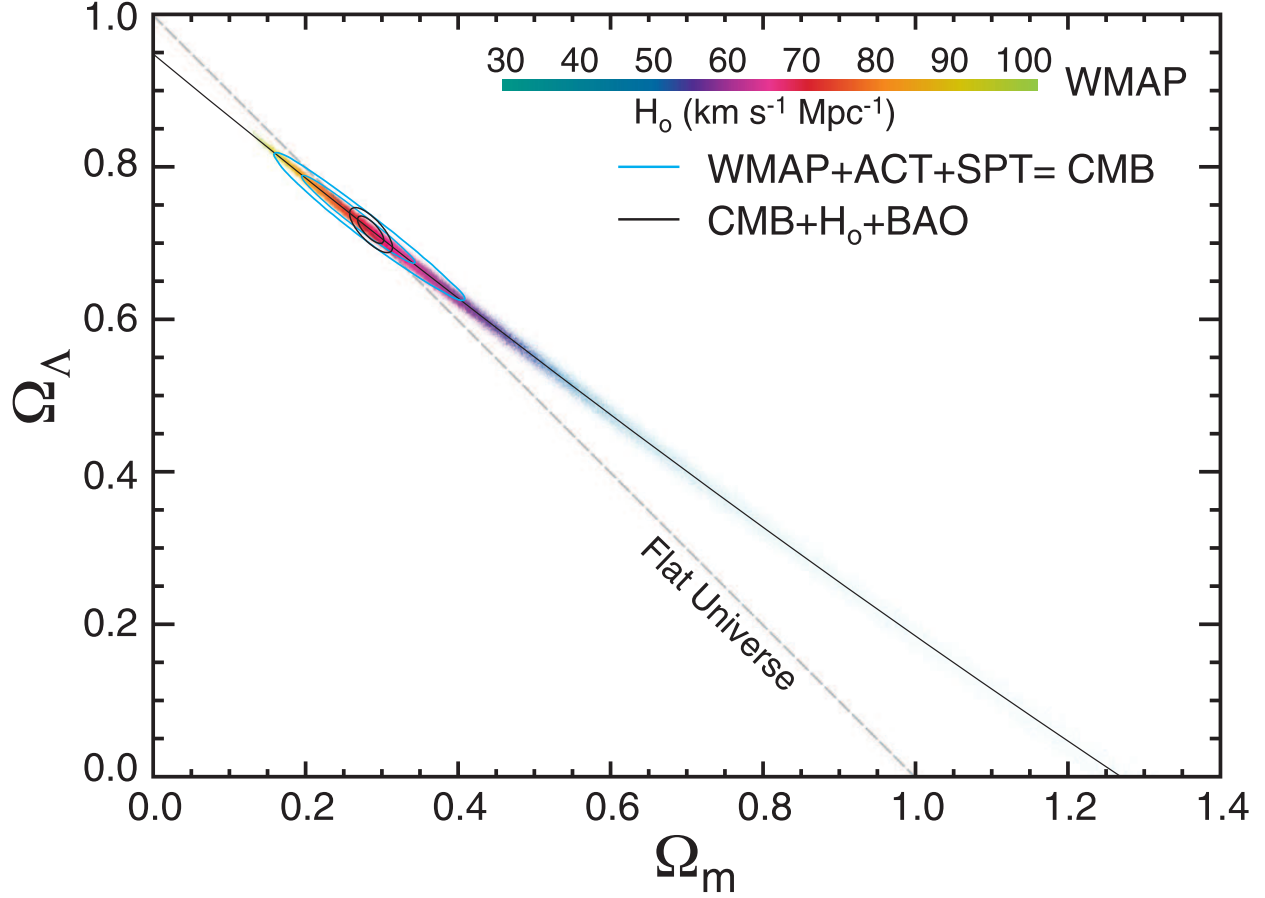


Fig. 43.— Constraints on curvature. Flat universes fall on the $\Omega_m + \Omega_\Lambda = 1$ line. Allowed regions are shown for *WMAP*, CMB, and CMB combined with BAO and H_0 data, all with a hard prior of $H_0 < 100 \text{ km s}^{-1} \text{ Mpc}^{-1}$. *WMAP* data is represented by 290,000 Markov chain points, colored by their value of H_0 . The *WMAP* data follow a geometric degeneracy ridge represented by the slightly curved line, a parabola with equation $\Omega_\Lambda = 0.0620 \Omega_m^2 - 0.825 \Omega_m + 0.947$. The most likely point in the *WMAP*-only chain has $\Omega_\Lambda = 0.721$ and $\Omega_m = 0.279$, which is flat to three significant figures, even though this constraint was not enforced. The *WMAP* data alone require $\Omega_\Lambda > 0.58$ at 68% CL and $\Omega_\Lambda > 0.22$ at 95% CL. The contours show constraints when adding high- l CMB data (blue) and BAO and H_0 data (black). These constraints are consistent with those from *WMAP* alone, with the tightest constraint being $\Omega_{\text{tot}} = 1.0027^{+0.0038}_{-0.0039}$ (Hinshaw et al. 2012).

(A color version of this figure is available in the online journal.)

Markov chains. With flat priors on each, the six parameters are: $\Omega_b h^2$, $\Omega_c h^2$, Ω_Λ , $10^9 \Delta_{\mathcal{R}}^2$, n_s , and τ . (Technically, we also include A_{SZ} in both the pre-*WMAP* and *WMAP* chains and the covariance matrix. A_{SZ} is largely unconstrained by both data sets and is instead constrained by the hard prior of $0 \leq A_{SZ} \leq 2$, so it has negligible effect on the parameter volume and is only included so we can marginalize over it.) Overall, we conclude that 99.9985% of the allowed pre-*WMAP* six-parameter Λ CDM models have been ruled out by *WMAP* data alone. Only 0.0015% remain. In addition to the large improvement in CMB measurement precision, the accuracy improvement arising from the reduction in systematic error afforded by *WMAP* is considerable.

Departing from the simplest Λ CDM model, we consider a Λ CDM model with tensors, by adding the tensor-to-scalar ratio, r . For this seven-parameter model, the reduction of the cosmological volume is a factor of 117,000.

Of course, when *WMAP* data are combined with a rich array of other significant cosmological data the stress-test for Λ CDM has been extraordinary. It is notable that only six parameters are required to achieve a sufficient fit to all cosmological data and that the underlying Λ CDM has not broken. Quite the contrary, a set of precise and accurate parameters now form a standard model of cosmology within the framework of the big bang theory (an expanding and cooling universe) and inflation (an underlying tilted power spectrum of primordial Gaussian-random adiabatic fluctuations).

Table 17. Cosmological Parameter Summary

Parameter	Symbol	WMAP ^a	WMAP+eCMB+BAO+ H_0 ^{a, b}
6-parameter ΛCDM fit parameters^c			
Physical baryon density	$\Omega_b h^2$	0.02264 ± 0.00050	0.02223 ± 0.00033
Physical cold dark matter density	$\Omega_c h^2$	0.1138 ± 0.0045	0.1153 ± 0.0019
Dark energy density ($w = -1$)	Ω_Λ	0.721 ± 0.025	$0.7135^{+0.0095}_{-0.0096}$
Curvature perturbations ($k_0 = 0.002 \text{ Mpc}^{-1}$) ^d	$10^9 \Delta_{\mathcal{R}}^2$	2.41 ± 0.10	2.464 ± 0.072
Scalar spectral index	n_s	0.972 ± 0.013	0.9608 ± 0.0080
Reionization optical depth	τ	0.089 ± 0.014	0.081 ± 0.012
Amplitude of SZ power spectrum template	A_{SZ}	< 2.0 (95% CL)	< 1.0 (95% CL)
6-parameter ΛCDM fit: derived parameters^e			
Age of the universe (Gyr)	t_0	13.74 ± 0.11	13.772 ± 0.059
Hubble parameter, $H_0 = 100h \text{ km/s/Mpc}$	H_0	70.0 ± 2.2	69.32 ± 0.80
Density fluctuations @ $8h^{-1} \text{ Mpc}$	σ_8	0.821 ± 0.023	$0.820^{+0.013}_{-0.014}$
Velocity fluctuations @ $8h^{-1} \text{ Mpc}$	$\sigma_8 \Omega_m^{0.5}$	0.434 ± 0.029	0.439 ± 0.012
Velocity fluctuations @ $8h^{-1} \text{ Mpc}$	$\sigma_8 \Omega_m^{0.6}$	0.382 ± 0.029	0.387 ± 0.012
Baryon density/critical density	Ω_b	0.0463 ± 0.0024	0.04628 ± 0.00093
Cold dark matter density/critical density	Ω_c	0.233 ± 0.023	$0.2402^{+0.0088}_{-0.0087}$
Matter density/critical density ($\Omega_c + \Omega_b$)	Ω_m	0.279 ± 0.025	$0.2865^{+0.0096}_{-0.0095}$
Physical matter density	$\Omega_m h^2$	0.1364 ± 0.0044	0.1376 ± 0.0020
Current baryon density (cm^{-3}) ^f	n_b	$(2.542 \pm 0.056) \times 10^{-7}$	$(2.497 \pm 0.037) \times 10^{-7}$
Current photon density (cm^{-3}) ^g	n_γ	410.72 ± 0.26	410.72 ± 0.26
Baryon/photon ratio	η	$(6.19 \pm 0.14) \times 10^{-10}$	$(6.079 \pm 0.090) \times 10^{-10}$
Redshift of matter-radiation equality	z_{eq}	3265^{+106}_{-105}	3293 ± 47
Angular diameter distance to z_{eq} (Mpc)	$d_A(z_{\text{eq}})$	14194 ± 117	14173^{+66}_{-65}
Horizon scale at z_{eq} (h/Mpc)	k_{eq}	0.00996 ± 0.00032	0.01004 ± 0.00014
Angular horizon scale at z_{eq}	l_{eq}	139.7 ± 3.5	140.7 ± 1.4
Epoch of photon decoupling	z_*	$1090.97^{+0.85}_{-0.86}$	1091.64 ± 0.47
Age at photon decoupling (yr)	t_*	376371^{+4115}_{-4111}	374935^{+1731}_{-1729}
Angular diameter distance to z_* (Mpc) ^h	$d_A(z_*)$	14029 ± 119	14007^{+67}_{-66}
Epoch of baryon decoupling	z_d	1020.7 ± 1.1	1019.92 ± 0.80
Co-moving sound horizon, photons (Mpc)	$r_s(z_*)$	145.8 ± 1.2	145.65 ± 0.58
Co-moving sound horizon, baryons (Mpc)	$r_s(z_d)$	152.3 ± 1.3	152.28 ± 0.69
Acoustic scale, $\theta_* = r_s(z_*)/d_A(z_*)$ (degrees)	θ_*	0.5953 ± 0.0013	0.59578 ± 0.00076
Acoustic scale, $l_* = \pi/\theta_*$	l_*	302.35 ± 0.65	$302.13^{+0.39}_{-0.38}$
Shift parameter	R	1.728 ± 0.016	1.7329 ± 0.0058
Conformal time to recombination	τ_{rec}	283.9 ± 2.4	283.2 ± 1.0
Redshift of reionization	z_{reion}	10.6 ± 1.1	10.1 ± 1.0
Time of reionization (Myr)	t_{reion}	453^{+63}_{-64}	482^{+66}_{-67}
7-parameter ΛCDM fit parametersⁱ			
Relativistic degrees of freedom ^j	N_{eff}	> 1.7 (95% CL)	3.84 ± 0.40
Running scalar spectral index ^k	$dn_s/d \ln k$	-0.019 ± 0.025	-0.023 ± 0.011
Tensor to scalar ratio ($k_0 = 0.002 \text{ Mpc}^{-1}$) ^l	r	< 0.38 (95% CL)	< 0.13 (95% CL)

Table 17—Continued

Parameter	Symbol	WMAP ^a	WMAP+eCMB+BAO+ H_0 ^{a, b}
Tensor spectral index ^l	n_t	> -0.048 (95% CL)	> -0.016 (95% CL)
Curvature $(1 - \Omega_{\text{tot}})^{\text{m}}$	Ω_k	$-0.037^{+0.044}_{-0.042}$	$-0.0027^{+0.0039}_{-0.0038}$
Fractional Helium abundance, by mass	Y_{He}	< 0.42 (95% CL)	0.299 ± 0.027
Massive neutrino density ⁿ	$\Omega_\nu h^2$	< 0.014 (95% CL)	< 0.0047 (95% CL)
Neutrino mass limit (eV) ⁿ	$\sum m_\nu$	< 1.3 (95% CL)	< 0.44 (95% CL)
Limits on parameters beyond ΛCDM			
Dark energy (const.) equation of state ^o	w	$-1.71 < w < -0.34$ (95% CL)	$-1.073^{+0.090}_{-0.089}$
Uncorrelated isocurvature modes	α_0	< 0.15 (95% CL)	< 0.047 (95% CL)
Anticorrelated isocurvature modes	α_{-1}	< 0.012 (95% CL)	< 0.0039 (95% CL)

^aUnless otherwise stated, the values given are the mean of the parameter in the Markov chain, and the 1- σ region determined by removing the lowest and the highest 15.87% probability tails of the Markov chain to leave the central 68% region.

^bThe WMAP+eCMB+BAO+ H_0 data set (Hinshaw et al. 2012) includes the following. The H_0 data consists of a Gaussian prior on the present-day value of the Hubble constant, $H_0 = 73.8 \pm 2.4 \text{ km s}^{-1} \text{ Mpc}^{-1}$ (Riess et al. 2011). The BAO priors...

^cThe 6 parameters in this section are the parameters varied in the chain. A seventh parameter, A_{SZ} , is also varied but is constrained to be between 0 and 2. The WMAP data do not strongly constrain A_{SZ} , which is why the 95% CL interval simply returns the prior. The eCMB data set does constrain the SZ effect, and prefers lower amplitudes of the SZ template. We call this a 6-parameter fit because only 6 parameters are needed to fit the data well; the A_{SZ} parameter is used only to marginalize over the SZ effect and therefore include it in the error bars. All parameters varied in the Markov chains have flat priors, and in this chain only the A_{SZ} parameter requires hard constraints limiting how much it can fluctuate.

^d $k = 0.002 \text{ Mpc}^{-1} \longleftrightarrow l_{\text{eff}} \approx 30.$

^eThese additional parameters are determined by the parameters being varied in the Markov chain. Because these are not the parameters directly being sampled, we are not necessarily assuming flat priors on these parameters.

^fBaryon density is given in units of proton masses per cubic centimeter.

^g $T_{\text{CMB}} = 2.72548 \pm 0.00057 \text{ K}$, from Fixsen (2009). This parameter n_γ is not varied in the Markov chains; the error bar is determined directly from the error in CMB temperature.

^hComoving angular diameter distance.

ⁱThe parameters reported in this section place limits on deviations from the simple 6-parameter Λ CDM model. A complete listing of all parameter values and uncertainties for each of the extended models studied is available on LAMBDA.

^jAllows N_{eff} number of relativistic species, with the prior $0 < N_{\text{eff}} < 10$.

^kAllows running in scalar spectral index but no tensor modes.

^lAllows tensor modes but no running in scalar spectral index. We constrain the tensor to scalar ratio at $k = 0.002 \text{ Mpc}^{-1}$ to be $r > 0$, and the tensor spectral index is related to the tensor to scalar ratio by $n_t = -r/8$.

^mAllows non-zero curvature, $\Omega_k \neq 0$.

ⁿAllows a massive neutrino component, $\Omega_\nu > 0$.

^oAllows $w \neq -1$, but constrains it to be $-2.5 \leq w \leq 0$ and assumes w is constant with redshift and $\Omega_k = 0$.

9. Conclusion

1) We have updated the raw data archive to include the full nine years of *WMAP* data. We have updated the pointing, calibration, and transmission imbalance factor solutions.

2) We have updated our beam maps and window functions based on the full nine years of *WMAP* data. We have made full sky maps of the five-band data in temperature and polarization, and we characterize the noise.

3) In addition to the standard map-making, we have implemented a new beam-symmetrized set of maps designed to reduce the effects of the asymmetric beams. These maps reduce the latitude dependence of the power spectrum and thus we confirm that the power asymmetry was largely due to the asymmetric beams, as expected. This has no effect on the overall power spectrum and cosmological parameters, but is important to the notion of statistical isotropy, which is now more rigorously supported. The beam-symmetrized maps are not used for most cosmological analyses due to the complexity of the resulting noise, but they are used in foreground analysis.

4) We solve for new calibrations of Jupiter and Saturn, and we improve our model that separates the Saturn spheroid and ring components. The final two years of *WMAP* observations include Saturn data with the rings nearly edge-on.

5) We provide new point source catalogs, using previous methods. One is based on filtering all five *WMAP* bands, and the other is based on removing the CMB from the Q-, V-, and W-band maps and then searching for peaks.

6) a) Our analysis of the diffuse foregrounds generally uses the five bands of *WMAP* data in conjunction with other data sets. *WMAP* was designed to observe in the spectral region where the ratio of the CMB to foreground anisotropy is at its maximum while not allowing strong spectral lines to fall within any *WMAP* bandpass. It is clear that the choice of *WMAP* frequencies succeeded in reaching these goals. The five widely spaced *WMAP* bands and especially the low-frequency K-band radiometer have been invaluable in characterizing foregrounds.

b) For most cosmological analyses we apply a Galactic cut and make a small correction for remaining emission using templates, but the ILC method is helpful and effective in separating the full sky CMB from foregrounds. This separation can be done more accurately than the separation of foreground emission components from each other, for which there are degeneracies. We present a new ILC map. For the first time we now also provide an error estimate for this map that includes bias and foreground-CMB covariance.

c) To elucidate the characteristics and nature of the diffuse foreground components, we

implement the Maximum Entropy Method (MEM), Markov Chain Monte Carlo (MCMC) fits, and χ^2 fits. These are implemented with differing assumptions and priors. Each of these methods has strengths and weaknesses, but the combination provides insight. Methods with less reliance on external templates make for noisier fits with greater degeneracy between emission components. Methods with greater reliance on external templates help to reduce noise and break degeneracies, but introduce errors, because the templates are not of the same quality as the *WMAP* data.

d) We decompose the foreground emission into synchrotron, free-free, spinning dust, and thermal dust components. The peak of the spinning dust spectrum lies below the K-band frequency (the lowest frequency *WMAP* radiometer) and is generally a sub-dominant emission component. The theoretically predicted Cold Neutral Medium (CNM) peak is at 17.8 GHz, but we solve for a peak frequency scale factor of ≈ 0.85 that places the fitted peak frequency near 15 GHz. The physical parameters that define the CNM are certainly only approximate, and their variation across the Galaxy is almost certainly responsible for complex spectral shape variations beyond just an amplitude and frequency shift. (Throughout this paper we use the term “spinning dust” without regard to the accuracy of the implied underlying physical model, but simply as the origin of a spectral template form to fit, where we allow both frequency and intensity adjustments. The actual physical emission mechanism(s) of this component may not yet be fully understood.)

e) Free-free emission is generally strong in the *WMAP* bands and the dominant foreground at high latitude in Q- and V-bands, but free-free emission is not as well traced by $H\alpha$ emission maps as one might have hoped or expected. This is true even when the $H\alpha$ emission is corrected for reflection and optical depth effects.

f) We find a systematic Galactic plane discrepancy at the 20% level between the thermal dust template map based on a model fit to *IRAS* and *COBE* data and extrapolated to the *WMAP* bands, compared with our *WMAP* thermal dust fits with an inner plane/outer plane error morphology. At high Galactic latitude the thermal dust template appears to be reasonable. The dust spectral index appears to be ≈ 1.8 (for antenna temperature).

g) We find strong evidence that the synchrotron emission spectral index varies across the sky and is generally flatter in the plane and steepens with Galactic latitude. In addition, the synchrotron spectral index appears to steepen with frequency. Within the *WMAP* bands the spectra of free-free, synchrotron, and spinning dust (which generally peaks at about 15 GHz and steepens at K- and Ka-bands) are far from orthogonal. Yet, there is no spinning dust emission in the Haslam 408 MHz map, so that radio map is helpful for removing degeneracies. The foreground contributions at K-band are roughly 50% synchrotron, 35% free-free, and 15% for a spinning dust like component. Free-free emission dominates in Q- and V-bands,

and thermal dust emission dominates in W-band.

h) The original claim of discovery of a “haze” of free-free emitting gas with diminished $H\alpha$ (Finkbeiner 2004) has been ruled out. Evidence of a distinct synchrotron haze feature depends on model choices in fitting, and no *WMAP* model requires a haze component to provide a good fit to the data. *WMAP* MCMCg and Model 9 foreground fits show a general hardening (flattening) of the synchrotron spectral index from the Galactic poles to the plane, without a distinct haze feature. K-band fit residuals in the haze region are $\lesssim 10\%$ of the brightness identified by the Planck Collaboration IX (2012) as a $\beta_s \sim -2.55$ synchrotron haze. However, a real haze could have been inappropriately absorbed into other components of the *WMAP* decomposition, which has degeneracies. Likewise, the Planck haze could result from modeling assumptions, which are different from the assumptions of each of the three *WMAP* models. Based on currently available data, we conclude that the existence of a distinct localized haze depends on the fitting and analysis methods used. Additional data, particularly at frequencies below K-band, would help constrain model degeneracies.

i) We define a Galactic cut for fitting and removing template-traced emission for the high latitude sky and then a small additional cut for safety. The remaining high latitude sky is used for power spectrum calculation and parameter determination. This portion of the template-corrected sky is strongly dominated by CMB anisotropy.

7) We implemented a new unbiased and optimal estimation of the TT power spectrum that uses C^{-1} weighting, as opposed to the unbiased MASTER quadratic estimator. We also present the TE, EE, TB, and BB power spectra. A six parameter flat Λ CDM model is fit to these power spectra.

8) We examined the goodness-of-fit of the Λ CDM model to the power spectrum data. The χ^2 of the high- l TT power spectrum is dominated by an even- l versus odd- l effect, as seen in the seven year analysis. This is notable since the seven-year power spectrum was determined by MASTER and the nine-year by C^{-1} . Therefore the even-odd effect cannot be an artifact of the computation method. We continue to believe that the effect is not significant as we have made posterior choices to select and examine the effect (such as a particular range of multipole moments) and there exists no known theory to produce it, especially since even sharp features in k -space do not remain sharp in l -space.

9) The quadrupole amplitude is below of the median expectation of the best fit power spectrum by $< 2\sigma$, so it is not anomalously low. No new theory could be significantly preferred (i.e., by more than 2σ) based on the quadrupole value alone. The quadrupole-octupole alignment remains approximately the same in the nine-year as seven-year data, but a new estimate of the uncertainties based on the underlying ILC map indicates that we can-

not reliably remove foregrounds to the level needed to demonstrate a significant alignment. Having addressed the quadrupole value, the quadrupole-octupole alignment, and the general goodness-of-fit, we find no convincing evidence of CMB anomalies beyond the normal statistical ranges that should be anticipated to occur in a rich dataset.

10) An analysis of the CMB maps find no compelling evidence for deviations from Gaussianity. We find $f_{\text{NL}}^{\text{loc}} = 37.2 \pm 19.9$, with $-3 < f_{\text{NL}}^{\text{loc}} < 77$ at 95% CL. We also find $f_{\text{NL}}^{\text{eq}} = 51 \pm 136$, with $-221 < f_{\text{NL}}^{\text{eq}} < 323$ at 95% CL, and $f_{\text{NL}}^{\text{orth}} = -245 \pm 100$, with $-445 < f_{\text{NL}}^{\text{orth}} < -45$ at 95% CL. We do not find any of these quantities differ significantly from zero. It should be noted that three quantities are computed, increasing the chance of an otherwise less likely outcome.

11) Cosmological models are fit to the power spectrum (Hinshaw et al. 2012). A six parameter flat Λ CDM model continues to fit all of the *WMAP* data well. These parameters also appear to be consistent with a wide range of other cosmological data as well. The six parameter cosmological volume determined by *WMAP* data alone is a factor of 68,000 times smaller than the CMB constraints before *WMAP* as assessed by the “Last Stand Before *WMAP*” paper of Wang et al. (2003). (Since the optical depth to scattering was not constrained at all in that assessment, we assigned to it a constraint of $\tau < 0.3$ in carrying out the volume calculation.) Adding a seventh parameter suggests a reduction of the cosmological volume by even more, a factor of 117,000.

12) When *WMAP* data are combined with a rich array of other significant cosmological data the stress-test for Λ CDM is extraordinary. It is notable that only six parameters are required to achieve a sufficient fit to all cosmological data and that the underlying Λ CDM has not broken. Quite the contrary, a set of precise and accurate parameters now form a standard model of cosmology within the framework of the big bang theory (an expanding and cooling universe) and inflation (an underlying tilted power spectrum of primordial Gaussian-random adiabatic fluctuations). General relativity combined with the Friedmann-Lemaître-Robertson-Walker metric leads to the Friedmann equation, which provides the background cosmology. Inflation can provide the initial conditions, including the generation of primordial perturbations via fluctuations of the inflaton and gravitational fields. Inflation predicts that the universe is nearly flat. We find $\Omega_k = -0.0031_{-0.0039}^{+0.0038}$ and $|\Omega_k| < 0.0094$ at 95% confidence, within 0.95% of flat/Euclidean. If restricted to $\Omega_k > 0$ (a negative curvature open universe) as suggested by the creation of our universe from the landscape, then $\Omega_k < 0.0062$ at 95% CL. A small deviation from flatness is expected and is worthy of future searches. Inflation is also strongly supported by the observed features that the fluctuations are adiabatic, with Gaussian random phases. The detection of a deviation of the scalar spectral index from unity reported earlier by *WMAP* now has high statistical significance ($n_s = 0.9608 \pm 0.0080$). The

CMB has been central to posing the horizon, flatness, and structure problems for which inflation and general relativity provide solutions.

13) Within the horizon, acoustic waves modify the primordial perturbations in a manner that depends on the values of the cosmological parameters. The sub-horizon CMB measurements drive the determination of the cosmological parameters and the degeneracies are broken with the addition of other cosmological observations, such as measurements of the Hubble constant and the baryon acoustic oscillations as a function of redshift determined from large galaxy surveys. Using this fact, we find that Big Bang nucleosynthesis is well supported and there is no compelling evidence for a non-standard number of neutrino species ($N_{\text{eff}} = 3.84 \pm 0.40$).

14) The requirement for both cold dark matter, which gravitates but does not interact with photons, and a substantial mass-energy component consistent with a cosmological constant, which causes an accelerated expansion of the universe as characterized by Type Ia supernovae measurements, is unavoidable because of the precision of the available data and the multiple methods of measurement. The CMB fluctuations require dark matter and dark energy. The inability to predict a value for vacuum energy was a pre-existing physics problem, but particle physics has no problem positing massive particles that do not interact with photons as candidates for the CDM. If the massive particles do not decay or annihilate, their identity makes little difference to cosmology. It may well turn out that the dominant mass-energy component of our universe is a cosmological constant arising from vacuum energy, and that the vacuum energy is fundamentally not a specifically predictable quantity. It will be exciting to see how current theories develop, and especially fascinating how well these theories can be tested with data. The CMB is a unique remnant of the early universe which has been our primary cosmological observable. It continues to be imperative to learn all that we can from it.

The *WMAP* mission was made possible by the support of NASA. We are grateful to Marian Pospieszalski of the National Radio Astronomy Observatory (NRAO) for his design of the microwave amplifiers that enabled the mission, and to NRAO for the development of the flight amplifiers. We also thank the project managers, Rich Day and Liz Citrin, and system engineers, Mike Bay, and Cliff Jackson, who were both expert and effective in leading the mission to launch, on-schedule and on-budget. It was a special pleasure for the science team to work closely with Cliff Jackson from the earliest times of the proposal development through to the post-launch activities. NASA has never had a finer engineer and we wish him well in his retirement. We also recognize the extraordinary efforts of the engineers, technicians, machinists, data analysts, budget analysts, managers, administrative staff, and reviewers who were all key parts of the team that created the *WMAP* spacecraft.

C.L.B. was supported, in part, by the Johns Hopkins University. K.M.S. was supported at the Perimeter Institute by the Government of Canada through Industry Canada and by the Province of Ontario through the Ministry of Research & Innovation. E.K. was supported in part by NASA grants NNX08AL43G and NNX11AD25G and NSF grants AST-0807649 and PHY-0758153. We acknowledge use of the HEALPix (Gorski et al. 2005), CAMB (Lewis et al. 2000), and CMBFAST (Seljak & Zaldarriaga 1996) packages. Some computations were performed on the GPC supercomputer at the SciNet HPC Consortium. We thank SciNet, which is funded by the Canada Foundation for Innovation under the auspices of Compute Canada, the Government of Ontario, Ontario Research Fund – Research Excellence, and the University of Toronto. We acknowledge the use of the Legacy Archive for Microwave Background Data Analysis (LAMBDA). Support for LAMBDA is provided by NASA Headquarters.

A. Band Center Frequencies

Figure 44 shows small year-to-year variations of Galactic plane brightness measured from yearly maps in K-, Ka-, Q-, and V-bands. Each yearly map was correlated against the nine-year map for pixels at $|b| < 10^\circ$. A linear slope and offset was fit to each correlation, and the slope values are shown in Figure 44. Results for W-band are not shown because the scatter in the yearly slopes is large and no significant variation was detected. Analysis of DA maps has shown that the measured variation is consistent in Q1 and Q2, and in V1 and V2.

The K–Q band brightness variations were previously presented for the seven-year data in Jarosik et al. (2011), where they were described as variations in the *WMAP* calibration. Further analysis has shown that the CMB signal in yearly maps does not show such variation. Yearly variations of the CMB dipole amplitude in year 1-7 maps are less than $\pm 0.025\%$ for many DAs. We have also found that the Galactic plane brightness variations depend on spectral index, with greater variation for regions of steeper spectral index, so we conclude that they are caused by variations in the effective center frequencies of the *WMAP* bandpasses over the mission. As the observatory’s thermal control surfaces age, a gradual warming of the *WMAP* instrument’s physical temperature occurs (Greason et al. 2012). Given the instrument amplifier fixed voltage bias scheme, an increase in temperature (or device aging) can induce corresponding changes in the drain current and gain, and an associated perturbation in the effective bandpass.

We determine the fractional variation in center frequency for each band as follows. Assuming the sky signal in a given pixel p can be characterized by a power law spectrum

with thermodynamic temperature spectral index β_p , the measured sky brightness for a given year i is

$$T_i(p) = T_0(p) \left(\frac{\nu_i}{\nu_0} \right)^{\beta_p}, \quad (\text{A1})$$

where $T_0(p)$ is the sky brightness at a fiducial frequency ν_0 and ν_i is the effective frequency for year i . We assume $T_0(p)$ is constant in time. For small frequency drifts, $\Delta\nu_i/\nu_0 \equiv (\nu_i - \nu_0)/\nu_0 \ll 1$, it is useful to work with the linearized form,

$$T_i(p) = T_0(p) [1 + \beta_p(\Delta\nu_i/\nu_0)]. \quad (\text{A2})$$

If we choose $\nu_0 \equiv \langle \nu_i \rangle$, where the mean is over years i , then $T_0(p) = \langle T_i(p) \rangle$ and the fractional variation in frequency is

$$\frac{\Delta\nu_i}{\langle \nu_i \rangle} = \left(\frac{T_i(p)}{\langle T_i(p) \rangle} - 1 \right) / \beta_p \quad (\text{A3})$$

For each band and each year, we calculate the pixel averaged $T_i/\langle T_i \rangle$ for Galactic plane pixels in selected spectral index ranges as the $T_i(p)$ vs $\langle T_i(p) \rangle$ correlation slope. Spectral index was calculated using the neighboring *WMAP* band or bands, e.g., $\beta(\text{K-Ka})$ was used for K-band and the mean of $\beta(\text{K-Ka})$ and $\beta(\text{Ka-Q})$ was used for Ka-band. Each spectral index bin for a given band gives a result for the variation of $\Delta\nu_i/\langle \nu_i \rangle$ over the mission. These results were found to be consistent with each other, and an average (excluding bins with high scatter) was adopted for the variations shown for each band in Figure 44.

No correction for bandpass drift is applied in our map-making. Since the *WMAP* observations are made simultaneously in the different bands, the map-making always forms band maps that have a common epoch, and each band map can be treated as having a single effective band center frequency valid for that epoch. Our previously published band center frequencies (see Table 4 of Jarosik et al. (2011) for point sources and Table 11 of Jarosik et al. (2003a) for diffuse emission) are based on pre-flight measurements, so presumably are valid for year 1 of the flight data. For nine-year data, a correction based on Figure 44 should be applied. The correction is a reduction of the pre-flight center frequency by 0.13, 0.12, 0.11, and 0.06% for K-, Ka-, Q-, and V-band, respectively. This correction is included in the center frequencies for point sources listed in Table 3.

B. *WMAP* Nine-Year Five-band Point Source Catalog

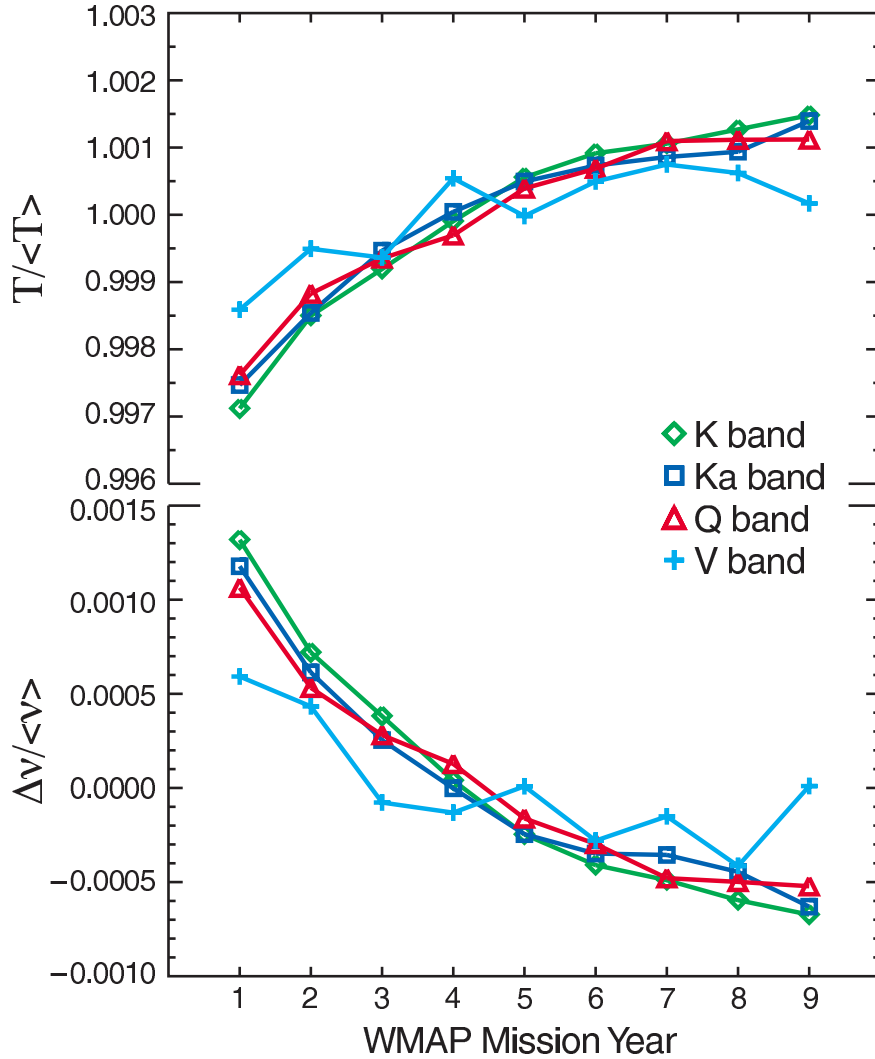


Fig. 44.— Top - Measurements of the year-to-year fractional brightness variation of the Galactic plane in *WMAP* skymaps, obtained by correlating Galactic plane signal in each single year map with Galactic plane signal in the nine-year map. There is a small dependence of these variations on spectral index, which shows that they are caused by variations in effective *WMAP* band center frequencies over the mission. Bottom - The year-to-year fractional variation of *WMAP* band center frequency derived from Galactic plane brightness variations measured for selected spectral index bins.

(A color version of this figure is available in the online journal.)

Table 18. *WMAP* Nine-Year Five-band Point Source Catalog

RA [hms]	Dec [dm]	ID	K [Jy]	Ka [Jy]	Q [Jy]	V [Jy]	W [Jy]	α	5 GHz ID
00 04 08	−47 43		0.6 ± 0.02	0.7 ± 0.04	0.5 ± 0.05	0.5 ± 0.08	...	-0.1 ± 0.3	PMN J0004-4736
00 06 06	−06 23	060	2.2 ± 0.04	1.6 ± 0.05	1.8 ± 0.07	1.9 ± 0.1	1.3 ± 0.2	-0.3 ± 0.1	PMN J0006-0623
00 10 33	11 01		0.8 ± 0.03	1.0 ± 0.05	1.2 ± 0.06	1.6 ± 0.1	1.1 ± 0.2	0.5 ± 0.2	GB6 J0010+1058
00 12 46	−39 53	202	1.3 ± 0.03	1.1 ± 0.04	1.1 ± 0.05	0.9 ± 0.09	...	-0.3 ± 0.2	PMN J0013-3954
00 25 24	−26 03		0.9 ± 0.03	0.8 ± 0.05	0.6 ± 0.06	-0.4 ± 0.3	PMN J0025-2602 ^a
00 26 06	−35 10		0.7 ± 0.03	0.9 ± 0.05	0.9 ± 0.05	0.8 ± 0.09	0.9 ± 0.2	0.2 ± 0.2	PMN J0026-3512
00 29 33	05 54		1.1 ± 0.03	1.2 ± 0.05	1.2 ± 0.06	0.9 ± 0.1	1.4 ± 0.2	0.1 ± 0.2	GB6 J0029+0554B ^a
00 38 15	−25 01		0.8 ± 0.03	0.8 ± 0.05	0.7 ± 0.06	0.8 ± 0.1	...	-0.1 ± 0.2	PMN J0038-2459
00 38 33	−02 08		0.7 ± 0.03	0.2 ± 0.05	0.7 ± 0.06	-0.2 ± 0.4	PMN J0038-0207
00 43 12	52 09		1.4 ± 0.03	0.7 ± 0.04	0.8 ± 0.05	0.5 ± 0.09	...	-1.2 ± 0.2	GB6 J0043+5203
00 46 14	−84 18		0.8 ± 0.03	1.0 ± 0.04	0.8 ± 0.05	0.7 ± 0.08	0.7 ± 0.1	-0.0 ± 0.2	PMN J0044-8422 ^a
00 47 21	−25 14	062	1.1 ± 0.03	1.0 ± 0.05	1.2 ± 0.05	0.9 ± 0.1	1.3 ± 0.2	0.0 ± 0.1	PMN J0047-2517
00 48 05	−73 12		1.9 ± 0.05	1.4 ± 0.08	1.3 ± 0.1	-0.6 ± 0.3	PMN J0047-7308
00 49 07	72 27		1.9 ± 0.03	1.6 ± 0.04	1.3 ± 0.05	0.9 ± 0.08	1.3 ± 0.2	-0.5 ± 0.1	...
00 49 13	−42 19		...	1.3 ± 0.05	0.6 ± 0.06	-3.1 ± 1	...
00 49 47	−57 39	179	1.5 ± 0.03	1.5 ± 0.04	1.4 ± 0.05	1.5 ± 0.08	1.2 ± 0.1	-0.0 ± 0.1	PMN J0050-5738
00 50 50	−06 49		1.4 ± 0.03	1.3 ± 0.05	1.1 ± 0.06	1.4 ± 0.1	1.0 ± 0.2	-0.1 ± 0.1	PMN J0051-0650
00 50 55	−42 23		1.3 ± 0.03	1.5 ± 0.04	1.3 ± 0.05	0.9 ± 0.08	1.0 ± 0.2	-0.0 ± 0.1	PMN J0051-4226
00 50 57	−09 27	077	1.0 ± 0.03	1.0 ± 0.05	1.3 ± 0.06	1.1 ± 0.1	1.1 ± 0.2	0.2 ± 0.2	PMN J0050-0928
00 57 40	−01 27		1.0 ± 0.03	1.0 ± 0.05	1.0 ± 0.06	0.9 ± 0.1	0.6 ± 0.2	-0.1 ± 0.2	PMN J0057-0123
00 57 50	30 20		0.6 ± 0.04	0.7 ± 0.05	0.4 ± 0.06	0.8 ± 0.1	...	0.1 ± 0.3	GB6 J0057+3021
00 58 01	54 49		...	1.4 ± 0.05	0.8 ± 0.06	0.3 ± 0.08	...	-2.6 ± 0.6	...
00 59 41	−56 56		0.8 ± 0.03	0.9 ± 0.04	1.0 ± 0.04	0.8 ± 0.08	0.6 ± 0.1	0.2 ± 0.2	PMN J0058-5659
01 00 27	−72 11		3.6 ± 0.04	2.6 ± 0.06	2.0 ± 0.05	1.3 ± 0.08	0.8 ± 0.2	-1.0 ± 0.08	PMN J0059-7210
01 06 43	−40 34	171	2.6 ± 0.03	2.6 ± 0.05	2.4 ± 0.06	2.1 ± 0.1	1.6 ± 0.1	-0.2 ± 0.07	PMN J0106-4034
01 08 27	13 19	079	1.6 ± 0.03	1.2 ± 0.05	0.7 ± 0.06	0.7 ± 0.1	...	-0.9 ± 0.2	GB6 J0108+1319
01 08 45	01 35	081	2.0 ± 0.04	2.1 ± 0.06	1.9 ± 0.06	1.4 ± 0.1	1.1 ± 0.2	-0.2 ± 0.1	GB6 J0108+0135 ^a
01 16 18	−11 36		1.0 ± 0.03	0.8 ± 0.05	0.9 ± 0.06	1.3 ± 0.1	0.8 ± 0.2	0.0 ± 0.2	PMN J0116-1136
01 19 02	−73 26		1.5 ± 0.05	1.0 ± 0.05	0.6 ± 0.05	0.6 ± 0.09	0.9 ± 0.2	-0.9 ± 0.2	...
01 21 44	11 51		1.9 ± 0.04	1.4 ± 0.05	1.4 ± 0.06	0.6 ± 0.1	1.2 ± 0.2	-0.5 ± 0.1	GB6 J0121+1149
01 22 12	04 22		1.0 ± 0.04	0.9 ± 0.05	1.0 ± 0.06	0.8 ± 0.1	1.4 ± 0.2	0.0 ± 0.2	GB6 J0121+0422
01 25 21	−00 10	086	1.0 ± 0.03	1.2 ± 0.05	1.3 ± 0.06	0.9 ± 0.1	...	0.3 ± 0.2	PMN J0125-0005 ^a
01 25 22	−52 52		0.5 ± 0.04	0.5 ± 0.05	0.4 ± 0.04	0.4 ± 0.08	1.2 ± 0.1	0.4 ± 0.2	...
01 32 41	−16 53	097	1.9 ± 0.04	2.1 ± 0.05	1.8 ± 0.06	1.8 ± 0.1	2.3 ± 0.2	0.0 ± 0.09	PMN J0132-1654
01 33 04	−52 01	168	0.7 ± 0.03	1.0 ± 0.04	0.8 ± 0.04	0.3 ± 0.08	0.4 ± 0.1	0.1 ± 0.2	PMN J0133-5159
01 33 28	−36 27		0.6 ± 0.02	0.4 ± 0.04	0.3 ± 0.05	-1.0 ± 0.5	PMN J0134-3629 ^a
01 34 20	−38 44		0.3 ± 0.02	0.4 ± 0.04	0.4 ± 0.05	0.5 ± 0.08	...	0.4 ± 0.3	PMN J0134-3843
01 37 01	47 52	080	4.1 ± 0.04	4.1 ± 0.06	3.9 ± 0.07	3.6 ± 0.1	1.8 ± 0.2	-0.1 ± 0.05	GB6 J0136+4751
01 37 22	33 15		0.9 ± 0.04	0.4 ± 0.06	0.3 ± 0.07	-1.9 ± 0.6	GB6 J0137+3309
01 37 38	−24 29		1.2 ± 0.03	1.4 ± 0.05	1.3 ± 0.05	1.4 ± 0.09	...	0.1 ± 0.1	PMN J0137-2430
01 52 30	22 10		0.8 ± 0.04	0.8 ± 0.06	1.0 ± 0.06	1.2 ± 0.1	...	0.4 ± 0.2	GB6 J0152+2206
01 57 44	−46 01		0.7 ± 0.03	0.9 ± 0.04	1.1 ± 0.04	0.8 ± 0.09	...	0.6 ± 0.2	PMN J0157-4600
02 04 46	15 14	092	1.2 ± 0.04	1.2 ± 0.06	1.3 ± 0.06	1.2 ± 0.1	1.0 ± 0.2	-0.0 ± 0.2	GB6 J0204+1514
02 05 01	32 12	085	2.1 ± 0.04	1.8 ± 0.06	1.7 ± 0.07	1.2 ± 0.1	...	-0.5 ± 0.1	GB6 J0205+3212
02 05 21	−17 05		0.5 ± 0.03	0.2 ± 0.05	0.7 ± 0.05	0.7 ± 0.1	0.8 ± 0.2	0.5 ± 0.3	PMN J0204-1701

Table 18—Continued

RA [hms]	Dec [dm]	ID	K [Jy]	Ka [Jy]	Q [Jy]	V [Jy]	W [Jy]	α	5 GHz ID
02 10 52	−51 00	158	2.7 ± 0.03	2.5 ± 0.05	2.6 ± 0.05	2.5 ± 0.1	1.9 ± 0.1	−0.1 ± 0.06	PMN J0210-5101
02 12 01	−61 43		0.6 ± 0.03	0.5 ± 0.05	0.6 ± 0.05	0.3 ± 0.08	0.8 ± 0.1	0.0 ± 0.2	...
02 18 09	01 40	096	1.9 ± 0.04	1.8 ± 0.05	1.5 ± 0.06	1.1 ± 0.1	...	−0.3 ± 0.1	GB6 J0217+0144
02 20 48	35 57		1.4 ± 0.03	1.4 ± 0.05	1.4 ± 0.07	1.2 ± 0.1	1.8 ± 0.2	−0.0 ± 0.1	GB6 J0221+3556
02 22 49	−34 39	137	1.1 ± 0.02	1.2 ± 0.03	0.8 ± 0.04	0.6 ± 0.08	...	−0.2 ± 0.1	PMN J0222-3441
02 23 13	43 03	084	2.0 ± 0.04	1.3 ± 0.05	1.3 ± 0.06	1.3 ± 0.1	1.1 ± 0.2	−0.6 ± 0.1	GB6 J0223+4259 ^a
02 31 13	−47 44		0.8 ± 0.03	0.8 ± 0.04	1.0 ± 0.04	1.3 ± 0.08	2.0 ± 0.2	0.5 ± 0.1	PMN J0231-4746
02 31 39	13 20		1.3 ± 0.04	1.6 ± 0.06	1.3 ± 0.06	1.2 ± 0.1	...	0.1 ± 0.2	GB6 J0231+1323
02 37 58	28 48	093	3.6 ± 0.04	3.3 ± 0.07	3.1 ± 0.09	2.3 ± 0.1	...	−0.4 ± 0.08	GB6 J0237+2848
02 38 47	16 36		1.5 ± 0.04	1.7 ± 0.07	1.7 ± 0.06	2.1 ± 0.1	1.7 ± 0.2	0.2 ± 0.1	GB6 J0238+1637
02 40 02	−23 09		0.6 ± 0.03	0.2 ± 0.04	0.2 ± 0.05	0.4 ± 0.09	...	−0.8 ± 0.4	PMN J0240-2309
02 41 18	−08 21		1.0 ± 0.03	0.8 ± 0.05	0.6 ± 0.06	−0.6 ± 0.3	PMN J0241-0815
02 45 09	−44 56		0.4 ± 0.03	0.5 ± 0.04	0.7 ± 0.04	0.5 ± 0.08	1.0 ± 0.2	0.6 ± 0.2	PMN J0245-4459
02 53 32	−54 41	155	2.5 ± 0.03	2.7 ± 0.05	2.5 ± 0.05	2.2 ± 0.1	1.7 ± 0.1	−0.1 ± 0.07	PMN J0253-5441
02 59 31	−00 18		1.2 ± 0.04	1.4 ± 0.05	1.4 ± 0.06	1.3 ± 0.1	...	0.2 ± 0.2	PMN J0259-0020
03 03 39	−62 12	162	1.6 ± 0.03	1.7 ± 0.05	1.6 ± 0.05	1.6 ± 0.08	1.7 ± 0.1	0.0 ± 0.09	PMN J0303-6211
03 03 47	47 17		0.7 ± 0.03	0.9 ± 0.05	0.8 ± 0.06	0.6 ± 0.1	...	0.1 ± 0.2	GB6 J0303+4716
03 08 31	04 05	102	1.5 ± 0.04	1.4 ± 0.06	1.4 ± 0.06	1.3 ± 0.1	1.4 ± 0.2	−0.1 ± 0.1	GB6 J0308+0406
03 09 21	10 27		1.0 ± 0.04	1.5 ± 0.06	1.4 ± 0.06	1.4 ± 0.1	...	0.4 ± 0.2	GB6 J0309+1029
03 09 59	−61 02	160	1.2 ± 0.03	1.4 ± 0.04	1.0 ± 0.04	0.9 ± 0.08	...	−0.2 ± 0.1	PMN J0309-6058
03 12 12	−76 47	174	1.2 ± 0.03	1.4 ± 0.04	1.4 ± 0.04	1.6 ± 0.08	1.1 ± 0.1	0.2 ± 0.1	PMN J0311-7651
03 12 55	01 33		0.7 ± 0.04	0.5 ± 0.06	0.6 ± 0.06	0.8 ± 0.1	0.9 ± 0.2	0.0 ± 0.3	GB6 J0312+0132
03 19 46	41 31	094	13.5 ± 0.04	10.9 ± 0.06	9.5 ± 0.07	7.6 ± 0.1	5.6 ± 0.2	−0.6 ± 0.02	GB6 J0319+4130
03 22 19	−37 11	138	18.6 ± 3.4	12.9 ± 1.6	10.8 ± 1.8	8.5 ± 2.3	...	−0.8 ± 0.3	1Jy 0320-37 ^b
03 25 27	22 24		0.5 ± 0.04	0.6 ± 0.06	0.8 ± 0.07	0.7 ± 0.1	...	0.5 ± 0.3	GB6 J0325+2223 ^a
03 29 48	−23 54	123	1.3 ± 0.03	1.3 ± 0.04	1.3 ± 0.05	1.5 ± 0.08	0.7 ± 0.1	−0.0 ± 0.1	PMN J0329-2357
03 34 15	−40 07	146	1.7 ± 0.03	1.7 ± 0.04	1.8 ± 0.05	1.9 ± 0.08	1.3 ± 0.1	0.1 ± 0.09	PMN J0334-4008
03 36 55	−12 56		1.2 ± 0.03	1.1 ± 0.05	1.0 ± 0.05	1.3 ± 0.1	...	−0.0 ± 0.2	PMN J0336-1302
03 37 19	−36 12		0.4 ± 0.03	0.9 ± 0.04	0.6 ± 0.04	0.6 ± 0.08	...	0.6 ± 0.3	PMN J0336-3615
03 39 24	−01 43	106	2.5 ± 0.05	2.4 ± 0.06	2.2 ± 0.07	1.9 ± 0.1	2.3 ± 0.2	−0.2 ± 0.09	PMN J0339-0146
03 40 26	−21 20		1.1 ± 0.03	1.3 ± 0.04	1.0 ± 0.05	1.2 ± 0.09	1.0 ± 0.2	0.0 ± 0.1	PMN J0340-2119
03 48 25	−16 04		0.6 ± 0.03	0.4 ± 0.05	0.7 ± 0.06	0.7 ± 0.09	...	0.2 ± 0.3	PMN J0348-1610
03 48 55	−27 47	129	1.5 ± 0.03	1.2 ± 0.04	1.1 ± 0.04	1.1 ± 0.07	0.8 ± 0.1	−0.4 ± 0.1	PMN J0348-2749
03 50 06	−26 12		0.9 ± 0.05	1.1 ± 0.04	1.0 ± 0.04	1.2 ± 0.08	0.8 ± 0.1	0.1 ± 0.2	...
03 58 49	10 26		0.7 ± 0.04	0.4 ± 0.06	...	0.6 ± 0.1	...	−0.5 ± 0.5	GB6 J0358+1026
04 03 01	25 56		1.2 ± 0.03	1.1 ± 0.05	0.8 ± 0.06	0.6 ± 0.1	...	−0.6 ± 0.2	GB6 J0403+2600
04 03 59	−36 05	136	2.8 ± 0.03	3.1 ± 0.05	3.2 ± 0.05	2.9 ± 0.09	2.3 ± 0.1	0.1 ± 0.06	PMN J0403-3605
04 05 38	−13 04	114	2.1 ± 0.04	1.8 ± 0.05	1.5 ± 0.05	1.2 ± 0.1	0.8 ± 0.2	−0.6 ± 0.1	PMN J0405-1308
04 06 41	−12 43		2.0 ± 0.04	0.6 ± 0.07	0.5 ± 0.06	0.5 ± 0.1	1.0 ± 0.2	−1.2 ± 0.2	...
04 07 07	−38 25	141	1.2 ± 0.03	1.0 ± 0.05	1.1 ± 0.04	1.0 ± 0.08	...	−0.2 ± 0.1	PMN J0406-3826
04 08 32	−75 06		0.9 ± 0.03	0.6 ± 0.04	0.4 ± 0.04	−1.3 ± 0.3	PMN J0408-7507
04 11 07	76 54	082	0.9 ± 0.03	0.8 ± 0.04	0.7 ± 0.05	0.6 ± 0.08	...	−0.5 ± 0.2	1Jy 0403+76
04 16 35	−20 51		1.2 ± 0.03	1.4 ± 0.05	1.2 ± 0.05	1.1 ± 0.09	...	0.0 ± 0.1	PMN J0416-2056
04 23 17	−01 20	110	7.7 ± 0.04	7.9 ± 0.07	7.6 ± 0.08	6.8 ± 0.1	5.8 ± 0.2	−0.1 ± 0.03	PMN J0423-0120
04 23 35	02 17		1.3 ± 0.03	1.4 ± 0.05	1.0 ± 0.07	1.0 ± 0.1	...	−0.2 ± 0.2	GB6 J0422+0219
04 24 50	00 35	109	0.9 ± 0.04	1.2 ± 0.05	1.4 ± 0.07	1.6 ± 0.1	1.2 ± 0.2	0.6 ± 0.2	GB6 J0424+0036

Table 18—Continued

RA [hms]	Dec [dm]	ID	K [Jy]	Ka [Jy]	Q [Jy]	V [Jy]	W [Jy]	α	5 GHz ID
04 25 26	−37 57	140	1.6 ± 0.04	0.9 ± 0.05	0.8 ± 0.05	1.2 ± 0.09	...	-0.7 ± 0.2	PMN J0424-3756
04 28 39	−37 57		1.8 ± 0.04	1.9 ± 0.06	1.9 ± 0.05	1.6 ± 0.08	1.3 ± 0.1	-0.1 ± 0.09	PMN J0428-3756 ^a
04 33 13	05 20	108	2.8 ± 0.04	2.6 ± 0.07	2.4 ± 0.08	2.0 ± 0.1	1.5 ± 0.2	-0.3 ± 0.09	GB6 J0433+0521
04 38 31	−12 48		0.5 ± 0.03	0.8 ± 0.05	1.0 ± 0.06	1.1 ± 0.1	0.6 ± 0.2	0.7 ± 0.2	PMN J0438-1251
04 40 14	−43 33	147	2.1 ± 0.04	2.0 ± 0.05	1.8 ± 0.05	1.6 ± 0.09	1.2 ± 0.1	-0.3 ± 0.1	PMN J0440-4332
04 42 52	−00 18		1.0 ± 0.03	0.8 ± 0.05	0.7 ± 0.06	1.0 ± 0.1	1.6 ± 0.2	0.1 ± 0.2	PMN J0442-0017
04 49 05	−80 59	175	1.6 ± 0.03	1.9 ± 0.05	1.8 ± 0.05	1.8 ± 0.08	1.3 ± 0.1	0.0 ± 0.08	PMN J0450-8100
04 53 19	−28 07	131	1.8 ± 0.03	2.0 ± 0.05	1.9 ± 0.05	1.6 ± 0.08	1.5 ± 0.1	0.0 ± 0.09	PMN J0453-2807
04 55 56	−46 17	151	4.2 ± 0.04	4.0 ± 0.06	3.9 ± 0.06	3.3 ± 0.1	2.6 ± 0.1	-0.2 ± 0.05	PMN J0455-4616
04 56 58	−23 22	128	2.6 ± 0.03	2.5 ± 0.04	2.3 ± 0.06	2.0 ± 0.08	2.6 ± 0.1	-0.1 ± 0.06	PMN J0457-2324
04 57 10	−21 45		0.8 ± 0.03	0.8 ± 0.04	0.6 ± 0.05	...	1.0 ± 0.2	-0.0 ± 0.2	...
05 01 14	−22 59		1.1 ± 0.05	0.9 ± 0.08	0.9 ± 0.1	-0.3 ± 0.4	...
05 01 19	−01 59		0.7 ± 0.03	1.0 ± 0.05	0.8 ± 0.06	1.1 ± 0.1	1.0 ± 0.2	0.3 ± 0.2	PMN J0501-0159
05 06 16	−06 24		1.4 ± 0.03	1.1 ± 0.05	1.2 ± 0.07	0.6 ± 0.1	...	-0.5 ± 0.2	...
05 06 56	−61 07	154	2.3 ± 0.03	2.0 ± 0.04	1.7 ± 0.04	0.7 ± 0.07	1.7 ± 0.1	-0.4 ± 0.08	PMN J0506-6109 ^a
05 13 49	−21 55	127	1.3 ± 0.03	1.3 ± 0.04	1.1 ± 0.05	1.0 ± 0.08	...	-0.2 ± 0.1	PMN J0513-2159
05 17 11	−62 19		0.8 ± 0.03	...	0.8 ± 0.03	0.3 ± 0.06	0.6 ± 0.1	-0.1 ± 0.2	PMN J0515-6220
05 19 43	−45 46	150	7.7 ± 0.03	5.9 ± 0.05	5.1 ± 0.06	4.0 ± 0.1	2.3 ± 0.1	-0.7 ± 0.03	PMN J0519-4546 ^a
05 23 02	−36 27	139	4.8 ± 0.03	4.4 ± 0.05	4.1 ± 0.06	3.9 ± 0.1	3.8 ± 0.2	-0.2 ± 0.04	PMN J0522-3628
05 25 03	−23 37		0.9 ± 0.02	1.0 ± 0.04	0.8 ± 0.05	0.8 ± 0.07	0.8 ± 0.1	-0.1 ± 0.2	PMN J0525-2338 ^a
05 25 54	−48 28		0.9 ± 0.03	1.4 ± 0.04	1.2 ± 0.05	1.5 ± 0.08	1.1 ± 0.1	0.4 ± 0.1	PMN J0526-4830 ^a
05 27 09	03 38		1.4 ± 0.03	1.5 ± 0.05	1.5 ± 0.06	1.2 ± 0.1	0.8 ± 0.2	0.0 ± 0.1	GB6 J0527+0331
05 27 34	−12 41	122	1.6 ± 0.04	1.6 ± 0.05	1.4 ± 0.05	1.3 ± 0.09	1.3 ± 0.2	-0.2 ± 0.1	PMN J0527-1241
05 28 35	19 16		...	0.7 ± 0.2	0.5 ± 0.08	-1.6 ± 4	...
05 33 22	18 46		0.4 ± 0.04	0.6 ± 0.05	0.6 ± 0.06	0.9 ± 0.1	0.9 ± 0.2	0.7 ± 0.3	GB6 J0533+1836
05 33 35	48 24		0.8 ± 0.03	0.5 ± 0.05	0.8 ± 0.06	...	0.9 ± 0.2	-0.1 ± 0.2	GB6 J0533+4822
05 34 35	−61 07		0.8 ± 0.02	0.8 ± 0.03	0.7 ± 0.03	0.7 ± 0.06	0.7 ± 0.1	-0.1 ± 0.1	PMN J0534-6106
05 36 02	19 59		0.5 ± 0.1	1.0 ± 0.2	1.8 ± 2	...
05 36 16	−66 09		0.4 ± 0.02	0.7 ± 0.03	0.5 ± 0.03	0.4 ± 0.05	...	0.4 ± 0.3	PMN J0535-6601
05 38 51	−44 05	148	6.3 ± 0.03	6.6 ± 0.05	6.9 ± 0.06	6.7 ± 0.1	6.1 ± 0.2	0.1 ± 0.03	PMN J0538-4405
05 39 49	−28 42		0.3 ± 0.03	0.6 ± 0.04	0.6 ± 0.04	0.8 ± 0.08	...	1.0 ± 0.3	PMN J0539-2839
05 40 46	−54 15	152	1.1 ± 0.02	1.3 ± 0.04	1.2 ± 0.05	1.6 ± 0.07	1.1 ± 0.1	0.2 ± 0.1	PMN J0540-5418
05 42 30	49 51	095	1.7 ± 0.04	1.4 ± 0.05	1.1 ± 0.06	1.2 ± 0.1	...	-0.6 ± 0.2	GB6 J0542+4951
05 43 27	−73 29		0.4 ± 0.02	0.7 ± 0.03	0.6 ± 0.04	0.5 ± 0.06	0.5 ± 0.1	0.4 ± 0.2	PMN J0541-7332
05 46 30	−67 18		...	0.3 ± 0.03	0.6 ± 0.04	0.6 ± 0.05	0.9 ± 0.08	0.8 ± 0.2	...
05 46 45	−64 12	156	0.6 ± 0.02	0.3 ± 0.03	0.4 ± 0.03	...	0.9 ± 0.08	0.0 ± 0.2	PMN J0546-6415
05 50 30	−57 31	153	1.4 ± 0.03	1.3 ± 0.04	1.3 ± 0.04	1.2 ± 0.07	0.8 ± 0.1	-0.2 ± 0.1	PMN J0550-5732
05 51 54	37 43		1.3 ± 0.03	1.4 ± 0.05	1.3 ± 0.06	0.6 ± 0.1	1.0 ± 0.2	-0.1 ± 0.2	GB6 J0551+3751 ^a
05 52 39	−66 36		...	0.1 ± 0.02	0.4 ± 0.04	0.6 ± 0.06	...	2.1 ± 0.6	...
05 55 48	39 45	100	3.4 ± 0.04	2.4 ± 0.06	1.9 ± 0.07	1.0 ± 0.1	1.4 ± 0.2	-0.9 ± 0.1	GB6 J0555+3948
06 06 36	71 47		1.0 ± 0.03	1.1 ± 0.04	1.0 ± 0.04	0.8 ± 0.07	1.4 ± 0.1	0.1 ± 0.1	...
06 07 03	67 23	091	1.5 ± 0.03	1.2 ± 0.04	0.7 ± 0.05	0.6 ± 0.08	...	-0.9 ± 0.2	GB6 J0607+6720 ^a
06 08 49	−22 20		1.3 ± 0.02	1.2 ± 0.04	1.2 ± 0.05	0.7 ± 0.08	0.8 ± 0.1	-0.2 ± 0.1	PMN J0608-2220
06 09 38	−15 41	126	3.7 ± 0.04	3.1 ± 0.06	2.8 ± 0.07	2.2 ± 0.09	1.1 ± 0.2	-0.5 ± 0.07	PMN J0609-1542
06 09 50	−60 54		0.3 ± 0.02	0.3 ± 0.04	0.4 ± 0.03	0.8 ± 0.06	0.8 ± 0.1	0.8 ± 0.2	PMN J0610-6058
06 15 33	−78 42		0.3 ± 0.03	0.4 ± 0.04	0.2 ± 0.04	0.5 ± 0.08	...	0.4 ± 0.4	PMN J0618-7842

Table 18—Continued

RA [hms]	Dec [dm]	ID	K [Jy]	Ka [Jy]	Q [Jy]	V [Jy]	W [Jy]	α	5 GHz ID
06 21 28	–25 13		0.3 ± 0.03	0.2 ± 0.04	0.2 ± 0.04	-1.1 ± 0.8	PMN J0621-2504
06 23 14	–64 36		1.0 ± 0.02	1.0 ± 0.03	1.0 ± 0.03	1.0 ± 0.04	1.1 ± 0.08	-0.0 ± 0.08	PMN J0623-6436
06 27 06	–05 53		1.5 ± 0.04	0.7 ± 0.05	0.4 ± 0.06	-2.0 ± 0.3	PMN J0627-0553
06 29 31	–19 57	130	1.5 ± 0.03	1.4 ± 0.04	1.3 ± 0.05	0.6 ± 0.08	...	-0.3 ± 0.1	PMN J0629-1959
06 30 39	–09 33		1.5 ± 0.03	1.0 ± 0.05	0.9 ± 0.06	0.7 ± 0.1	1.2 ± 0.2	-0.6 ± 0.1	...
06 34 37	–23 36		0.7 ± 0.02	0.6 ± 0.04	0.5 ± 0.05	0.5 ± 0.07	...	-0.5 ± 0.3	PMN J0634-2335
06 35 51	–75 17	167	4.6 ± 0.03	4.3 ± 0.04	3.9 ± 0.04	3.1 ± 0.08	2.6 ± 0.1	-0.3 ± 0.04	PMN J0635-7516
06 36 35	–20 32	134	1.3 ± 0.03	1.5 ± 0.04	0.9 ± 0.05	1.1 ± 0.08	...	-0.0 ± 0.1	PMN J0636-2041 ^a
06 39 32	73 27	087	0.7 ± 0.03	0.5 ± 0.04	0.7 ± 0.04	0.9 ± 0.08	...	0.1 ± 0.2	GB6 J0639+7324
06 46 30	44 50	099	2.9 ± 0.04	2.3 ± 0.06	2.1 ± 0.06	1.5 ± 0.1	2.0 ± 0.2	-0.5 ± 0.08	GB6 J0646+4451
06 48 23	–17 45		...	0.6 ± 0.04	0.6 ± 0.05	0.7 ± 0.09	0.9 ± 0.2	0.3 ± 0.4	PMN J0648-1744
06 50 20	–16 35		3.1 ± 0.03	2.9 ± 0.05	2.5 ± 0.07	1.6 ± 0.09	2.2 ± 0.2	-0.4 ± 0.07	PMN J0650-1637 ^a
06 51 56	–64 51		0.1 ± 0.02	0.4 ± 0.03	0.4 ± 0.03	0.6 ± 0.06	...	1.4 ± 0.4	...
06 59 49	17 07		1.4 ± 0.03	1.4 ± 0.05	1.3 ± 0.06	1.1 ± 0.1	...	-0.1 ± 0.2	GB6 J0700+1709
07 20 06	–62 21		0.5 ± 0.02	0.8 ± 0.04	1.0 ± 0.04	0.8 ± 0.07	0.9 ± 0.1	0.6 ± 0.2	PMN J0719-6218
07 21 52	71 21		2.0 ± 0.03	2.2 ± 0.05	2.2 ± 0.05	2.2 ± 0.09	2.6 ± 0.2	0.2 ± 0.07	GB6 J0721+7120
07 25 54	–00 52		0.7 ± 0.03	1.1 ± 0.05	1.6 ± 0.07	1.9 ± 0.1	1.4 ± 0.2	0.9 ± 0.1	PMN J0725-0054
07 26 48	67 43		0.6 ± 0.02	0.4 ± 0.04	0.5 ± 0.05	0.7 ± 0.08	...	-0.1 ± 0.3	GB6 J0728+6748
07 30 19	–11 41		5.3 ± 0.04	5.1 ± 0.06	4.8 ± 0.07	3.9 ± 0.1	2.4 ± 0.2	-0.3 ± 0.04	PMN J0730-1141
07 34 09	50 20		1.1 ± 0.03	1.3 ± 0.05	1.4 ± 0.06	1.1 ± 0.1	2.0 ± 0.2	0.3 ± 0.1	GB6 J0733+5022 ^a
07 38 07	17 43	113	1.3 ± 0.04	0.8 ± 0.05	0.9 ± 0.06	0.9 ± 0.1	...	-0.5 ± 0.2	GB6 J0738+1742
07 39 16	01 36	124	1.6 ± 0.03	1.5 ± 0.05	1.8 ± 0.07	1.7 ± 0.1	1.3 ± 0.2	0.1 ± 0.1	GB6 J0739+0136
07 41 22	31 11	107	1.3 ± 0.04	1.1 ± 0.06	0.8 ± 0.07	0.8 ± 0.1	...	-0.5 ± 0.2	GB6 J0741+3112
07 43 45	–67 27	161	1.4 ± 0.03	0.9 ± 0.04	0.7 ± 0.04	0.6 ± 0.07	1.2 ± 0.1	-0.5 ± 0.1	PMN J0743-6726 ^a
07 45 28	10 15	118	1.1 ± 0.04	1.2 ± 0.05	0.9 ± 0.06	0.6 ± 0.1	...	-0.1 ± 0.2	GB6 J0745+1011
07 46 04	–00 45		0.9 ± 0.03	0.8 ± 0.05	0.8 ± 0.06	0.7 ± 0.1	...	-0.2 ± 0.2	PMN J0745-0044
07 48 08	–16 47		1.3 ± 0.03	1.7 ± 0.05	1.4 ± 0.05	0.7 ± 0.09	...	0.2 ± 0.1	PMN J0748-1639 ^a
07 48 39	23 55		0.9 ± 0.04	1.0 ± 0.06	0.9 ± 0.07	1.0 ± 0.1	...	0.1 ± 0.2	GB6 J0748+2400
07 50 53	12 30	117	3.7 ± 0.04	3.5 ± 0.06	3.4 ± 0.08	2.9 ± 0.1	2.6 ± 0.2	-0.2 ± 0.07	GB6 J0750+1231
07 53 45	53 54		1.1 ± 0.03	1.4 ± 0.05	1.0 ± 0.07	0.7 ± 0.1	...	0.1 ± 0.2	GB6 J0753+5353 ^a
07 57 04	09 57	120	1.1 ± 0.03	1.0 ± 0.05	1.3 ± 0.06	1.2 ± 0.1	1.5 ± 0.2	0.2 ± 0.1	GB6 J0757+0956
08 05 47	61 33		0.8 ± 0.03	0.7 ± 0.05	0.8 ± 0.06	0.6 ± 0.09	0.7 ± 0.2	-0.2 ± 0.2	...
08 08 19	–07 50	133	1.6 ± 0.03	1.7 ± 0.05	1.6 ± 0.06	1.7 ± 0.1	1.5 ± 0.2	-0.0 ± 0.1	PMN J0808-0751
08 11 37	01 44		0.8 ± 0.03	0.5 ± 0.05	0.5 ± 0.06	0.6 ± 0.1	...	-0.5 ± 0.3	GB6 J0811+0146
08 13 16	48 18		1.1 ± 0.03	1.1 ± 0.05	1.2 ± 0.07	0.5 ± 0.1	...	-0.0 ± 0.2	GB6 J0813+4813
08 16 24	–24 25	145	0.8 ± 0.03	1.2 ± 0.04	1.2 ± 0.05	0.8 ± 0.08	0.5 ± 0.1	0.4 ± 0.2	PMN J0816-2421
08 18 25	42 22		1.2 ± 0.04	1.6 ± 0.05	1.3 ± 0.07	1.2 ± 0.1	1.6 ± 0.2	0.2 ± 0.1	GB6 J0818+4222
08 23 18	22 24		1.2 ± 0.04	1.4 ± 0.06	1.3 ± 0.08	1.3 ± 0.1	1.0 ± 0.2	0.1 ± 0.2	GB6 J0823+2223
08 24 50	39 14		1.0 ± 0.04	1.1 ± 0.06	0.9 ± 0.07	0.7 ± 0.1	...	-0.1 ± 0.2	GB6 J0824+3916 ^a
08 25 48	03 11	125	1.9 ± 0.04	2.0 ± 0.06	1.8 ± 0.07	1.9 ± 0.1	1.2 ± 0.2	-0.0 ± 0.1	GB6 J0825+0309
08 26 09	–22 32		0.9 ± 0.03	0.7 ± 0.04	0.7 ± 0.05	0.9 ± 0.09	...	-0.1 ± 0.2	PMN J0826-2230
08 30 54	24 10	112	1.0 ± 0.04	1.4 ± 0.06	1.1 ± 0.07	1.7 ± 0.1	1.9 ± 0.2	0.5 ± 0.1	GB6 J0830+2410
08 34 17	55 32		1.0 ± 0.03	0.8 ± 0.05	0.7 ± 0.06	1.0 ± 0.1	1.5 ± 0.2	-0.1 ± 0.2	GB6 J0834+5534
08 36 47	–20 14	144	2.6 ± 0.04	2.3 ± 0.06	1.9 ± 0.05	1.1 ± 0.09	1.2 ± 0.2	-0.6 ± 0.09	PMN J0836-2017
08 37 57	58 23		1.5 ± 0.03	1.5 ± 0.05	1.3 ± 0.06	1.0 ± 0.1	...	-0.3 ± 0.1	GB6 J0837+5825
08 40 41	13 12	121	1.8 ± 0.04	1.7 ± 0.06	1.5 ± 0.07	1.2 ± 0.1	...	-0.3 ± 0.1	GB6 J0840+1312

Table 18—Continued

RA [hms]	Dec [dm]	ID	K [Jy]	Ka [Jy]	Q [Jy]	V [Jy]	W [Jy]	α	5 GHz ID
08 41 27	70 54	089	2.1 ± 0.03	2.1 ± 0.05	2.0 ± 0.05	1.8 ± 0.08	1.1 ± 0.1	-0.2 ± 0.08	GB6 J0841+7053
08 47 50	-07 04		0.9 ± 0.03	0.9 ± 0.05	1.2 ± 0.06	1.0 ± 0.1	1.1 ± 0.2	0.3 ± 0.2	PMN J0847-0703
08 51 17	-59 21		0.5 ± 0.03	0.8 ± 0.05	1.1 ± 0.05	0.7 ± 0.08	1.0 ± 0.1	0.7 ± 0.2	PMN J0851-5924
08 54 47	20 06	115	4.5 ± 0.05	5.0 ± 0.08	5.0 ± 0.08	4.8 ± 0.1	4.0 ± 0.2	0.1 ± 0.05	GB6 J0854+2006
09 02 16	-14 14		1.3 ± 0.03	1.5 ± 0.05	1.6 ± 0.06	1.4 ± 0.1	1.6 ± 0.2	0.2 ± 0.1	PMN J0902-1415
09 03 16	46 48		1.1 ± 0.04	0.9 ± 0.06	0.7 ± 0.06	0.6 ± 0.1	0.9 ± 0.2	-0.4 ± 0.2	GB6 J0903+4650
09 04 12	-31 08		0.6 ± 0.02	0.7 ± 0.04	0.9 ± 0.05	0.7 ± 0.08	0.9 ± 0.2	0.4 ± 0.2	PMN J0904-3110
09 04 20	-57 33		0.7 ± 0.03	1.1 ± 0.04	1.1 ± 0.05	1.0 ± 0.08	1.1 ± 0.2	0.4 ± 0.1	PMN J0904-5735
09 07 53	-20 21		1.2 ± 0.03	1.0 ± 0.05	0.5 ± 0.06	1.0 ± 0.1	1.0 ± 0.2	-0.4 ± 0.2	PMN J0907-2026
09 09 18	01 18	132	1.8 ± 0.04	1.5 ± 0.06	1.4 ± 0.07	1.1 ± 0.1	...	-0.5 ± 0.2	GB6 J0909+0121
09 09 50	42 54		0.9 ± 0.04	1.0 ± 0.06	0.9 ± 0.06	0.7 ± 0.1	...	-0.1 ± 0.2	GB6 J0909+4253
09 14 40	02 49		1.5 ± 0.04	1.7 ± 0.06	1.6 ± 0.07	1.1 ± 0.1	2.1 ± 0.2	0.1 ± 0.1	GB6 J0914+0245
09 18 14	-12 03	143	2.1 ± 0.04	0.9 ± 0.05	0.6 ± 0.06	-2.3 ± 0.3	PMN J0918-1205
09 20 43	44 41		1.6 ± 0.04	1.4 ± 0.06	1.5 ± 0.05	1.7 ± 0.1	1.2 ± 0.2	-0.0 ± 0.1	GB6 J0920+4441
09 21 06	62 14		1.1 ± 0.03	1.0 ± 0.04	0.9 ± 0.05	0.8 ± 0.09	...	-0.2 ± 0.2	GB6 J0921+6215
09 21 39	-26 19		1.4 ± 0.04	1.3 ± 0.05	1.2 ± 0.06	1.2 ± 0.1	0.8 ± 0.2	-0.3 ± 0.1	PMN J0921-2618
09 23 14	-40 04		1.1 ± 0.03	1.1 ± 0.04	1.2 ± 0.04	0.9 ± 0.08	0.7 ± 0.1	-0.1 ± 0.1	PMN J0922-3959 ^a
09 24 06	28 16		1.0 ± 0.04	0.9 ± 0.06	1.1 ± 0.06	0.8 ± 0.1	1.0 ± 0.2	-0.0 ± 0.2	GB6 J0923+2815
09 27 05	39 01	105	8.1 ± 0.04	6.9 ± 0.07	6.3 ± 0.07	5.2 ± 0.1	3.6 ± 0.2	-0.4 ± 0.03	GB6 J0927+3902
09 29 14	50 16		0.6 ± 0.03	0.7 ± 0.05	0.6 ± 0.05	0.8 ± 0.09	1.1 ± 0.2	0.3 ± 0.2	GB6 J0929+5013
09 48 55	40 38	104	1.4 ± 0.03	1.7 ± 0.05	1.7 ± 0.06	1.9 ± 0.1	1.6 ± 0.2	0.3 ± 0.1	GB6 J0948+4039
09 55 45	69 36	088	1.5 ± 0.04	1.5 ± 0.05	1.1 ± 0.04	1.1 ± 0.09	1.2 ± 0.2	-0.3 ± 0.1	GB6 J0955+6940
09 56 39	25 14		0.8 ± 0.03	1.0 ± 0.05	0.9 ± 0.06	0.8 ± 0.1	...	0.1 ± 0.2	GB6 J0956+2515
09 57 22	55 26		1.0 ± 0.03	0.8 ± 0.05	0.9 ± 0.05	0.6 ± 0.09	...	-0.3 ± 0.2	GB6 J0957+5522
09 58 10	47 22	098	1.3 ± 0.03	1.4 ± 0.05	1.6 ± 0.05	1.2 ± 0.09	...	0.2 ± 0.1	GB6 J0958+4725
09 59 07	65 31		1.1 ± 0.03	1.1 ± 0.04	0.9 ± 0.04	0.8 ± 0.08	0.8 ± 0.1	-0.3 ± 0.1	GB6 J0958+6534
10 05 56	34 57		0.6 ± 0.03	0.6 ± 0.05	0.4 ± 0.07	-0.3 ± 0.5	GB6 J1006+3453 ^a
10 14 15	23 03	119	1.1 ± 0.03	0.9 ± 0.05	0.9 ± 0.06	1.0 ± 0.1	...	-0.3 ± 0.2	GB6 J1014+2301
10 15 11	-45 11		1.3 ± 0.03	1.0 ± 0.04	0.9 ± 0.04	-0.7 ± 0.2	PMN J1014-4508
10 17 40	35 51		0.7 ± 0.03	0.9 ± 0.05	0.8 ± 0.06	0.9 ± 0.1	...	0.2 ± 0.2	GB6 J1018+3550
10 18 48	-31 31		1.1 ± 0.03	1.0 ± 0.04	0.7 ± 0.06	0.5 ± 0.09	...	-0.6 ± 0.2	PMN J1018-3123
10 22 16	40 02		1.1 ± 0.03	1.2 ± 0.05	1.3 ± 0.06	0.5 ± 0.1	...	0.2 ± 0.2	GB6 J1022+4004
10 32 49	41 17	103	1.2 ± 0.03	0.9 ± 0.05	0.8 ± 0.05	0.8 ± 0.1	1.4 ± 0.2	-0.3 ± 0.1	GB6 J1033+4115
10 33 42	60 50		0.9 ± 0.03	1.0 ± 0.04	0.9 ± 0.04	0.6 ± 0.07	0.8 ± 0.1	-0.1 ± 0.2	GB6 J1033+6051 ^a
10 35 24	-20 06		0.8 ± 0.03	0.4 ± 0.05	0.2 ± 0.06	0.4 ± 0.1	...	-1.4 ± 0.5	PMN J1035-2011 ^a
10 36 31	-37 38		0.9 ± 0.03	0.8 ± 0.04	0.4 ± 0.05	-0.5 ± 0.3	PMN J1036-3744
10 37 21	-29 34		1.8 ± 0.04	1.7 ± 0.05	1.5 ± 0.06	1.3 ± 0.1	1.7 ± 0.2	-0.2 ± 0.1	PMN J1037-2934
10 38 33	05 10	142	1.3 ± 0.03	0.9 ± 0.05	1.2 ± 0.06	0.9 ± 0.1	...	-0.4 ± 0.2	GB6 J1038+0512
10 41 28	06 11		0.9 ± 0.03	1.2 ± 0.05	1.0 ± 0.06	0.8 ± 0.1	...	0.1 ± 0.2	GB6 J1041+0610
10 41 46	-47 34	163	1.1 ± 0.03	...	0.7 ± 0.04	...	1.6 ± 0.2	-0.2 ± 0.2	PMN J1041-4740
10 42 59	24 04		0.7 ± 0.03	0.7 ± 0.05	0.9 ± 0.06	...	1.8 ± 0.2	0.6 ± 0.2	GB6 J1043+2408
10 47 03	71 42	083	1.1 ± 0.03	0.9 ± 0.05	0.6 ± 0.04	-0.8 ± 0.3	GB6 J1048+7143
10 47 59	-19 10		1.3 ± 0.03	1.0 ± 0.05	0.5 ± 0.06	-1.1 ± 0.3	PMN J1048-1909
10 56 22	81 12		1.2 ± 0.03	1.1 ± 0.04	0.9 ± 0.05	0.8 ± 0.09	0.8 ± 0.2	-0.3 ± 0.2	...
10 58 27	01 34	149	5.3 ± 0.04	5.0 ± 0.06	4.8 ± 0.07	4.7 ± 0.1	3.1 ± 0.2	-0.2 ± 0.04	GB6 J1058+0133
10 59 12	-80 03	176	2.5 ± 0.03	2.7 ± 0.05	2.7 ± 0.05	2.6 ± 0.1	1.9 ± 0.1	0.1 ± 0.06	PMN J1058-8003

Table 18—Continued

RA [hms]	Dec [dm]	ID	K [Jy]	Ka [Jy]	Q [Jy]	V [Jy]	W [Jy]	α	5 GHz ID
11 02 01	72 27		1.2 ± 0.03	1.2 ± 0.05	1.2 ± 0.04	0.6 ± 0.09	...	-0.2 ± 0.2	GB6 J1101+7225 ^a
11 02 08	-44 02		0.6 ± 0.02	0.8 ± 0.03	0.6 ± 0.05	0.9 ± 0.08	...	0.4 ± 0.2	PMN J1102-4404
11 07 15	-44 46	166	1.7 ± 0.03	1.7 ± 0.04	1.6 ± 0.05	1.4 ± 0.08	0.8 ± 0.1	-0.2 ± 0.09	PMN J1107-4449
11 18 07	-46 33		1.2 ± 0.02	0.8 ± 0.03	0.8 ± 0.05	0.8 ± 0.08	0.8 ± 0.2	-0.6 ± 0.1	PMN J1118-4634
11 18 32	-12 32		1.2 ± 0.03	1.1 ± 0.05	1.1 ± 0.06	0.5 ± 0.1	1.1 ± 0.2	-0.3 ± 0.2	PMN J1118-1232 ^a
11 18 48	12 38		1.0 ± 0.03	0.8 ± 0.05	0.9 ± 0.06	0.8 ± 0.1	...	-0.3 ± 0.2	GB6 J1118+1234
11 27 05	-18 58	159	1.4 ± 0.03	1.4 ± 0.05	1.6 ± 0.06	1.4 ± 0.1	1.9 ± 0.2	0.1 ± 0.1	PMN J1127-1857
11 30 11	-14 51	157	2.1 ± 0.04	1.7 ± 0.05	2.0 ± 0.07	1.2 ± 0.1	2.3 ± 0.2	-0.2 ± 0.1	PMN J1130-1449
11 30 49	38 14	101	1.0 ± 0.03	1.0 ± 0.05	1.0 ± 0.05	0.8 ± 0.09	1.3 ± 0.2	0.0 ± 0.1	GB6 J1130+3815 ^a
11 37 30	-74 14		0.9 ± 0.03	0.7 ± 0.04	0.3 ± 0.05	0.4 ± 0.09	...	-0.8 ± 0.3	PMN J1136-7415
11 45 10	-69 58		0.8 ± 0.03	0.9 ± 0.04	0.9 ± 0.05	1.0 ± 0.08	1.0 ± 0.1	0.2 ± 0.1	PMN J1145-6953
11 46 07	-48 43		0.8 ± 0.02	1.0 ± 0.04	0.7 ± 0.05	1.0 ± 0.09	1.2 ± 0.2	0.2 ± 0.1	PMN J1145-4836 ^a
11 46 54	40 00		1.1 ± 0.03	1.3 ± 0.04	1.3 ± 0.05	0.9 ± 0.09	...	0.2 ± 0.2	GB6 J1146+3958 ^a
11 47 06	-38 11	169	2.2 ± 0.04	2.3 ± 0.06	2.2 ± 0.07	2.0 ± 0.1	1.6 ± 0.2	-0.1 ± 0.09	PMN J1147-3812
11 50 27	-79 27		1.5 ± 0.03	1.1 ± 0.04	0.6 ± 0.05	0.8 ± 0.09	...	-1.0 ± 0.2	PMN J1150-7918
11 50 45	-00 26		0.7 ± 0.03	0.4 ± 0.05	0.6 ± 0.06	-0.4 ± 0.4	PMN J1150-0024
11 52 33	-08 45		0.9 ± 0.03	0.9 ± 0.05	1.2 ± 0.06	0.6 ± 0.1	...	0.2 ± 0.2	PMN J1152-0841
11 53 12	49 32	090	2.2 ± 0.03	2.1 ± 0.05	2.1 ± 0.06	1.7 ± 0.08	1.3 ± 0.1	-0.2 ± 0.08	GB6 J1153+4931 ^a
11 54 15	-35 14		0.9 ± 0.03	0.9 ± 0.05	0.9 ± 0.06	0.8 ± 0.1	...	-0.0 ± 0.2	PMN J1154-3504
11 55 42	81 03	078	0.9 ± 0.03	0.7 ± 0.04	0.7 ± 0.05	0.9 ± 0.09	1.3 ± 0.2	-0.1 ± 0.2	1Jy 1150+81
11 57 44	16 36		1.0 ± 0.03	1.1 ± 0.05	1.1 ± 0.06	1.0 ± 0.1	1.1 ± 0.2	0.0 ± 0.2	GB6 J1157+1639
11 59 35	29 14	111	2.2 ± 0.04	2.2 ± 0.06	2.1 ± 0.07	1.6 ± 0.1	0.8 ± 0.2	-0.2 ± 0.1	GB6 J1159+2914
12 03 30	48 08		0.9 ± 0.02	0.7 ± 0.04	0.6 ± 0.05	0.2 ± 0.08	0.7 ± 0.2	-0.5 ± 0.2	GB6 J1203+4803 ^a
12 05 51	-26 39		1.1 ± 0.04	1.0 ± 0.05	1.0 ± 0.06	0.9 ± 0.1	1.3 ± 0.2	-0.0 ± 0.2	PMN J1205-2634
12 06 57	-52 18		0.0 ± 0.04	1.5 ± 0.04	1.1 ± 0.05	0.8 ± 0.08	...	-1.0 ± 0.3	PMN J1205-5217 ^a
12 08 20	-24 00	172	1.1 ± 0.03	1.1 ± 0.06	0.5 ± 0.06	0.8 ± 0.1	...	-0.5 ± 0.3	...
12 09 04	-52 23		...	1.7 ± 0.04	0.7 ± 0.05	0.5 ± 0.08	...	-2.6 ± 0.5	...
12 11 39	-52 35		4.2 ± 0.03	2.5 ± 0.04	1.9 ± 0.06	1.2 ± 0.08	...	-1.3 ± 0.08	PMN J1212-5245 ^a
12 15 58	-17 29	173	1.6 ± 0.03	1.3 ± 0.05	1.3 ± 0.06	0.9 ± 0.1	0.8 ± 0.2	-0.5 ± 0.1	PMN J1215-1731
12 18 58	48 31		0.9 ± 0.02	1.1 ± 0.03	0.9 ± 0.04	1.0 ± 0.08	0.5 ± 0.1	0.1 ± 0.1	GB6 J1219+4830
12 19 21	05 49	164	3.0 ± 0.04	2.3 ± 0.06	2.1 ± 0.06	1.3 ± 0.1	1.3 ± 0.2	-0.7 ± 0.09	GB6 J1219+0549A ^a
12 22 12	04 13		0.6 ± 0.03	0.6 ± 0.05	0.7 ± 0.06	0.7 ± 0.1	...	0.2 ± 0.3	GB6 J1222+0413
12 24 28	-83 08	178	1.0 ± 0.03	1.2 ± 0.04	1.1 ± 0.05	1.1 ± 0.08	...	0.2 ± 0.2	PMN J1224-8312
12 24 40	21 24		0.6 ± 0.03	0.5 ± 0.05	0.5 ± 0.06	0.6 ± 0.1	...	-0.2 ± 0.3	GB6 J1224+2122
12 29 06	02 03	170	24.2 ± 0.04	22.1 ± 0.06	20.9 ± 0.07	18.6 ± 0.1	15.2 ± 0.2	-0.3 ± 0.01	GB6 J1229+0202
12 30 51	12 23	165	21.4 ± 0.04	16.6 ± 0.06	14.2 ± 0.07	10.6 ± 0.1	8.0 ± 0.2	-0.7 ± 0.01	GB6 J1230+1223
12 39 31	07 27		1.2 ± 0.03	1.1 ± 0.05	0.9 ± 0.06	1.3 ± 0.1	...	-0.2 ± 0.2	GB6 J1239+0730
12 39 44	-10 25		0.9 ± 0.03	0.8 ± 0.05	0.8 ± 0.06	1.0 ± 0.1	1.3 ± 0.2	0.1 ± 0.2	PMN J1239-1023
12 46 52	-25 46	177	1.3 ± 0.03	1.1 ± 0.06	1.5 ± 0.06	1.8 ± 0.1	0.8 ± 0.2	0.2 ± 0.1	PMN J1246-2547
12 48 54	-46 00		0.6 ± 0.03	0.5 ± 0.05	0.7 ± 0.05	0.5 ± 0.09	0.9 ± 0.2	0.2 ± 0.2	PMN J1248-4559
12 55 11	-71 32		0.5 ± 0.03	0.2 ± 0.04	0.2 ± 0.04	0.3 ± 0.08	...	-0.8 ± 0.5	PMN J1254-7138
12 56 12	-05 47	181	17.7 ± 0.04	18.4 ± 0.07	18.4 ± 0.07	17.4 ± 0.1	14.6 ± 0.2	0.0 ± 0.01	PMN J1256-0547
12 58 09	-31 59	180	1.4 ± 0.03	1.2 ± 0.05	1.3 ± 0.06	0.6 ± 0.1	1.1 ± 0.2	-0.3 ± 0.1	PMN J1257-3154
12 58 27	32 26		0.6 ± 0.03	0.6 ± 0.04	0.4 ± 0.05	0.5 ± 0.1	...	-0.3 ± 0.3	GB6 J1257+3229 ^a
12 58 50	-22 22		1.0 ± 0.04	0.9 ± 0.05	0.7 ± 0.06	1.0 ± 0.1	...	-0.3 ± 0.2	PMN J1258-2219
12 59 17	51 41		0.4 ± 0.03	0.6 ± 0.04	0.6 ± 0.04	0.5 ± 0.08	1.2 ± 0.1	0.6 ± 0.2	GB6 J1259+5141 ^a

Table 18—Continued

RA [hms]	Dec [dm]	ID	K [Jy]	Ka [Jy]	Q [Jy]	V [Jy]	W [Jy]	α	5 GHz ID
13 02 33	57 46		0.7 ± 0.03	0.8 ± 0.04	0.5 ± 0.04	0.6 ± 0.08	1.1 ± 0.2	0.0 ± 0.2	GB6 J1302+5748
13 05 18	−10 31		0.8 ± 0.04	0.7 ± 0.05	0.5 ± 0.06	1.1 ± 0.1	1.2 ± 0.2	0.2 ± 0.2	PMN J1305-1033
13 05 55	−49 30		1.2 ± 0.03	1.0 ± 0.05	1.0 ± 0.05	1.1 ± 0.09	1.0 ± 0.2	$−0.2 \pm 0.1$	PMN J1305-4928
13 10 40	32 22	052	2.6 ± 0.03	2.5 ± 0.05	2.4 ± 0.06	1.5 ± 0.09	1.3 ± 0.2	$−0.3 \pm 0.08$	GB6 J1310+3220
13 16 08	−33 38	182	1.9 ± 0.04	1.9 ± 0.05	2.2 ± 0.06	2.1 ± 0.1	1.6 ± 0.2	0.1 ± 0.09	PMN J1316-3339
13 18 06	−42 05		0.4 ± 0.06	0.6 ± 0.1	...	1.1 ± 1	...
13 24 29	−10 49		0.7 ± 0.03	1.0 ± 0.05	0.8 ± 0.06	1.2 ± 0.1	1.5 ± 0.2	0.6 ± 0.2	PMN J1324-1049
13 27 20	22 10		0.8 ± 0.03	1.1 ± 0.05	0.8 ± 0.05	0.6 ± 0.1	1.5 ± 0.2	0.3 ± 0.2	GB6 J1327+2210 ^a
13 28 40	32 03		1.3 ± 0.03	0.7 ± 0.05	0.5 ± 0.05	0.5 ± 0.09	...	$−1.5 \pm 0.3$...
13 30 52	25 02		1.1 ± 0.03	1.2 ± 0.05	1.3 ± 0.05	1.0 ± 0.1	...	0.2 ± 0.2	GB6 J1330+2509 ^a
13 31 19	30 31	026	2.3 ± 0.03	1.7 ± 0.05	1.3 ± 0.05	0.7 ± 0.09	...	$−1.0 \pm 0.1$	GB6 J1331+3030
13 32 49	01 59		1.6 ± 0.03	1.8 ± 0.05	1.6 ± 0.06	1.5 ± 0.1	1.5 ± 0.2	$−0.0 \pm 0.1$	GB6 J1332+0200
13 33 14	27 24		0.8 ± 0.03	1.0 ± 0.05	1.0 ± 0.05	1.0 ± 0.1	...	0.4 ± 0.2	GB6 J1333+2725 ^a
13 36 51	−33 58	185	2.1 ± 0.04	1.7 ± 0.05	1.3 ± 0.06	0.9 ± 0.1	0.8 ± 0.2	$−0.7 \pm 0.1$	PMN J1336-3358
13 37 40	−12 57	188	6.1 ± 0.04	6.4 ± 0.06	6.6 ± 0.07	6.3 ± 0.1	5.2 ± 0.2	0.0 ± 0.03	PMN J1337-1257
13 43 27	66 00		0.5 ± 0.03	0.2 ± 0.04	0.3 ± 0.04	$−1.6 \pm 0.7$	GB6 J1344+6606 ^a
13 47 45	12 18		1.0 ± 0.03	1.2 ± 0.05	1.2 ± 0.06	1.0 ± 0.1	...	0.2 ± 0.2	GB6 J1347+1217
13 52 22	31 22		0.8 ± 0.03	0.4 ± 0.04	0.6 ± 0.05	0.7 ± 0.09	0.9 ± 0.2	$−0.1 \pm 0.2$	GB6 J1352+3126
13 54 49	−10 42	197	1.2 ± 0.03	0.8 ± 0.05	0.5 ± 0.06	0.7 ± 0.1	...	$−0.9 \pm 0.3$	PMN J1354-1041
13 56 41	76 44		0.7 ± 0.03	0.6 ± 0.05	0.6 ± 0.04	0.9 ± 0.09	0.6 ± 0.2	0.1 ± 0.2	... ^c
13 56 55	19 18	004	1.7 ± 0.04	1.6 ± 0.05	1.5 ± 0.05	1.5 ± 0.1	1.0 ± 0.2	$−0.2 \pm 0.1$	GB6 J1357+1919
13 57 11	−15 33		0.5 ± 0.03	0.8 ± 0.2	0.4 ± 0.4	PMN J1357-1527
14 09 00	−07 49	203	0.8 ± 0.03	0.7 ± 0.05	0.8 ± 0.06	...	0.5 ± 0.2	$−0.1 \pm 0.3$	1Jy 1406-076
14 11 07	52 16		1.0 ± 0.03	0.4 ± 0.04	0.4 ± 0.05	$−1.9 \pm 0.4$	GB6 J1411+5212
14 15 51	13 23		1.1 ± 0.03	1.2 ± 0.05	0.9 ± 0.06	0.7 ± 0.1	0.8 ± 0.2	$−0.1 \pm 0.2$	GB6 J1415+3120
14 17 54	46 11		0.8 ± 0.03	0.8 ± 0.04	0.8 ± 0.04	$−0.1 \pm 0.2$	GB6 J1417+4606
14 19 30	54 26		0.7 ± 0.03	0.6 ± 0.04	0.7 ± 0.04	0.8 ± 0.08	...	0.1 ± 0.2	GB6 J1419+5423 ^a
14 19 40	38 22	042	1.1 ± 0.02	1.3 ± 0.04	1.4 ± 0.04	1.0 ± 0.07	1.0 ± 0.1	0.2 ± 0.1	GB6 J1419+3822
14 20 10	27 03		0.9 ± 0.03	1.3 ± 0.04	1.1 ± 0.05	1.0 ± 0.09	1.1 ± 0.2	0.3 ± 0.1	GB6 J1419+2706 ^a
14 27 29	−33 03	193	0.9 ± 0.03	1.4 ± 0.05	1.7 ± 0.06	1.9 ± 0.1	...	0.9 ± 0.1	PMN J1427-3306
14 27 53	−42 06	191	3.0 ± 0.04	2.7 ± 0.06	2.5 ± 0.07	2.3 ± 0.1	1.8 ± 0.2	$−0.3 \pm 0.07$	PMN J1427-4206
14 37 15	63 35		0.7 ± 0.03	0.3 ± 0.04	0.3 ± 0.04	0.7 ± 0.08	...	$−0.3 \pm 0.3$	GB6 J1436+6336 ^a
14 38 21	−22 06		1.3 ± 0.03	1.1 ± 0.05	1.2 ± 0.06	1.4 ± 0.1	...	$−0.0 \pm 0.1$	PMN J1438-2204 ^a
14 42 54	51 57		0.9 ± 0.03	1.1 ± 0.04	1.0 ± 0.04	1.0 ± 0.08	...	0.2 ± 0.2	GB6 J1443+5201
14 46 28	−16 22		1.1 ± 0.03	1.0 ± 0.05	1.1 ± 0.06	1.0 ± 0.1	0.9 ± 0.2	$−0.0 \pm 0.2$	PMN J1445-1628
14 54 18	−37 49		1.3 ± 0.03	1.2 ± 0.05	1.1 ± 0.06	1.0 ± 0.1	...	$−0.2 \pm 0.2$	PMN J1454-3747
14 57 13	−35 37		0.6 ± 0.03	0.7 ± 0.05	1.1 ± 0.06	1.3 ± 0.1	1.4 ± 0.2	0.7 ± 0.2	PMN J1457-3538
14 58 16	71 40	071	1.2 ± 0.03	0.7 ± 0.05	0.5 ± 0.04	0.6 ± 0.08	0.9 ± 0.1	$−0.7 \pm 0.2$	GB6 J1459+7140
15 03 02	−41 56		2.7 ± 0.04	2.3 ± 0.06	2.0 ± 0.06	1.6 ± 0.1	1.5 ± 0.2	$−0.5 \pm 0.09$	PMN J1503-4154
15 04 27	10 30	006	1.9 ± 0.04	2.0 ± 0.05	1.7 ± 0.06	1.2 ± 0.1	1.5 ± 0.2	$−0.2 \pm 0.1$	GB6 J1504+1029
15 06 54	−16 41		1.1 ± 0.04	0.6 ± 0.06	0.7 ± 0.07	0.8 ± 0.1	1.1 ± 0.2	$−0.4 \pm 0.2$	PMN J1507-1652 ^a
15 07 05	42 32		0.4 ± 0.03	0.3 ± 0.04	0.7 ± 0.04	0.7 ± 0.08	...	0.8 ± 0.3	GB6 J1506+4239
15 10 37	−05 46		0.9 ± 0.04	1.0 ± 0.05	0.9 ± 0.06	0.9 ± 0.1	1.0 ± 0.2	0.0 ± 0.2	PMN J1510-0543
15 12 45	−09 05	207	2.1 ± 0.04	2.0 ± 0.05	2.0 ± 0.06	2.1 ± 0.1	1.7 ± 0.2	$−0.1 \pm 0.09$	1Jy 1510-08
15 13 58	−10 14		1.1 ± 0.04	0.9 ± 0.06	0.7 ± 0.06	0.7 ± 0.1	1.1 ± 0.2	$−0.3 \pm 0.2$	PMN J1513-1012
15 16 42	00 15	002	1.7 ± 0.04	2.1 ± 0.05	2.0 ± 0.06	2.0 ± 0.1	1.5 ± 0.2	0.1 ± 0.1	GB6 J1516+0015

Table 18—Continued

RA [hms]	Dec [dm]	ID	K [Jy]	Ka [Jy]	Q [Jy]	V [Jy]	W [Jy]	α	5 GHz ID
15 16 59	19 25		0.6 ± 0.03	0.5 ± 0.04	0.7 ± 0.05	1.0 ± 0.09	...	0.4 ± 0.2	GB6 J1516+1932
15 17 43	-24 21	205	2.2 ± 0.04	2.2 ± 0.06	2.1 ± 0.07	2.0 ± 0.1	1.5 ± 0.2	-0.1 ± 0.09	PMN J1517-2422
15 34 54	01 26		0.8 ± 0.03	0.6 ± 0.05	0.8 ± 0.06	0.7 ± 0.1	...	-0.2 ± 0.2	GB6 J1534+0131
15 40 58	14 46		0.9 ± 0.03	0.7 ± 0.05	0.6 ± 0.05	0.7 ± 0.09	...	-0.5 ± 0.2	GB6 J1540+1447
15 49 32	02 36	005	2.6 ± 0.04	2.7 ± 0.06	2.5 ± 0.07	1.9 ± 0.1	2.2 ± 0.2	-0.1 ± 0.08	GB6 J1549+0237
15 49 35	50 35		0.8 ± 0.03	0.5 ± 0.04	0.6 ± 0.04	-0.7 ± 0.3	GB6 J1549+5038
15 50 37	05 26	007	2.8 ± 0.04	2.6 ± 0.06	2.2 ± 0.07	1.9 ± 0.1	1.6 ± 0.2	-0.4 ± 0.08	GB6 J1550+0527
16 02 08	33 28		1.1 ± 0.03	0.9 ± 0.04	1.1 ± 0.04	0.7 ± 0.08	1.4 ± 0.1	-0.1 ± 0.1	GB6 J1602+3326
16 04 30	57 18		0.9 ± 0.03	1.1 ± 0.04	1.2 ± 0.04	0.8 ± 0.07	0.9 ± 0.1	0.2 ± 0.1	GB6 J1604+5714 ^a
16 08 55	10 27	009	1.7 ± 0.04	1.6 ± 0.05	1.8 ± 0.05	1.9 ± 0.1	1.7 ± 0.2	0.1 ± 0.1	GB6 J1608+1029
16 13 41	34 12	023	3.7 ± 0.03	3.2 ± 0.05	2.9 ± 0.05	2.3 ± 0.09	1.8 ± 0.1	-0.4 ± 0.06	GB6 J1613+3412
16 17 57	-77 16	183	2.3 ± 0.03	2.1 ± 0.05	1.9 ± 0.05	1.6 ± 0.08	1.0 ± 0.1	-0.4 ± 0.08	PMN J1617-7717
16 23 41	-68 15		0.8 ± 0.02	0.9 ± 0.03	0.6 ± 0.05	-0.2 ± 0.2	PMN J1624-6809
16 32 56	82 27	076	1.5 ± 0.03	1.7 ± 0.04	1.5 ± 0.06	1.9 ± 0.08	0.7 ± 0.1	0.1 ± 0.09	... ^d
16 35 16	38 07	033	3.8 ± 0.03	4.2 ± 0.05	4.2 ± 0.05	3.8 ± 0.1	3.4 ± 0.2	0.0 ± 0.04	GB6 J1635+3808
16 37 30	47 13		1.2 ± 0.03	1.2 ± 0.04	1.3 ± 0.04	1.2 ± 0.08	...	0.1 ± 0.1	GB6 J1637+4717
16 38 15	57 22	056	1.7 ± 0.03	1.7 ± 0.04	1.6 ± 0.05	1.6 ± 0.07	1.5 ± 0.1	-0.1 ± 0.08	GB6 J1638+5720
16 42 26	68 54	069	2.2 ± 0.03	2.1 ± 0.04	2.0 ± 0.04	1.9 ± 0.08	2.0 ± 0.1	-0.1 ± 0.06	GB6 J1642+6856 ^a
16 42 53	39 48	035	7.2 ± 0.03	6.7 ± 0.05	6.2 ± 0.05	5.4 ± 0.1	4.6 ± 0.2	-0.3 ± 0.03	GB6 J1642+3948
16 42 57	-77 14		0.7 ± 0.03	0.7 ± 0.04	0.6 ± 0.04	0.8 ± 0.08	1.2 ± 0.1	0.2 ± 0.2	PMN J1644-7715
16 48 14	41 09		0.7 ± 0.03	0.8 ± 0.04	1.1 ± 0.04	0.9 ± 0.08	0.9 ± 0.1	0.5 ± 0.2	GB6 J1648+4104 ^a
16 51 05	04 56	010	1.5 ± 0.04	0.7 ± 0.05	0.4 ± 0.06	0.7 ± 0.1	...	-1.5 ± 0.3	GB6 J1651+0459
16 54 12	39 41	036	1.3 ± 0.03	1.2 ± 0.04	1.1 ± 0.04	0.5 ± 0.08	0.6 ± 0.1	-0.3 ± 0.1	GB6 J1653+3945 ^a
16 57 18	57 07		0.3 ± 0.02	0.3 ± 0.04	0.5 ± 0.04	0.8 ± 0.07	0.7 ± 0.1	1.0 ± 0.3	GB6 J1657+5705
16 58 04	47 49		1.3 ± 0.03	1.5 ± 0.04	0.9 ± 0.04	-0.3 ± 0.2	...
16 58 05	07 42	013	1.8 ± 0.04	1.9 ± 0.06	1.8 ± 0.07	1.6 ± 0.09	...	-0.1 ± 0.1	GB6 J1658+0741
16 58 50	05 16		0.9 ± 0.03	0.6 ± 0.05	0.6 ± 0.05	0.6 ± 0.1	...	-0.6 ± 0.3	GB6 J1658+0515
16 59 50	68 26		0.2 ± 0.02	0.4 ± 0.03	0.5 ± 0.03	0.8 ± 0.06	1.3 ± 0.1	1.2 ± 0.2	GB6 J1700+6830
17 01 31	39 57		0.7 ± 0.03	0.8 ± 0.04	1.0 ± 0.05	0.9 ± 0.08	1.5 ± 0.2	0.4 ± 0.1	GB6 J1701+3954
17 03 34	-62 13	198	1.8 ± 0.03	2.0 ± 0.04	1.9 ± 0.06	1.9 ± 0.09	0.7 ± 0.2	0.0 ± 0.09	PMN J1703-6212
17 07 39	01 47		0.8 ± 0.03	0.7 ± 0.05	1.0 ± 0.06	0.6 ± 0.1	...	0.1 ± 0.2	GB6 J1707+0148
17 16 16	68 42		0.6 ± 0.02	0.7 ± 0.03	0.4 ± 0.03	0.6 ± 0.06	...	-0.2 ± 0.2	GB6 J1716+6836
17 20 09	00 50		1.2 ± 0.05	0.7 ± 0.06	0.9 ± 0.07	0.7 ± 0.1	0.7 ± 0.2	-0.6 ± 0.2	GB6 J1720+0049
17 24 05	-65 00	196	2.4 ± 0.03	2.0 ± 0.05	1.6 ± 0.05	1.6 ± 0.09	1.0 ± 0.1	-0.5 ± 0.09	PMN J1723-6500
17 27 18	45 30	043	1.1 ± 0.03	1.0 ± 0.04	0.9 ± 0.05	0.9 ± 0.08	1.1 ± 0.1	-0.1 ± 0.1	GB6 J1727+4530
17 28 19	04 28		0.2 ± 0.03	0.4 ± 0.05	0.5 ± 0.05	0.7 ± 0.1	...	1.4 ± 0.5	GB6 J1728+0426
17 34 17	38 57	038	1.2 ± 0.03	1.4 ± 0.04	1.2 ± 0.05	1.2 ± 0.08	...	0.1 ± 0.1	GB6 J1734+3857
17 35 52	36 16		0.8 ± 0.03	0.6 ± 0.04	0.7 ± 0.05	0.4 ± 0.1	...	-0.3 ± 0.3	GB6 J1735+3616
17 36 12	-79 34	186	1.2 ± 0.03	1.5 ± 0.04	1.5 ± 0.04	0.9 ± 0.08	...	0.2 ± 0.1	PMN J1733-7935
17 37 03	06 26		0.8 ± 0.03	1.1 ± 0.05	0.8 ± 0.05	0.8 ± 0.1	0.9 ± 0.2	0.2 ± 0.2	GB6 J1737+0620 ^a
17 37 23	-56 45		1.4 ± 0.03	1.1 ± 0.05	1.1 ± 0.06	-0.4 ± 0.2	...
17 38 14	50 20		0.9 ± 0.03	0.4 ± 0.04	0.4 ± 0.05	0.5 ± 0.08	...	-0.9 ± 0.3	...
17 40 11	47 39		0.8 ± 0.03	0.7 ± 0.04	0.8 ± 0.04	0.9 ± 0.08	0.9 ± 0.1	0.1 ± 0.2	GB6 J1739+4738
17 40 37	52 13	048	1.3 ± 0.02	1.2 ± 0.04	1.2 ± 0.04	1.2 ± 0.07	1.0 ± 0.1	-0.1 ± 0.1	GB6 J1740+5211
17 47 42	70 03	068	0.6 ± 0.02	0.7 ± 0.03	0.7 ± 0.03	0.8 ± 0.05	0.9 ± 0.08	0.2 ± 0.1	GB6 J1748+7005
17 51 36	09 37		4.6 ± 0.04	4.8 ± 0.06	4.8 ± 0.07	4.5 ± 0.1	3.7 ± 0.2	-0.0 ± 0.04	GB6 J1751+0938

Table 18—Continued

RA [hms]	Dec [dm]	ID	K [Jy]	Ka [Jy]	Q [Jy]	V [Jy]	W [Jy]	α	5 GHz ID
17 53 30	28 48	022	2.0 ± 0.03	1.9 ± 0.05	1.8 ± 0.05	1.7 ± 0.08	1.4 ± 0.1	-0.2 ± 0.08	GB6 J1753+2847
17 53 42	44 01		0.5 ± 0.03	0.6 ± 0.04	0.9 ± 0.05	...	0.6 ± 0.1	0.7 ± 0.3	GB6 J1753+4410 ^a
17 59 01	66 33	064	0.7 ± 0.01	0.5 ± 0.01	0.6 ± 0.03	0.5 ± 0.05	0.5 ± 0.08	-0.4 ± 0.1	GB6 J1758+6638 ^a
17 59 55	38 53		1.0 ± 0.03	0.6 ± 0.04	0.6 ± 0.05	0.5 ± 0.08	...	-0.9 ± 0.2	GB6 J1800+3848 ^a
18 00 34	78 27	072	2.1 ± 0.03	2.1 ± 0.05	1.9 ± 0.05	1.8 ± 0.09	1.3 ± 0.1	-0.2 ± 0.08	1Jy 1803+78
18 01 36	44 03		1.4 ± 0.03	1.6 ± 0.05	1.6 ± 0.05	1.6 ± 0.08	0.9 ± 0.1	0.1 ± 0.1	GB6 J1801+4404
18 03 03	-65 07	199	1.2 ± 0.03	1.2 ± 0.04	1.4 ± 0.05	0.7 ± 0.08	0.9 ± 0.2	0.0 ± 0.1	PMN J1803-6507
18 06 44	69 49	067	1.4 ± 0.02	1.3 ± 0.03	1.1 ± 0.04	0.9 ± 0.05	1.0 ± 0.08	-0.4 ± 0.08	GB6 J1806+6949
18 08 34	57 01		0.5 ± 0.02	0.6 ± 0.04	1.0 ± 0.04	1.1 ± 0.07	...	1.0 ± 0.2	GB6 J1808+5709 ^a
18 09 01	45 45		0.6 ± 0.03	0.6 ± 0.04	0.5 ± 0.04	0.4 ± 0.08	...	-0.1 ± 0.3	GB6 J1808+4542
18 11 55	06 48		0.8 ± 0.03	0.7 ± 0.05	0.8 ± 0.05	0.5 ± 0.1	...	-0.2 ± 0.2	GB6 J1812+0651
18 12 33	55 51		0.2 ± 0.02	0.2 ± 0.04	0.4 ± 0.04	0.7 ± 0.08	0.6 ± 0.1	1.2 ± 0.3	...
18 19 51	-55 21		0.7 ± 0.03	0.2 ± 0.05	0.5 ± 0.05	-0.8 ± 0.4	PMN J1819-5521
18 20 04	-63 42	200	1.6 ± 0.03	1.4 ± 0.04	1.5 ± 0.05	1.6 ± 0.09	1.5 ± 0.2	-0.1 ± 0.1	PMN J1819-6345
18 24 08	56 49	053	1.5 ± 0.03	1.2 ± 0.04	1.3 ± 0.04	1.0 ± 0.07	0.9 ± 0.1	-0.4 ± 0.1	GB6 J1824+5650
18 25 19	67 38		0.1 ± 0.03	0.4 ± 0.04	0.9 ± 0.08	2.0 ± 0.5	...
18 29 42	48 45	046	3.0 ± 0.03	2.9 ± 0.05	2.6 ± 0.05	2.1 ± 0.09	1.7 ± 0.1	-0.3 ± 0.06	GB6 J1829+4844
18 32 49	68 42		0.4 ± 0.03	0.7 ± 0.05	0.6 ± 0.09	1.0 ± 0.4	GB6 J1832+6848
18 34 33	-58 56		1.3 ± 0.03	1.3 ± 0.04	1.2 ± 0.05	0.7 ± 0.09	1.0 ± 0.2	-0.2 ± 0.1	PMN J1834-5856
18 35 07	32 46		0.9 ± 0.03	0.8 ± 0.04	0.6 ± 0.05	0.4 ± 0.08	0.7 ± 0.2	-0.4 ± 0.2	GB6 J1835+3241
18 37 29	-71 05	192	2.1 ± 0.03	2.0 ± 0.05	1.7 ± 0.05	1.4 ± 0.06	...	-0.4 ± 0.08	PMN J1837-7108
18 38 17	67 22		...	0.7 ± 0.04	0.9 ± 0.04	0.8 ± 0.06	0.6 ± 0.09	0.1 ± 0.3	GB6 J1838+6722
18 40 36	79 47	073	1.5 ± 0.03	1.0 ± 0.04	0.6 ± 0.04	-1.3 ± 0.2	1Jy 1845+79
18 42 48	68 09	066	1.3 ± 0.02	1.4 ± 0.04	1.4 ± 0.03	1.5 ± 0.05	0.9 ± 0.09	0.1 ± 0.07	GB6 J1842+6809 ^a
18 48 27	32 20		0.5 ± 0.03	0.2 ± 0.04	0.2 ± 0.05	...	0.9 ± 0.2	0.2 ± 0.3	GB6 J1848+3219
18 49 32	67 05	065	1.9 ± 0.02	2.1 ± 0.04	2.1 ± 0.03	2.1 ± 0.07	...	0.2 ± 0.06	GB6 J1849+6705 ^a
18 50 41	28 23	028	1.6 ± 0.03	1.3 ± 0.04	1.3 ± 0.04	0.8 ± 0.08	...	-0.5 ± 0.1	GB6 J1850+2825
18 52 37	40 27		0.5 ± 0.03	0.7 ± 0.04	0.7 ± 0.05	0.7 ± 0.3	GB6 J1852+4019
19 01 46	-36 59		1.6 ± 0.04	1.6 ± 0.05	1.3 ± 0.06	1.9 ± 0.1	4.6 ± 0.2	0.5 ± 0.08	...
19 02 49	31 54	034	1.5 ± 0.03	1.4 ± 0.04	1.0 ± 0.04	-0.5 ± 0.2	GB6 J1902+3159
19 11 07	-20 07		2.4 ± 0.04	2.6 ± 0.06	2.7 ± 0.07	2.6 ± 0.1	2.5 ± 0.2	0.1 ± 0.07	PMN J1911-2006
19 15 12	-80 04		1.0 ± 0.03	0.6 ± 0.04	0.5 ± 0.05	-1.0 ± 0.3	PMN J1912-8010
19 23 30	-21 05	008	2.3 ± 0.04	2.3 ± 0.05	2.6 ± 0.07	2.5 ± 0.1	2.0 ± 0.2	0.1 ± 0.09	PMN J1923-2104
19 24 28	33 21		0.6 ± 0.03	0.7 ± 0.04	0.8 ± 0.04	0.8 ± 0.08	0.9 ± 0.2	0.3 ± 0.2	GB6 J1924+3329
19 24 52	-29 14		14.5 ± 0.04	13.7 ± 0.07	12.9 ± 0.07	11.7 ± 0.1	9.5 ± 0.2	-0.2 ± 0.02	PMN J1924-2914
19 27 40	61 19	059	0.9 ± 0.02	0.8 ± 0.04	0.7 ± 0.04	0.9 ± 0.07	...	-0.1 ± 0.2	GB6 J1927+6117
19 27 43	73 57	070	3.8 ± 0.03	3.7 ± 0.04	3.3 ± 0.05	3.0 ± 0.08	1.6 ± 0.1	-0.2 ± 0.04	GB6 J1927+7357
19 37 05	-39 58		1.0 ± 0.03	1.0 ± 0.05	1.0 ± 0.06	1.2 ± 0.1	...	0.0 ± 0.2	PMN J1937-3957
19 38 37	04 51		0.9 ± 0.03	0.7 ± 0.05	0.6 ± 0.06	-0.8 ± 0.3	GB6 J1938+0448 ^a
19 38 54	-63 41		0.9 ± 0.03	0.7 ± 0.04	0.7 ± 0.05	0.7 ± 0.1	...	-0.4 ± 0.2	PMN J1939-6342 ^a
19 39 17	-15 25		1.1 ± 0.03	1.2 ± 0.05	1.3 ± 0.06	0.8 ± 0.1	...	0.1 ± 0.2	PMN J1939-1525
19 40 43	-69 19		1.0 ± 0.02	1.0 ± 0.04	0.7 ± 0.04	-0.4 ± 0.2	...
19 41 52	-76 01		0.2 ± 0.03	0.5 ± 0.04	0.6 ± 0.04	1.0 ± 0.08	1.2 ± 0.1	1.2 ± 0.2	PMN J1942-7555 ^a
19 51 25	67 49		0.8 ± 0.02	1.2 ± 0.04	1.0 ± 0.04	1.0 ± 0.07	...	0.4 ± 0.1	GB6 J1951+6743
19 52 18	02 34		0.7 ± 0.03	0.7 ± 0.05	0.5 ± 0.06	0.7 ± 0.1	...	-0.1 ± 0.3	GB6 J1952+0230
19 55 40	51 39	051	1.2 ± 0.03	1.0 ± 0.04	0.9 ± 0.04	0.6 ± 0.08	...	-0.6 ± 0.2	GB6 J1955+5131

Table 18—Continued

RA [hms]	Dec [dm]	ID	K [Jy]	Ka [Jy]	Q [Jy]	V [Jy]	W [Jy]	α	5 GHz ID
19 58 02	−38 44	003	3.1 ± 0.04	3.2 ± 0.06	2.9 ± 0.07	2.5 ± 0.1	1.8 ± 0.2	-0.2 ± 0.07	PMN J1957-3845
20 00 58	−17 49	011	2.1 ± 0.04	2.0 ± 0.05	2.2 ± 0.06	2.3 ± 0.1	2.1 ± 0.2	0.1 ± 0.08	PMN J2000-1748
20 05 12	64 25		0.5 ± 0.02	0.8 ± 0.04	0.6 ± 0.04	0.3 ± 0.07	0.8 ± 0.1	0.3 ± 0.2	GB6 J2006+6424 ^a
20 05 51	77 53		0.7 ± 0.02	0.7 ± 0.04	0.7 ± 0.04	1.2 ± 0.07	0.8 ± 0.1	0.5 ± 0.1	1Jy 2007+77
20 07 45	66 15		0.8 ± 0.02	0.7 ± 0.04	0.6 ± 0.04	0.2 ± 0.08	...	-0.6 ± 0.2	GB6 J2007+6607
20 09 24	−48 49		1.1 ± 0.03	0.9 ± 0.05	0.6 ± 0.05	0.5 ± 0.1	...	-0.9 ± 0.3	PMN J2009-4849
20 09 54	72 32		0.6 ± 0.02	0.7 ± 0.04	0.9 ± 0.04	0.8 ± 0.07	0.8 ± 0.1	0.3 ± 0.2	GB6 J2009+7229
20 11 22	−15 48	014	1.9 ± 0.04	1.2 ± 0.05	1.0 ± 0.06	0.9 ± 0.1	...	-1.0 ± 0.2	PMN J2011-1546
20 16 14	65 56		0.8 ± 0.02	1.0 ± 0.04	0.9 ± 0.04	1.0 ± 0.07	...	0.2 ± 0.2	GB6 J2015+6554 ^a
20 22 29	61 36	063	1.5 ± 0.03	1.5 ± 0.05	1.4 ± 0.04	0.9 ± 0.08	0.6 ± 0.1	-0.3 ± 0.1	GB6 J2022+6137
20 23 49	54 27		0.4 ± 0.03	1.0 ± 0.04	1.1 ± 0.04	0.9 ± 0.08	0.7 ± 0.1	0.7 ± 0.2	GB6 J2023+5427
20 24 25	17 11	031	1.2 ± 0.03	1.3 ± 0.05	1.2 ± 0.05	1.3 ± 0.1	0.9 ± 0.2	0.1 ± 0.1	GB6 J2024+1718
20 25 44	−07 36		0.7 ± 0.04	1.0 ± 0.06	1.2 ± 0.06	1.3 ± 0.1	...	0.6 ± 0.2	PMN J2025-0735
20 34 46	−68 46	194	0.7 ± 0.03	0.8 ± 0.04	1.0 ± 0.04	1.1 ± 0.06	1.0 ± 0.1	0.4 ± 0.1	PMN J2035-6846
20 35 10	10 54		0.5 ± 0.03	0.8 ± 0.05	0.6 ± 0.06	...	1.2 ± 0.2	0.6 ± 0.2	GB6 J2035+1055
20 56 12	−47 16	208	2.9 ± 0.04	3.1 ± 0.06	2.9 ± 0.07	2.7 ± 0.1	2.6 ± 0.2	-0.1 ± 0.06	PMN J2056-4714
20 56 36	31 22		2.7 ± 0.03	0.6 ± 0.09	...	-1.5 ± 0.3	...
21 01 31	03 44		1.3 ± 0.03	1.1 ± 0.05	0.7 ± 0.06	1.1 ± 0.1	1.1 ± 0.2	-0.4 ± 0.2	GB6 J2101+0341
21 02 56	−78 31		0.6 ± 0.03	0.4 ± 0.04	0.7 ± 0.05	0.4 ± 0.3	PMN J2105-7825 ^a
21 07 27	−25 22		0.9 ± 0.03	0.9 ± 0.05	0.6 ± 0.06	0.6 ± 0.1	...	-0.4 ± 0.3	PMN J2107-2526
21 09 34	−41 11	001	1.5 ± 0.03	1.4 ± 0.05	1.1 ± 0.06	1.2 ± 0.1	1.8 ± 0.2	-0.2 ± 0.1	PMN J2109-4110
21 09 42	35 37	049	0.6 ± 0.03	0.7 ± 0.04	0.6 ± 0.04	0.7 ± 0.07	...	0.1 ± 0.2	GB6 J2109+3532 ^a
21 21 00	−80 44		0.1 ± 0.03	0.3 ± 0.04	0.5 ± 0.05	0.7 ± 0.1	...	1.6 ± 0.6	...
21 23 42	05 36	027	1.9 ± 0.04	1.4 ± 0.05	1.1 ± 0.06	0.9 ± 0.1	0.6 ± 0.2	-0.9 ± 0.1	GB6 J2123+0535
21 24 18	25 13		0.8 ± 0.03	0.6 ± 0.05	0.6 ± 0.06	0.3 ± 0.1	1.3 ± 0.2	-0.0 ± 0.2	...
21 31 33	−12 06	017	2.7 ± 0.04	2.5 ± 0.07	2.5 ± 0.07	2.3 ± 0.1	1.6 ± 0.2	-0.2 ± 0.08	PMN J2131-1207
21 34 07	−01 53	020	2.3 ± 0.04	2.1 ± 0.06	1.7 ± 0.06	1.8 ± 0.1	1.9 ± 0.2	-0.3 ± 0.09	PMN J2134-0153
21 36 37	00 41	025	4.9 ± 0.04	3.7 ± 0.07	3.0 ± 0.07	1.8 ± 0.1	1.5 ± 0.2	-0.9 ± 0.07	GB6 J2136+0041
21 39 17	14 25	041	2.5 ± 0.04	2.4 ± 0.06	2.0 ± 0.07	1.4 ± 0.1	1.3 ± 0.2	-0.4 ± 0.1	GB6 J2139+1423
21 43 25	17 43	044	1.2 ± 0.03	1.6 ± 0.05	0.9 ± 0.05	1.2 ± 0.1	0.9 ± 0.2	-0.0 ± 0.1	GB6 J2143+1743 ^a
21 47 29	−75 40		1.0 ± 0.03	0.8 ± 0.04	0.9 ± 0.05	0.5 ± 0.08	...	-0.4 ± 0.2	PMN J2147-7536 ^a
21 47 52	−77 59	184	1.8 ± 0.03	1.7 ± 0.04	1.4 ± 0.05	0.8 ± 0.08	...	-0.5 ± 0.1	PMN J2146-7755
21 48 05	06 57	037	7.3 ± 0.04	6.9 ± 0.06	6.7 ± 0.07	6.2 ± 0.1	5.0 ± 0.2	-0.2 ± 0.03	GB6 J2148+0657
21 51 50	−30 27		1.2 ± 0.03	1.1 ± 0.05	1.3 ± 0.06	1.4 ± 0.1	1.5 ± 0.2	0.2 ± 0.1	PMN J2151-3028
21 57 06	−69 42	190	3.9 ± 0.03	3.1 ± 0.05	2.8 ± 0.05	2.2 ± 0.08	...	-0.6 ± 0.06	PMN J2157-6941
21 58 05	−15 02	018	1.9 ± 0.04	1.8 ± 0.07	1.8 ± 0.06	1.3 ± 0.1	...	-0.2 ± 0.1	PMN J2158-1501
22 02 51	42 17	058	3.8 ± 0.03	4.0 ± 0.05	3.9 ± 0.05	3.5 ± 0.1	...	-0.0 ± 0.05	GB6 J2202+4216
22 03 20	31 46	054	2.8 ± 0.03	2.4 ± 0.05	2.2 ± 0.06	1.7 ± 0.09	1.4 ± 0.2	-0.4 ± 0.08	GB6 J2203+3145
22 03 23	17 23	045	1.4 ± 0.03	1.6 ± 0.05	1.5 ± 0.05	1.2 ± 0.1	...	0.1 ± 0.1	GB6 J2203+1725
22 06 12	−18 38	016	2.0 ± 0.04	1.6 ± 0.05	1.4 ± 0.06	1.0 ± 0.1	...	-0.6 ± 0.1	PMN J2206-1835
22 07 07	−53 48		1.0 ± 0.03	0.8 ± 0.04	0.7 ± 0.05	0.3 ± 0.09	...	-0.6 ± 0.2	PMN J2207-5346
22 11 42	23 53	050	1.1 ± 0.03	1.6 ± 0.05	1.7 ± 0.05	1.5 ± 0.09	1.2 ± 0.2	0.4 ± 0.1	GB6 J2212+2355
22 12 43	−25 27		0.8 ± 0.03	0.8 ± 0.05	0.5 ± 0.06	1.1 ± 0.1	...	0.1 ± 0.2	PMN J2213-2529 ^a
22 18 50	−03 35	030	2.0 ± 0.04	1.3 ± 0.05	1.4 ± 0.06	1.3 ± 0.1	...	-0.6 ± 0.1	PMN J2218-0335
22 25 36	21 19		1.1 ± 0.03	1.3 ± 0.05	1.3 ± 0.06	0.9 ± 0.09	1.2 ± 0.2	0.1 ± 0.1	GB6 J2225+2118
22 25 46	−04 55	029	6.4 ± 0.04	5.8 ± 0.06	5.2 ± 0.07	4.4 ± 0.1	3.3 ± 0.2	-0.4 ± 0.04	PMN J2225-0457

Table 18—Continued

RA [hms]	Dec [dm]	ID	K [Jy]	Ka [Jy]	Q [Jy]	V [Jy]	W [Jy]	α	5 GHz ID
22 29 42	−08 33	024	2.2 ± 0.04	2.6 ± 0.06	2.6 ± 0.07	3.1 ± 0.1	2.5 ± 0.2	0.2 ± 0.08	PMN J2229-0832
22 29 49	−20 50		0.9 ± 0.03	0.8 ± 0.05	0.8 ± 0.06	1.0 ± 0.1	1.0 ± 0.2	−0.1 ± 0.2	PMN J2229-2049
22 31 02	−39 38		0.9 ± 0.03	1.2 ± 0.05	0.8 ± 0.05	1.1 ± 0.1	0.7 ± 0.2	0.1 ± 0.2	PMN J2230-3942
22 32 37	11 44	047	3.8 ± 0.04	4.2 ± 0.06	4.3 ± 0.07	4.4 ± 0.1	4.9 ± 0.2	0.2 ± 0.05	GB6 J2232+1143
22 35 09	−48 34	206	2.0 ± 0.03	2.0 ± 0.05	1.9 ± 0.06	1.7 ± 0.09	1.7 ± 0.2	−0.1 ± 0.08	PMN J2235-4835
22 36 21	28 25	057	1.1 ± 0.03	1.5 ± 0.05	1.4 ± 0.06	1.5 ± 0.1	...	0.4 ± 0.1	GB6 J2236+2828
22 39 30	−57 01	201	1.5 ± 0.03	1.6 ± 0.04	1.5 ± 0.05	1.3 ± 0.08	1.5 ± 0.1	−0.0 ± 0.09	PMN J2239-5701
22 42 34	−64 08		0.5 ± 0.03	0.8 ± 0.04	0.6 ± 0.04	0.7 ± 0.07	1.3 ± 0.1	0.5 ± 0.2	...
22 43 13	−25 48		0.7 ± 0.03	0.9 ± 0.05	0.7 ± 0.06	1.0 ± 0.1	1.0 ± 0.2	0.3 ± 0.2	PMN J2243-2544
22 45 31	−56 15		0.3 ± 0.02	0.2 ± 0.04	−1.4 ± 2	PMN J2246-5607
22 46 14	−12 07	021	2.1 ± 0.04	1.3 ± 0.05	1.2 ± 0.06	1.3 ± 0.1	1.2 ± 0.2	−0.8 ± 0.1	PMN J2246-1206
22 47 35	−37 01		0.3 ± 0.03	0.4 ± 0.05	0.8 ± 0.05	0.9 ± 0.1	0.8 ± 0.2	1.1 ± 0.3	PMN J2247-3657
22 53 49	13 39		0.6 ± 0.05	0.1 ± 0.08	0.2 ± 0.06	0.5 ± 0.1	1.7 ± 0.2	0.7 ± 0.2	GB6 J2254+1341 ^a
22 53 59	16 08	055	9.8 ± 0.04	10.6 ± 0.06	11.1 ± 0.07	12.3 ± 0.1	12.2 ± 0.2	0.2 ± 0.02	GB6 J2253+1608
22 55 43	42 01		1.0 ± 0.02	0.6 ± 0.04	0.7 ± 0.05	0.3 ± 0.09	...	−0.9 ± 0.2	GB6 J2255+4202
22 56 32	−20 12	019	0.9 ± 0.03	0.8 ± 0.05	0.9 ± 0.06	0.5 ± 0.1	...	−0.2 ± 0.2	PMN J2256-2011
22 58 05	−27 56	012	4.6 ± 0.04	4.7 ± 0.06	4.4 ± 0.07	3.9 ± 0.1	3.2 ± 0.2	−0.1 ± 0.05	PMN J2258-2758
23 02 46	−68 09		0.7 ± 0.03	0.4 ± 0.04	0.3 ± 0.04	−1.4 ± 0.5	PMN J2303-6807 ^a
23 11 33	34 28		0.7 ± 0.03	0.6 ± 0.05	0.7 ± 0.06	0.6 ± 0.09	...	−0.2 ± 0.3	GB6 J2311+3425
23 15 04	−31 36		1.1 ± 0.03	1.0 ± 0.05	0.9 ± 0.06	0.7 ± 0.1	...	−0.4 ± 0.2	PMN J2314-3138
23 15 56	−50 19	204	1.4 ± 0.03	1.3 ± 0.04	1.1 ± 0.05	0.6 ± 0.08	...	−0.4 ± 0.1	PMN J2315-5018
23 21 34	27 33		0.6 ± 0.03	0.4 ± 0.05	0.5 ± 0.06	0.7 ± 0.1	...	−0.2 ± 0.3	GB6 J2322+2732
23 22 25	44 48		1.2 ± 0.02	1.3 ± 0.04	1.0 ± 0.05	0.6 ± 0.08	0.7 ± 0.2	−0.2 ± 0.1	GB6 J2322+4445 ^a
23 22 51	51 06		1.0 ± 0.03	0.8 ± 0.04	0.7 ± 0.04	0.9 ± 0.08	...	−0.3 ± 0.2	GB6 J2322+5057 ^a
23 27 37	09 38		1.0 ± 0.03	0.8 ± 0.05	0.8 ± 0.06	1.3 ± 0.1	...	0.1 ± 0.2	GB6 J2327+0940 ^a
23 29 06	−47 32		1.6 ± 0.03	1.0 ± 0.04	1.1 ± 0.05	0.8 ± 0.09	1.2 ± 0.1	−0.5 ± 0.1	PMN J2329-4730
23 30 40	10 57		1.0 ± 0.03	1.2 ± 0.05	1.2 ± 0.06	1.1 ± 0.1	...	0.2 ± 0.2	GB6 J2330+1100
23 31 21	−16 00	032	0.8 ± 0.03	0.6 ± 0.05	0.4 ± 0.06	1.0 ± 0.1	...	−0.1 ± 0.2	PMN J2331-1556
23 33 44	−23 39		1.1 ± 0.03	1.0 ± 0.05	1.0 ± 0.06	1.1 ± 0.1	...	−0.0 ± 0.2	PMN J2333-2343 ^a
23 34 11	07 35		1.1 ± 0.03	1.3 ± 0.05	1.2 ± 0.06	1.5 ± 0.1	...	0.3 ± 0.2	GB6 J2334+0736
23 35 01	−01 28		0.6 ± 0.03	0.6 ± 0.05	0.8 ± 0.06	0.6 ± 0.1	1.0 ± 0.2	0.3 ± 0.2	PMN J2335-0131
23 35 27	−52 44	195	1.4 ± 0.03	1.0 ± 0.03	0.7 ± 0.04	0.5 ± 0.08	...	−1.0 ± 0.2	PMN J2336-5236 ^a
23 45 34	−16 00		1.7 ± 0.04	1.3 ± 0.05	1.5 ± 0.06	1.8 ± 0.1	...	−0.1 ± 0.1	PMN J2345-1555
23 46 51	09 30		1.3 ± 0.03	1.3 ± 0.05	0.8 ± 0.06	−0.4 ± 0.2	GB6 J2346+0930 ^a
23 48 01	−49 33		0.7 ± 0.02	0.9 ± 0.04	1.1 ± 0.05	1.0 ± 0.09	...	0.5 ± 0.2	...
23 48 12	−16 30	039	1.9 ± 0.04	1.9 ± 0.05	2.1 ± 0.07	2.2 ± 0.1	1.2 ± 0.2	0.1 ± 0.09	PMN J2348-1631
23 54 22	45 50	074	1.2 ± 0.03	1.0 ± 0.04	1.2 ± 0.05	1.0 ± 0.09	0.9 ± 0.2	−0.2 ± 0.1	GB6 J2354+4553
23 55 34	81 53		1.1 ± 0.03	0.7 ± 0.04	0.7 ± 0.05	0.8 ± 0.08	...	−0.5 ± 0.2	NVSS J2356+8152
23 56 01	49 53	075	1.1 ± 0.02	1.1 ± 0.04	0.9 ± 0.05	0.3 ± 0.08	...	−0.2 ± 0.2	GB6 J2355+4950
23 57 50	−53 14	189	1.7 ± 0.03	1.4 ± 0.05	1.3 ± 0.04	1.4 ± 0.07	1.2 ± 0.1	−0.3 ± 0.09	PMN J2357-5311
23 58 07	−10 15		1.5 ± 0.03	1.8 ± 0.05	1.6 ± 0.06	1.1 ± 0.1	1.4 ± 0.2	0.1 ± 0.1	PMN J2358-1020
23 58 49	−60 50	187	2.0 ± 0.03	1.6 ± 0.04	1.5 ± 0.04	1.5 ± 0.08	...	−0.4 ± 0.09	PMN J2358-6054

^aIndicates the source has multiple possible identifications.

^bSource J0322-3711 (Fornax A) is extended, and the fluxes listed were obtained by aperture photometry.

^cSource J1356+7644 is outside of the declination range of the GB6 and PMN catalogs. It was identified as QSO NVSSJ135755+764320 by Trushkin (2006, private communication).

^dSource J1632+8227 is outside of the declination range of the GB6 and PMN catalogs. It was identified as NGC 6251 by Trushkin (2003).

C. *WMAP* Nine-Year CMB-free QVW Point Source Catalog

Table 19. WMAP Nine-Year CMB-free QVW Point Source Catalog

RA [hms]	Dec [dm]	ID	Q [Jy]	V [Jy]	W [Jy]	5 GHz ID
00 04 29	−47 35		0.4 ± 0.1	0.5 ± 0.2	-0.3 ± 0.3	PMN J0004-4736
00 06 14	−06 25	060	2.0 ± 0.2	1.7 ± 0.2	0.7 ± 0.4	PMN J0006-0623
00 10 29	10 59		1.0 ± 0.2	1.2 ± 0.2	0.8 ± 0.3	GB6 J0010+1058
00 13 23	40 55		0.6 ± 0.2	0.5 ± 0.2	0.9 ± 0.3	GB6 J0013+4051
00 19 41	25 58		0.6 ± 0.2	0.3 ± 0.2	0.4 ± 0.3	GB6 J0019+2602
00 26 07	−35 12		1.3 ± 0.2	0.6 ± 0.2	0.6 ± 0.3	PMN J0026-3512
00 29 44	05 54		0.8 ± 0.2	0.4 ± 0.2	0.9 ± 0.3	GB6 J0029+0554B ^a
00 38 13	−02 05		0.6 ± 0.2	0.4 ± 0.2	0.7 ± 0.3	PMN J0038-0207
00 38 20	−24 59		0.6 ± 0.2	1.0 ± 0.2	0.8 ± 0.3	PMN J0038-2459
00 42 40	52 09		0.5 ± 0.2	0.2 ± 0.2	-0.5 ± 0.3	GB6 J0043+5203
00 47 29	−25 16	062	0.9 ± 0.2	0.7 ± 0.2	0.8 ± 0.3	PMN J0047-2517
00 47 44	−73 10		1.0 ± 0.2	0.9 ± 0.2	0.5 ± 0.3	PMN J0047-7308
00 48 59	31 55		0.5 ± 0.2	0.5 ± 0.2	0.5 ± 0.3	GB6 J0048+3157
00 49 08	−57 36	179	1.0 ± 0.2	0.9 ± 0.2	0.5 ± 0.3	PMN J0050-5738 ^a
00 50 57	−09 33	077	0.6 ± 0.2	0.7 ± 0.2	0.6 ± 0.3	PMN J0050-0928
00 51 15	−06 48		0.9 ± 0.2	1.1 ± 0.2	0.8 ± 0.3	PMN J0051-0650
00 51 40	70 48		0.4 ± 0.2	0.0 ± 0.2	-0.2 ± 0.3	...
00 57 43	30 25		0.8 ± 0.2	0.5 ± 0.2	0.2 ± 0.3	GB6 J0057+3021
00 58 50	00 04		0.5 ± 0.2	0.3 ± 0.2	0.1 ± 0.3	1Jy 0056-00
00 59 15	−56 56		0.7 ± 0.2	0.6 ± 0.2	0.5 ± 0.3	PMN J0058-5659
01 00 31	−72 09		1.0 ± 0.2	0.8 ± 0.2	0.3 ± 0.3	PMN J0059-7210
01 06 48	−40 33	171	2.1 ± 0.1	1.9 ± 0.2	1.2 ± 0.3	PMN J0106-4034
01 08 24	01 34	081	1.5 ± 0.2	1.1 ± 0.2	0.8 ± 0.3	GB6 J0108+0135 ^a
01 08 39	13 20	079	0.7 ± 0.2	0.6 ± 0.2	0.1 ± 0.3	GB6 J0108+1319
01 11 45	22 53		0.6 ± 0.2	0.0 ± 0.2	0.2 ± 0.3	GB6 J0112+2244
01 12 10	35 21		0.8 ± 0.2	0.4 ± 0.2	0.3 ± 0.3	GB6 J0112+3522
01 13 00	49 47		0.4 ± 0.2	0.5 ± 0.2	0.2 ± 0.3	GB6 J0113+4948
01 16 22	−11 36		1.1 ± 0.2	0.9 ± 0.2	0.4 ± 0.3	PMN J0116-1136
01 18 54	−21 37		0.5 ± 0.2	0.4 ± 0.2	0.3 ± 0.3	PMN J0118-2141
01 22 00	11 53		1.4 ± 0.2	0.5 ± 0.2	0.3 ± 0.3	GB6 J0121+1149
01 25 29	−00 09	086	0.9 ± 0.2	0.7 ± 0.2	0.2 ± 0.3	PMN J0125-0005 ^a
01 27 44	49 04		0.6 ± 0.3	0.4 ± 0.3	0.3 ± 0.3	GB6 J0128+4901 ^a
01 32 46	−16 57	097	1.5 ± 0.2	1.4 ± 0.2	0.9 ± 0.3	PMN J0132-1654
01 34 09	−38 41		0.6 ± 0.2	0.6 ± 0.2	0.7 ± 0.3	PMN J0134-3843
01 36 59	47 53	080	3.1 ± 0.2	3.1 ± 0.2	1.9 ± 0.3	GB6 J0136+4751
01 37 33	−24 30		1.5 ± 0.2	1.3 ± 0.2	1.2 ± 0.3	PMN J0137-2430
01 37 48	33 07		0.5 ± 0.2	0.1 ± 0.2	0.3 ± 0.3	GB6 J0137+3309

Table 19—Continued

RA [hms]	Dec [dm]	ID	Q [Jy]	V [Jy]	W [Jy]	5 GHz ID	
01 41 30	−09 28		0.5 ± 0.2	0.6 ± 0.2	0.2 ± 0.3	PMN J0141-0928	^a
01 49 06	53 50		0.4 ± 0.2	-0.1 ± 0.2	-0.5 ± 0.3	...	
01 52 37	22 06		1.1 ± 0.2	1.0 ± 0.2	0.5 ± 0.3	GB6 J0152+2206	
01 55 07	47 37		0.4 ± 0.2	0.3 ± 0.2	0.2 ± 0.3	GB6 J0154+4743	
02 04 57	15 16	092	1.0 ± 0.2	0.8 ± 0.2	0.4 ± 0.3	GB6 J0204+1514	
02 04 59	−17 03		0.9 ± 0.2	0.7 ± 0.2	0.3 ± 0.3	PMN J0204-1701	
02 05 13	32 09	085	1.6 ± 0.2	0.9 ± 0.2	0.9 ± 0.3	GB6 J0205+3212	
02 10 46	−51 01	158	2.5 ± 0.1	2.4 ± 0.2	1.7 ± 0.3	PMN J0210-5101	
02 18 02	01 38	096	0.4 ± 0.2	0.7 ± 0.2	0.1 ± 0.3	GB6 J0217+0144	
02 21 18	35 49		0.8 ± 0.2	0.5 ± 0.2	0.4 ± 0.3	GB6 J0221+3556	
02 22 46	−34 43	137	0.5 ± 0.1	0.6 ± 0.2	0.1 ± 0.3	PMN J0222-3441	
02 23 19	42 59	084	1.2 ± 0.2	0.4 ± 0.2	0.5 ± 0.3	GB6 J0223+4259	^a
02 29 19	−78 37		0.3 ± 0.1	0.1 ± 0.2	0.2 ± 0.3	PMN J0229-7847	
02 31 37	13 29		0.8 ± 0.2	0.7 ± 0.2	0.3 ± 0.3	GB6 J0231+1323	
02 37 48	28 48	093	2.6 ± 0.2	2.4 ± 0.2	2.0 ± 0.3	GB6 J0237+2848	
02 38 40	16 34		1.5 ± 0.2	1.6 ± 0.2	1.4 ± 0.3	GB6 J0238+1637	
02 41 06	−08 15		0.6 ± 0.2	0.5 ± 0.2	-0.1 ± 0.3	PMN J0241-0815	
02 42 33	11 05		0.8 ± 0.2	0.7 ± 0.2	0.9 ± 0.3	GB6 J0242+1101	^a
02 53 22	−54 41	155	1.9 ± 0.1	1.9 ± 0.2	1.4 ± 0.3	PMN J0253-5441	
02 59 25	−00 16		0.7 ± 0.2	0.4 ± 0.2	0.1 ± 0.3	PMN J0259-0020	
03 03 45	47 17		0.7 ± 0.2	0.4 ± 0.2	0.6 ± 0.3	GB6 J0303+4716	
03 03 51	−62 10	162	1.3 ± 0.2	1.3 ± 0.2	0.6 ± 0.3	PMN J0303-6211	
03 04 52	33 50		0.5 ± 0.2	0.3 ± 0.2	0.2 ± 0.3	GB6 J0304+3348	
03 08 33	04 06	102	0.9 ± 0.2	0.9 ± 0.2	0.7 ± 0.3	GB6 J0308+0406	
03 09 14	10 25		1.0 ± 0.2	1.0 ± 0.2	0.3 ± 0.3	GB6 J0309+1029	
03 09 33	−60 55	160	0.5 ± 0.2	0.5 ± 0.2	0.4 ± 0.3	PMN J0309-6058	
03 12 45	41 22		0.8 ± 0.7	0.5 ± 0.5	0.4 ± 0.4	GB6 J0313+4120	
03 14 05	−76 55	174	0.8 ± 0.1	0.5 ± 0.2	0.7 ± 0.3	PMN J0311-7651	^a
03 19 48	41 31	094	8.7 ± 0.2	7.0 ± 0.2	5.1 ± 0.3	GB6 J0319+4130	
03 22 08	−37 12	138	2.3 ± 0.1	1.2 ± 0.2	0.3 ± 0.3	PMN J0321-3711	
03 25 33	22 23		0.9 ± 0.2	0.7 ± 0.2	0.5 ± 0.4	GB6 J0325+2223	^a
03 29 55	−23 54	123	0.9 ± 0.1	0.9 ± 0.2	0.6 ± 0.3	PMN J0329-2357	
03 34 20	−40 08	146	1.6 ± 0.2	1.6 ± 0.2	1.1 ± 0.3	PMN J0334-4008	
03 36 48	−13 06		0.5 ± 0.2	0.3 ± 0.2	-0.0 ± 0.3	PMN J0336-1302	
03 39 21	−01 45	106	1.9 ± 0.2	1.7 ± 0.2	1.8 ± 0.3	PMN J0339-0146	
03 40 23	−21 22		0.8 ± 0.2	1.0 ± 0.2	0.6 ± 0.3	PMN J0340-2119	
03 48 27	−16 09		0.7 ± 0.2	0.6 ± 0.2	0.9 ± 0.3	PMN J0348-1610	

Table 19—Continued

RA [hms]	Dec [dm]	ID	Q [Jy]	V [Jy]	W [Jy]	5 GHz ID
03 48 53	–27 54	129	0.6 ± 0.1	0.7 ± 0.2	0.4 ± 0.3	PMN J0348-2749
03 51 15	–11 57		0.4 ± 0.2	0.2 ± 0.2	0.3 ± 0.3	PMN J0351-1153
03 59 07	10 23		0.6 ± 0.2	0.3 ± 0.2	0.0 ± 0.4	GB6 J0358+1026
04 02 51	–01 43		0.2 ± 0.2	-0.4 ± 0.2	-0.8 ± 0.4	...
04 02 56	26 03		0.5 ± 0.2	0.6 ± 0.2	-0.2 ± 0.4	GB6 J0403+2600
04 03 49	–36 02	136	2.7 ± 0.2	2.5 ± 0.2	2.0 ± 0.3	PMN J0403-3605
04 03 59	09 13		0.1 ± 0.2	-0.1 ± 0.2	-0.3 ± 0.3	GB6 J0404+0909
04 05 33	–13 01	114	1.3 ± 0.2	1.1 ± 0.2	0.7 ± 0.3	PMN J0405-1308
04 06 49	–38 27	141	0.8 ± 0.2	0.7 ± 0.2	0.6 ± 0.3	PMN J0406-3826
04 07 11	07 43		0.6 ± 0.2	-0.1 ± 0.2	-0.3 ± 0.3	GB6 J0407+0742
04 07 54	–12 16		0.7 ± 0.2	0.7 ± 0.2	0.4 ± 0.3	PMN J0407-1211
04 11 01	11 27		0.3 ± 0.2	-0.2 ± 0.2	-0.6 ± 0.3	...
04 11 12	76 56	082	0.6 ± 0.2	0.6 ± 0.2	0.5 ± 0.3	1Jy 0403+76
04 11 53	11 19		0.2 ± 0.2	-0.2 ± 0.2	-0.2 ± 0.3	...
04 16 19	–20 51		0.6 ± 0.2	0.4 ± 0.2	0.8 ± 0.3	PMN J0416-2056
04 23 10	–01 18	110	6.3 ± 0.2	5.9 ± 0.2	4.4 ± 0.3	PMN J0423-0120
04 23 10	02 22		0.4 ± 0.2	0.4 ± 0.2	0.3 ± 0.3	GB6 J0422+0219
04 24 34	00 37	109	1.5 ± 0.6	0.9 ± 0.4	1.2 ± 0.4	GB6 J0424+0036
04 24 42	–37 56	140	1.3 ± 0.1	1.1 ± 0.2	0.7 ± 0.3	PMN J0424-3756
04 29 00	–37 59		1.3 ± 0.1	1.3 ± 0.2	0.8 ± 0.3	PMN J0428-3756 ^a
04 33 17	05 22	108	2.1 ± 0.2	2.1 ± 0.2	1.7 ± 0.4	GB6 J0433+0521
04 40 25	–43 30	147	1.3 ± 0.2	0.9 ± 0.2	0.8 ± 0.3	PMN J0440-4332
04 42 32	–00 14		0.9 ± 0.2	0.8 ± 0.2	0.6 ± 0.3	PMN J0442-0017
04 50 50	–81 04	175	1.4 ± 0.1	1.2 ± 0.2	0.9 ± 0.3	PMN J0450-8100
04 53 26	–28 03	131	1.2 ± 0.1	1.4 ± 0.2	1.0 ± 0.3	PMN J0453-2807
04 55 21	–46 16	151	3.1 ± 0.2	2.6 ± 0.2	1.8 ± 0.3	PMN J0455-4616
04 57 00	–23 24	128	2.3 ± 0.1	1.9 ± 0.2	1.7 ± 0.3	PMN J0457-2324
04 57 30	06 40		0.5 ± 0.2	0.6 ± 0.2	0.4 ± 0.3	GB6 J0457+0645 ^a
05 01 22	–02 02		1.0 ± 0.2	0.5 ± 0.2	0.6 ± 0.3	PMN J0501-0159
05 03 13	02 05		0.6 ± 0.2	0.2 ± 0.2	-0.3 ± 0.4	GB6 J0503+0202
05 04 28	–07 32		0.4 ± 0.2	-0.1 ± 0.2	0.1 ± 0.3	...
05 06 24	–06 40		0.4 ± 0.2	0.2 ± 0.2	0.3 ± 0.3	PMN J0506-0645
05 06 52	–61 05	154	1.4 ± 0.1	0.9 ± 0.2	0.7 ± 0.3	PMN J0506-6109 ^a
05 09 54	10 18		0.3 ± 0.2	-0.0 ± 0.2	-0.0 ± 0.3	GB6 J0509+1012
05 10 44	–31 36		0.4 ± 0.1	-0.0 ± 0.2	0.2 ± 0.3	PMN J0510-3142
05 13 49	–22 00	127	0.6 ± 0.2	0.5 ± 0.2	0.9 ± 0.3	PMN J0513-2159
05 16 36	–62 05		0.7 ± 0.2	0.5 ± 0.2	0.2 ± 0.3	PMN J0516-6207

Table 19—Continued

RA [hms]	Dec [dm]	ID	Q [Jy]	V [Jy]	W [Jy]	5 GHz ID	
05 19 36	−45 44	150	4.3 ± 0.2	3.3 ± 0.2	2.3 ± 0.3	PMN J0519-4546	^a
05 23 00	−36 31	139	3.3 ± 0.2	3.2 ± 0.2	2.9 ± 0.3	PMN J0522-3628	
05 27 09	−12 33	122	1.1 ± 0.2	0.6 ± 0.2	0.5 ± 0.3	PMN J0527-1241	
05 33 26	48 21		0.9 ± 0.2	0.8 ± 0.2	0.8 ± 0.3	GB6 J0533+4822	
05 35 38	−66 10		0.4 ± 0.6	0.1 ± 0.3	0.2 ± 0.3	PMN J0535-6601	^a
05 36 20	−33 55		0.3 ± 0.1	0.3 ± 0.2	-0.2 ± 0.3	PMN J0536-3401	
05 38 42	−44 07	148	6.0 ± 0.2	5.8 ± 0.2	4.9 ± 0.3	PMN J0538-4405	
05 40 01	−28 42		0.7 ± 0.1	0.4 ± 0.2	0.5 ± 0.3	PMN J0539-2839	
05 40 13	−54 15	152	0.8 ± 0.1	0.6 ± 0.2	0.4 ± 0.3	PMN J0540-5418	
05 42 02	49 57	095	0.9 ± 0.2	0.3 ± 0.2	0.1 ± 0.3	GB6 J0542+4951	
05 42 03	−73 36		0.4 ± 0.1	0.3 ± 0.2	0.0 ± 0.2	PMN J0541-7332	
05 42 13	47 34		0.4 ± 0.2	0.3 ± 0.2	0.5 ± 0.4	GB6 J0541+4729	
05 49 40	−57 35	153	0.9 ± 0.1	0.7 ± 0.2	0.4 ± 0.3	PMN J0550-5732	^a
05 52 02	37 51		0.7 ± 0.2	0.5 ± 0.2	0.4 ± 0.3	GB6 J0552+3754	^a
05 55 32	39 40	100	1.3 ± 0.2	0.6 ± 0.2	0.4 ± 0.3	GB6 J0555+3948	
06 06 09	40 31		0.7 ± 0.2	0.3 ± 0.2	0.2 ± 0.3	GB6 J0605+4030	
06 08 11	−60 33		0.4 ± 0.1	0.3 ± 0.2	-0.1 ± 0.2	PMN J0607-6031	
06 08 42	67 14	091	0.3 ± 0.1	0.2 ± 0.2	-0.5 ± 0.3	GB6 J0607+6720	
06 09 02	−22 16		0.6 ± 0.1	0.6 ± 0.2	0.4 ± 0.3	PMN J0608-2220	
06 09 44	−15 43	126	2.7 ± 0.2	2.1 ± 0.2	0.8 ± 0.3	PMN J0609-1542	
06 20 16	−25 11		0.4 ± 0.1	0.2 ± 0.2	0.0 ± 0.3	PMN J0620-2515	
06 23 03	−64 36		0.6 ± 0.1	0.6 ± 0.2	0.7 ± 0.2	PMN J0623-6436	
06 25 40	82 01		0.4 ± 0.1	0.0 ± 0.2	-0.0 ± 0.3	1Jy 0615+82	
06 27 06	−05 52		0.3 ± 0.2	0.2 ± 0.2	-0.3 ± 0.3	PMN J0627-0553	
06 27 27	−35 36		0.3 ± 0.1	-0.2 ± 0.2	-0.6 ± 0.3	PMN J0627-3529	
06 29 35	−20 01	130	1.0 ± 0.2	0.7 ± 0.2	0.8 ± 0.3	PMN J0629-1959	^a
06 34 27	−23 31		0.4 ± 0.2	0.4 ± 0.2	0.2 ± 0.3	PMN J0634-2335	
06 34 48	−75 14	167	3.1 ± 0.1	2.5 ± 0.2	1.6 ± 0.2	PMN J0635-7516	
06 36 27	−20 36	134	0.5 ± 0.2	0.6 ± 0.2	0.4 ± 0.3	PMN J0636-2041	^a
06 39 16	73 23	087	0.7 ± 0.1	0.4 ± 0.2	0.6 ± 0.3	GB6 J0639+7324	
06 44 31	−23 11		0.2 ± 0.2	0.2 ± 0.2	0.2 ± 0.3	...	
06 44 32	−24 40		0.2 ± 0.1	-0.0 ± 0.2	-0.3 ± 0.3	...	
06 46 20	44 48	099	1.8 ± 0.2	1.3 ± 0.2	1.0 ± 0.3	GB6 J0646+4451	
06 47 16	−20 28		0.2 ± 0.2	0.2 ± 0.2	0.2 ± 0.3	...	
06 48 10	−30 40		0.4 ± 0.1	0.2 ± 0.2	0.1 ± 0.3	PMN J0648-3044	
06 48 23	−17 50		0.5 ± 0.2	0.4 ± 0.2	0.6 ± 0.3	PMN J0648-1744	
06 50 20	−16 33		1.7 ± 0.2	1.6 ± 0.2	1.1 ± 0.3	PMN J0650-1637	^a

Table 19—Continued

RA [hms]	Dec [dm]	ID	Q [Jy]	V [Jy]	W [Jy]	5 GHz ID
06 50 30	60 02		0.5 ± 0.2	0.2 ± 0.2	0.6 ± 0.3	GB6 J0650+6001
06 54 14	37 05		0.4 ± 0.2	0.4 ± 0.2	0.5 ± 0.3	GB6 J0653+3705
06 58 06	–61 24		0.3 ± 0.1	0.2 ± 0.2	0.2 ± 0.3	...
06 59 52	17 12		1.0 ± 0.2	0.5 ± 0.2	0.4 ± 0.3	GB6 J0700+1709
07 02 06	26 40		0.2 ± 0.2	0.0 ± 0.2	-0.6 ± 0.4	GB6 J0702+2644
07 10 44	47 34		0.7 ± 0.2	0.7 ± 0.2	-0.4 ± 0.3	GB6 J0710+4732 ^a
07 15 57	–68 31		0.3 ± 0.1	-0.0 ± 0.2	0.2 ± 0.2	PMN J0715-6829
07 17 39	45 39		0.6 ± 0.2	0.6 ± 0.2	0.4 ± 0.4	GB6 J0717+4538
07 19 40	33 11		0.6 ± 0.2	0.2 ± 0.2	0.3 ± 0.3	GB6 J0719+3307
07 21 11	04 03		0.3 ± 0.2	0.4 ± 0.2	-0.0 ± 0.3	GB6 J0721+0406
07 22 08	71 21		2.0 ± 0.1	1.9 ± 0.2	2.1 ± 0.3	GB6 J0721+7120
07 25 06	14 24		0.6 ± 0.2	0.5 ± 0.2	0.3 ± 0.3	GB6 J0725+1425
07 25 46	–00 48		1.4 ± 0.2	1.2 ± 0.2	0.8 ± 0.3	PMN J0725-0054
07 28 17	67 49		0.5 ± 0.2	0.3 ± 0.2	0.2 ± 0.3	GB6 J0728+6748
07 30 06	–11 38		3.9 ± 0.2	3.0 ± 0.2	1.7 ± 0.3	PMN J0730-1141
07 34 08	50 22		0.4 ± 0.2	1.0 ± 0.2	1.0 ± 0.4	GB6 J0733+5022
07 34 53	–77 12		0.3 ± 0.1	-0.1 ± 0.2	-0.1 ± 0.3	PMN J0734-7711
07 38 17	17 45	113	0.8 ± 0.2	0.7 ± 0.2	0.1 ± 0.3	GB6 J0738+1742
07 39 26	01 37	124	1.8 ± 0.2	1.7 ± 0.2	1.0 ± 0.3	GB6 J0739+0136
07 40 12	29 00		0.4 ± 0.2	0.2 ± 0.2	-0.2 ± 0.4	GB6 J0740+2852
07 41 41	31 15	107	0.4 ± 0.2	0.3 ± 0.2	0.3 ± 0.3	GB6 J0741+3112
07 43 01	–67 28	161	0.4 ± 0.2	0.5 ± 0.2	0.6 ± 0.3	PMN J0743-6726 ^a
07 45 28	10 00		0.4 ± 0.2	0.0 ± 0.2	-0.4 ± 0.3	GB6 J0745+1011 ^a
07 46 07	–00 42		0.5 ± 0.2	0.6 ± 0.2	0.7 ± 0.3	PMN J0745-0044
07 48 28	23 59		1.0 ± 0.2	0.6 ± 0.2	0.6 ± 0.4	GB6 J0748+2400
07 48 41	–16 42		0.3 ± 0.2	0.1 ± 0.2	-0.5 ± 0.3	PMN J0748-1639 ^a
07 50 18	48 12		0.6 ± 0.2	0.3 ± 0.2	0.1 ± 0.3	GB6 J0750+4814
07 50 50	12 32	117	2.7 ± 0.2	2.5 ± 0.2	2.0 ± 0.3	GB6 J0750+1231 ^a
07 53 08	53 49		0.4 ± 0.2	0.3 ± 0.2	0.5 ± 0.3	GB6 J0753+5353
07 56 20	–73 47		0.2 ± 0.1	0.1 ± 0.2	-0.2 ± 0.3	PMN J0757-7353 ^a
07 57 01	09 53	120	1.4 ± 0.2	1.2 ± 0.2	1.0 ± 0.3	GB6 J0757+0956
08 07 42	49 51		0.4 ± 0.2	-0.1 ± 0.2	-0.2 ± 0.3	GB6 J0808+4950 ^a
08 08 17	–07 50	133	1.2 ± 0.2	1.5 ± 0.2	0.9 ± 0.3	PMN J0808-0751
08 11 18	01 46		0.7 ± 0.2	0.4 ± 0.2	0.6 ± 0.4	GB6 J0811+0146
08 16 56	–24 20	145	0.5 ± 0.2	0.4 ± 0.2	0.2 ± 0.3	PMN J0816-2421
08 23 40	22 29		0.7 ± 0.2	0.4 ± 0.2	0.1 ± 0.4	GB6 J0823+2223
08 24 45	55 43		0.3 ± 0.2	0.2 ± 0.2	-0.0 ± 0.3	GB6 J0824+5552

Table 19—Continued

RA [hms]	Dec [dm]	ID	Q [Jy]	V [Jy]	W [Jy]	5 GHz ID	
08 25 09	39 14		0.9 ± 0.2	0.7 ± 0.2	0.2 ± 0.3	GB6 J0824+3916	^a
08 25 37	03 07	125	1.2 ± 0.2	1.3 ± 0.2	0.7 ± 0.4	GB6 J0825+0309	
08 26 03	−22 28		0.5 ± 0.2	0.7 ± 0.2	0.0 ± 0.3	PMN J0826-2230	
08 30 43	24 09	112	1.2 ± 0.2	1.2 ± 0.2	1.5 ± 0.4	GB6 J0830+2410	
08 31 56	04 35		0.7 ± 0.2	0.6 ± 0.2	0.7 ± 0.3	GB6 J0831+0429	
08 36 26	−20 17	144	1.7 ± 0.2	1.1 ± 0.2	0.9 ± 0.3	PMN J0836-2017	
08 37 54	58 21		0.4 ± 0.1	0.6 ± 0.2	0.1 ± 0.3	GB6 J0837+5825	
08 39 29	01 03		0.6 ± 0.2	0.3 ± 0.2	$−0.5 \pm 0.4$	GB6 J0839+0104	
08 40 54	13 13	121	1.3 ± 0.2	0.8 ± 0.2	0.7 ± 0.3	GB6 J0840+1312	
08 41 16	70 54	089	1.9 ± 0.1	1.7 ± 0.2	0.8 ± 0.3	GB6 J0841+7053	
08 47 27	−07 03		0.5 ± 0.2	0.7 ± 0.2	0.1 ± 0.3	PMN J0847-0703	
08 49 44	−35 35		0.4 ± 0.1	0.2 ± 0.2	$−0.1 \pm 0.3$	PMN J0849-3541	
08 55 00	20 07	115	3.8 ± 0.2	4.2 ± 0.2	3.2 ± 0.4	GB6 J0854+2006	
08 58 34	−19 49		0.3 ± 0.2	0.3 ± 0.2	$−0.2 \pm 0.3$	PMN J0858-1950	
08 59 38	−22 45		0.3 ± 0.2	0.1 ± 0.2	$−1.0 \pm 0.3$...	
09 02 49	46 54		0.4 ± 0.2	0.5 ± 0.2	0.5 ± 0.3	GB6 J0903+4650	
09 06 12	−57 40		0.5 ± 0.2	0.5 ± 0.2	0.2 ± 0.3	PMN J0906-5740	
09 07 10	−20 21		0.6 ± 0.2	0.5 ± 0.2	$−0.1 \pm 0.3$	PMN J0906-2019	
09 09 12	01 23	132	1.5 ± 0.2	1.4 ± 0.2	1.0 ± 0.3	GB6 J0909+0121	
09 09 34	42 52		1.0 ± 0.2	0.5 ± 0.2	0.9 ± 0.3	GB6 J0909+4253	
09 14 27	02 49		0.9 ± 0.2	0.5 ± 0.2	1.1 ± 0.4	GB6 J0914+0245	
09 17 52	−12 08	143	0.9 ± 0.2	0.4 ± 0.2	0.2 ± 0.3	PMN J0918-1205	
09 20 53	44 39		1.7 ± 0.2	1.4 ± 0.2	0.9 ± 0.3	GB6 J0920+4441	
09 21 46	62 17		0.8 ± 0.2	0.5 ± 0.2	0.7 ± 0.3	GB6 J0921+6215	
09 21 48	−26 21		1.0 ± 0.2	0.8 ± 0.2	0.6 ± 0.3	PMN J0921-2618	
09 22 41	−39 59		0.7 ± 0.1	0.5 ± 0.2	0.5 ± 0.3	PMN J0922-3959	
09 24 16	28 18		0.5 ± 0.2	0.6 ± 0.2	0.6 ± 0.3	GB6 J0923+2815	
09 27 07	39 00	105	5.7 ± 0.2	4.9 ± 0.2	3.1 ± 0.3	GB6 J0927+3902	
09 28 12	−20 36		0.3 ± 0.2	0.5 ± 0.2	0.8 ± 0.3	PMN J0927-2034	
09 30 13	−38 15		0.2 ± 0.2	0.2 ± 0.2	$−0.1 \pm 0.3$...	
09 48 59	40 40	104	1.1 ± 0.2	1.1 ± 0.2	0.9 ± 0.3	GB6 J0948+4039	
09 55 21	69 41	088	0.7 ± 0.1	0.8 ± 0.2	0.5 ± 0.3	GB6 J0955+6940	
09 56 41	25 16		0.7 ± 0.2	0.5 ± 0.2	0.8 ± 0.3	GB6 J0956+2515	
09 57 24	55 25		0.9 ± 0.1	0.6 ± 0.2	0.3 ± 0.3	GB6 J0957+5522	^a
09 58 31	65 31		0.8 ± 0.1	0.6 ± 0.2	0.4 ± 0.3	GB6 J0958+6534	
09 58 37	47 28	098	0.9 ± 0.1	0.5 ± 0.2	0.3 ± 0.3	GB6 J0958+4725	^a
10 14 48	22 59	119	0.6 ± 0.2	0.4 ± 0.2	0.4 ± 0.3	GB6 J1014+2301	

Table 19—Continued

RA [hms]	Dec [dm]	ID	Q [Jy]	V [Jy]	W [Jy]	5 GHz ID
10 14 51	–45 10		0.4 ± 0.1	0.2 ± 0.2	0.4 ± 0.3	PMN J1014-4508
10 32 43	60 35		0.3 ± 0.1	0.0 ± 0.2	-0.0 ± 0.2	GB6 J1031+6036
10 33 03	41 18	103	0.8 ± 0.2	0.5 ± 0.2	0.6 ± 0.3	GB6 J1033+4115
10 35 05	–20 13		0.7 ± 0.2	0.4 ± 0.2	0.4 ± 0.3	PMN J1035-2011 ^a
10 37 00	–37 43		0.5 ± 0.2	0.2 ± 0.2	0.4 ± 0.3	PMN J1036-3744
10 37 10	–29 37		1.4 ± 0.2	1.2 ± 0.2	1.4 ± 0.3	PMN J1037-2934
10 38 59	05 09	142	0.9 ± 0.2	0.7 ± 0.2	0.6 ± 0.3	GB6 J1038+0512 ^a
10 41 11	06 16		1.2 ± 0.2	0.5 ± 0.2	0.4 ± 0.3	GB6 J1041+0610 ^a
10 41 30	–47 42	163	0.5 ± 0.1	0.3 ± 0.2	0.1 ± 0.3	PMN J1041-4740
10 43 17	24 08		0.9 ± 0.2	0.5 ± 0.2	0.8 ± 0.3	GB6 J1043+2408
10 48 12	–19 07		0.8 ± 0.2	0.6 ± 0.2	-0.1 ± 0.3	PMN J1048-1909
10 48 30	71 44	083	0.9 ± 0.1	0.6 ± 0.2	0.7 ± 0.3	GB6 J1048+7143
10 57 21	81 11		0.4 ± 0.2	0.5 ± 0.2	0.8 ± 0.3	...
10 57 51	–80 02	176	2.1 ± 0.1	2.2 ± 0.2	1.4 ± 0.3	PMN J1058-8003
10 58 26	01 35	149	4.3 ± 0.2	4.2 ± 0.2	3.1 ± 0.3	GB6 J1058+0133
11 02 24	72 25		0.5 ± 0.2	0.6 ± 0.2	0.0 ± 0.3	GB6 J1101+7225
11 06 55	–44 51	166	1.0 ± 0.2	0.9 ± 0.2	0.7 ± 0.3	PMN J1107-4449
11 18 07	–46 35		0.5 ± 0.2	0.4 ± 0.2	0.2 ± 0.3	PMN J1118-4634
11 18 12	–12 34		0.6 ± 0.2	0.6 ± 0.2	0.8 ± 0.3	PMN J1118-1232
11 18 52	12 37		0.7 ± 0.2	0.6 ± 0.2	0.5 ± 0.3	GB6 J1118+1234
11 25 33	26 12		0.5 ± 0.2	0.4 ± 0.2	0.4 ± 0.3	GB6 J1125+2610
11 27 18	–18 54	159	1.3 ± 0.2	1.2 ± 0.2	0.9 ± 0.3	PMN J1127-1857
11 30 18	–14 52	157	1.9 ± 0.2	1.4 ± 0.2	1.1 ± 0.3	PMN J1130-1449
11 31 09	38 18	101	0.7 ± 0.2	0.6 ± 0.2	0.5 ± 0.3	GB6 J1130+3815
11 45 21	–48 34		0.5 ± 0.2	0.6 ± 0.2	0.6 ± 0.3	PMN J1145-4836
11 45 58	–69 55		0.7 ± 0.2	0.5 ± 0.2	0.6 ± 0.3	PMN J1145-6953
11 47 05	39 57		0.8 ± 0.2	0.5 ± 0.2	0.8 ± 0.3	GB6 J1146+3958
11 47 07	–38 08	169	1.6 ± 0.2	1.7 ± 0.2	0.8 ± 0.3	PMN J1147-3812
11 50 04	24 16		0.3 ± 0.2	0.4 ± 0.2	0.2 ± 0.3	GB6 J1150+2417
11 50 30	–00 23		0.7 ± 0.2	0.2 ± 0.2	-0.1 ± 0.3	PMN J1150-0024
11 52 13	–08 42		0.8 ± 0.2	0.6 ± 0.2	0.8 ± 0.3	PMN J1152-0841
11 52 25	80 55	078	0.7 ± 0.2	0.4 ± 0.2	0.5 ± 0.3	1Jy 1150+81
11 53 13	49 30	090	1.5 ± 0.2	1.5 ± 0.2	1.0 ± 0.3	GB6 J1153+4931
11 54 21	–35 10		0.4 ± 0.2	0.6 ± 0.2	-0.3 ± 0.3	PMN J1154-3504
11 59 37	29 15	111	1.8 ± 0.1	1.7 ± 0.2	0.9 ± 0.3	GB6 J1159+2914
12 03 02	–05 29		0.3 ± 0.2	-0.1 ± 0.2	-0.3 ± 0.3	PMN J1202-0528 ^a
12 03 55	48 06		0.5 ± 0.2	0.2 ± 0.2	0.7 ± 0.3	GB6 J1203+4803

Table 19—Continued

RA [hms]	Dec [dm]	ID	Q [Jy]	V [Jy]	W [Jy]	5 GHz ID
12 08 54	−24 10	172	0.5 ± 0.2	0.2 ± 0.2	0.2 ± 0.3	PMN J1209-2406
12 11 50	−52 38		0.9 ± 0.2	0.5 ± 0.2	0.3 ± 0.3	PMN J1212-5245 ^a
12 16 02	−17 35	173	0.7 ± 0.2	0.6 ± 0.2	0.7 ± 0.3	PMN J1215-1731
12 19 29	05 48	164	1.6 ± 0.2	1.1 ± 0.2	0.9 ± 0.3	GB6 J1219+0549A ^a
12 22 18	04 14		1.0 ± 0.5	0.7 ± 0.3	0.9 ± 0.3	GB6 J1222+0413
12 22 48	80 37		0.3 ± 0.2	0.3 ± 0.2	0.3 ± 0.3	...
12 25 14	21 21		0.8 ± 0.2	0.5 ± 0.2	0.1 ± 0.3	GB6 J1224+2122
12 29 03	02 04	170	18.7 ± 0.2	17.0 ± 0.2	13.1 ± 0.3	GB6 J1229+0202
12 30 47	12 23	165	12.5 ± 0.2	9.6 ± 0.2	7.0 ± 0.3	GB6 J1230+1223
12 46 47	−25 45	177	1.3 ± 0.2	1.4 ± 0.2	1.0 ± 0.3	PMN J1246-2547
12 48 14	−46 00		0.8 ± 0.2	0.6 ± 0.2	0.9 ± 0.3	PMN J1248-4559
12 54 36	11 40		0.4 ± 0.2	0.0 ± 0.2	-0.1 ± 0.3	GB6 J1254+1141
12 56 11	−05 46	181	16.8 ± 0.2	16.1 ± 0.2	12.1 ± 0.3	PMN J1256-0547
12 56 58	−71 31		0.2 ± 0.1	-0.1 ± 0.2	-0.6 ± 0.3	...
12 58 02	32 31		0.6 ± 0.2	0.2 ± 0.2	0.1 ± 0.3	GB6 J1257+3229 ^a
12 58 19	−31 53	180	0.6 ± 0.2	0.5 ± 0.2	0.7 ± 0.3	PMN J1257-3154
12 59 44	51 40		0.7 ± 0.1	0.5 ± 0.2	0.6 ± 0.3	GB6 J1259+5141
13 05 02	−49 34		0.5 ± 0.2	0.4 ± 0.2	0.1 ± 0.3	PMN J1305-4928
13 10 33	32 23	052	1.9 ± 0.1	1.7 ± 0.2	0.9 ± 0.3	GB6 J1310+3220
13 16 09	−33 37	182	1.6 ± 0.2	1.7 ± 0.2	0.7 ± 0.3	PMN J1316-3339
13 19 02	−12 25		0.3 ± 0.2	-0.0 ± 0.2	-0.3 ± 0.3	PMN J1319-1217
13 26 55	22 08		0.7 ± 0.2	0.5 ± 0.2	0.8 ± 0.3	GB6 J1327+2210
13 29 22	31 57	040	0.3 ± 0.2	0.2 ± 0.2	0.2 ± 0.3	GB6 J1329+3154
13 31 16	30 26	026	1.4 ± 0.2	0.7 ± 0.2	0.5 ± 0.3	GB6 J1331+3030
13 32 10	−05 03		0.4 ± 0.2	0.4 ± 0.2	0.3 ± 0.3	PMN J1332-0509
13 33 05	02 01		0.8 ± 0.2	0.5 ± 0.2	0.8 ± 0.3	GB6 J1332+0200
13 35 51	−08 23		0.5 ± 0.2	0.3 ± 0.2	0.2 ± 0.3	PMN J1336-0830
13 36 32	−33 59	185	0.8 ± 0.2	0.6 ± 0.2	0.6 ± 0.3	PMN J1336-3358
13 37 29	−13 00	188	5.8 ± 0.2	5.3 ± 0.2	4.0 ± 0.3	PMN J1337-1257
13 43 28	66 05		0.4 ± 0.1	0.2 ± 0.2	0.3 ± 0.3	GB6 J1344+6606 ^a
13 49 22	53 34		0.2 ± 0.1	0.0 ± 0.2	-0.1 ± 0.3	GB6 J1349+5341
13 52 08	31 25		0.5 ± 0.1	0.3 ± 0.2	0.5 ± 0.3	GB6 J1352+3126
13 54 41	−10 43	197	0.7 ± 0.2	0.6 ± 0.2	0.1 ± 0.3	PMN J1354-1041
13 57 08	19 18	004	1.4 ± 0.2	1.4 ± 0.2	0.7 ± 0.3	GB6 J1357+1919
13 58 35	76 45		0.9 ± 0.1	0.6 ± 0.2	0.4 ± 0.3	...
13 59 16	01 52		0.4 ± 0.2	0.4 ± 0.2	0.2 ± 0.3	GB6 J1359+0159
14 08 56	−07 51	203	0.8 ± 0.2	0.4 ± 0.2	0.6 ± 0.3	1Jy 1406-076

Table 19—Continued

RA [hms]	Dec [dm]	ID	Q [Jy]	V [Jy]	W [Jy]	5 GHz ID
14 09 21	–27 00		0.5 ± 0.2	0.0 ± 0.2	0.2 ± 0.3	PMN J1409-2657
14 11 32	52 13		0.4 ± 0.2	0.2 ± 0.2	0.2 ± 0.3	GB6 J1411+5212
14 16 00	13 15		0.5 ± 0.2	0.4 ± 0.2	-0.2 ± 0.3	GB6 J1415+1320
14 19 41	54 27		0.8 ± 0.1	1.0 ± 0.2	0.8 ± 0.3	GB6 J1419+5423 ^a
14 20 15	38 19	042	0.7 ± 0.1	0.5 ± 0.2	0.5 ± 0.2	GB6 J1419+3822
14 27 21	–33 06	193	1.2 ± 0.2	1.1 ± 0.2	0.6 ± 0.3	PMN J1427-3306 ^a
14 27 44	–42 07	191	2.0 ± 0.2	2.1 ± 0.2	1.1 ± 0.3	PMN J1427-4206
14 36 35	23 25		0.4 ± 0.1	0.2 ± 0.2	-0.5 ± 0.3	GB6 J1436+2320 ^a
14 37 58	–22 06		0.5 ± 0.2	0.7 ± 0.2	0.3 ± 0.3	PMN J1438-2204
14 39 35	49 57		0.4 ± 0.2	0.3 ± 0.2	0.2 ± 0.3	GB6 J1439+4958
14 42 55	51 59		0.6 ± 0.1	0.8 ± 0.2	0.5 ± 0.3	GB6 J1443+5201
14 46 42	17 25		0.3 ± 0.2	0.4 ± 0.2	0.8 ± 0.3	GB6 J1446+1721
14 54 21	–37 50		0.9 ± 0.2	0.6 ± 0.2	1.0 ± 0.4	PMN J1454-3747
14 57 11	–35 37		0.9 ± 0.2	0.6 ± 0.2	1.4 ± 0.3	PMN J1457-3538
14 58 23	71 42	071	0.7 ± 0.1	0.5 ± 0.2	0.6 ± 0.3	GB6 J1459+7140
15 03 12	–41 54		1.1 ± 0.2	0.8 ± 0.2	0.7 ± 0.3	PMN J1503-4154 ^a
15 04 30	10 28	006	1.4 ± 0.2	1.0 ± 0.2	1.0 ± 0.3	GB6 J1504+1029
15 07 02	42 42		0.6 ± 0.1	0.5 ± 0.2	0.6 ± 0.3	GB6 J1506+4239
15 07 11	–16 53		1.0 ± 0.2	0.6 ± 0.2	0.5 ± 0.3	PMN J1507-1652
15 10 43	–05 46		1.0 ± 0.2	0.4 ± 0.2	0.5 ± 0.3	PMN J1510-0543
15 12 41	–09 01	207	2.1 ± 0.2	1.6 ± 0.2	1.6 ± 0.3	1Jy 1510-08
15 13 41	–10 13		0.8 ± 0.2	0.9 ± 0.3	0.8 ± 0.3	PMN J1513-1012
15 16 43	00 13	002	1.2 ± 0.2	1.5 ± 0.2	0.9 ± 0.3	GB6 J1516+0015
15 16 56	19 30		0.6 ± 0.2	0.5 ± 0.2	0.6 ± 0.3	GB6 J1516+1932
15 17 46	–24 25	205	1.7 ± 0.2	1.7 ± 0.2	1.3 ± 0.3	PMN J1517-2422
15 33 50	–22 45		0.2 ± 0.2	-0.2 ± 0.2	-0.2 ± 0.3	PMN J1534-2244
15 34 53	01 26		0.7 ± 0.2	0.6 ± 0.2	0.2 ± 0.3	GB6 J1534+0131
15 40 51	14 47		0.7 ± 0.1	0.5 ± 0.2	0.2 ± 0.3	GB6 J1540+1447
15 49 12	50 34		0.8 ± 0.1	0.4 ± 0.2	0.2 ± 0.3	GB6 J1549+5038
15 49 32	02 36	005	2.1 ± 0.2	1.9 ± 0.2	1.8 ± 0.3	GB6 J1549+0237
15 50 32	05 27	007	1.8 ± 0.2	1.8 ± 0.2	1.2 ± 0.3	GB6 J1550+0527
15 55 07	–79 12		0.5 ± 0.2	-0.1 ± 0.2	0.1 ± 0.3	PMN J1556-7914
16 02 05	33 25		0.5 ± 0.2	0.4 ± 0.2	0.6 ± 0.3	GB6 J1602+3326
16 03 58	57 18		0.5 ± 0.1	0.6 ± 0.2	0.4 ± 0.3	GB6 J1604+5714 ^a
16 08 43	10 30	009	1.3 ± 0.1	1.2 ± 0.2	0.6 ± 0.3	GB6 J1608+1029
16 13 41	34 12	023	2.6 ± 0.1	2.2 ± 0.2	1.4 ± 0.3	GB6 J1613+3412
16 18 37	–77 20	183	1.5 ± 0.2	1.2 ± 0.2	0.8 ± 0.3	PMN J1617-7717

Table 19—Continued

RA [hms]	Dec [dm]	ID	Q [Jy]	V [Jy]	W [Jy]	5 GHz ID
16 26 16	41 30		0.4 ± 0.1	0.4 ± 0.2	0.2 ± 0.3	GB6 J1625+4134
16 32 43	82 31	076	1.2 ± 0.1	1.0 ± 0.2	0.7 ± 0.3	...
16 35 19	38 08	033	3.1 ± 0.4	3.2 ± 0.4	2.6 ± 0.3	GB6 J1635+3808
16 37 38	47 15		1.0 ± 0.2	0.8 ± 0.2	0.7 ± 0.3	GB6 J1637+4717
16 38 19	57 19	056	1.4 ± 0.1	1.3 ± 0.2	1.1 ± 0.3	GB6 J1638+5720
16 42 28	68 53	069	2.0 ± 0.1	1.8 ± 0.2	1.3 ± 0.2	GB6 J1642+6856 ^a
16 42 57	39 48	035	5.3 ± 0.3	5.0 ± 0.3	3.9 ± 0.3	GB6 J1642+3948
16 45 42	−77 16		0.5 ± 0.2	0.5 ± 0.2	0.4 ± 0.3	PMN J1644-7715
16 48 10	−64 35		0.4 ± 0.1	0.5 ± 0.2	0.4 ± 0.3	PMN J1647-6437
16 48 14	41 02		0.6 ± 0.5	0.5 ± 0.4	0.2 ± 0.3	GB6 J1648+4104 ^a
16 51 11	04 58	010	1.0 ± 0.2	0.5 ± 0.2	0.1 ± 0.3	GB6 J1651+0459
16 53 51	39 49		0.6 ± 0.4	0.6 ± 0.4	0.2 ± 0.3	GB6 J1653+3945
16 58 08	07 42	013	1.4 ± 0.2	1.3 ± 0.2	1.0 ± 0.3	GB6 J1658+0741
16 58 10	47 31		0.3 ± 0.2	0.2 ± 0.2	0.1 ± 0.3	GB6 J1658+4737 ^a
16 58 11	47 52		0.3 ± 0.2	$−0.0 \pm 0.2$	0.0 ± 0.3	...
17 00 25	68 27		0.5 ± 0.2	0.6 ± 0.2	0.8 ± 0.3	GB6 J1700+6830
17 02 56	−62 16	198	1.3 ± 0.1	1.1 ± 0.2	0.7 ± 0.3	PMN J1703-6212
17 15 53	68 38		0.5 ± 0.1	0.3 ± 0.2	0.4 ± 0.2	GB6 J1716+6836
17 19 07	17 44		0.5 ± 0.2	0.4 ± 0.2	0.4 ± 0.3	GB6 J1719+1745
17 21 55	−61 49		0.4 ± 0.2	0.2 ± 0.2	0.2 ± 0.3	PMN J1721-6154
17 23 07	−64 59	196	1.3 ± 0.1	1.0 ± 0.2	0.9 ± 0.3	PMN J1723-6500
17 24 04	40 00		0.5 ± 0.2	0.4 ± 0.2	0.3 ± 0.3	GB6 J1724+4004 ^a
17 27 10	45 30	043	0.7 ± 0.1	0.9 ± 0.2	0.7 ± 0.3	GB6 J1727+4530
17 28 25	04 28		1.0 ± 0.2	1.0 ± 0.2	0.6 ± 0.3	GB6 J1728+0426
17 28 37	12 15		0.3 ± 0.2	$−0.1 \pm 0.2$	$−0.5 \pm 0.3$	GB6 J1728+1215
17 34 28	38 57	038	1.1 ± 0.2	1.0 ± 0.2	0.8 ± 0.3	GB6 J1734+3857
17 35 14	−79 33	186	0.8 ± 0.1	0.6 ± 0.2	0.4 ± 0.3	PMN J1733-7935
17 36 04	36 19		0.5 ± 0.1	0.2 ± 0.2	0.3 ± 0.3	GB6 J1735+3616 ^a
17 37 00	06 22		0.6 ± 0.2	0.6 ± 0.2	0.3 ± 0.3	GB6 J1737+0620
17 37 54	−56 34		0.5 ± 0.2	0.3 ± 0.2	0.6 ± 0.3	PMN J1737-5633
17 40 11	47 40		0.6 ± 0.1	0.5 ± 0.2	0.8 ± 0.3	GB6 J1739+4738
17 40 30	52 10	048	1.1 ± 0.1	0.9 ± 0.2	0.6 ± 0.3	GB6 J1740+5211
17 49 00	70 03	068	0.4 ± 0.2	0.6 ± 0.2	0.7 ± 0.2	GB6 J1748+7005
17 51 32	09 39		4.4 ± 0.2	4.3 ± 0.2	3.4 ± 0.3	GB6 J1751+0938
17 53 23	44 08		0.4 ± 0.2	0.6 ± 0.2	0.5 ± 0.3	GB6 J1753+4410
17 53 50	28 50	022	1.6 ± 0.1	1.5 ± 0.2	0.7 ± 0.3	GB6 J1753+2847
17 56 41	15 36		0.5 ± 0.1	0.2 ± 0.2	0.3 ± 0.3	GB6 J1756+1535 ^a

Table 19—Continued

RA [hms]	Dec [dm]	ID	Q [Jy]	V [Jy]	W [Jy]	5 GHz ID	
17 58 22	66 37	064	0.6 ± 0.1	0.5 ± 0.2	0.6 ± 0.2	GB6 J1758+6638	^a
18 00 19	38 48		0.6 ± 0.1	0.3 ± 0.2	0.2 ± 0.3	GB6 J1800+3848	^a
18 00 42	78 27	072	1.6 ± 0.1	1.6 ± 0.2	1.2 ± 0.3	1Jy 1803+78	
18 01 25	44 04		1.4 ± 0.2	1.2 ± 0.2	0.7 ± 0.3	GB6 J1801+4404	
18 03 22	–65 09	199	0.8 ± 0.2	0.5 ± 0.2	0.8 ± 0.3	PMN J1803-6507	
18 06 47	69 48	067	1.2 ± 0.1	1.1 ± 0.2	0.7 ± 0.2	GB6 J1806+6949	
18 08 35	45 43		0.6 ± 0.2	0.5 ± 0.2	0.2 ± 0.3	GB6 J1808+4542	
18 12 10	06 49		0.6 ± 0.2	0.6 ± 0.2	0.5 ± 0.3	GB6 J1812+0651	
18 20 03	–63 48	200	0.9 ± 0.2	1.0 ± 0.2	0.7 ± 0.3	PMN J1819-6345	
18 20 08	–55 18		0.6 ± 0.2	0.3 ± 0.2	0.3 ± 0.3	PMN J1819-5521	
18 22 41	15 56		0.4 ± 0.2	0.3 ± 0.2	-0.1 ± 0.3	GB6 J1822+1600	
18 22 58	68 54		0.3 ± 0.2	0.2 ± 0.2	0.0 ± 0.3	GB6 J1823+6857	^a
18 23 59	56 51	053	1.2 ± 0.1	1.0 ± 0.2	0.7 ± 0.3	GB6 J1824+5650	
18 29 40	48 44	046	2.3 ± 0.1	1.7 ± 0.2	1.2 ± 0.3	GB6 J1829+4844	
18 33 02	28 36		0.2 ± 0.1	0.1 ± 0.2	-0.1 ± 0.3	GB6 J1832+2833	
18 34 33	–58 56		0.8 ± 0.1	0.5 ± 0.2	0.4 ± 0.3	PMN J1834-5856	
18 35 05	32 37		0.6 ± 0.1	0.4 ± 0.2	0.1 ± 0.3	GB6 J1835+3241	
18 37 37	–71 08	192	1.1 ± 0.1	1.0 ± 0.2	0.8 ± 0.3	PMN J1837-7108	
18 41 35	68 09	066	0.8 ± 0.2	0.5 ± 0.2	0.6 ± 0.3	GB6 J1842+6809	
18 42 13	79 45	073	0.6 ± 0.2	0.6 ± 0.2	0.2 ± 0.3	1Jy 1845+79	
18 48 21	32 20		0.6 ± 0.1	0.4 ± 0.2	0.9 ± 0.3	GB6 J1848+3219	
18 49 24	67 04	065	2.0 ± 0.2	1.9 ± 0.2	1.5 ± 0.3	GB6 J1849+6705	^a
18 50 04	28 25	028	0.4 ± 0.1	0.4 ± 0.2	0.2 ± 0.3	GB6 J1850+2825	
18 53 41	33 03		0.3 ± 0.2	0.3 ± 0.2	-0.1 ± 0.3	GB6 J1853+3301	^a
18 55 03	73 54		0.5 ± 0.2	0.4 ± 0.2	0.1 ± 0.3	GB6 J1854+7351	
19 03 13	31 57	034	0.4 ± 0.1	0.4 ± 0.2	0.2 ± 0.3	GB6 J1902+3159	^a
19 11 11	–20 07		2.4 ± 0.2	2.3 ± 0.2	2.0 ± 0.3	PMN J1911-2006	
19 12 37	37 45		0.4 ± 0.2	0.1 ± 0.2	0.1 ± 0.3	GB6 J1912+3740	^a
19 13 27	–80 07		0.5 ± 0.2	0.3 ± 0.2	0.0 ± 0.3	PMN J1912-8010	
19 17 49	–19 30		0.3 ± 0.3	0.0 ± 0.3	0.1 ± 0.4	PMN J1917-1921	
19 17 51	55 20		0.3 ± 0.1	0.1 ± 0.2	0.1 ± 0.3	GB6 J1918+5520	
19 23 30	–21 05	008	2.3 ± 0.2	2.3 ± 0.2	1.5 ± 0.3	PMN J1923-2104	
19 24 50	–29 14		11.7 ± 0.2	11.0 ± 0.2	7.7 ± 0.3	PMN J1924-2914	
19 27 18	61 18	059	0.9 ± 0.1	0.7 ± 0.2	0.5 ± 0.3	GB6 J1927+6117	
19 27 43	74 02	070	2.3 ± 0.1	2.2 ± 0.2	1.2 ± 0.3	GB6 J1927+7357	
19 28 22	32 43		0.3 ± 0.1	0.1 ± 0.2	-0.0 ± 0.3	GB6 J1927+3236	
19 36 54	–39 54		1.1 ± 0.2	0.9 ± 0.2	1.1 ± 0.3	PMN J1937-3957	

Table 19—Continued

RA [hms]	Dec [dm]	ID	Q [Jy]	V [Jy]	W [Jy]	5 GHz ID	
19 38 15	04 52		0.3 ± 0.2	0.2 ± 0.2	-0.2 ± 0.3	GB6 J1938+0448	^a
19 39 34	-15 26		0.5 ± 0.2	0.5 ± 0.2	0.6 ± 0.3	PMN J1939-1525	
19 41 08	45 59		-0.1 ± 0.2	-0.2 ± 0.2	-0.3 ± 0.3	GB6 J1940+4605	^a
19 45 26	-55 28		0.4 ± 0.2	0.1 ± 0.2	-0.4 ± 0.3	PMN J1945-5520	
19 55 50	51 33	051	0.8 ± 0.1	0.7 ± 0.2	0.6 ± 0.3	GB6 J1955+5131	^a
19 58 03	-38 45	003	2.7 ± 0.2	2.2 ± 0.2	1.3 ± 0.3	PMN J1957-3845	
20 00 54	-17 46	011	1.7 ± 0.2	1.7 ± 0.2	1.2 ± 0.3	PMN J2000-1748	
20 02 52	14 58		0.2 ± 0.2	0.2 ± 0.2	-0.2 ± 0.3	GB6 J2002+1501	
20 04 14	77 46		0.9 ± 0.1	0.6 ± 0.2	0.4 ± 0.3	1Jy 2007+77	
20 06 49	64 22		0.5 ± 0.1	0.5 ± 0.2	0.2 ± 0.2	GB6 J2006+6424	^a
20 07 01	66 10		0.4 ± 0.1	0.4 ± 0.2	0.1 ± 0.3	GB6 J2007+6607	
20 08 59	-48 51		0.7 ± 0.2	0.6 ± 0.2	0.1 ± 0.3	PMN J2009-4849	
20 10 18	72 33		0.9 ± 0.1	0.6 ± 0.2	0.8 ± 0.3	GB6 J2009+7229	
20 11 15	-15 45	014	1.6 ± 0.2	1.0 ± 0.2	0.8 ± 0.3	PMN J2011-1546	
20 22 20	61 40	063	1.0 ± 0.1	0.6 ± 0.2	0.1 ± 0.3	GB6 J2022+6137	
20 22 46	76 09		0.2 ± 0.2	0.2 ± 0.2	0.1 ± 0.3	...	
20 23 26	54 30		0.4 ± 0.2	0.5 ± 0.2	0.5 ± 0.3	GB6 J2023+5427	
20 25 41	-07 32		0.9 ± 0.2	1.0 ± 0.2	0.6 ± 0.3	PMN J2025-0735	
20 31 49	12 15		0.5 ± 0.2	0.5 ± 0.2	0.5 ± 0.3	GB6 J2031+1219	
20 35 28	-68 42	194	0.6 ± 0.1	0.5 ± 0.2	0.6 ± 0.3	PMN J2035-6846	
20 56 10	-47 14	208	2.1 ± 0.2	2.1 ± 0.2	1.5 ± 0.3	PMN J2056-4714	
20 56 40	-32 06		0.6 ± 0.2	0.5 ± 0.2	0.6 ± 0.3	PMN J2056-3207	
21 01 25	03 40		0.4 ± 0.2	0.7 ± 0.2	0.6 ± 0.4	GB6 J2101+0341	
21 05 41	-78 23		0.5 ± 0.2	0.6 ± 0.2	0.4 ± 0.3	PMN J2105-7825	
21 07 05	-25 25		0.5 ± 0.2	0.5 ± 0.2	0.1 ± 0.3	PMN J2107-2526	
21 09 22	35 32	049	0.8 ± 0.2	0.5 ± 0.2	0.3 ± 0.3	GB6 J2109+3532	
21 09 24	-41 08	001	1.1 ± 0.2	0.8 ± 0.2	0.7 ± 0.3	PMN J2109-4110	
21 14 56	-80 53		0.5 ± 0.1	0.4 ± 0.2	0.2 ± 0.3	PMN J2116-8053	
21 19 39	-80 56		0.3 ± 0.1	0.2 ± 0.2	0.4 ± 0.3	PMN J2116-8053	
21 20 10	32 19		-0.0 ± 0.2	-0.2 ± 0.2	-0.2 ± 0.3	...	
21 22 42	38 02		0.1 ± 0.1	-0.0 ± 0.2	-0.0 ± 0.3	GB6 J2122+3754	
21 23 43	05 34	027	1.2 ± 0.2	0.9 ± 0.2	0.5 ± 0.3	GB6 J2123+0535	
21 29 13	-15 39		0.4 ± 0.2	0.2 ± 0.2	0.4 ± 0.3	PMN J2129-1538	^a
21 31 37	-12 07	017	2.0 ± 0.2	1.6 ± 0.2	0.6 ± 0.3	PMN J2131-1207	
21 33 34	38 02		0.1 ± 0.1	0.1 ± 0.2	-0.1 ± 0.3	GB6 J2133+3812	
21 34 07	-01 54	020	1.7 ± 0.2	1.5 ± 0.2	1.3 ± 0.3	PMN J2134-0153	
21 36 40	00 41	025	3.2 ± 0.2	1.9 ± 0.2	1.0 ± 0.3	GB6 J2136+0041	

Table 19—Continued

RA [hms]	Dec [dm]	ID	Q [Jy]	V [Jy]	W [Jy]	5 GHz ID
21 37 35	36 59		0.3 ± 0.1	-0.0 ± 0.2	0.2 ± 0.3	...
21 39 05	14 24	041	1.2 ± 0.1	1.0 ± 0.2	0.8 ± 0.3	GB6 J2139+1423
21 43 12	17 44	044	0.3 ± 0.2	0.5 ± 0.2	0.3 ± 0.3	GB6 J2143+1743 ^a
21 47 15	09 30		0.7 ± 0.3	0.6 ± 0.2	0.7 ± 0.3	GB6 J2147+0929
21 47 31	-78 02	184	0.5 ± 0.2	0.6 ± 0.2	0.1 ± 0.3	PMN J2146-7755 ^a
21 48 05	06 57	037	6.1 ± 0.2	5.7 ± 0.2	4.2 ± 0.3	GB6 J2148+0657
21 48 47	-75 37		0.4 ± 0.1	0.2 ± 0.2	-0.0 ± 0.3	PMN J2147-7536
21 51 53	-30 27		1.2 ± 0.2	1.3 ± 0.2	0.8 ± 0.3	PMN J2151-3028
21 55 03	22 59		0.4 ± 0.2	0.1 ± 0.2	-0.1 ± 0.3	GB6 J2155+2250
21 57 08	-69 40	190	2.3 ± 0.1	1.7 ± 0.2	1.2 ± 0.3	PMN J2157-6941
21 58 10	-15 02	018	1.5 ± 0.2	1.3 ± 0.2	0.9 ± 0.3	PMN J2158-1501
22 03 13	31 46	054	2.1 ± 0.1	1.7 ± 0.2	0.8 ± 0.3	GB6 J2203+3145
22 03 23	17 26	045	1.4 ± 0.2	1.2 ± 0.2	0.9 ± 0.3	GB6 J2203+1725 ^a
22 06 08	-18 38	016	0.9 ± 0.2	0.9 ± 0.2	0.6 ± 0.3	PMN J2206-1835
22 07 52	-53 43		0.8 ± 0.2	0.5 ± 0.2	0.3 ± 0.3	PMN J2207-5346
22 11 55	23 56	050	0.9 ± 0.2	0.9 ± 0.2	0.9 ± 0.3	GB6 J2212+2355
22 18 57	-03 34	030	1.2 ± 0.4	1.1 ± 0.3	0.4 ± 0.4	PMN J2218-0335
22 25 29	21 18		1.0 ± 0.2	0.8 ± 0.2	1.0 ± 0.3	GB6 J2225+2118
22 25 44	-04 57	029	4.8 ± 0.2	4.3 ± 0.2	3.2 ± 0.3	PMN J2225-0457 ^a
22 29 41	-08 26	024	2.2 ± 0.2	2.1 ± 0.2	0.8 ± 0.3	PMN J2229-0832
22 29 46	-20 48		0.7 ± 0.2	0.5 ± 0.2	1.0 ± 0.3	PMN J2229-2049
22 30 22	-13 26		0.5 ± 0.2	0.3 ± 0.2	0.1 ± 0.3	PMN J2230-1325
22 32 03	11 42	047	2.7 ± 0.2	2.6 ± 0.2	1.9 ± 0.3	GB6 J2232+1143
22 35 21	-48 38	206	1.6 ± 0.2	1.4 ± 0.2	1.5 ± 0.3	PMN J2235-4835
22 36 22	28 31	057	1.1 ± 0.2	0.8 ± 0.2	0.8 ± 0.3	GB6 J2236+2828
22 39 30	-57 06	201	0.7 ± 0.2	0.7 ± 0.2	0.7 ± 0.3	PMN J2239-5701
22 46 24	-12 08	021	1.8 ± 0.2	1.3 ± 0.2	0.6 ± 0.3	PMN J2246-1206
22 53 56	16 08	055	10.2 ± 0.2	11.4 ± 0.2	10.6 ± 0.3	GB6 J2253+1608
22 55 05	42 02		0.5 ± 0.1	0.3 ± 0.2	-0.5 ± 0.3	GB6 J2255+4202
22 56 54	-20 12	019	0.5 ± 0.2	0.4 ± 0.2	0.3 ± 0.3	PMN J2256-2011
22 57 58	-27 57	012	3.6 ± 0.2	3.4 ± 0.2	2.6 ± 0.3	PMN J2258-2758
23 01 40	37 32		0.5 ± 0.2	0.5 ± 0.2	0.2 ± 0.3	GB6 J2301+3726
23 03 00	-18 38		0.5 ± 0.2	0.4 ± 0.2	0.4 ± 0.3	PMN J2303-1841
23 03 45	-68 05		0.7 ± 0.1	0.4 ± 0.2	0.3 ± 0.3	PMN J2303-6807
23 11 00	34 23		0.7 ± 0.2	0.4 ± 0.2	0.4 ± 0.3	GB6 J2311+3425
23 12 12	45 34		0.3 ± 0.1	-0.1 ± 0.2	-0.9 ± 0.3	GB6 J2311+4543
23 13 23	72 47		0.3 ± 0.1	0.4 ± 0.2	-0.0 ± 0.3	GB6 J2312+7241

D. Smoothed Noise

We use maps that have been smoothed to a common resolution for several *WMAP* analyses. This appendix discusses how much the smoothing reduces the random instrument noise. This smoothing also correlates the noise between pixels. Here, we only calculate the diagonal elements of the noise covariance matrix in pixel space; the correlations are beyond the scope of this appendix. Also, the noise calculated here should be added in quadrature to the 0.2% *WMAP* calibration error.

For discussing beam smoothing, we use the same notation as Equation (4) of Hill et al. (2009).

$$B_l = \Omega_B b_l = 2\pi \int_{-1}^1 b(\theta) P_l(\cos \theta) d \cos \theta. \quad (\text{D1})$$

In this case, we use the beam to describe the additional smoothing that we apply to the map to bring the total smoothing up to 1 degree FWHM.

The pixel temperature value, T_p^{convol} , in a convolved map is a weighted sum of the nearby pixel values,

$$T_p^{\text{convol}} = \sum_i w_{i,p} T_i, \quad (\text{D2})$$

where $w_{i,p}$ gives the weight that each original pixel with index i gives to convolved pixel p . The weights $w_{i,p}$ define the beam used for smoothing. From this formula and a noise estimate in the original pixels, we propagate errors directly, assuming uncorrelated noise in the original pixels.

$$\sigma^2(T_p^{\text{convol}}) = \sum_i w_{i,p}^2 \sigma^2(T_i), \quad (\text{D3})$$

where $\sigma^2(T_p^{\text{convol}})$ is the noise variance in the convolved pixel p and $\sigma^2(T_i)$ is the noise variance in the original pixel i .

The noise in each convolved pixel can be rapidly computed by smoothing a map of unsmoothed noise variance values, $\sigma_0^2/N_{\text{obs},i}$. However, the smoothing must be done using the squared weights, which requires determining the Legendre transform of the beam once it has been squared in real space, $b(\theta)^2$.

$$\Omega'_b b'_l = 2\pi \int_{-1}^1 b^2(\theta) P_l(\cos \theta) d \cos \theta. \quad (\text{D4})$$

The values for the required beam smoothing, $\Omega'_b b'_l$, can be computed numerically by calculating $b(\theta)$ on a one-dimensional finely spaced grid in θ , squaring it, and computing the above integral as a sum.

Table 19—Continued

RA [hms]	Dec [dm]	ID	Q [Jy]	V [Jy]	W [Jy]	5 GHz ID
23 15 14	−31 37		0.5 ± 0.2	0.5 ± 0.2	-0.0 ± 0.3	PMN J2314-3138
23 15 42	−50 14	204	0.5 ± 0.1	0.5 ± 0.2	-0.1 ± 0.3	PMN J2315-5018
23 22 05	51 00		0.5 ± 0.1	0.5 ± 0.2	0.1 ± 0.3	GB6 J2322+5057
23 22 06	27 26		0.4 ± 0.2	0.3 ± 0.2	0.6 ± 0.3	GB6 J2322+2732 ^a
23 23 35	−03 21		0.6 ± 0.2	0.7 ± 0.2	0.2 ± 0.3	PMN J2323-0317
23 27 33	09 40		1.2 ± 0.2	0.8 ± 0.2	0.8 ± 0.3	GB6 J2327+0940
23 29 19	−47 26		1.3 ± 0.2	0.7 ± 0.2	0.8 ± 0.3	PMN J2329-4730
23 30 32	11 02		0.5 ± 0.2	0.7 ± 0.2	0.3 ± 0.3	GB6 J2330+1100
23 31 38	−15 55	032	0.4 ± 0.2	0.5 ± 0.2	0.5 ± 0.3	PMN J2331-1556
23 33 39	−23 41		0.9 ± 0.2	0.6 ± 0.2	0.4 ± 0.3	PMN J2333-2343 ^a
23 35 41	−52 48	195	0.5 ± 0.1	0.2 ± 0.2	0.1 ± 0.3	PMN J2334-5251
23 46 55	09 30		0.5 ± 0.2	0.4 ± 0.2	0.3 ± 0.3	GB6 J2346+0930 ^a
23 48 02	−16 31	039	1.8 ± 0.2	1.7 ± 0.2	1.0 ± 0.3	PMN J2348-1631
23 54 18	45 54	074	0.8 ± 0.2	0.8 ± 0.2	0.9 ± 0.3	GB6 J2354+4553
23 55 23	49 46	075	0.3 ± 0.2	0.1 ± 0.2	0.6 ± 0.3	GB6 J2355+4950 ^a
23 57 18	−68 19		0.4 ± 0.1	0.0 ± 0.2	-0.1 ± 0.3	PMN J2356-6820
23 57 30	81 53		0.5 ± 0.1	0.7 ± 0.2	0.6 ± 0.3	NVSS J2356+8152
23 57 49	−45 57		0.2 ± 0.2	0.2 ± 0.2	0.2 ± 0.3	PMN J2358-4555
23 57 52	−53 09	189	1.6 ± 0.1	1.2 ± 0.2	1.0 ± 0.3	PMN J2357-5311
23 58 56	−60 56	187	1.0 ± 0.1	0.6 ± 0.2	0.1 ± 0.3	PMN J2358-6054
23 59 43	39 18		0.5 ± 0.2	0.3 ± 0.2	-0.1 ± 0.3	GB6 J2358+3922 ^a

^aIndicates the source has multiple possible identifications.

The above description of smoothed noise assumes it will be reported in a map with a pixel size much smaller than the beam size. In the opposite case, where the final pixel size is much larger than the beam size, the noise can be averaged down ignoring the beam, since the effect of the beam will be small. However, there is an intermediate case where the pixel size and beam size are comparable, such as with r6 maps of 1 degree smoothed data. In this case, a more careful treatment of the pixel window function could be useful. Instead of approximating the pixel window function as an azimuthally symmetric beam, we take a more brute-force approach, outlined below.

We have r9 maps of $N_{\text{obs},i}$. Suppose we want to know the noise properties of the corresponding temperature map smoothed to 1 degree FWHM and then degraded to r6. To determine this, we calculate the real-space smoothing function needed to bring the beam smoothing up to 1 degree; we call this $b(\theta)$. This will be a 1 degree FWHM beam b_l^1 divided by the *WMAP* instrument beam b_l' for that DA. We approximate $b(\theta)$ numerically by finding the Legendre transform of the needed smoothing, $b_l = b_l^1/b_l'$, on a one-dimensional list of angles θ . Then, for each r6 pixel, we find all r9 pixels within 2 degrees of the r6 pixel center. We determine the weights $w_{i,p}$, where i is an index over r9 pixels within 2 degrees of the r6 pixel center, and p is an index over r9 pixels inside the r6 pixel. As before, we have

$$w_{i,p} = b(\theta_{i,p}) \quad (\text{D5})$$

where $\theta_{i,p}$ is the angle between the centers of pixels i and p , and the weights have been rescaled so that $\sum_i w_{i,p} = 1$. The radius of two degrees was chosen so that noise outside of that circle would be negligibly averaged into the r6 pixel, given our beam smoothing size.

Since the noise for the r9 pixels of the smoothed map is averaged into an r6 pixel, we must account for this in our error propagation. We assume flat weighting for the degrade from r9 to r6, in the following description. There are 64 r9 pixels in an r6 pixel. The temperatures (pixels with index p) are averaged into an r6 pixel (with index q) as

$$T_q^{\text{degraded}} = \frac{1}{64} \sum_p \sum_i w_{i,p} T_i. \quad (\text{D6})$$

The formula for propagation of errors is

$$\sigma^2(T_q^{\text{degraded}}) = \sum_i \left(\frac{\partial T_q}{\partial T_i} \right)^2 \sigma^2(T_i), \quad (\text{D7})$$

which then becomes

$$\sigma^2(T_q^{\text{degraded}}) = \sum_i \left(\frac{1}{64} \sum_p w_{i,p} \right)^2 \frac{\sigma_0^2}{N_{\text{obs},i}}. \quad (\text{D8})$$

Alternatively, we can quote an effective $N_{\text{obs},q}^{\text{eff}}$ value for a r6 pixel as

$$\frac{1}{N_{\text{obs},q}^{\text{eff}}} \equiv \sum_i \left(\frac{1}{64} \sum_p w_{i,p} \right)^2 \frac{1}{N_{\text{obs},i}}. \quad (\text{D9})$$

Since this is the number more commonly reported in our data files, we use this.

There appear to be artifacts in these $N_{\text{obs},q}^{\text{eff}}$ maps. This is most readily visible when a simple binned version of $N_{\text{obs},q}$ which ignores the effects of smoothing is divided out. In this case, the above noise propagation predicts what appears to be suppressed noise levels (greater N_{obs}) near the edges of the base tiles in the polar cap regions of the HEALPix pixelization.

These results can be verified by creating white noise realizations at r9, smoothing them, binning them to r6, and then checking the variance of the noise in each pixel. When this comparison is done, some of these artifacts remain in these simulations as well, so it appears the pixelization (slightly varying pixel shapes) is causing a real effect in the smoothed noise. The fluctuations that appear to be due to the HEALPix pixelization are on order of 10% in $N_{\text{obs},q}$ in all bands.

The median values of $N_{\text{obs},q}$ over the whole sky for the two approaches (white noise sims vs. the above propagation of errors) differ by about 5% at K-band (where the additional smoothing is smallest), and roughly 1% in other bands. The above propagation of errors appears to underestimate the noise slightly (overestimate $N_{\text{obs},q}$).

E. Bandpass Integration

In this section we first discuss the full integration over the bandpass based on data from Jarosik et al. (2003a), and then we discuss a useful approximation to that integration based on three frequencies in each band. This is the approximation used for foreground fitting in Section 5.3.6.

The full integration of different foreground spectra over the *WMAP* bandpasses can be done as follows, based on the description of the radiometers in Jarosik et al. (2003a). After computing $r_{\text{avg}}(\nu_i)$ from Equation (46) of that paper using the discretized bandpass measurements, we combine the measurements as if we were doing an unweighted average of the maps in thermodynamic temperature, as follows. First, we normalize the bandpass for each radiometer so that

$$\sum_i r_{\text{avg}}(\nu_i) = 1 \quad (\text{E1})$$

We note the small shift in bandpass that we describe in Appendix A. Then, we interpolate the foreground spectrum onto the specific frequencies at which the *WMAP* bands were measured, ν_i , average the frequency over the spectrum, and convert from antenna to thermodynamic temperature. The measured foreground thermodynamic temperature response to a foreground spectrum $f(\nu)$ given in antenna temperature, averaged over all the radiometers in one *WMAP* band, is

$$T_{\text{band}}[f(\nu)] = \frac{1}{N_{\text{radiometers}}} \sum_{j=1}^{N_{\text{radiometers}}} \sum_i \frac{r_{\text{avg},j}(\nu_i)}{w'(\nu_i)} f(\nu_i) \quad (\text{E2})$$

where $w'(\nu)$ is as defined in Jarosik et al. (2003a): it is the derivative of the single-polarization Planck spectrum with respect to temperature, divided by k_B to make it unitless. It depends on both CMB temperature and frequency, but the derivative is taken with respect to CMB temperature.

$$w(\nu) \equiv \frac{h\nu}{e^x - 1} \quad x \equiv \frac{h\nu}{k_B T} \quad (\text{E3})$$

$$w'(\nu) \equiv \left| \frac{1}{k_B} \frac{dw(\nu)}{dT} \right|_{T=T_{\text{CMB}}} = \frac{x^2 e^x}{(e^x - 1)^2} \quad (\text{E4})$$

Note that this assumes an unweighted average of the maps. If we were to do an optimal weighted average, the total bandpass would have some small spatial dependence with pixel, as the number of observations varies between DAs.

In practice, it is the complexity and shape of the foregrounds that limits the foreground fitting. The detailed bandpass discussion above is more accurate, but fast approximations are useful. Jarosik et al. (2003a) provides a useful approximation given by Equation (50) of his paper for spectra that are power laws in antenna temperature. This allows one to determine the effective frequency of the bandpass and therefore rapidly calculate the measured antenna temperature from the power law. However, power laws are always concave upward on a plot of antenna temperature as a function of frequency with both axes linear. Since we also want to fit a spinning dust spectrum which is concave downward, we invent another approximation.

Instead of doing the full integration discussed above for each band, this approximation only requires a weighted average of the antenna temperature at three frequencies. The thermodynamic temperature measured by *WMAP* in a specific band is approximated as

$$T = \frac{\Delta T}{\Delta T_A} \sum_{i=1}^3 w_i T_A(\nu_i) \quad (\text{E5})$$

where $T_A(\nu_i)$ is the antenna temperature foreground spectrum measured at frequencies ν_i , and $\Delta T/\Delta T_A$ is the conversion from antenna to thermodynamic temperature. The frequencies and weights used are in Table 20. The weights are chosen so that any spectrum that is

a second order polynomial in antenna temperature will have its integral evaluated exactly (to the accuracy with which the bandpasses were measured). These weights are therefore including information about the full shape of the bandpass. We do not expect to have spectra that are second order polynomials; most of the antenna temperature spectra are either power laws (rarely with powers of precisely 0, 1, or 2) or special fitting functions, but they can typically be approximated well as a smooth quadratic over the width of the *WMAP* bandpasses. The fitting frequencies are somewhat arbitrary. They were chosen by taking a canonical center frequency for each band and two frequencies about 9% higher and lower. Then they were adjusted by hand so that the weights were roughly equal and so the frequencies were multiples of 0.1 GHz. Further adjustment could be done, but the current numbers appear to work well. Because of this arbitrariness of the frequencies in Table 20, they should not be taken to be a meaningful representation of the center or width of the bandpass.

The error in this approximation is typically less than the *WMAP* calibration error of 0.2%, for smooth spectra such as power laws. In Q band, for low frequency scale factors, the error in the spinning dust spectrum can be on order of 1%. However, it is not clear that we know the shape of the spinning dust spectrum to that accuracy. This is intended to be a rapid and reasonably accurate way of integrating over the *WMAP* bands. If more accurate methods are needed, such as for very steep spectra or for spectra with emission lines, then a full integration over the bandpass should be done.

REFERENCES

- Acquaviva, V., Bartolo, N., Matarrese, S., & Riotto, A. 2003, *Nucl.Phys.*, B667, 119
- Ali-Haïmoud, Y., Hirata, C. M., & Dickinson, C. 2009, *MNRAS*, 395, 1055
- Alishahiha, M., Silverstein, E., & Tong, D. 2004, *Phys.Rev.*, D70, 123505
- Barnes, C., et al. 2002, *ApJS*, 143, 567
- . 2003, *ApJS*, 148, 51
- Barrett, R., et al. 1994, *Templates for the Solution of Linear Systems: Building Blocks for Iterative Methods*, 2nd Edition (Philadelphia, PA: SIAM)
- Battaglia, N., Bond, J. R., Pfrommer, C., & Sievers, J. L. 2012, *ApJ*, 758, 75
- Bennett, C. L., et al. 1992, *ApJ*, 396, L7
- . 2003a, *ApJS*, 148, 97

Table 20. Interpolation data^a for $T = (\Delta T / \Delta T_A) \sum_{i=1}^3 w_i T_A(\nu_i)$

Band	ν_1^b	ν_2^b	ν_3^b	w_1	w_2	w_3	$\Delta T / \Delta T_A^c$
K	20.6	22.8	24.9	0.332906	0.374325	0.292768	1.013438
Ka	30.4	33.0	35.6	0.322425	0.387532	0.290043	1.028413
Q	37.8	40.7	43.8	0.353635	0.342752	0.303613	1.043500
V	55.7	60.7	66.2	0.337805	0.370797	0.291399	1.098986
W	87.0	93.5	100.8	0.337633	0.367513	0.294854	1.247521

^aAs stated in the text, the frequencies shown here have an arbitrariness that prevents them from being a meaningful representation of the center frequency or width of the *WMAP* bandpasses. The weights w_i account for this arbitrariness; they make the overall approximation accurate. The weights and conversion factors are given to a precision of about 6 significant figures. Our approximation is not that accurate; we provide this precision to allow people to more easily reproduce our results and to make round-off error negligible.

^bFrequencies are given in GHz.

^cThis is the antenna to thermodynamic conversion for an unweighted average of radiometers, which should be used for this approximation.

- . 2003b, *ApJS*, 148, 1
- . 2003c, *ApJ*, 583, 1
- . 2011, *ApJS*, 192, 17
- Bond, J., Jaffe, A. H., & Knox, L. 1998, *Phys.Rev.*, D57, 2117
- Bond, J. R., Jaffe, A. H., & Knox, L. 2000, *ApJ*, 533, 19
- Brandt, T. D. & Draine, B. T. 2012, *ApJ*, 744, 129
- Buchbinder, E. I., Khoury, J., & Ovrut, B. A. 2007, *JHEP*, 0711, 076
- Chen, X., Huang, M.-x., Kachru, S., & Shiu, G. 2007, *JCAP*, 0701, 002
- Chen, X. & Wright, E. L. 2008, *ApJ*, 681, 747
- . 2009, *ApJ*, 694, 222
- Cheung, C., Creminelli, P., Fitzpatrick, A. L., Kaplan, J., & Senatore, L. 2008a, *JHEP*, 0803, 014
- Cheung, C., Fitzpatrick, A. L., Kaplan, J., & Senatore, L. 2008b, *JCAP*, 0802, 021
- Creminelli, P., Nicolis, A., Senatore, L., Tegmark, M., & Zaldarriaga, M. 2006, *JCAP*, 0605, 004
- Creminelli, P. & Senatore, L. 2007, *JCAP*, 0711, 010
- Creminelli, P. & Zaldarriaga, M. 2004, *JCAP*, 0410, 006
- Dennison, B., Simonetti, J. H., & Topasna, G. A. 1998, *Publications of the Astronomical Society of Australia*, 15, 147
- Dickinson, C., Davies, R. D., & Davis, R. J. 2003, *MNRAS*, 341, 369
- Dickinson, C., Peel, M., & Vidal, M. 2011, *MNRAS*, 418, L35
- Dickinson, C., et al. 2009, *ApJ*, 705, 1607
- Dobler, G. & Finkbeiner, D. P. 2008, *ApJ*, 680, 1222
- Dobler, G., Finkbeiner, D. P., Cholis, I., Slatyer, T., & Weiner, N. 2010, *ApJ*, 717, 825
- Duncan, A. R., Stewart, R. T., Haynes, R. F., & Jones, K. L. 1995, *MNRAS*, 277, 36

- Dunkley, J., et al. 2009, *ApJS*, 180, 306
- Dvali, G., Gruzinov, A., & Zaldarriaga, M. 2004, *Phys.Rev.*, D69, 023505
- Eriksen, H. K., et al. 2007, *ApJ*, 656, 641
- Finkbeiner, D. P. 2003, *ApJS*, 146, 407, accepted (astro-ph/0301558)
- . 2004, *ApJ*, 614, 186
- Finkbeiner, D. P., Davis, M., & Schlegel, D. J. 1999, *ApJ*, 524, 867
- Fixsen, D. J. 2009, *ApJ*, 707, 916
- Fixsen, D. J., et al. 2011, *ApJ*, 734, 5
- Gaustad, J. E., McCullough, P. R., Rosing, W., & Van Buren, D. 2001, *PASP*, 113, 1326
- Gervasi, M., Tartari, A., Zannoni, M., Boella, G., & Sironi, G. 2008, *ApJ*, 682, 223
- Gold, B., Odegard, N., Weiland, J., Hill, R., Kogut, A., et al. 2011, *Astrophys.J.Suppl.*, 192, 15
- Gold, B., et al. 2009, *ApJS*, 180, 265
- . 2011, *ApJS*, 192, 15
- Gorski, K. M., Hivon, E., Banday, A. J., Wandelt, B. D., Hansen, F. K., Reinecke, M., & Bartlemann, M. 2005, *ApJ*, 622, 759
- Greason, M. R., et al. 2012, Wilkinson Microwave Anisotropy Probe (WMAP): Nine Year Explanatory Supplement, http://lambda.gsfc.nasa.gov/data/map/doc/MAP_supplement.pdf
- Gregory, P. C., Scott, W. K., Douglas, K., & Condon, J. J. 1996, *ApJS*, 103, 427
- Griffith, M. R., Wright, A. E., Burke, B. F., & Ekers, R. D. 1994, *ApJS*, 90, 179
- . 1995, *ApJS*, 97, 347
- Groeneboom, N. E. & Eriksen, H. K. 2009, *ApJ*, 690, 1807
- Gruzinov, A. 2005, *Phys.Rev.*, D71, 027301
- Haffner, L. M., Reynolds, R. J., Tufte, S. L., et al. 2003, *ApJ*, 149, in press

- Hanson, D., Lewis, A., & Challinor, A. 2010, *Phys. Rev. D*, 81, 103003
- Hanson, D., Smith, K. M., Challinor, A., & Liguori, M. 2009, *Phys.Rev.*, D80, 083004
- Haslam, C. G. T., Klein, U., Salter, C. J., Stoffel, H., Wilson, W. E., Cleary, M. N., Cooke, D. J., & Thomasson, P. 1981, *A&A*, 100, 209
- Haslam, C. G. T., Salter, C. J., Stoffel, H., & Wilson, W. E. 1982, *A&AS*, 47, 1
- Healey, S. E., Fuhrmann, L., Taylor, G. B., Romani, R. W., & Readhead, A. C. S. 2009, *AJ*, 138, 1032
- Hill, R. S., et al. 2009, *ApJS*, 180, 246
- Hinshaw, G., et al. 2003a, *ApJS*, 148, 63
- . 2003b, *ApJS*, 148, 135
- . 2007, *ApJS*, 170, 288
- . 2009, *ApJS*, 180, 225
- . 2012, Submitted to *ApJS*, –
- Hivon, E., Górski, K. M., Netterfield, C. B., Crill, B. P., Prunet, S., & Hansen, F. 2002, *ApJ*, 567, 2
- Jarosik, N., et al. 2003a, *ApJS*, 145, 413
- . 2003b, *ApJS*, 148, 29
- . 2007, *ApJS*, 170, 263
- . 2011, *ApJS*, 192, 14
- Kogut, A., et al. 1992, *ApJ*, 401, 1
- . 2003, *ApJS*, 148, 161
- . 2007, *ApJ*, 665, 355
- Komatsu, E., Spergel, D. N., & Wandelt, B. D. 2005, *Astrophys.J.*, 634, 14
- Komatsu, E., et al. 2003, *ApJS*, 148, 119
- . 2009, *ApJS*, 180, 330

- . 2011, *ApJS*, 192, 18
- Kühr, H., Witzel, A., Pauliny-Toth, I. I. K., & Nauber, U. 1981, *A&AS*, 45, 367
- Lanz, L. 2012, in *ADA7 - Seventh Conference on Astronomical Data Analysis*, held in Cargèse, Corsica, France, 14-18 May 2012. Online at <http://ada7.cosmostat.org/proceedings.php>, id. 6 94 GHz., ed. J.-L. Starck & C. Surace
- Larson, D., Dunkley, J., Hinshaw, G., Komatsu, E., Nolta, M., et al. 2011, *Astrophys.J.Suppl.*, 192, 16
- Larson, D., et al. 2011, *ApJS*, 192, 16
- Lawson, K. D., Mayer, C. J., Osborne, J. L., & Parkinson, M. L. 1987, *MNRAS*, 225, 307
- Lazarian, A. & Draine, B. T. 2000, *ApJ*, 536, L15
- Lehners, J.-L. & Steinhardt, P. J. 2008a, *Phys. Rev. D*, 78, 023506
- . 2008b, *Phys. Rev.*, D77, 063533
- Lehtinen, K., Juvela, M., & Mattila, K. 2010, *A&A*, 517, A79
- Lewis, A., Challinor, A., & Hanson, D. 2011, *JCAP*, 1103, 018
- Lewis, A., Challinor, A., & Lasenby, A. 2000, *ApJ*, 538, 473
- Linde, A. D. & Mukhanov, V. F. 1997, *Phys.Rev.*, D56, 535
- López-Caraballo, C. H., Rubiño-Martín, J. A., Rebolo, R., & Génova-Santos, R. 2011, *ApJ*, 729, 25
- Lyth, D. H., Ungarelli, C., & Wands, D. 2003, *Phys.Rev.*, D67, 023503
- Maldacena, J. M. 2003, *JHEP*, 0305, 013
- Mather, J. C., et al. 1990, *ApJ*, 354, L37
- . 1994, *ApJ*, 420, 439
- Mattila, K., Juvela, M., & Lehtinen, K. 2007, *ApJ*, 654, L131
- Meyerdierks, H., Heithausen, A., & Reif, K. 1991, *A&A*, 245, 247
- Nolta, M. R., et al. 2009, *ApJS*, 180, 296

- O’Dea, D. T., Clark, C. N., Contaldi, C. R., & MacTavish, C. J. 2012, *MNRAS*, 419, 1795
- Oster, L. 1961, *ApJ*, 134, 1010
- Page, L., et al. 2003a, *ApJS*, 148, 39
- . 2003b, *ApJS*, 148, 233
- . 2003c, *ApJ*, 585, 566
- . 2007, *ApJS*, 170, 335
- Paladini, R., Burigana, C., Davies, R. D., Maino, D., Bersanelli, M., Cappellini, B., Platania, P., & Smoot, G. 2003, *A&A*, 397, 213
- Peiris, H. V., et al. 2003, *ApJS*, 148, 213
- Penzias, A. A. & Wilson, R. W. 1965, *ApJ*, 142, 419
- Planck Collaboration IX. 2012, *ArXiv e-prints*
- Ramos, E. P. R. G., Vio, R., & Andreani, P. 2011, *A&A*, 528, A75
- Refregier, A., Spergel, D. N., & Herbig, T. 2000, *ApJ*, 531, 31
- Riess, A. G., et al. 2011, *ApJ*, 730, 119
- Rubiño-Martín, J. A., López-Caraballo, C. H., Génova-Santos, R., & Rebolo, R. 2012, *Advances in Astronomy*, 2012
- Schlegel, D. J., Finkbeiner, D. P., & Davis, M. 1998, *ApJ*, 500, 525
- Scodeller, S., Hansen, F. K., & Marinucci, D. 2012, *ApJ*, 753, 27
- Seljak, U. & Zaldarriaga, M. 1996, *ApJ*, 469, 437
- Senatore, L., Smith, K. M., & Zaldarriaga, M. 2010, *JCAP*, 1001, 028
- Sievers, J. L., et al. 2003, *ApJ*, 591, 599
- Silsbee, K., Ali-Haïmoud, Y., & Hirata, C. M. 2011, *MNRAS*, 411, 2750
- Smith, K. M., Senatore, L., & Zaldarriaga, M. 2009, *JCAP*, 0909, 006
- Smith, K. M., Zahn, O., & Dore, O. 2007, *Phys.Rev.*, D76, 043510
- Smith, K. M. & Zaldarriaga, M. 2011, *Mon.Not.Roy.Astron.Soc.*, 417, 2

- Smoot, G. F., et al. 1992, *ApJ*, 396, L1
- Spergel, D. N., et al. 2003, *ApJS*, 148, 175
- . 2007, *ApJS*, 170, 377
- Strong, A. W., Orlando, E., & Jaffe, T. R. 2011, *A&A*, 534, A54
- Tartari, A., Zannoni, M., Gervasi, M., Boella, G., & Sironi, G. 2008, *ApJ*, 688, 32
- Tegmark, M. 1997, *Phys.Rev.*, D55, 5895
- Tegmark, M. & de Oliveira-Costa, A. 1998, *ApJ*, 500, L83
- Trushkin, S. A. 2003, *Bull. Spec. Astrophys. Obs. N. Caucasus*, 55, 90
- Verde, L., et al. 2003, *ApJS*, 148, 195
- Wang, X., Tegmark, M., Jain, B., & Zaldarriaga, M. 2003, *Phys. Rev.*, D68, 123001
- Wehus, I. K., Ackerman, L., Eriksen, H. K., & Groeneboom, N. E. 2009, *ApJ*, 707, 343
- Weiland, J. L., et al. 2011, *ApJS*, 192, 19
- Witt, A. N., Gold, B., Barnes, III, F. S., DeRoo, C. T., Vihj, U. P., & Madsen, G. J. 2010, *ApJ*, 724, 1551
- Woermann, B., Gaylard, M. J., & Otrupcek, R. 2000, *MNRAS*, 315, 241
- Wright, A. E., Griffith, M. R., Burke, B. F., & Ekers, R. D. 1994, *ApJS*, 91, 111
- Wright, A. E., Griffith, M. R., Hunt, A. J., Troup, E., Burke, B. F., & Ekers, R. D. 1996, *ApJS*, 103, 145
- Wright, E. L., et al. 1992, *ApJ*, 396, L13
- . 2009, *ApJS*, 180, 283
- Zaldarriaga, M. 2004, *Phys.Rev.*, D69, 043508